

**Beyond the Band Edge: Extending the Reach of Colloidal Nanocrystals
in Active Photonic Devices**

Ivo Tanghe

Doctoral dissertation submitted to obtain the academic degree of
Doctor of Engineering Physics

Supervisors

Prof. Dries Van Thourhout, PhD* - Prof. Pieter Geiregat, PhD**

* Department of Information Technology
Faculty of Engineering and Architecture, Ghent University

** Department of Chemistry
Faculty of Sciences, Ghent University

June 2023



ISBN 978-94-6355-719-1

NUR 926, 971

Wettelijk depot: D/2023/10.500/51

Members of the Examination Board

Chair

Prof. Em. Daniël De Zutter, PhD, Ghent University

Other members entitled to vote

Prof. Alberto Curto, PhD, Ghent University

Prof. Zeger Hens, PhD, Ghent University

Prof. Poul Petersen, PhD, Ruhr Universität Bochum, Germany

Prof. Riccardo Sapienza, PhD, Imperial College London, United Kingdom

Prof. Henk Vrielinck, PhD, Ghent University

Supervisors

Prof. Dries Van Thourhout, PhD, Ghent University

Prof. Pieter Geiregat, PhD, Ghent University

Dankwoord

It is Sunday evening at the time of writing, the submission deadline quickly approaching. Here I am, reflecting back on the five and a half years, thinking of who to thank. So many people, so much thanks to give.

I started my PhD full of hope, looking at the latest research of our team and thinking about how I would take all of this to the next level: make some top of the line mode-locked lasers (yes, that was once the goal). Reality soon caught up with me. My contract started in October of 2018, and until the first lockdowns due to covid, I did not manage to create any working lasers (so I cannot even use the lockdown as an excuse). Not only did the various approaches I took yield nothing, I was not even able to reproduce the work from the colleagues who came before me. Whoops.

With varying levels of enthusiasm, I kept trying, and failing. But when the final year of my contract started (2022) I had given up hope of creating any type of working device, and was ready to wrap up my PhD based on spectroscopy alone. But then things quickly changed, since the first demonstration of on-chip amplification with bulk CdS rapidly led to more success, and more or less a year ago as I am writing this, the first bulk CdS lasers were demonstrated. So this is what it felt to actually make something that worked. Newly encouraged, we managed to quite rapidly turn this first success into a thorough analysis and understanding, showing that we actually had something remarkable on our hands. Now, the next steps do not only seem easy and reachable, they seem just a matter of doing.

As my work guided me to various fields, there are many people to thank without whom this work would not be possible. First, I would like to thank Pieter Geiregat who after snagging me up for my master's dissertation has introduced me to the field of non-linear spectroscopy and has supported me when expressing my ambition in pursuing a PhD. In the other faculty, I have to specifically thank my promotor Dries Van Thourhout and my former colleague Lukas Elsinger. With their help I was able to navigate working in the cleanroom and learning the basics of photonics necessary to make, measure and understand integrated devices.

Besides them, I have to thank my other colleagues on the colloidal QD team who I have worked with over the years. Zeger, who's ability to spot the correct answer while I am stuck on a problem continually impresses me and has on numerous occasions helped me moving forward. Iwan, who's voice I often hear in my head, saying "stop simulating and actually go do something", a push I sometimes need since actually doing something seems to go against my very nature. Besides the professors I had fellow PhD students and Post-docs in the team: Chao, Korneel, Servet, Yuhao, Filipe, Onur, Delphine, Carmelita and Chandu. You have each helped me in your own specific way, and for that I am very grateful.

This work involves using Colloidal Nanocrystals, which are made through a wet chemical synthesis. I am not a chemist, so I do not know how to do a wet chemical synthesis. Safe to say, without people providing me with samples throughout the years, Iwan's words would have fallen on deaf ears. With that being said, I want to thank Shalini, Renu and Ali for making CdSe nanoplatelets for me to use. I'd also like to thank Emile, Natalia and Margarita for the CdSe/CdS Quantum Dots. Last but not least, I would also like to thank Ali and Margarita for making the bulk nanocrystals. Specifically, Margarita was able to optimize the CdS bulk synthesis that at first gave some nice preliminary Transient Absorption results, and turned it into a material with very exciting prospects. Without her work, this book would most definitely contain a chapter less. I also have to thank Hannes, who provided me with a ZnSe/ZnS sample. Without you, Figure 8.21 would not have been possible.

I would also like to thank Pieter S., Pengshang, Chandu and Gabriele for including me in various TMD projects throughout the years. It was always nice to put some of my abilities to use for completely different projects.

I spent a lot of time in the lab doing spectroscopy, and I am very glad to have had colleagues working with me there who were always understanding the necessity for flexibility and cooperation. Besides the people already listed, I would like to extend my thanks also to Jasper, Davide and Dobromil.

Talking about ultrafast spectroscopy, I have to thank Kai-Wen, Isabella and Ronnie for various measurements done through the years in Wellington. This data gathered in the complete other side of the world was the cherry on top for one of my papers, and of high importance in many chapters in this work.

Moving on more to the photonics side, we are fortunate enough to have excellent permanent staff around in the cleanroom who are always available to assist if needed. Steven and Liesbet for general cleanroom management and Muhammad who was ready every waking minute with e-beam assistance. On the same token I would like to thank Clemens for giving me lots of guidance when it comes to doing measurements in the lab.

Jasper and Tom, I owe you my gratitude for helping me out so much over the last year for trying to get photonic crystal theory into my thick skull. It has been great to work closely together with you and the master thesis students this year.

I started the PhD together with two people that I had studied with together, who through the years have always been ready for discussions about random ideas (about how to win from casino's, launching a new currency and making a UGent based podcast), but who's insights have been really valuable, and for that I'd like to thank you Isaac and Stijn. My first weeks I also got to know Khannan, who and is very knowledgeable about integrated photonics and has helped me understand many different concepts. I couldn't have wished for a better office mate. I hope to attend

all your defences soon! (but I was the first, don't forget that).

Last but not least, it has been my absolute privilege in supervising many master thesis students over the years. This was the absolute highlight of my work. Trying to mentor people in the field has shown me my own gaps of knowledge, as hard as it is to admit, and your tricky questions have learned me more than you know. So for that, I would like to thank Korneel, Servet, Rutger, Kai-Wen, Jan and Fatemeh.

Ik moet uiteraard ook enkele mensen uit mijn persoonlijk leven bedanken. Eerst en vooral, mijn liefste Unuzeleirs, je zal mij nooit anders dan vol lof en liefde over jullie allemaal horen praten. Doorheen de jaren waren jullie mijn rots in de branding, mijn ridders op het witte paard, mijn veilige haven. Zonder jullie steun was ik al lang de moed verloren geraakt en daarom hou ik van jullie allemaal. Jullie hebben elk op je eigen manier deze reis mogelijk gemaakt, en ik wil jullie dan ook bedanken door jullie namen hier te ver-eeuwigen, in inkt op papier. Kwestie van absoluut geen volgorde in de namen te steken heb ik volgorde dan ook gerandomiseerd: Pello, Leon, Jesse, Felix, Sophie, Rian, Gilles, Marie, Thomas, Jorge, Igor, Laure, Ahmet, Ushua, Margot, Lucie, Christian, Jolan, Amber, Jakob. Merci om er te zijn voor mij, om mijn hart te luchten maar ook om alles even te vergeten en gewoon te genieten!

Verder wil ik ook nog specifiek mijn vader Wim en mijn broer Gilles bedanken. Van jonge leeftijd werd mijn interesse in wetenschap aangewakkerd door onze vele discussies. Dit is dus ook jullie verdienste!

De belangrijkste persoon hou ik natuurlijk voor op het einde: Diete, je was er van het begin tot nu bij, ik draag dan ook mijn doctoraat met heel veel liefde aan jou op. Je onuitputtelijke steun de voorbije jaren heeft me meer geholpen dan je beseft. Al het falen betekende niets wetende dat ik thuis kon komen en bij jou kon zijn, en alle successen voelden zo veel beter wetende dat ik ze met jou kon vieren. Laten we het einde van dit hoofdstuk dan ook samen vieren!

Ivo Tanghe
May 2023

Contents

List of Acronyms	xiii
Nederlandse Samenvatting	xix
English Summary	xxv
I Background	xxxi
1 Introduction	1
1.1 Research Background	1
1.2 Thesis Outline	9
1.3 Publications	12
1.3.1 List of Articles	12
1.3.2 List of Conference Contributions	13
2 Colloidal Nanocrystals	21
2.1 Introduction	21
2.2 Wet Chemical Synthesis	22
2.3 Linear Optical Properties	24
2.3.1 Absorption and Emission of Light	24
2.3.2 Quantum Confinement and the Optical Band Gap	25
2.3.3 Maxwell-Garnett Effective Medium Approximation	27
2.3.3.1 Intrinsic Absorption	29

2.3.4	Maxwell-Garnett and Intrinsic Absorption for General NCs	31
2.3.4.1	Multi-layered QD or Gradient QD	32
2.4	Non-linear Optical Properties	34
2.4.1	Optical Gain in Colloidal Nanocrystals	34
2.4.2	Transient Absorption Spectroscopy	35
2.4.2.1	Measurement Setup	37
2.4.2.2	Effects measured through Transient Absorption Spectroscopy	39
2.4.2.3	Material Properties from Transient Absorption	40
2.4.3	Modelling of the Optical Gain in Colloidal Nanocrystals	43
2.4.3.1	Strong Confinement	43
2.4.3.2	Without Strong Confinement	45
2.4.4	Ultrafast Photoluminescence	47
2.4.5	Ultrafast Phase Effects	49
2.5	Thin Films of Colloidal Nanocrystals	53
2.5.1	Film Deposition Methods	53
2.5.1.1	Drop-casting	53
2.5.1.2	Spincoating	54
2.5.1.3	Langmuir-Blodgett Deposition	55
2.5.1.4	Inkjet Printing	55
2.5.2	Patterning NCs through Lift-off	56
3	Integrated Photonics	63
3.1	Introduction	63
3.2	Silicon Nitride Platform for Visible Photonics	64
3.3	Integrated Photonic Components	67
3.3.1	Passive Components	67
3.3.1.1	Waveguides	67
3.3.1.2	Coupled Waveguides	69
3.3.1.3	Ring Resonators	71

3.3.2	Active Components	74
3.3.2.1	Active Waveguides	74
3.3.2.2	Fabry-Perot Lasers	77
3.3.2.3	Disk and Ring Lasers	79
3.3.2.4	Distributed Bragg Reflector Lasers	81
3.3.2.5	1D Distributed Feedback Lasers	82
3.3.2.6	2D Distributed Feedback Lasers	85
3.3.2.7	Photonic Crystal Lasers	86
3.3.2.8	Mach-Zehnder Interferometers	91

II Broadband Ultrafast Properties of Colloidal Nanocrystals **95**

4	Gain Through Core/Shell Quantum Dots with Thick CdS Shells	97
4.1	Introduction	97
4.2	Material Description	99
4.3	Energy Level Calculations	100
4.4	Transient Absorption Spectroscopy Measurements	106
4.4.1	Low Fluency Measurements	106
4.4.2	High Fluency Measurements	108
4.5	State Filling	115
4.5.1	Explanation of the Model	115
4.5.2	Adding the Temperature	115
4.5.3	Applying the model to the $k \cdot p$ calculations	116
4.6	Conclusions	121
5	Bulk CdS Colloidal Nanocrystals	127
5.1	Introduction	127
5.2	Material Description	129
5.2.1	Synthesis	130
5.2.1.1	Materials and Precursors	130
5.2.1.2	Synthesis Protocols	131

5.2.2	Intrinsic Absorption	131
5.2.3	Cross-section	132
5.2.4	Structural Characterisation	132
5.3	Gain Measurements in gCdS	133
5.4	Modelling of the Material	136
5.4.1	Bulk Gain Model	136
5.4.1.1	Band Gap Renormalisation	139
5.4.2	Second order recombination	142
5.5	Conclusions	145
6	Carrier Temperature in Bulk Nanocrystals	151
6.1	Introduction	151
6.2	Carrier Temperature	153
6.3	Model Derivation	156
6.3.1	Temperature from Change in Absorption	156
6.3.2	Temperature from Ultrafast Luminescence	159
6.3.3	Comparison	162
6.4	High Energy Limits	164
6.4.1	About C_C and C_V	164
6.4.1.1	$\nu \gg e^{-1} \Rightarrow \frac{n}{N_{i,eff}} \gg e^{-1}$	165
6.4.1.2	$\nu \ll e^{-1} \Rightarrow \frac{n}{N_{i,eff}} \ll e^{-1}$	166
6.4.2	Exponential Decays	168
6.4.3	Experimental Results	171
6.5	Conclusions	173
7	Transient Phase Effects in Colloidal Nanocrystals	177
7.1	Definitions	179
7.2	Iterative Algorithm	180
7.2.1	Maxwell Garnet Effective Medium	180
7.2.2	Kramers-Krönig Relations	181
7.2.3	Complete Procedure	183
7.3	Phase shift Calculation of Composite Media	185
7.4	4.5ML CdSe Colloidal Quantum Wells	186
7.4.1	Material Description	186

7.4.2	Intrinsic Absorption Coefficient	187
7.4.2.1	Exact vs. approximated depolarisation factors	188
7.4.3	Refractive Index in Ground State	190
7.4.4	Refractive Index under Excitation	191
7.4.4.1	TA data	191
7.4.4.2	Oscillator Strength	194
7.4.4.3	Resonant excitation	194
7.4.4.4	Polarized Excitation	195
7.4.4.5	Discussion	195
7.4.5	Verification through FDI Measurements	197
7.5	Transient Phase Effects in Colloidal CdSe/CdS Quantum Dots	198
7.5.1	Material Description	198
7.5.2	Intrinsic Absorption Coefficient	199
7.5.3	Refractive Index in Ground State	200
7.5.4	Refractive Index under excitation	200
7.6	Transient Phase Effects in bulk CdS colloidal NCs	202
7.6.1	Material Description	202
7.6.2	Intrinsic Absorption Coefficient	202
7.6.3	Refractive Index in Ground State	202
7.6.4	Refractive Index under Excitation	203
7.7	Conclusions	204

III Colloidal Nanocrystals in Integrated Photonic Devices 209

8	Lasers with Bulk CdS Nanocrystals	211
8.1	Amplified Spontaneous Emission in Bulk CdS thin films .	213
8.2	Photonic Crystal Slab Lasers	217
8.2.1	Simulating PhC Lasers	217
8.2.1.1	Single Period with Incoming Plane Wave	218
8.2.1.2	1D PhC Devices	219
8.2.1.3	2D PhC Devices	223

8.2.1.4	Photonic Bandstructure Simulations . . .	228
8.2.2	Photonic Crystal Slab Lasers with bulk CdS NCs .	234
8.2.2.1	Laser Measurements	235
8.3	On-Chip Optical Gain in other Bulk Nanocrystals	240
8.3.1	CdSe ASE and Lasing	240
8.3.2	ZnSe ASE and Lasing	242
8.4	Conclusions	243
9	Thermal Optimization of Colloidal Nanocrystal Lasers	247
9.1	Introduction	249
9.1.1	Thermal Conductivities	249
9.1.1.1	NC layer	249
9.1.1.2	Dielectric Surroundings	250
9.1.2	Thermal Power in the System	250
9.1.3	Boundary Conditions	252
9.1.4	Example	252
9.2	The Stack as a Series of Resistors	254
9.3	Thermal Substrates and Coatings	257
9.4	Disk and ring lasers	259
9.5	Slot Waveguides	261
9.5.1	Simulations	262
9.5.2	Processing	263
9.6	Conclusions	267
10	Transient Phase in Integrated Devices	271
10.1	Introduction	272
10.2	Optically operated Mach-Zehnder Interferometers based on CdSe/CdS QDs	273
10.2.1	From Intrinsic to Device Properties	273
10.2.2	Mach-Zehnder Interferometer Design	275
10.2.3	Linear Characterisation	276
10.2.4	Proposed Modulation Measurement	278
10.3	Refractive Index Change in Ring Lasers	281

10.4 Conclusions	284
IV Conclusions and Perspectives	287
V Appendices	295
A Dielectric sphere in a uniform electric field	297
B Extras on $k \cdot p$ simulations	301
B.1 Theoretical Analysis of the electronic Structure	301
B.1.1 Overview on Selection Rules in Spherical Nanocrystals	302
B.1.2 Electronic Structure of CdSe/CdS Nanocrystals . .	303
B.1.3 Supporting Experimental Data	315

List of Acronyms

A

ASE	Amplified Spontaneous Emission
AWG	Arrayed Waveguide Grating

B

BGR	Band Gap Renormalisation
BTA	Boltzmann Tail Approximation

C

CdSe	Cadmium Selenide
CdS	Cadmium Sulphide
CdO	Cadmium Oxide
CB	Conduction Band
CaF ₂	Calcium di-Fluoride
CHB	cyclohexylbenzene
CsPbBr ₃	Cesium Lead Bromide
CsSnBr ₃	Cesium Tin Bromide
CW	Continuous Wave

D

DOS	Density Of States
dB	Decibel
DBR	Distributed Bragg Reflector

DFB

Distributed Feedback

E

e-beam

electron-beam

ER

Extinction Ratio

F

FDTD

Finite-Difference Time-Domain

FD

Fermi-Dirac

FDI

Frequency Domain Interferometry

FSR

Free Spectral Range

FP

Fabry Perot

FOM

Figure of Merit

FF

Far Field

FIB

Focused Ion Beam

FWHM

Full Width Half Max

FE

Finite Elements

G

GaAs

Gallium Arsenide

GSQD

Giant Shell Quantum Dot

H

HH

Heavy Hole

I

InP

Indium Phosphide

InGaAs

Indium Gallium Arsenide

IR

Infrared

ICP

Inductively Coupled Plasma

IB

Intraband

K

KK

Kramers-Krönig

L

LED

Light Emitting Diode

LF

Local Field

LH

Light Hole

LF-HT

Low Frequency - High Temperature

LPCVD

Low-Pressure

Chemical-Vapour-Deposition

M

ML

Monolayer

MG

Maxwell-Garnett

MBE

Molecular Beam Epitaxy

MF-HT

Mixed Frequency - High

Temperature

MF-LT

Mixed Frequency - Low

Temperature

MZI

Mach-Zehnder Interferometer

MaPbBr₃

Methylammonium Lead Tribromide

N

NC

Nanocrystal

NPL

Nano Platelet

NIR

Near Infrared

NF

Near Field

O

OIOH

oleyl alcohol

OPA

Optical Parametric Amplifier

OD

Optical Density

ODE

1-octadecene

OA

Oleic Acid

P

PbS

PbSe

PL

PPI

PECVD

Chemical-Vapour-Deposition

PIC

PhC

PML

Lead Sulphide

Lead Selenide

Photoluminescence

Pixels Per Inch

Plasma-Enhanced

Photonic Integrated Circuit

Photonic Crystal

Perfectly Matched Layer

Q

QD

QY

Quantum Dot

Quantum Yield

R

RPM

RT

Rounds Per Minute

Round Trip

S

SEM

SC

SiO_x

SiN_x

SOI

S

Se

SoCl₂

Scanning Electron Microscopy

Spincoating

Silicon Oxide

Silicon Nitride

Silicon-On-Insulator

Sulphur

Selenium

Thionyl Chloride

T

TOPO

TDPA

TOP

Trioctylphosphine oxide

n-tetradecylphosphonic acid

trioctylphosphine

Contents

TOP-Se	trioctylphosphine selenide
TEM	Transmission Electron Microscopy
TAS	Transient Absorption Spectroscopy
TGPLS	Transient Grating
Photoluminescence Spectroscopy	
TEM	Transversal Electromagnetic
TE	Transversal Electric
TM	Transversal Magnetic
TMM	Transfer Matrix Method
TRI	Transient Refractive Index
TMD	Transition-Metal Dichalcogenides
U	
UV	Ultra Violet
UV/VIS	Ultra Violet/Visible
V	
VB	Valence Band
VSL	Variable Stripe Length
VCSEL	Vertical-Cavity
Surface-Emitting-Laser	
W	
wz	wurtzite
WGM	Whispering Gallery Mode
X	
X	Exciton
XX	Bi-exciton
XRD	X-Ray Diffraction
Z	
ZnSe	Zinc Selenide

ZnS

Zinc Sulphide

zb

Zinc Blende

Nederlandse Samenvatting

Colloïdale nanokristallen (NC's) zijn zeer kleine (nanometerschaal) halfgeleiderdeeltjes die typisch uit een paar duizend atomen bestaan en die colloïdaal stabiel worden gehouden door het oppervlak te passiveren met organische liganden, dit zijn vetzuren zoals oliezuur. Door hun kleine formaat zijn ladingsdragers sterk opgesloten in de ruimte, wat de opto-elektronische eigenschappen van NC's beïnvloedt in vergelijking met hun bulk-tegenhanger. De kwantumopsluiting veroorzaakt een toename van de bandgap E_g van het materiaal. Hoe kleiner het deeltje, hoe groter de bandgap, waardoor het golflengtegebied van emissie en optische versterking verschuift. Bovendien wordt de Density Of States (DOS) gediscrèteerd, waardoor de oscillatorsterkte in smalle banden wordt gegroepeerd.

Colloïdale NC's worden gemaakt door middel van een natte chemische synthese, die in hoge mate kan worden gecontroleerd om de gewenste grootte te creëren. Door de grootte, het materiaal (CdSe, CdS, ZnSe, ZnS, PbS, PbSe, InP, InAs, ...) en geometrie (0D-dot, 1D-staaf, 2D-plaat) te wijzigen, ontstaat er veel vrijheid om elk nanokristal te vervaardigen dat je zou kunnen wensen voor toepassing, in een breed golflengtegebied (350-2000 nm). Het uitbreiden van deze lijst van materialen en geometrieën is een zeer actief onderzoeksgebied. Het maken van complexere heterogene structuren, waarbij bijvoorbeeld een materiaal in een kern wordt omgeven door een ander materiaal in een schil (zoals CdSe/CdS), kan

worden gebruikt voor verdere controle van de opto-elektronische eigenschappen, en maakt de materialen nog veelzijdiger, terwijl deze schil ook het NC-oppervlak beschermt tegen vallen voor ladingsdragers. Dit alles kan worden gekoppeld aan het feit dat al deze NC's uiteindelijk op dezelfde manier worden verwerkt: het zijn hele kleine halfgeleiderdeeltjes verspreid in een oplosmiddel. Deze vergelijkbare verwerking maakt ze zeer aantrekkelijk voor fotonische toepassingen, en dit werk gaat over het gebruik van colloïdale NC's in geïntegreerde fotonica.

Fotonica is de wetenschap en toepassing van het opwekken, detecteren en manipuleren van licht door emissie, transmissie, modulatie, signaalverwerking, schakelen, versterken en waarnemen. Simpel gezegd: het is de studie van licht. Meer specifiek maakt geïntegreerde fotonica gebruik van platformen die voor het eerst zijn ontwikkeld voor elektronica om licht op de chip te geleiden en te manipuleren, op micro- en nanoschaal. In dit werk ligt de focus op geïntegreerde siliciumfotonica. Aangezien silicium een materiaal is met een indirecte bandgap, moet heterogene integratie plaatsvinden om geïntegreerde lichtbronnen te creëren. Colloïdale NC's zijn een interessante kandidaat om dit te proberen. Bovendien, aangezien colloïdale NC's voornamelijk emissie en optische versterking in het zichtbare gebied vertonen, is silicium hier problematisch vanwege de hoge absorptie. Om dit te omzeilen wordt Silicium Nitride (SiN_x) gegroeid op Silicium Oxide (SiO_x) gebruikt, materialen die niet in het hele zichtbare gebied licht absorberen.

Het bouwen van geïntegreerde colloïdale NC-lasers op een SiN_x -platform is in het verleden al aangetoond. Hier onderzoeken we verschillende manieren om eerder gemaakte geïntegreerde lasers te verbeteren: (1) door de versterkingsmechanismen in colloïdale NC's diepgaand te onderzoeken en te kijken naar alternatieve materialen, en (2) door de fotonische trilholte te optimaliseren. Verder worden alternatieve toepassingen voor colloïdale NC's in geïntegreerde apparaten onderzocht, aangezien het in staat zijn om een materiaal naar transparantie en optische versterking te duwen ook de materiaaleigenschappen op andere manieren beïnvloedt, namelijk door de brekingsindex te veranderen.

In een eerste studie wordt de gain in de schil van CdSe/CdS Giant Shell Quantum Dot (GSQD) systemen onderzocht. De enorme schil en excitatie met hoge energie leiden tot interessante en eerder niet bekeken versterkingsmechanismen. Meerdere energietoestanden in de schaal tonen extra versterkingsbanden, die eerder ook Amplified Spontaneous Emission (ASE) vertoonden. Deze toestanden worden berekend door middel van $k \cdot p$ simulaties en vergeleken met de meting, waardoor we versterkingsdrempels kunnen voorspellen via een toestandsvullend model. Hoewel de versterkingsstatistieken van deze specifieke monsters geen verbetering laten zien ten opzichte van andere rapporten van CdSe/CdS QD's, is er veel inzicht verkregen over draaggolfdynamiek onder excitatie met hoge excitatiedichtheid, en over een breed spectraal gebied.

Verder werden bulk CdS NC's bestudeerd voor optische versterking. Bulk betekent dat ze een grotere straal hebben dan de Bohr-straal, zodat er geen sterke opsluiting optreedt in het systeem. De bandgap is bijgevolg gelijk aan de bulkbandgap van CdS. Ondanks de relatief lage kwantumopbrengst bij deze stalen, zijn de versterkingsstatistieken zeer indrukwekkend en tonen ze een verbetering ten opzichte van elke versterkingsmetriek in vergelijking met het typische werkpaardmateriaal voor op colloïdale NC gebaseerde geïntegreerde lasers, CdSe/CdS QD's, in het cyaan/groene spectrale gebied. Deze versterkingsstatistieken worden verklaard door middel van bulkfysica, waar we in feite laten zien dat dit gebrek aan opsluiting precies is wat leidt tot de enorme versterkingscoëfficiënten. De uitstekende overeenstemming tussen de theorie en het experiment suggereert dat deze hypothese juist is, en dat dit voornamelijk te danken is aan een zeer sterke Band Gap Renormalisatie (BGR). Deze opwindende resultaten wijzen op de mogelijkheid om zeer heldere en laagdrempelige geïntegreerde groene lasers te creëren.

De studie van optische versterking in colloïdale NC's, waar veranderingen in absorptie worden gemeten, vertelt slechts de helft van het verhaal van niet-lineaire eigenschappen als gevolg van hoge excitatie. In feite wordt de volledige diëlektrische functie gewijzigd, wat zowel de absorptie als de faseverandering door een materiaal beïnvloedt. Eerder werd de li-

neaire diëlektrische functie van colloïdale NC's bepaald (voor QD's) via een iteratieve benadering waarbij zowel de Kramers-Krönig-relatie als de Maxwell-Garnett effectieve mediumbenadering wordt gebruikt. We breiden deze benadering hier uit met anisotrope deeltjes en passen deze toe op 4.5 ML (Mono Laag) CdSe-kwantumbronnen of nanoplaatjes (NPL's). De gevonden brekingsindexveranderingen en afgeleide faseveranderingen worden vergeleken met de resultaten van Frequentie-Domein-Interferometrie. Uit de uitstekende overeenstemming blijkt dat dit algoritme tot goede resultaten leidt. Het algoritme wordt ook toegepast op CdSe/CdS QD's en de bulk-CdS NC's. Dit laat zien dat er brekingsindexveranderingen zijn in spectrale gebieden met nauwelijks verandering in absorptie, ideaal voor het maken van modulatoren.

We gaan verder met geïntegreerde apparaten en demonstreren ASE en lasering in de bulk CdS NC's. De ASE toont een laagdrempelige werking en versterkingswaarden die kunnen worden gerelateerd aan de gevonden Transiente Absorptie versterkingswaarden. Voor laser werking werd gekozen voor oppervlakte-emitterende roosters of fotonische kristallen, vanwege de relatief eenvoudige verwerking hoeft de NC-laag alleen aan het einde afgezet te worden. Dit is gerelateerd aan Lumerical-simulaties om het lasermechanisme uit te leggen en om mogelijke routes voor verbetering voor te stellen. De lasers werken over een breed spectraal gebied en met lage drempels en zonder enige verzadiging, wat suggereert dat de hoge versterkingsgroottes die in oplossing worden gevonden in feite correct zijn. De laserwerking wordt eerst getoond met femtoseconde-excitatie, maar nanoseconde-excitatie-lasering wordt ook getoond, met kleinere lijnbreedten, wat aantoont dat deze NC's laserwerking vertonen met quasi-CW-excitatie.

Om van quasi-CW naar CW over te gaan moet thermisch beheer worden uitgevoerd. Daarom wordt een studie gedaan over de wisselwerking tussen optische opsluiting en thermisch beheer, meestal door middel van simulaties. De effecten op veranderende verwerking op verschillende soorten laserarchitecturen worden getoond. Het veranderen en verdunnen van het substraat, het toevoegen van coatings en het verminderen van het

colloïdale NC-materiaal in het apparaat zijn enkele van de suggesties die gedaan zijn om de thermische belasting te verminderen. Er wordt getoond dat een fabricageroute naar golfgeleiders met gevulde sleuven gaat, wat de thermische belasting zou verminderen, en er worden pogingen beschreven om dergelijke structuren te bereiken. Deze fabricage wordt gedaan door ofwel het lift-off-proces te wijzigen door een etsstap op te nemen, of door gebruik te maken van inkjetprinten.

Ten slotte, zoals de eerder beschreven brekingsindexveranderingen suggereren, is het mogelijk om colloïdale NC's te gebruiken om modulatoren te bouwen. We presenteren een processtroom om Mach-Zehnder-interferometers te fabriceren met overcoate CdSe/CdS QD's. Deze zijn (lineair) gemeten op hun verliezen en laten aanvaardbare resultaten zien. Er wordt een meetopstelling voorgesteld om ook eventuele modulatie te kunnen meten. Fase-effecten worden ook besproken in laserapparaten, waar sterke excitatie de laserpieken kan veranderen, wat relatief kleine effecten vertoont.

English Summary

Colloidal nanocrystals (NCs) are very small (nanometer scale) semiconductor particles consisting typically of a few thousand atoms, kept colloidally stable by passivating the surface with organic ligands, which are fatty acids like oleic acid. Their small size causes carriers to be strongly confined in space which affects their optoelectronic properties compared to their bulk counterpart. The quantum confinement causes an increase in the bandgap E_g of the material. The smaller the particle, the bigger the bandgap, shifting the wavelength region of emission and optical gain. Furthermore, the Density Of States (DOS) becomes discretized, which groups the oscillator strength into narrow bands.

Colloidal NCs are made through a wet chemical synthesis, which can be controlled to a great extent to create the size desired. By changing the size, material (CdSe, CdS, ZnSe, ZnS, PbS, PbSe, InP, InAs, ...), and geometry (0D dot, 1D rod, 2D plate), a lot of freedom exists to manufacture any nanocrystal you might desire, in a wide wavelength region (350-2000 nm). Expanding on this list of materials and geometries is a very active area of research. Making more complex heterogeneous structures, where for example one material in a core is surrounded by a different material in a shell (like CdSe/CdS) can be used for further control of the optoelectronic properties, and as such make the materials even more versatile, while also protecting the NC surface from traps. All this can be coupled to the fact that all these NCs end up being processed in the same way: they are very small semiconductor particles dispersed in a solvent. This similar

processing makes them very attractive for photonic applications, and this work deals with using colloidal NCs in integrated photonics.

Photonics is the science and application of light generation, detection and manipulation through emission, transmission, modulation, signal processing, switching, amplification, and sensing. Simply put: it is the study of light. Specifically, integrated photonics uses platforms first developed for electronics to guide and manipulate light on-chip, on the micro- and nano-scale. In this work, the focus lies on integrated silicon photonics. Since silicon is a material with an indirect bandgap, heterogeneous integration must be done to create integrated light sources. Colloidal NCs are a valid candidate to attempt this. Furthermore, since colloidal NCs mainly show emission and optical gain in the visible region, silicon is problematic due to the high absorption here. To circumvent this, Silicon Nitride (SiN_x) grown on Silicon Oxide (SiO_x) is used, materials that do not absorb light for the entire visible region.

Building integrated colloidal NC lasers on a SiN_x platform has been shown in the past. Here, we look into various ways to improve on previously made integrated lasers: (1) by investigating the gain mechanisms in colloidal NCs in-depth and looking at alternative materials, and (2) by optimizing the photonic cavity. Furthermore, alternative applications for colloidal NCs in integrated devices is investigated, since being able to push a material towards transparency and optical gain also influences the material properties in other ways, namely changing the refractive index.

In a first study, gain in the shell of CdSe/CdS Giant Shell Quantum Dot (GSQD) systems is investigated. The huge shell, and high energy excitation leads to interesting and previously not looked at gain mechanisms. Multiple energy states in the shell show additional gain bands, which previously have shown Amplified Spontaneous Emission (ASE) as well. These states are calculated through $k \cdot p$ simulations, and compared to the measurement, allowing us to predict gain thresholds through a state filling model. Although the gain metrics of these particular samples do not show improvement over other reports of CdSe/CdS QDs, there was much insight gained about carrier dynamics under high fluency excitation,

over a wide spectral region.

Furthermore, bulk CdS NCs were studied for optical gain. Bulk meaning that they have a bigger radius than the Bohr radius, leading to no more strong confinement in the system. The band gap is as such equal to the bulk band gap of CdS. Despite the relatively low quantum yield in these samples, the gain metrics are very impressive, showing improvement over every gain metric compared to the typical workhorse material for colloidal NC based integrated lasers, CdSe/CdS QDs, and in the cyan/green spectral region. These gain metrics are explained through bulk physics, where we show in fact that this lack of confinement is exactly what leads to the huge gain coefficients. The excellent agreement reached between the theory and experiment suggests that this hypothesis is correct, and that this is mainly due to very strong Band Gap Renormalisation (BGR). These exciting results indicate the possibility of creating very bright and low threshold integrated green lasers.

The study of optical gain in colloidal NCs, where changes in absorption are measured, only tells half the story of non-linear properties due to high excitation. In fact, the full dielectric function is altered, which affects both the absorption and the phase change throughout a material. Previously, the linear dielectric function of colloidal NCs was determined (for QDs) through an iterative approach where both the Kramers-Krönig relation and the Maxwell-Garnett effective medium approach is used. We extend here this approach to include anisotropic particles, and apply it to 4.5 ML CdSe quantum wells or nanoplatelets (NPLs). The found refractive index changes and derived phase changes are compared to Frequency-Domain-Interferometry results, with excellent agreement, showing that this algorithm leads to good results. The algorithm is applied to CdSe/CdS QDs as well, and the bulk CdS NCs. This shows that there are refractive index changes in spectral regions with barely any change in absorption, ideal for making modulators.

Moving on to integrated devices, we demonstrate ASE and lasing in the bulk CdS NCs. The ASE shows low threshold operation, and gain magnitudes that can be related to the TA gain magnitudes that were

found. For lasing, surface emitting gratings or Photonic Crystals were chosen, due to relative easy processing, the NC layer just needs to be deposited at the end. This is related to Lumerical simulations to explain the lasing mechanism, and to suggest possible routes for improvement. The lasers operate over a wide spectral region and with low thresholds and without any saturation, suggesting that the high gain magnitudes found in solution are in fact correct. The lasing is first shown with femtosecond excitation, but nanosecond excitation lasing is also shown, with smaller linewidths, showing that these NCs show lasing with quasi-CW excitation.

From quasi-CW to CW, thermal management has to be done. As such, a deep dive into the trade-off between optical confinement and thermal management is done, mostly through simulations. The effects on changing processing on various types of laser architectures is shown. Changing and thinning the substrate, adding coatings and reducing the colloidal NC material in the device are some of the suggestions done to reduce the thermal load. A fabrication route is shown to go to filled slot waveguides, which would reduce the thermal load, and attempts to reach such structures is described. This fabrication is done either by altering the lift-off process to include an etching step, or by use of inkjet printing.

Finally, as the refractive index changes described earlier suggest, it is possible to use colloidal NCs to build modulators. We present a process flow to fabricate Mach-Zehnder Interferometers with overcoated CdSe/CdS QDs. These have been measured (linearly) for their losses, showing acceptable results. A measurement setup is proposed to be able to measure possible modulation as well. Phase effects are also discussed in laser devices, where strong excitation can change the lasing peaks, showing relative minor effects.

Poetic Summary

*In the world of science and light,
There are tiny particles that shine so bright,
Colloidal nanocrystals, small and stable,
With optoelectronic properties that are able.*

*Quantum confinement shifts the wavelength range,
And discretizes the Density of States for a change,
A wet chemical synthesis creates these gems,
With size, material, and geometry, the options never end.*

*Heterogeneous structures give more control,
Over optoelectronic properties, that's the goal,
These particles dispersed in a solvent so fine,
Make them perfect for photonic applications, oh so divine.*

*Integrated photonics guides and manipulates light,
On micro and nano-scales, a beautiful sight,
Silicon photonics are the focus here,
Colloidal NCs may help to make light sources clear.*

*Gain mechanisms and photonic cavity, both must be optimized,
 For colloidal NC lasers on SiNx, to be recognized,
 CdSe/CdS Giant Shell Quantum Dots are explored,
 With multiple energy states and gain bands to be adored.*

*Bulk CdS NCs, a new discovery,
 Showing impressive gain metrics, oh so lovely,
 Band Gap Renormalization leads to high coefficients,
 Possibility of creating bright and low threshold green lasers is
 magnificent.*

*The non-linear properties of colloidal NCs are vast,
 The full dielectric function changes, impacting both phase and cast,
 Linear dielectric function is now determined,
 To unlock the full potential, more research is encouraged and confirmed.*

*In conclusion, colloidal nanocrystals are fascinating to see,
 With a world of possibilities, they open up to you and me,
 Integrated photonics and optoelectronics, a bright future in sight,
 Thanks to these tiny particles that shine so bright.*

Part I

Background

Chapter 1

Introduction

1.1 Research Background

Colloidal Nanocrystals Colloidal nanocrystals (NCs) are very small (nanometer scale) semiconductor particles consisting typically of a few thousand atoms, kept colloidally stable by passivating the surface with organic ligands, which typically consist of fatty acids like oleic acid. Their small size causes carriers to be strongly confined in space which affects their optoelectronic properties compared to their bulk counterpart. The quantum confinement causes an increase in the bandgap E_g of the material. The smaller the particle, the bigger the bandgap, shifting the wavelength region of emission and optical gain. Furthermore, the Density Of States (DOS) becomes discretized, which groups the oscillator strength into narrow bands.

Colloidal NCs are made through a wet chemical synthesis, which can be controlled to a great extent to create the size desired. By changing the size, material (CdSe, CdS, ZnSe, ZnS, PbS, PbSe, InP, InAs, ...), and geometry (0D dot, 1D rod, 2D plate), a lot of freedom exists to manufacture any nanocrystal you might desire for application, in a wide wavelength region (350-2000 nm). Expanding on this list of materials and geometries is a very active area of research. Making more complex heterogeneous

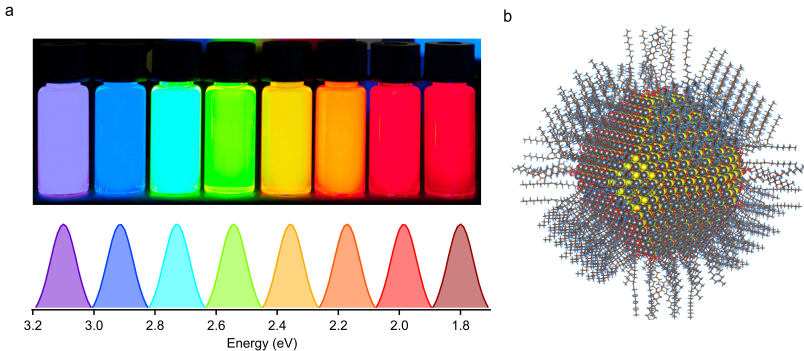


Figure 1.1: (a) Different CdSe colloidal QD samples from small to big (left to right). (b) Schematic of a QD with inorganic core and organic ligands on the surface.¹

structures, where for example one material in a core is surrounded by a different material in a shell can be used for further control of the optoelectronic properties, and as such makes the materials even more versatile, while also protecting the NC surface from traps. Independent of all these properties, colloidal NCs are all semiconductor particles dispersed in a solvent, allowing them all to be processed in the same way. This similar processing makes them very attractive for photonic applications.

The first mention of colloidal NCs in literature is made by Rossetti *et al.*², where they show the size-dependent properties of colloidal CdS Quantum Dots (QDs): a blueshift in bandgap from the bulk value of around 500 nm (2.48 eV) for a bulk particle (> 10 nm diameter), to 286 nm (4.33 eV) for a very small particle (2.1 nm diameter). This sparked follow up research³ which besides CdS also included ZnS QDs (moving to higher energies), and later also to CdSe⁴. As CdSe has a bulk bandgap of 1.74 eV (710 nm), tuning the size allowed to make nanocrystals that emit across the entire visible range.

Over the years, improvements have been made towards better Quantum Yield (QY) to make them highly efficient emitters, for instance by creating the core/shell CdSe/CdS structure⁵, which has become the go-to material in more recent research.

The first work revolving around using colloidal nanocrystals in lasers dates from 2000, in the publication by the team of Klimov *et al.*⁶. Here, CdSe QDs are shown to be able to be pushed into optical gain. This is first shown in solution, but also in thin film, where Amplified Spontaneous Emission (ASE) is demonstrated. At this point in time, colloidal QDs had mostly been investigated for their use as emitters under low excitation density, with a possible application being LEDs. With this breakthrough, a new (sub)-field of Colloidal Nanocrystals was born: the investigation of these materials for their non-linear properties, to be used in lasers.

With these results, Klimov envisioned that it would be possible to use Colloidal Nanocrystals to compete with epitaxially grown direct gap semiconductors. As was put in the paper⁶:

Lasing has previously been demonstrated for epitaxially grown III-V QDs⁷⁻⁹. These dots have relatively large lateral sizes (typically >10 nm); therefore, the spacing between their electronic states is smaller than room temperature carrier energies (weak confinement), and the lasing threshold is temperature sensitive. Further, large lateral dimensions and difficulties in size control limit their spectral tunability using quantum confinement effects. As a result, the emission wavelengths in epitaxial dots are usually controlled by a material's composition rather than by the QD size⁹.

The pitch is clear: compared to epitaxially grown QDs, colloidal NCs show much promise regarding temperature insensitive operation and spectral tuning. This challenge has been issued more than twenty years ago, what improvements to colloidal NC lasing have since then been made? Impressive advancements have been made in the recent years from the group of Edward Sargent showing microsecond sustained lasing¹¹ and continuous-wave lasing¹², showing impressive control of temperature in these devices, crucial for stable operation. Meanwhile, the group of Victor Klimov focused more on electrical injection by both showing that optically exciting devices with a stack of materials that should allow for

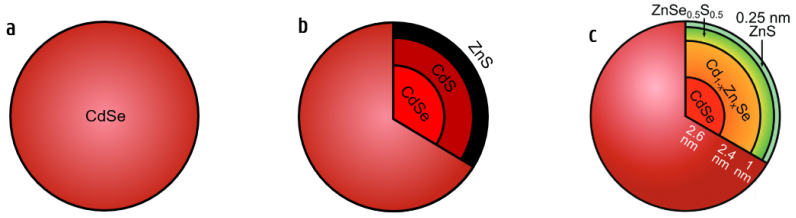


Figure 1.2: (a) Core only CdSe Quantum Dot. (b) Core/shell system of CdSe/CdS, with a ZnS surface for passivation. (c) The complex core/graded shell system used by Ahn *et al.*¹⁰.

electrical injection is possible^{10,13}, and showing optical gain by electrical injection¹⁴. The QDs used in this work went through quite an evolution from the early CdSe/ZnS: a CdSe core is first shelled by a graded $\text{Cd}_x\text{Zn}_{1-x}\text{Se}$ shell, and finally capped by a thin $\text{ZnSe}_{0.5}\text{S}_{0.5}$ layer¹⁰, see also Figure 1.2. This specific shelling is used to optimize the optical gain lifetime in the device, by decreasing the Auger rate. In their last work, electrically pumped ASE is shown, but not yet lasing, and this at 80 K. Showing ASE but not yet lasing indicates that the cavity losses are at this point still too high. Although CdSe/CdS based QD systems are the current state-of-the-art to demonstrate colloidal QD electrically injected lasers, they are at a stage where they have been engineered to such a degree that it is hard to see how they can still be improved. So, looking into other colloidal NCs is definitely worthwhile for lasing applications, as shown by recent advancements that have shown impressive metrics for CdSe 4.5ML (Monolayer) Quantum Wells^{15,16}, and perovskites¹⁷.

Integrated Photonics The material itself is not enough, it must be integrated on a platform also. For this, we turn to *Integrated Photonics*. Photonics is the science and application of light generation, detection and manipulation through emission, transmission, modulation, signal processing, switching, amplification, and sensing¹⁸. Simply put: it is the study of light. While “light” encompasses the complete electromagnetic spectrum, the area of photonics specifically focusses on visible and

(near-)infrared emission, although efforts are being made toward shorter-(UV)¹⁹, and longer (THz radiation)²⁰ wavelengths. The term photonics derives from the word “photon”, the fundamental quantum of the electromagnetic field. The field of photonics started booming in the 1960s with the first semiconductor laser and developments of optical fibers in the 1970s.

Based on how photonics started, we can see that the first application of photonics was data transmission: optical fibers became obligatory for high-speed communication, and it is still an active area of research. However, the quickly growing semiconductor industry of the latter half of the 20th century posed a huge opportunity for the field. What if the idea of electronics, where electrons are manipulated on tiny devices by applying voltages, could be translated to photonics? Guiding light on-chip would allow to create scalable, cheap technology. This would allow to tackle a whole new range of applications, and naturally help with data transmission as well.

These ideas were first used by various teams where the first results came out of Bell Labs in the US^{21,22} by Dragone *et al.* A key development toward practical application was made by this team, and by the team of Meint Smit of the Delft University of Technology²³, when they developed the Arrayed Waveguide Grating (AWG), a core component in modern internet and phone technology, see Figure 1.3a. The AWG allows for multiplexing of light, i.e. splitting up (or recombining) a broadband light source into its separate wavelength components, allowing for a significant transmission capacity increase of an optical fiber. Light coupled in a chip could be manipulated and redirected. With this technological component created on-chip and a first practical use, the field of *Integrated Photonics* was born. Starting from this breakthrough, many new discoveries were made that built a library of photonic components to be used together in chips with ever increasing complexity.

Integrated photonics was developed on multiple platforms (silicon, III-V materials like InP, GaAs), but this work is carried out specifically in the field of silicon photonics. The integrated silicon platform has the huge

advantage of having been worked on for more than fifty years for integrated electronics, and all the developed techniques can be borrowed for photonics. However, compared to the electronics, there is a big complication for integrated photonics. In electronics, generating a current is quite trivial. In photonics, this is not the case, because even just generating light emission is not efficient on silicon since it is an indirect semiconductor. And even then, for many applications light being guided is not sufficient, but specifically *coherent* light is needed: light coming from a laser source. The work in this thesis tackles this specific problem: we try to understand and use specific materials to create on-chip light sources, based on an integrated silicon platform, which can be expanded to include visible wavelengths.

Attempts have been made for many years to integrate other materials on a silicon platform, to create robust, cheap and efficient light sources on silicon chips, typically referred to as *heterogeneous integration*. Direct epitaxial growth is possible, although the lattice mismatch between different materials creates problems with dislocations. A smart method to resolve this problem is by using the so-called III-V nano-ridges²⁴, shown in Figure 1.3b. Here, in a first step a small III-V seed is grown using Molecular Beam Epitaxy (MBE) on a silicon layer. This seed will be filled with defects. In a secondary step, growth is continued where dislocations slowly disappear, finally ending with a pure crystalline nano-ridge sticking outside of the silicon, a brilliant way to avoid the lattice mismatch problem. This material can then be used as active material, typically by then continuing growth of epitaxial Quantum Dots or Quantum Wells on top of these ridges. By using this approach, direct growth of gain layers on silicon becomes possible, and it is a growing field of research.

Another method of heterogeneous integration started from bonding and flip-chip integration and is now maturing as *transfer printing*^{26–28}. For bonding, a wafer of III-V material is taken and pressed on top of a processed silicon wafer. Afterward the III-V wafer is processed to make light sources. Flip-chip integration reverses these steps: first the III-V and silicon fab separately process the wafers, and then the components are

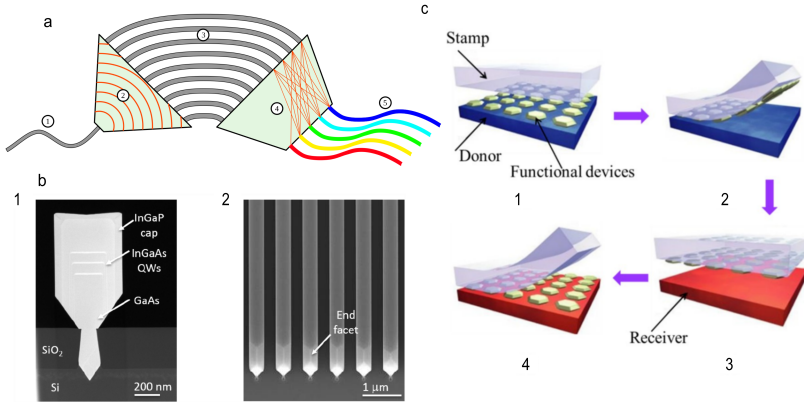


Figure 1.3: (a) Arrayed Waveguide Grating²⁵. (b) III-V nanoridge cross section (1), showing the seed grown out of silicon and the gain material (InGaAs QWs) embedded in the GaAs ridge. (2) shows the top view, where lines of these ridges are grown next to each other. (c) Principle of Transfer Printing from the source wafer (blue) to the target wafer (red)²⁶.

one-by-one transferred to the silicon wafer. Some final processing is done and the devices are finished. Both these methods have their downsides: bonding is not material efficient, and flip-chip integration is slow since alignment needs to be repeated for every single transferring operation, which inevitably also has consequences for the yield. The transfer printing process is shown in Figure 1.3c.

Transfer printing improves on these two techniques by parallelizing the idea of flip-chip integration: instead of transferring the devices one-by-one, a transfer printer picks up a matrix of $N \times M$ devices and transports them in one go. This massively speeds up the processing, and will increase the accuracy and yield as well since the processing before the transfer is naturally already aligned properly (spacing between devices is matched between source and target wafer).

Finally, in this work, we consider a different method of heterogeneous integration: using solution processed semiconductor NCs as active material, as discussed earlier. The cheap and scalable production of NCs gives

them an edge over other gain materials, and the integration is done by using simple, methods of making thin films using liquids, like spincoating. Inevitably, there are also downsides: the introduction of organics in thin films makes electrical contacting difficult, and leads to a higher thermal load. The basic Silicon-On-Insulator (SOI) platform cannot be used for many colloidal NC materials, since they operate in the visible range where the silicon absorbs all the light. For this, the move to Silicon Nitride (SiN_x) on Silicon was made.

The CMOS-compatible approach we follow at UGent has shown its promise through several publications, where femto-second²⁹ and nano-second³⁰ optically excited lasing on a fully integrated platform based on Silicon Nitride on Silicon was shown. Besides this, also integrated emitters in the form of LEDs³¹ have been developed, showing that the material stacks necessary to inject carriers electrically can be produced in-house, paving the way to make an integrated electrically excited laser.

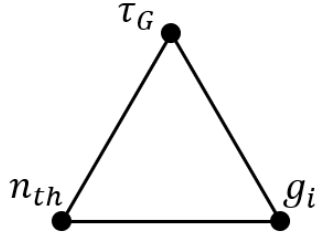


Figure 1.4: The three parameters that make up the gain trifecta in colloidal NCs: gain magnitude g_i , lifetime τ_G and threshold n_{th} .

1.2 Thesis Outline

This work considers two steps for improving colloidal NC lasing: optimisation of gain material, and optimisation of the photonic cavity, optically and thermally. In the first part of this work, an introduction to the fields of colloidal NCs and Integrated Photonics is given.

The second part discusses the spectroscopy done in this work, and the analysis of the results. As discussed in the previous Section, CdSe/CdS as a basis led to great improvements over the years. But there are limitations, specifically to the gain magnitudes that can be reached. By trying to increase the gain lifetime in the material, the NCs have grown bigger and bigger, leading to a reduction in the fraction of active volume. Bisschop *et al.*³² have in fact shown that a large core with a big shell leads to the highest possible gain magnitude (reaching maximum values of 3000 cm^{-1}). This while the gain lifetime, perhaps surprisingly, was also the highest of the cases studied (around 800 ps). These results can be placed against the QDs in the latest work by the team of Klimov, cited above and shown in Figure 1.2c. Here, impressive gain lifetimes of up to 1.3 ns are reached, but the intrinsic gain reached only goes to about 1000 cm^{-1} . Instead of optimizing both parameters, these more complex structures indicate the trade-off between gain magnitude and lifetime. Finally, a third parameter, the gain threshold n_{th} , is also necessary to optimize, which in this case

means it needs to be minimized. Reducing either the optical or electrical excitation density that needs to be injected in the system for lasing action automatically leads to lower thermal loads and more stable lasing action. We can combine these three parameters in the “gain trifecta”, displayed in Figure 1.4, as the ultimate goal for colloidal NCs to be reached: a high gain magnitude, with a long lifetime and a low gain threshold. To do so, it will be necessary to move away from the current CdSe/CdS based system, and look into either other geometries or materials.

In this work, we attempt to study all three of these parameters for two material systems: (1) the so-called Giant-Shell Quantum Dots (GSQDs), which have a tiny CdSe core and a huge CdS shell, first reported by Di Stasio *et al.*³³ (Chapter 4), and (2) a new candidate for optical gain, bulk CdS NCs, which are colloidal NCs with radii slightly larger than the Bohr radius, leading them to no longer have strong confinement. We will show that this system shows improvement in every way over the CdSe/CdS system, showing impressive values for all three parameters in the gain trifecta (Chapter 5).

Spending time in this work investigating the bulk CdS system and its gain mechanism, we discovered that current methods in literature reported to extract the carrier temperature from Transient Absorption Spectroscopy data are not accurate. Although qualitatively the used fitting procedure yields the same result, i.e. a broader signal yielding a higher temperature, there are problems with the actual temperature found. The derivation of the actual temperature from the high energy tail is done in Chapter 6, for both Transient Absorption data and Ultrafast Photoluminescence.

Finally, it has to be noted that optical gain is not the only non-linear property that can be put to use in an active device. Phase shifts caused by injected carriers can play a role, through modulation. Previously made frameworks already exist that allow to determine the dielectric function of colloidal NCs, based on the Kramers-Krönig relations and the Maxwell-Garnett effective medium approach^{34,35}. We extended this framework, first to anisotropic nanomaterials, allowing to insert any desired shape,

and second to Transient Absorption data. The latter allows us to determine changes in dielectric function due to injected carriers, and following from this, changed to the refractive index. This is explained in Chapter 7.

In a third part, colloidal NCs are brought onto the integrated SiNx platform, where Chapter 8 discusses the use of bulk NCs in optically excited lasers. Here, we opted for a Photonic Crystal Slab design, which was simulated in various ways, much of this is built on work performed by the Noda group³⁶, where much work about Photonic Crystal Surface Emitting Lasers (PCSELS) has been done. We furthermore show Amplified Spontaneous Emission, femtosecond lasing and nanosecond lasing.

This Part also includes a simulation approach to thermal optimisation of integrated colloidal NC lasers, where for various architectures both optical and thermal simulations are performed. While inherently optical confinement and thermal load will lead to a trade-off situation, in various ways optimisations can be done, which are discussed in Chapter 9. The insight gained here can be used in the future for designing optimized photonic cavities.

The final Chapter in this part, Chapter 10 builds on the work in Chapter 7, where foundations are laid for possible use of colloidal NCs in Mach-Zehnder Interferometers, and understanding refractive index shifts in integrated lasers. A linear characterisation of Mach-Zehnder Interferometers is done, and a measurement setup is described that could measure modulation using optical excitation.

Finally, the last part discusses some final considerations and future perspectives.

1.3 Publications

1.3.1 List of Articles

1. P. Zhou, I. Tanghe, P. Schiettecatte, D. Van Thourhout, Z. Hens, P. Geiregat, “*Ultrafast Carrier Dynamics in Colloidal WS_2 Nanosheets obtained through a Hot Injection Synthesis* - Journal of Chemical Physics 151(16).
2. A. Khan, V. Pinchetti, I. Tanghe, Z. Dang, B. Martin-Garcia, Z. Hens, D. Van Thourhout, P. Geiregat, S. Brovelli, I. Moreels, “*Tunable and Efficient Red to Near-Infrared Photoluminescence by Synergistic Exploitation of Core and Surface Silver Doping of CdSe Nanoplatelets*” - Chemistry of Materials. 31(4). p1450-1459.
3. P. Schiettecatte, D. Poonia, I. Tanghe, S. Maiti, M. Failla, S. Kinge, Z. Hens, L. D.A. Siebbeles, P. Geiregat, “*Unraveling the Photophysics of Liquid-Phase Exfoliated Two-Dimensional ReS_2 Nanoflakes*” - Journal of Physical Chemistry C. 125(38). p20993-21002.
4. P. Geiregat, C. Roda, I. Tanghe, S. Singh, A. Di Giacomo, D. Misao Lebrun, G. Grimaldi, J. Maes, D. Van Thourhout, I. Moreels, “*Localization-limited Exciton Oscillator Strength in Colloidal CdSe Nanoplatelets revealed by the Optically Induced Stark Effect*” - Light-Science and Applications 2021. 10(1).
5. L. Elsinger, R. Petit, F. Van Acker, N. Klaudia Zawacka, I. Tanghe, K. Neyts, C. Detavernier, P. Geiregat, Z. Hens, D. Van Thourhout, “*Waveguide-Coupled Colloidal Quantum Dot Light Emitting Diodes and Detectors on a Silicon Nitride Platform*” - Laser and Photonic Reviews 2021. 15(7).
6. I. Tanghe, J. Butkus, K. Chen, R. R. Tamming, S. Singh, Y. Ussembayev, K. Neyts, D. Van Thourhout, J. M. Hodgkiss, P. Geiregat, “*Broadband Optical Phase Modulation by Colloidal CdSe Quantum Wells*” - Nano Letters 2021. 22(1). p58-64.

7. I. Tanghe, J. Llusar, J. I. Climente, A. Barker, G. Paterno, F. Scotognella, A. Polovitsyn, A. Houssain Khan, Z. Hens, D. Van Thourhout, “*Role of Thermally Occupied Hole States in Room Temperature Broadband Gain in CdSe/CdS Gians-Shell Nanocrystals*” - Advanced Optical Materials 2022. 10(21).
8. C.S. Mutyala, G. Pippia, I. Tanghe, B. Martin-Garcia, A. Roussaki, P. Vandenamee, P. Schiettecatte, I. Moreels, P. Geiregat, “*Charge Carrier Dynamics in Colloidally Synthesized Monolayer MoX₂ Nanosheets*” - The Journal of Physical Chemistry Letters 2023. 14(10).
9. I. Tanghe, M. Samoli, I. Wagner, S. Ataberk Cayan, A. Hossain Khan, K. Chen, J. M. Hodgkiss, I. Moreels, D. Van Thourhout, Z. Hens, P. Geiregat, “*Disruptive Optical Gain from Bulk CdS Nanocrystals through Giant Band Gap Normalization*” - Nature Nanotechnology, out for review.

1.3.2 List of Conference Contributions

1. I. Tanghe, K. Chen, R. Tomar, S. Singh, I. Moreels, J. M. Hodgkiss, D. Van Thourhout, Z. Hens, P. Geiregat, “*Ultrafast Phase Modulation in CdSe Colloidal Quantum Wells*” - nanoGe Fall Meeting 2018.
2. L. Elsinger, Y. Zhu. W. Xie, I. Tanghe, S. Bisschop, V. Chandrasekaran, E. Brainis, P. Geiregat, Z. Hens, D. Van Thourhout, “*A Hybrid SiN QDOT platform for Visible Photonics*” - Conference on Lasers and Electro-Optics (CLEO) 2018.
3. P. Geiregat, I. Tanghe, R. Tomar, G. Grimaldi, J. Maes, A. Houtepen, Z. Hens, “*Optically Induced Stark Effect and the Exciton Oscillator Strength in Quasi-2D CdSe Nanoplatelets*” - Quantum Dots, 10th Biannual Conference.

4. P. Zhou, I. Tanghe, P. Schiettecatte, D. Van Thourhout, Z. Hens, P. Geiregat, “*Ultrafast Carrier Dynamics in colloidal WS₂ nanosheets*” - 2D Materials and Technology, 5th International Conference.
5. R. Tomar, I. Tanghe, A. Kulkarni, K. Chen, J. M. Hodgkiss, L. Siebbeles, D. Van Thourhout, Z. Hens, P. Geiregat, “*Optical Gain Spectroscopy of Solution Processable 2D Materials for Integrated Micro-Lasers*” - Advanced Materials and Nanotechnology, 9th International Conference 2019.
6. L. Elsinger, I. Tanghe, F. Van Acker, N. Klaudia Zawacka, R. Petit, K. Neyts, C. Detavernier, P. Geiregat, Z. Hens, D. Van Thourhout, “*A Waveguide-Coupled Colloidal Quantum Dot LED on a Silicon Nitride Platform*” - Conference on Lasers and Electro-Optics (CLEO) 2020.
7. K. Molken, I. Tanghe, D. Saxena, K. Wai Ng, R. Sapienza, P. Geiregat, D. Van Thourhout, “*Extended and Localized States in Colloidal Quantum Dots based Microring Lasers*” - Fall Meeting of the European Materials Research Society (E-MRS) 2021.
8. K. Molken, I. Tanghe, D. Saxena, K. Wai Ng, R. Sapienza, P. Geiregat, D. Van Thourhout, “*Coupled Micro Ring Lasers based on Hybrid Integration of Colloidal Quantum Dots*” - Conference on Lasers and Electro-Optics (CLEO) 2022.
9. I. Tanghe, R. R. Tamming, J. M. Hodgkiss, K. Chen, S. Singh, D. Van Thourhout, P. Geiregat, “*Broadband and Ultrafast Optical Phase Modulation by Colloidal 2D Semiconductors*” - Spring Meeting of the European Materials Research Society (E-MRS) 2022.
10. I. Tanghe, S. Ataberk Cayan, M. Samoli, I. Wagner, J. M. Hodgkiss, K. Chen, I. Moreels, Z. Hens, D. Van Thourhout, P. Geiregat, “*Disruptive Optical Gain Metrics in the Green and Near-Infrared Spectrum using Weakly Confined CdX (X=S,Se,Te) QUantum Dots*” -

- Spring Meeting of the European Materials Research Society (EMRS) 2022.
11. I. Tanghe, I. Wagner, M. Samoli, K. Chen, S. Ataberk Cayan, A. Khan, D. Van Thourhout, J. M. Hodgkiss, Z. Hens, I. Moreels, *“Disruptive Optical Gain in Bulk-Like CdS Quantum Dots through Strong Band Gap Renormalisation”* - nanoGe Spring Meeting 2022.
 12. D. Poonia, P. Schiettecatte, I. Tanghe, S. Maiti, M. Failla, S. Kinge, Z. Hens, L. Siebbeles, P. Geiregat, *“Unraveling the Photophysics of Liquid-Phase Exfoliated Two-Dimensional ReS₂ Nanoflakes”* - APS March Meeting 2022.
 13. I. Tanghe, M. Samoli, I. Wagner, S. Ataberk Cayan, I. Moreels, J. M. Hodgkiss, K. Chen, Z. Hens, D. Van Thourhout, P. Geiregat, *“Stimulated Emission from Bulk-Like CdS Quantum Dots Through Strong Band Gap Renormalisation”* - Fall Meeting of the Materials Research Society (MRS) 2022.
 14. I. Tanghe, I. Wagner, S. Ataberk Cayan, M. Samoli, J. Hodgkiss, Z. Hens, D. Van Thourhout, K. Chen, P. Geiregat, *“On the Determination of Carrier Temperature in Direct Gap Semiconductors”* - MATSUS (nanoGe) Spring Meeting 2023

Bibliography

- ¹ Wikipedia. Quantum dot — Wikipedia, the free encyclopedia. http://https://en.wikipedia.org/wiki/Quantum_dot, 2023. [Online; accessed 15-January-2023].
- ² R Rossetti, JL Ellison, JM Gibson, and Louis E Brus. Size effects in the excited electronic states of small colloidal cds crystallites. *The Journal of chemical physics*, 80(9):4464–4469, 1984.
- ³ R Rossetti, R Hull, JM Gibson, and Louis E Brus. Excited electronic states and optical spectra of zns and cds crystallites in the 15 to 50 Å size range: Evolution from molecular to bulk semiconducting properties. *The Journal of chemical physics*, 82(1):552–559, 1985.
- ⁴ Alexey I Ekimov, F Hache, MC Schanne-Klein, D Ricard, Chr Flytzanis, IA Kudryavtsev, TV Yazeva, AV Rodina, and Al L Efros. Absorption and intensity-dependent photoluminescence measurements on cdse quantum dots: assignment of the first electronic transitions. *JOSA B*, 10(1):100–107, 1993.
- ⁵ Xiaogang Peng, Michael C Schlamp, Andreas V Kadavanich, and A Paul Alivisatos. Epitaxial growth of highly luminescent cdse/cds core/shell nanocrystals with photostability and electronic accessibility. *Journal of the American Chemical Society*, 119(30):7019–7029, 1997.
- ⁶ V. I. Klimov, A.A. Mikhailovsky, Su Xu, A. Malko, J.A. Hollingsworth, C.A. Leatherdale, H.-J. Eisler, and M.G. Bawendi. Optical gain and stimulated emission in nanocrystal quantum dots. *Science*, 290(5490):314–317, oct 2000.
- ⁷ NN Ledentsov, VM Ustinov, A Yu Egorov, AE Zhukov, MV Maksimov, IG Tabatadze, and PS Kop'ev. Optical properties of heterostructures with ingaas-gaas quantum clusters. *Semiconductors*, 28(8):832–834, 1994.

- ⁸ N Kirstaedter, NN Ledentsov, M Grundmann, D Bimberg, VM Ustinov, SS Ruvimov, MV Maximov, Ps S Kop'ev, Zh I Alferov, U Richter, et al. Low threshold, large to injection laser emission from (inga) as quantum dots. *Electronics Letters*, 30(17):1416–1417, 1994.
- ⁹ Marius Grundmann. Feasibility of 5 gbit/s wavelength division multiplexing using quantum dot lasers. *Applied Physics Letters*, 77(26):4265–4267, 2000.
- ¹⁰ Namyong Ahn, Young-Shin Park, Clément Livache, Jun Du, Kivanc Gungor, Jaehoon Kim, and Victor I Klimov. Optically excited lasing in a cavity-based, high-current-density quantum dot electroluminescent device. *Advanced Materials*, page 2206613, 2022.
- ¹¹ Michael M Adachi, Fengjia Fan, Daniel P Sellan, Sjoerd Hoogland, Oleksandr Voznyy, Arjan J Houtepen, Kevin D Parrish, Pongsakorn Kanjanaboos, Jonathan A Malen, and Edward H Sargent. Microsecond-sustained lasing from colloidal quantum dot solids. *Nature communications*, 6(1):1–8, 2015.
- ¹² Fengjia Fan, Oleksandr Voznyy, P Randy, Kristopher T Bicanic, Michael M Adachi, James R McBride, Kemar R Reid, Young-shin Park, Xiyang Li, Ankit Jain, Rafael Quintero-bermudez, Mayuran Saravanapavanantham, Min Liu, Marek Korkusinski, Pawel Hawrylak, Victor I Klimov, Sandra J Rosenthal, Sjoerd Hoogland, and Edward H Sargent. Continuous-wave lasing in colloidal quantum dot solids enabled by facet-selective epitaxy. *Nature*, 544(7648):75–79, 2017.
- ¹³ Jeongkyun Roh, Young-Shin Park, Jaehoon Lim, and Victor I Klimov. Optically pumped colloidal-quantum-dot lasing in led-like devices with an integrated optical cavity. *Nature communications*, 11(1):1–10, 2020.
- ¹⁴ Jaehoon Lim, Young-Shin Park, and Victor I Klimov. Optical gain in colloidal quantum dots achieved with direct-current electrical pumping. *Nature materials*, 17(1):42–49, 2018.

- ¹⁵ Joel Q Grim, Sotirios Christodoulou, Francesco Di Stasio, Roman Krahne, Roberto Cingolani, Liberato Manna, and Iwan Moreels. Continuous-wave biexciton lasing at room temperature using solution-processed quantum wells. *Nature nanotechnology*, 9(11):891–895, 2014.
- ¹⁶ Burak Guzel Turk, Matthew Pelton, Murat Olutas, and Hilmi Volkan Demir. Giant modal gain coefficients in colloidal ii–vi nanoplatelets. *Nano Letters*, 19(1):277–282, 2018.
- ¹⁷ Haiming Zhu, Yongping Fu, Fei Meng, Xiaoxi Wu, Zizhou Gong, Qi Ding, Martin V Gustafsson, M Tuan Trinh, Song Jin, and XY Zhu. Lead halide perovskite nanowire lasers with low lasing thresholds and high quality factors. *Nature materials*, 14(6):636–642, 2015.
- ¹⁸ Richard S Quimby. *Photonics and lasers: an introduction*. John Wiley & Sons, 2006.
- ¹⁹ Chupao Lin, Juan Santo Domingo Peñaranda, Jolien Dendooven, Christophe Detavernier, David Schaubroeck, Nico Boon, Roel Baets, and Nicolas Le Thomas. Uv photonic integrated circuits for far-field structured illumination autofluorescence microscopy. *Nature Communications*, 13(1):1–9, 2022.
- ²⁰ Mattias Verstuyft, Elias Akiki, Benjamin Walter, Marc Faucher, Jean-François Lampin, Mathias Vanwolleghem, and Bart Kuyken. Proposal for an integrated silicon-photonics terahertz gas detector using photoacoustics. *Optics Express*, 28(15):22424–22442, 2020.
- ²¹ C Dragone. Offset multireflector antennas with perfect pattern symmetry and polarization discrimination. *Bell System Technical Journal*, 57(7):2663–2684, 1978.
- ²² C Dragone and MJ Gans. Imaging reflector arrangements to form a scanning beam using a small array. *Bell System Technical Journal*, 58(2):501–515, 1979.

- ²³ Meint K Smit and Cor Van Dam. Phasar-based wdm-devices: Principles, design and applications. *IEEE Journal of selected topics in quantum electronics*, 2(2):236–250, 1996.
- ²⁴ Yuting Shi, Bernardette Kunert, Yannick De Koninck, Marianna Pantouvaki, Joris Van Campenhout, and Dries Van Thourhout. Novel adiabatic coupler for iii-v nano-ridge laser grown on a si photonics platform. *Optics express*, 27(26):37781–37794, 2019.
- ²⁵ Wikipedia. Arrayed waveguide grating — Wikipedia, the free encyclopedia. <http://en.wikipedia.org/w/index.php?title=Arrayed%20waveguide%20grating&oldid=1037281809>, 2023. [Online; accessed 15-January-2023].
- ²⁶ Honglei Zhou, Weiyang Qin, Qingmin Yu, Huanyu Cheng, Xudong Yu, and Huaping Wu. Transfer printing and its applications in flexible electronic devices. *Nanomaterials*, 9(2):283, 2019.
- ²⁷ Jing Zhang, Bahawal Haq, James O’Callaghan, Angieska Gocalinska, Emanuele Pelucchi, António José Trindade, Brian Corbett, Geert Morthier, and Gunther Roelkens. Transfer-printing-based integration of a iii-v-on-silicon distributed feedback laser. *Optics express*, 26(7):8821–8830, 2018.
- ²⁸ Andreas De Groote, Paolo Cardile, Ananth Z Subramanian, Alin M Fecioru, Christopher Bower, Danae Delbeke, Roel Baets, and Günther Roelkens. Transfer-printing-based integration of single-mode waveguide-coupled iii-v-on-silicon broadband light emitters. *Optics Express*, 24(13):13754–13762, 2016.
- ²⁹ Weiqiang Xie, Thilo Stöferle, Gabriele Raino, Tangi Aubert, Suzanne Bisschop, Yunpeng Zhu, Rainer F Mahrt, Pieter Geiregat, Edouard Brainis, and Zeger Hens. On-chip integrated quantum-dot-silicon-nitride microdisk lasers. *Adv. Mater.*, 29(16):1604866, 2017.
- ³⁰ Yunpeng Zhu, Weiqiang Xie, Suzanne Bisschop, Tangi Aubert, Edouard Brainis, Pieter Geiregat, Zeger Hens, and Dries Van Thourhout. On-

- chip single-mode distributed feedback colloidal quantum dot laser under nanosecond pumping. *Acs Photonics*, 4(10):2446–2452, 2017.
- ³¹ Lukas Elsinger, Robin Petit, Frederik Van Acker, Natalia K Zawacka, Ivo Tanghe, Kristiaan Neyts, Christophe Detavernier, Pieter Geiregat, Zeger Hens, and Dries Van Thourhout. Waveguide-coupled colloidal quantum dot light emitting diodes and detectors on a silicon nitride platform. *Laser & Photonics Reviews*, 15(7):2000230, 2021.
- ³² S. Bisschop, P. Geiregat, T. Aubert, and Z. Hens. The Impact of Core/Shell Sizes on the Optical Gain Characteristics of CdSe/CdS Quantum Dots. *ACS Nano*, 12:9011–9021, 2018.
- ³³ Francesco Di Stasio, Anatolii Polovitsyn, Ilaria Angeloni, Iwan Moreels, and Roman Krahné. Broadband amplified spontaneous emission and random lasing from wurtzite CdSe/CdS "giant-shell" nanocrystals. *ACS Photonics*, 3(11):2083–2088, 2016.
- ³⁴ Iwan Moreels, Guy Allan, Bram De Geyter, Ludger Wirtz, Christophe Delerue, and Zeger Hens. Dielectric Function of Colloidal Lead Chalcogenide Quantum Dots Obtained by a Kramers-Krönig Analysis of the Absorbance Spectrum. *Phys. Rev. B*, 81(23):1–7, jun 2010.
- ³⁵ Marcelo Alves-Santos, Rosa Di Felice, and Guido Goldoni. Dielectric Functions of Semiconductor Nanoparticles from the Optical Absorption Spectrum: The Case of CdSe and CdS. *J. Phys. Chem. C*, 114(9):3776–3780, mar 2010.
- ³⁶ T Inoue, M Yoshida, MD Zoysa, K Ishizaki, and S Noda. Design of photonic-crystal surface-emitting lasers with enhanced in-plane optical feedback for high-speed operation. *Optics Express*, 28(4):5050–5057, 2020.

Chapter 2

Colloidal Nanocrystals

2.1 Introduction

In this Chapter, we describe the linear and non-linear photo-physics behind colloidal NCs, going from the chemistry, to their linear properties and, considering the goal of this work is to use them for lasing and other active devices, their non-linear properties. Finally, the different methods of making thin films with colloidal NCs are described.

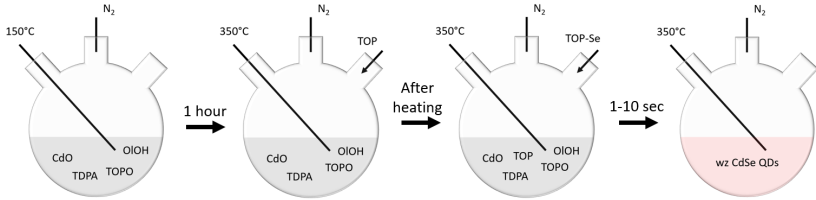


Figure 2.1: Synthesis example of CdSe core-only QDs.

2.2 Wet Chemical Synthesis

Colloidal NCs are typically synthesized through a hot-injection method. Here, a solvent containing precursors (like CdO), is heated up (50°C-360°C) and kept under nitrogen environment. A second precursor (containing Selenium, for example) is then rapidly injected in this saturated environment, which will initiate homogeneous nucleation and growth. Letting the nucleation and growth play out through time will determine the yield and size of the NCs. After the growth is complete the resulting sample can be washed to remove excess unreacted precursors and ligands, and (sometimes) centrifuged to select only the NCs of the desired size.

Secondary synthesis steps can be done, where the temperature and concentration of the NCs, precursors, and ligands are chosen in a specific way such that nucleation would not occur, but growth would. This leads to a shell growing on pre-existing NCs instead of new NCs forming. In the same way, specific reaction conditions, playing e.g. with surface reactivity, can allow for only certain types of growth, to aim specifically for growing colloidal platelets (1D confinement), or colloidal rods (2D confinement). Naturally, the numerous parameters that can be chosen give a lot of freedom and can be studied to determine the ideal set for synthesis. Because of this, this hot-injection synthesis is still an active area of research from which new and useful materials are routinely unveiled.

An example of a synthesis is shown in Figure 2.1. This procedure was taken from Drijvers *et al.*¹. CdO, *n*-tetradecylphosphonic acid (TDPA), oleyl alcohol (OIOH) and trioctylphosphine oxide (TOPO) are mixed to-

gether in a three-necked flask, heated to 150°C and kept under nitrogen condition for an hour. After this hour, the contents of the flask are heated to 350°C. When the solution became colorless (indicating dissolution of CdO), trioctylphosphine (TOP) is injected. When the solution stabilizes at 350°C, M-trioctylphosphine selenide (TOP-Se) is injected, after which CdSe QDs will start to form. Depending on the desired size, a time is chosen (typically between a few to a few tens of seconds), after which the reaction is quenched by using a colder water bath. The QDs can then be extracted from the flask.

2.3 Linear Optical Properties

As stated before, the optoelectronic properties of NCs change depending on the size, most importantly the optical band-gap E_g . Here, we are going to go more into detail about the most relevant linear properties for this work, and how they are affected by the NC size.

2.3.1 Absorption and Emission of Light

Consider a typical semiconductor. Here, a Valence Band (VB), filled with electrons, is separated by a band-gap of a certain energy (E_g), and above it there is a Conduction Band (CB), which is empty. In the linear regime, two processes can occur. A photon with energy $E \geq E_g$ can be absorbed, pushing an electron from the VB to the CB, or creating an electron-hole pair. When the electron and/or hole have excess kinetic energy (when $E > E_g$) they can relax to the band edge by emitting phonons (injecting heat in the system). After relaxation to the band edge, the electron-hole pair can bind together to form an exciton. This exciton can recombine and emit a photon with energy E_g . Emission of photons will always occur with energies of E_g with a certain broadening. The broadening mainly occurs due to two effects: (1) homogeneous broadening, where phonon coupling broadens the energy states, and (2) inhomogeneous broadening, where the bandgap is slightly different for different particles due to size inhomogeneity. Absorption will start for energies $E = E_g$, and will drastically shoot up for higher energies or photons with shorter wavelengths, due to the increase of Density Of States (DOS, typically referred to with ρ) above the band edge. The shape of the DOS increase will depend on the confinement in the system, that is, it will be different for 0D, 1D, 2D, and bulk systems. This simplified picture is a solid basis to explain many optical processes that occur in NCs, see also Figure 2.2a.

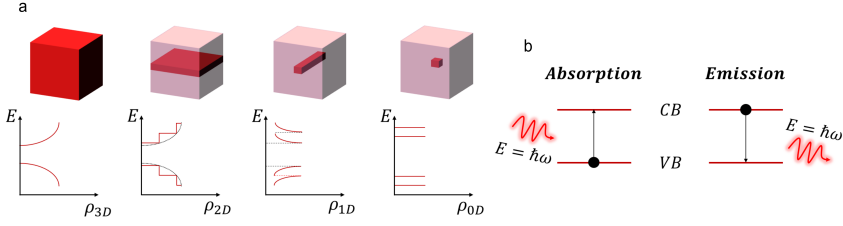


Figure 2.2: (a) Band structures for different geometries, going from no confinement or bulk (left) to 3D confinement or Quantum Dot (right). (b) Absorption and emission processes in semiconductors.

2.3.2 Quantum Confinement and the Optical Band Gap

At first we will consider only the situation of a 0D system, i.e. a Quantum Dot (QD).

Considering a carrier in a QD to be an electron-hole pair within a potential well, where the carrier is allowed to move around freely (so zero potential) (see Figure 2.3b). The general Schrödinger equation is

$$\left[-\frac{\hbar^2}{2m_e^*} \nabla_e^2 - \frac{\hbar^2}{2m_h^*} \nabla_h^2 + V_0(\vec{r}_e, \vec{r}_h) \right] = \Psi(\vec{r}_e, \vec{r}_h) \quad (2.3.1)$$

where m_e^* , m_h^* are the effective masses of the hole and the electron. The potential $V_0(\vec{r}_e, \vec{r}_h)$ will depend on the type of system. If we assume an infinite potential well first with width D , the Equation above can be solved both for electrons and holes, the sum of both giving the energy levels

$$E_n = \frac{\hbar^2 \pi^2 n^2}{2m_r D^2} \quad (2.3.2)$$

here, m_r is the reduced mass ($\frac{1}{m_r} = \frac{1}{m_e} + \frac{1}{m_h^*}$), and n are the discrete energy levels ($n = 1$ is the ground state). The smaller the QD, the further these energy levels will be apart, again showing the importance of the QD size.

The more accurate solution is to solve for the case where the exciton exists in an environment with dielectric constant ϵ in a potential well, and

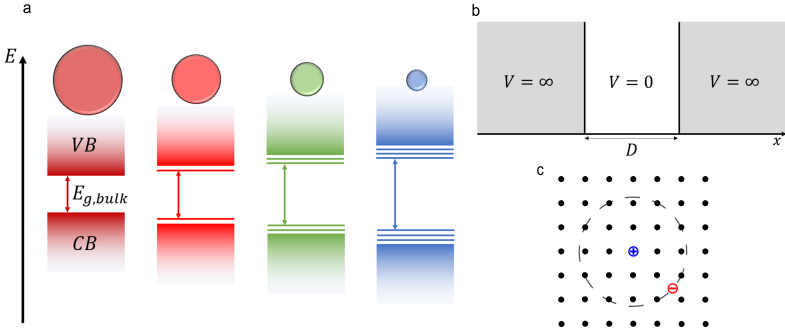


Figure 2.3: (a) Changes to the bandgap as a function of the size, small (left) to big (right). (b) Particle-in-a-box problem with infinite potential well. (c) Schematic of an exciton: a hydrogen-like system where the proton is replaced by a hole.

taking Coulomb screening into account (interaction between the electron and the hole). This will introduce a perturbation on the previous solution, and is called the Brus equation (for the first excited state):²

$$E_g = E_{g,bulk} + \frac{\hbar^2 \pi^2}{2m_r R^2} - \frac{1.786e^2}{\epsilon R} \quad (2.3.3)$$

with e the electron charge, and R is the radius of the QD. Like before, it can be seen that the band-gap energy depends both on the material ($E_{g,bulk}$), and the radius of the QD (R). As such both can be chosen to suit ones needs. As an example, CdSe has a bulk band gap of about 1.74 eV, leading to emission at 714 nm. Making a CdSe QD will *increase* the bandgap, so CdSe QDs can be used to make emitters from red to blue, but never go in the infrared.

For other NC geometries, similar methods can be found to find the size-induced energy levels. The geometry will create some changes but the same trend can be followed: smaller particles will lead to higher energies.

Looking at Figure 2.4, a slight shift between the NCs spontaneous emission and the start of the absorption can be observed. This is typically referred to as the Stokes shift, and is caused by various mechanisms, the most important being the fine structure splitting. This can cause a

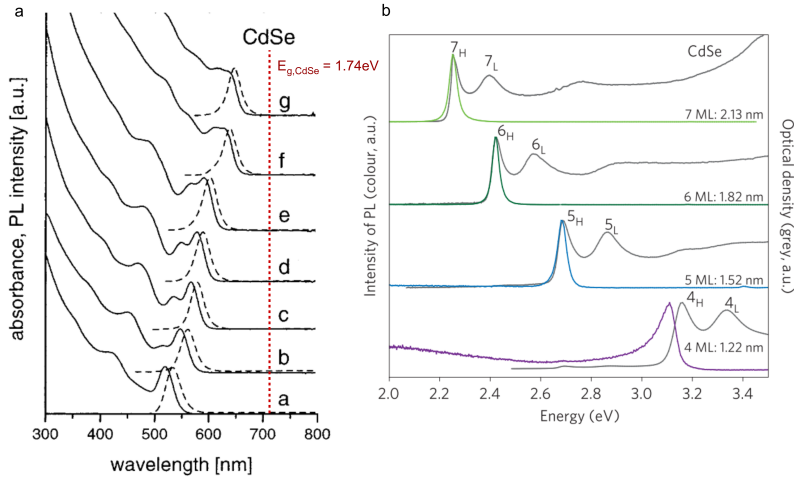


Figure 2.4: (a) Absorption and emission for CdSe QDs as a function of size. A clear Stokes-shift can be seen between the excitonic absorption and emission. Taken from Talapin *et al.*³. (b) Absorption and emission for different CdSe Quantum Wells. Taken from Ithurria *et al.*⁴.

redshift.

2.3.3 Maxwell-Garnett Effective Medium Approximation

Colloidal NCs in solution are a complex system: they constitute a mix of the solvent, the organic ligands around the NCs, and the semiconductor core (or core/shell, or any complicated NC engineered as the active material). To understand some general macroscopic properties of these complex systems, approximate theories like the Maxwell-Garnett (MG) Effective Medium Approximation can be used. This approximation helps to describe certain properties of the NCs in a simple manner.

We have to consider both the dielectric function of the medium or solvent ($\epsilon_s = n_s^2$, n_s being the refractive index), and the full complex dielectric function of the NC $\tilde{\epsilon} = \epsilon_R + i \cdot \epsilon_I$. Here, there is an imaginary

part since NCs absorb and emit light, and we assume there is only one semiconductor material present. We assume the solvent does not absorb in our spectral window of interest. For the case of spherical symmetry, the effective dielectric function $\tilde{\epsilon}_{eff}$ can be written as:⁵

$$\tilde{\epsilon}_{eff} = \frac{1 + 2\beta f}{1 - \beta f} \epsilon_s \quad (2.3.4)$$

which is known as the Clausius Mossotti relationship. Here, $\beta = \frac{\tilde{\epsilon} - \epsilon_s}{\tilde{\epsilon} + 2\epsilon_s}$, which is related to the polarizability (see Appendix A) and f is the volume fraction of the QDs, which in solution is usually very low, typically $f \approx 10^{-5}$. We will check this in more detail in the next Section. Using this, we can approximate both the real and imaginary part of the dielectric function

$$\epsilon_{eff,R} = \epsilon_s \quad (2.3.5)$$

$$\epsilon_{eff,I} = \frac{9\epsilon_s^2}{|\tilde{\epsilon} + 2\epsilon_s|} f \epsilon_I \quad (2.3.6)$$

Since the volume fraction is low, it makes sense that the real part of the dielectric function is purely determined by the solvent. For the imaginary part there is an influence of the semiconductor material, due to the solvent being not relevant at all here.

$\epsilon_{eff,I}$ can also be interpreted based on the local field factor f_{LF} , which, for spherical particles, is defined as

$$f_{LF} = \frac{3\epsilon_s}{\tilde{\epsilon} + 2\epsilon_s} \quad (2.3.7)$$

and is the difference between the local electric field inside of the QD \vec{E}_{local} , and the macroscopic electric field present in the medium \vec{E}

$$\vec{E}_{local} = f_{LF} \cdot \vec{E} \quad (2.3.8)$$

It is important to note that this local field is only isotropic because of the spherical symmetry. For non-spherical particles this no longer holds. Although we can still approximate the particles by ellipsoids, in which case the electric field will be constant over the particle in every dimension

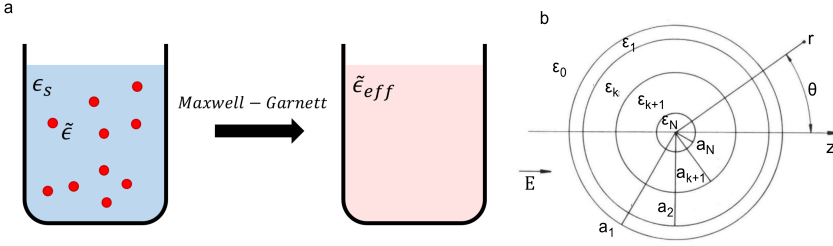


Figure 2.5: (a) Principle of the Maxwell-Garnett Effective Medium approach. (b) General, multi-layered Quantum Dot.

separately⁶. Using this interpretation, we can see that we can redefine $\epsilon_{eff,I}$ as

$$\epsilon_{eff,I} = |f_{LF}|^2 f \epsilon_I \quad (2.3.9)$$

Since semiconductor dielectric functions (both real and imaginary) are typically larger than those of organic solvents, the local field factor will be smaller than one, and as such, so will the local electric field be smaller than the macroscopic electric field. From this we see that the imaginary part of the dielectric function is simply the QD imaginary dielectric function, scaled by the volume fraction and the local field factor.

2.3.3.1 Intrinsic Absorption

The absorption can be quantified in many different ways. In the materials chemistry field, typically the absorbance A is used, which is defined using the logarithm base 10 in the Beer-Lambert law:

$$I_t = I_0 \times 10^{-A} \quad (2.3.10)$$

which can be solved for the absorbance A

$$A = \log \left(\frac{I_0}{I_t} \right) \quad (2.3.11)$$

In this situation, the sample is considered uniform, meaning A is the absorbance of the *total* sample. From this, the thickness dependent variable

α can be found, and coupled to the extinction coefficient κ^5 :

$$\alpha = \frac{\ln(10) \cdot A}{L} = \frac{4\pi\kappa}{\lambda} \quad (2.3.12)$$

This is the case for a “simple” medium. If we use the same formula for the composite medium, we can define the absorption coefficient of composite μ :

$$\mu = \frac{\ln(10) \cdot A}{L} = \frac{4\pi\kappa_{eff}}{\lambda} \quad (2.3.13)$$

from which naturally the effective extinction coefficient κ arises as determined through the MG effective medium approach. From the effective dielectric function both the effective refractive index and extinction coefficient can be found

$$\begin{cases} \epsilon_{eff,R} = n_{eff}^2 - \kappa_{eff}^2 \\ \epsilon_{eff,I} = 2n_{eff}\kappa_{eff} \end{cases} \Rightarrow \begin{cases} n_{eff} = \sqrt{\frac{|\tilde{\epsilon}_{eff}| + \epsilon_{eff,R}}{2}} \\ \kappa_{eff} = \sqrt{\frac{|\tilde{\epsilon}_{eff}| - \epsilon_{eff,R}}{2}} \end{cases}$$

Considering $n_{eff} = n_s$, we can use that $\epsilon_{eff,I} = 2n_{eff}\kappa_{eff}$ to rewrite the absorption coefficient of the composite μ as

$$\mu = \frac{4\pi\epsilon_{eff,I}}{\lambda \cdot 2n_{eff}} = \frac{2\pi}{\lambda} |f_{LF}|^2 f \epsilon_I \quad (2.3.14)$$

which links together the absorbance of a sample and the imaginary part of the dielectric function of the NC ϵ_I . We can make this volume fraction independent for a spherical particle by determining the *intrinsic absorption coefficient* μ_i

$$\mu_i = \frac{\mu}{f} = \frac{\ln(10) \cdot A}{f \cdot L} = \frac{2\pi}{\lambda n_s} |f_{LF}|^2 \epsilon_I = \frac{2\pi}{\lambda n_s} \frac{9\epsilon_s^2}{(\epsilon_R + 2\epsilon_s)^2 + \epsilon_I^2} \epsilon_I \quad (2.3.15)$$

which can be interpreted as the absorption if the entire space would be filled with NCs. A very important parameter used often to intrinsically compare material to one another, since certain metrics become sample independent, like optical gain (see later). It can also be used to translate properties to properties on film. Note that right now we can only link the intrinsic absorption coefficient to the *imaginary* part of the dielectric

function. Methods exist to also determine the real part, this will be followed up on in Chapter 7.

The intrinsic absorption can also be used to calculate the absorption cross section σ

$$\sigma = V_{NC} \cdot \mu_i \quad (2.3.16)$$

Knowing the intrinsic absorption of a NC at some reference wavelength λ_{ref} allows us to calculate back the intrinsic absorption spectrum-wide, since in principle it is just a matter of rescaling an experimental absorption spectrum A :

$$\mu_i(\lambda) = \frac{A(\lambda)}{A(\lambda_{ref})} \times \mu_i(\lambda_{ref}) \quad (2.3.17)$$

this allows for easily comparing different NC materials, and it will also be important when talking about optical gain, which we will come back to later.

2.3.4 Maxwell-Garnett and Intrinsic Absorption for General NCs

The previous situation holds only for the case of a core-only QD. This is due to the definition of β : it involves the polarizability of a dielectric sphere in a uniform environment (see Appendix A). Here, we take a step back and look for a more general case, that is, where the polarizability is not strictly known, and as an example then show how this would work for a n-layered QD, see also Figure 2.5b. Looking again at the definition of the intrinsic absorption

$$\mu_i = \frac{2\pi}{\lambda n_s} \epsilon_{eff,I} \quad (2.3.18)$$

which is in principle valid for general particles. The specific case for the core-only QD comes in when looking at the Clausius-Mossotti equation⁷

$$\frac{\tilde{\epsilon}_{eff} - \epsilon_s}{\tilde{\epsilon}_{eff} + 2\epsilon_s} = \frac{4\pi}{3} \cdot N\alpha \quad (2.3.19)$$

where N is the density of particles, and the polarizability α for a dielectric sphere is filled in. The general case can be solved for $\tilde{\epsilon}_{eff}$ to be

$$\tilde{\epsilon}_{eff} = \frac{1 + \frac{8\pi N\alpha}{3}}{1 - \frac{4\pi N\alpha}{3}} \quad (2.3.20)$$

which we can now solve separately for both real and imaginary parts

$$\epsilon_{eff,R} = \epsilon_s \quad (2.3.21)$$

$$\epsilon_{eff,I} = 4\pi N\epsilon_s \operatorname{Im}(\alpha) = 3f \cdot \frac{\operatorname{Im}(\alpha)}{r^3} \cdot \epsilon_s \quad (2.3.22)$$

which is in fact not so different from what we found previously. For the imaginary part, we used that $N \cdot \frac{4\pi}{3} r^3 = f$. α is defined as the polarizability. We can now re-define μ_i in a more general manner to be

$$\mu_i = \frac{2\pi}{\lambda n_s} \operatorname{Im}\left(3 \cdot \frac{\alpha}{r^3} \cdot \epsilon_s\right) \quad (2.3.23)$$

Filling in the polarizability of a simple dielectric sphere $\alpha = r^3 \frac{\tilde{\epsilon} - \epsilon_s}{\tilde{\epsilon} + 2\epsilon_s}$, we get the same result as before (see Appendix A).

Finding the polarizability for a general NC is not analytically possible, although there are situations where analytical solutions exist, such as for a multi-layered system with spherical symmetry or shelled ellipsoids. Below we discuss briefly an analytical solution for such a multi-layered system. In principle, all analytical cases will be more complex situations than the case discussed in Appendix A. Using FDTD methods to find the polarizability will often be much simpler than looking for analytical solutions.

2.3.4.1 Multi-layered QD or Gradient QD

Consider the situation, like in Appendix A, that instead of a uniform sphere now the sphere consists of multiple shells, each with their own radius a_k and ϵ_k . We count inwards, meaning the medium is denoted as ϵ_0 , outer shell is ϵ_1 and has radius a_1 , etc.

The solution will be similar, but naturally the boundary conditions must match between every layer, introducing an iteratively solvable set of

equations with much more bookkeeping than the situation of a uniform sphere. But one can see the solution will follow the same steps for every layer. This was done by Sihvola *et al.*^{8,9}, by using a clever transmission line analogy. The polarizability of such a system is shown below:

$$\alpha = \frac{(\epsilon_2 - \epsilon_1) \cdot a_2^3 + (2\epsilon_2 + \epsilon_1) \frac{(\epsilon_3 - \epsilon_2) \cdot a_3^3 + \dots}{(\epsilon_3 + 2\epsilon_2) + \dots}}{(\epsilon_1 - \epsilon_0) \cdot a_1^3 + (2\epsilon_1 + \epsilon_0) \frac{(\epsilon_2 - \epsilon_1) \cdot a_2^3 + (2\epsilon_2 + \epsilon_1) \frac{(\epsilon_3 - \epsilon_2) \cdot a_3^3 + \dots}{(\epsilon_3 + 2\epsilon_2) + \dots}}{(\epsilon_2 + 2\epsilon_1) + 2(\epsilon_2 - \epsilon_1) \cdot a_2^{-3} \frac{(\epsilon_3 - \epsilon_2) \cdot a_3^3 + \dots}{(\epsilon_3 + 2\epsilon_2) + \dots}}}$$

$$\frac{(\epsilon_2 - \epsilon_1) \cdot a_2^3 + (2\epsilon_2 + \epsilon_1) \frac{(\epsilon_3 - \epsilon_2) \cdot a_3^3 + \dots}{(\epsilon_3 + 2\epsilon_2) + \dots}}{(\epsilon_1 + 2\epsilon_0) + 2(\epsilon_1 - \epsilon_0) \cdot a_1^{-3} \frac{(\epsilon_2 - \epsilon_1) \cdot a_2^3 + (2\epsilon_2 + \epsilon_1) \frac{(\epsilon_3 - \epsilon_2) \cdot a_3^3 + \dots}{(\epsilon_3 + 2\epsilon_2) + \dots}}{(\epsilon_2 + 2\epsilon_1) + 2(\epsilon_2 - \epsilon_1) \cdot a_2^{-3} \frac{(\epsilon_3 - \epsilon_2) \cdot a_3^3 + \dots}{(\epsilon_3 + 2\epsilon_2) + \dots}}}$$

(2.3.24)

From this Equation, the iterative nature can be seen. Knowing a list of dielectric constants and radii of the different shells, this can easily be evaluated to find the polarizability, and from that the intrinsic absorbance.

A situation often occurring in literature¹⁰⁻¹² is the case of a core/shell QD. Here, the polarizability is defined as

$$\alpha = r^3 \frac{\epsilon_{sh}\epsilon_a - \epsilon_s\epsilon_b}{\epsilon_{sh}\epsilon_a + 2\epsilon_s\epsilon_b} \quad (2.3.25)$$

where

$$\epsilon_a = \epsilon_c \left(3 - 2 \frac{V_{sh}}{V_{QD}} \right) + 2\epsilon_{sh} \frac{V_{sh}}{V_{QD}} \quad (2.3.26)$$

$$\epsilon_b = \epsilon_c \frac{V_{sh}}{V_{QD}} + \epsilon_{sh} \left(3 - \frac{V_{sh}}{V_{QD}} \right) \quad (2.3.27)$$

with ϵ_c the dielectric constant of the core, ϵ_{sh} of the shell, and V_{sh}, V_{QD} the volume of the shell and total QD, respectively. One can verify that filling in Equation 2.3.24 for a core/shell system will give the same result as Equation 2.3.25. Here we can clearly see that besides the dielectric constants, starting from a core/shell structure, the intrinsic absorption also depends on the ratio of radii of the different layers. These typically are measured through analyzing TEM images.

2.4 Non-linear Optical Properties

So far, the description of Colloidal Nano Crystals has mostly been of their linear properties, or their properties in their ground state. Considering the goal in this work is to study NCs for lasing, we must naturally also discuss their non-linear properties: how do the NCs behave under strong optical excitation? In this section, we will explain the basics of the optical gain mechanics in colloidal NCs, and explain an often used experiment to determine some parameters with regard to optical gain. This is coupled back to certain state-filling physics that have been put forward in the past¹² to explain such gain.

2.4.1 Optical Gain in Colloidal Nanocrystals

Besides absorption and spontaneous emission put forward in Figure 2.2b, a third process can occur in a semiconductor called *stimulated emission*. This process is the enabler of any type of light amplification and any form of coherent light and is as such critical for laser operation (explained later). It is shown in Figure 2.6: in the situation that an electron-hole pair already exists in the NC, a secondary incoming photon can force the electron-hole pair to recombine and emit another photon, which will have the same directionality, phase, energy and polarisation as the first photon. In a situation where many excited NCs are present, a bundle of incoming photons can have a cascade effect to create a very strong, coherent light beam: the process of stimulated emission keeps occurring, exponentially amplifying the incoming photon bundle. Or: when an excited NC ensemble exists, a spontaneously emitted photon can be amplified by causing stimulated emission in other excited NCs.

For lasing operation we need to create a situation where there are many excited NCs, a situation which is called *population inversion*: here, more NCs in the ensemble are in the first excited state than the ground state. To reach population inversion, we must pump the system. Typically, this is either done by injecting a current of electrons and holes, or by using a

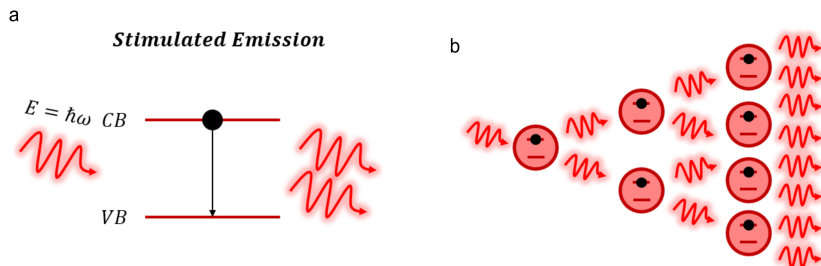


Figure 2.6: (a) Stimulated emission: an incoming photon causes a population inverted system to emit a secondary photon. (b) Cascading stimulated emission causing an exponential increase in the amount of photons.

strong optical light source. The latter is the method exclusively focused on in this work. A strong optical pump is also used to characterise the gain properties of the NCs, using Transient Absorption Spectroscopy, which is explained in the next section.

2.4.2 Transient Absorption Spectroscopy

To explain Transient Absorption Spectroscopy (TAS), we can consider a simple NC with just two energy levels: an empty conduction band, separated from a filled valence band by an energy E_g . The degeneracy of every level is two, which is a good approximation of the energy levels in QDs which are often S-like at the edges. The absorption spectrum of such a system would be a gaussian with a certain width depending on temperature around E_g . Now consider the situation where there is population inversion due to some kind of excitation: the CB is filled and the VB is empty. We can see that the absorption spectrum would be flipped: the same gaussian would appear, but now it is negative. Since the CB is filled, the process of absorption cannot occur any more. The only process that could occur due to an incoming photon is stimulated emission. So, a photon enters and two photons come out, exactly the opposite of absorption.

Imagine now that we can continuously probe the absorption as a function of time. After some time, one of the carriers in the CB would naturally decay, either by radiative recombination (emitting a photon), or some kind of trapping. Once this process happens, the net absorption that would be measured would be zero (it is transparent). This is because now an incoming photon will have the same probability of being absorbed or causing stimulated emission. Finally, some time later, the second carrier from the CB will drop back and we will be back in the steady-state situation, and see back the original gaussian. This flow is shown in Figure 2.7.

From this picture some quantities can be defined: one of which is the gain lifetime, denoted in Figure 2.7 as τ_{XX} , in general defined as τ_G . This is the length of time that the optical gain persists. The next is the gain magnitude g_i , here the system is fully inverted so it will be $-A_0$. In reality, reaching full inversion is no trivial thing, high excitation powers can be necessary to reach this. Finally, the gain threshold n_{th} can be found too, by sequentially increasing the excitation power and finding the first power for which transparency is reached. Depending on the type of NC, n_{th} is written as a carrier density (for bulk particles), or as $\langle N_{th} \rangle = n_{th}/V$ which denotes the amount of carriers per NC. These parameters will be more formally defined in the next Section.

This is exactly what is done in a TA experiment. A sample is pumped to introduce carriers in the system, and then the change in absorption is measured through time. Naturally, the situation explained here is an abstract simplification. In an actual material, the carriers can undergo multiple decay processes in general, excitation does not need to be resonant ($\hbar\omega > E_g$), multiple energy levels exist and we are dealing with a NC ensemble instead of a single NC which will not show such clear jumps in amplitude compared to the abstract situation. We will also measure many wavelengths at the same time instead of just one. But the basic principle stays the same. Many information can be determined from these experiments: the maximum gain can be found, the lifetime of the gain (in the situation described here as τ_{XX} , the power necessary to reach transpar-

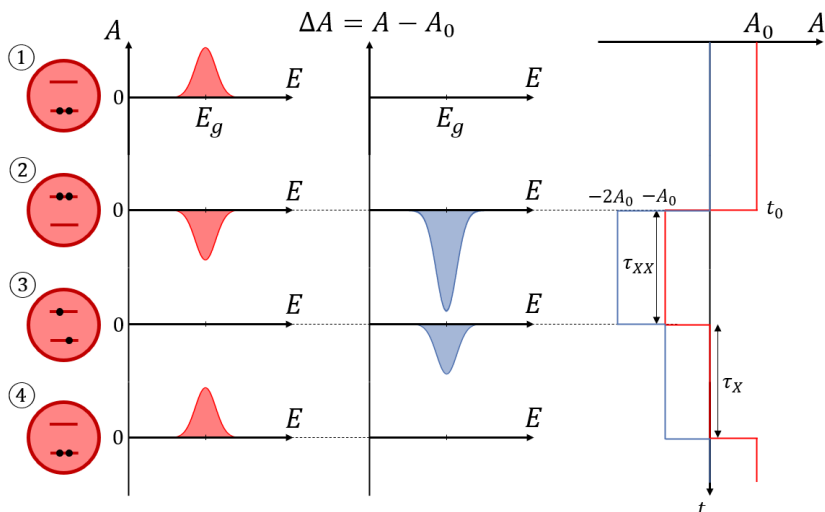


Figure 2.7: Continuously monitored absorption spectra under influence of a strong excitation. From top to bottom: before excitation, just after excitation, after the first carrier has decayed, after the second carrier has decayed. From this we can extract the plot on the right, which shows absorption through time. This shows that between t_0 and $t_0 + \tau_{XX}$, there is optical gain. This is when there are two carriers present in the NC.

ency, also called the “gain threshold”, and the spectral gain window. The intrinsic absorption coefficient also is important, because it allows us to translate the maximum gain to a *maximum intrinsic gain*, which allows for easy comparison between different materials: what would be the gain you could achieve filling the full space with a certain material? The intrinsic gain will tell us that.

2.4.2.1 Measurement Setup

Transient Absorption Spectroscopy is a measurement technique also referred to as a pump-probe technique. A femtosecond laser is used, which has very high energy (order mJ) and short (110 fs) pulses, at 800 nm. These pulses are split up into a pump (90%) and probe (10%). First,

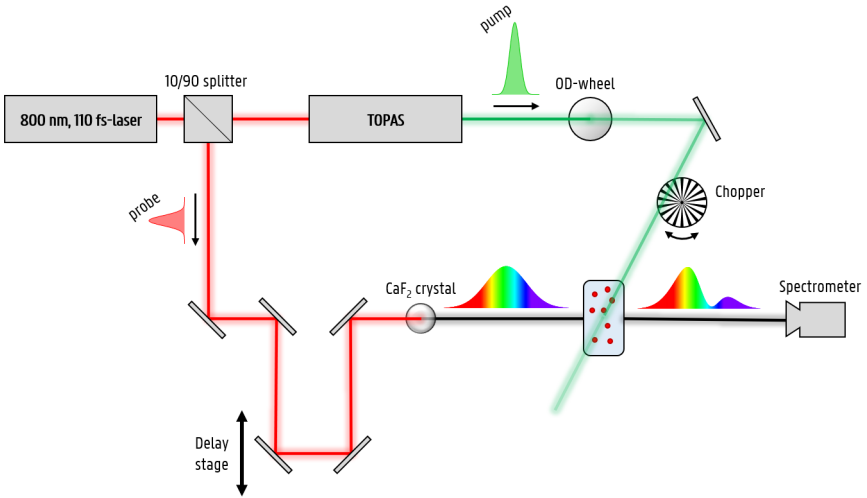


Figure 2.8: Schematic of the setup used to measure Transient Absorption.

the pump gets sent through an OPA (Optical Parametric Amplifier) to get the desired wavelength (350-1500 nm), and is then used to excite the sample. Then, the probe is delayed for a certain time Δt (limits are 0.2 ps to about 6 ns), gets sent through a crystal for broadening (by cascading non-linear effects a high energy single wavelength pulse is turned into a broadband pulse), and then used on the sample to do a “typical” absorption measurement: it goes through the sample and afterward the intensity is measured. A chopper is used to block half of the pump pulses, so every two probes that arrive in the detector, one measured the absorption under excitation, and the other measured the absorption without excitation. The difference between the two will then show us the change in absorption ΔA , this is also shown schematically in Figure 2.8.

The sample is dispersed in a cuvette with a non-absorbing solvent, and the concentration is chosen in such a way that the absorbance is 0.1-0.3 OD at the pump wavelength λ_p . This means that the incoming pump is absorbed for 20% to 50%, to make sure the pump intensity is still relatively uniform over the full length of the cuvette. The average amount

of excitons per NC $\langle N \rangle$, or average amount of absorbed photons per NC, can be calculated from the absorption cross section and the photon flux J_{ph}

$$\langle N \rangle = J_{ph} \sigma(\lambda_p) \times \frac{1 - e^{-A_0(\lambda_p)L}}{A_0(\lambda_p)L} \quad (2.4.1)$$

and related properties, like the carrier density $n = \langle N \rangle / V_{NC}$. The additional factor is a correction for the pump power changing over the length of the cuvette L . The photon flux can be calculated from measuring the power of the pump beam and correcting it

$$J_{ph} = \frac{P}{E_{ph} \cdot 0.5 \text{ kHz}} \frac{1}{A_{beam}} \quad (2.4.2)$$

with E_{ph} the energy of the photons in the pump, and the 0.5 kHz factor due to the typical chopper frequency of 1 kHz. The factor of two comes from the fact that half of the pulses are blocked. A_{beam} is the area of the pump spot, measured using a Thorlabs CCD Beam Profiler, with $A_{beam} = 2\pi\sigma_x\sigma_y$ with σ_i the standard deviation in the $i = x, y$ direction.

2.4.2.2 Effects measured through Transient Absorption Spectroscopy

Contrary to the simple mechanisms explained where we probe a two-level system, in an actual TA experiment a myriad of effects can occur and it is not always so simple to distinguish between them. We can categorize four different phenomena that can be seen¹³:

1. *Interband Bleach* - Absorbed carriers can decrease the absorption at certain energies because some or all of the available transitions are now blocked. This is typically referred to as a *bleach*.
2. *Intraband Absorption* - Introduced carriers can also increase the absorption at certain energies because new transitions become available, typically these are lower energy transitions since they occur in either the CB or VB separately, where a charge will get excited within the own energy band to a higher energy state.

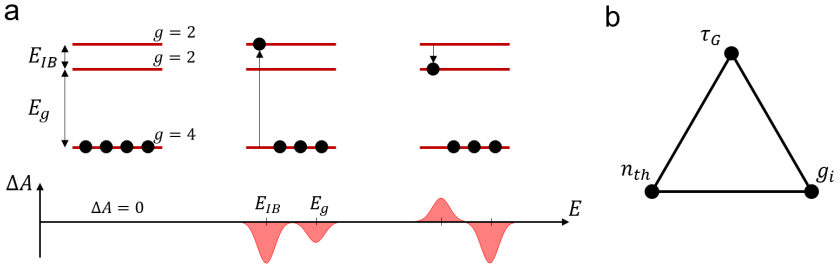


Figure 2.9: (a) Example of how exciting a multi level system would impact the absorption. On the left the system is at rest, in the middle a carrier was excited to a high energy state, and on the right the carrier has relaxed to the band edge. (b) the “gain trifecta”: the three intrinsic material properties of importance related to optical gain.

3. *Broadening or narrowing* - A more subtle effect where introduced carriers change the width of the excitonic transition, causing the gaussian to either broaden or narrow.
4. *Spectral shifts* - Caused by the Stark Effect, carriers introduce electric fields in the NC which will cause absorption features to shift.

A combination of these four phenomena can occur all at once, so interpreting the data can sometimes be tricky. The more complicated the experiment gets (i.e. not pumping resonantly, having many possible states, high power inducing temperature changes, ...) the trickier the interpretation will become. An example of some effects are shown in Figure 2.9, here a three level system is shown when excited and how the ΔA changes over time.

Measuring the change in absorption spectrally and over time allows us to create a ΔA -map, as shown in Figure 2.10.

2.4.2.3 Material Properties from Transient Absorption

If the change in absorption $\Delta A(\lambda, t)$ and the linear absorption $A_0(\lambda)$ were both measured for a sample, we can determine the non-linear absorption

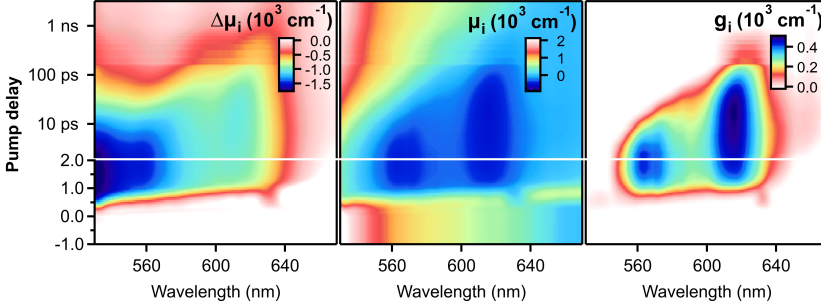


Figure 2.10: A TA experiment, rescaled change in absorption to intrinsic values (left), intrinsic non-linear absorption (middle), gain map where all the positive values from the middle map are made zero, and the negative values are changed sign ($g_i = -\mu_i$) (right).

$A(\lambda, t)$

$$A(\lambda, t) = \Delta A(\lambda, t) + A_0(\lambda) \quad (2.4.3)$$

from this map we can find out if a material is showing optical gain or not, for if $A < 0$ then more light will come out than in of that particular wavelength. By inverting the A -map, we can find the g -map ($g = -A$). Furthermore, rescaling A to the intrinsic absorption as was explained for the linear absorption, we can determine the *intrinsic gain coefficient*: $g_i = -\mu_i$

$$g_i(\lambda, t) = -\frac{A(\lambda, t)}{A_0(\lambda_{ref})} \times \mu_{i,0}(\lambda_{ref}) \quad (2.4.4)$$

where $\mu_{i,0}$ is defined as the linear intrinsic absorption. This intrinsic gain coefficient is very useful to compare gain characteristics of different NCs to each other, since it is a quantity normalized to volume: smaller NCs with lower gain per NC can give the same intrinsic gain as a bigger NC with higher gain per NC.

We can now formally define some important parameters. These are all wavelength/energy dependent.

1. $g_{i,max}$ – Maximum Intrinsic Gain reached in the sample. The DOS has a huge influence on this quantity, since a system can never be

more than fully inverted. More possible states leads to a higher possible gain magnitude. This leads to higher $g_{i,max}$ at higher energies.

2. τ_G – Inversion lifetime or Gain Lifetime. The gain lifetime indicates how long the gain persists. It will become maximized close to the band gap.
3. n_{th} – Gain Threshold. The amount of carriers needed for transparency. It will become minimized close to the bandgap. Depending on the geometry of the structure, it is expressed as $\langle N \rangle$, fluence in $\mu\text{J}/\text{cm}^2$, or carrier density cm^{-3}).

Optimizing a colloidal NC for gain translates to optimizing these three parameters (maximizing g_i and τ_G , and minimizing n_{th}), which is definitely not trivial. Various colloidal NC materials have great results for either the g_i , especially 4.5ML CdSe NPLs¹⁴ (values up to 76000 cm^{-1}), but showing below state-of-the-art lifetimes of up to 100 ps. By shelling NPLs, people managed to push up those lifetimes again, but at the cost of losing the very high gain magnitudes. An example of this is in the work of Cassidy *et al.*¹⁵, where a CdS/CdSe/CdS core/shell/shell structure is studied. The hole is mostly confined within the CdSe shell, effectively making a “curled up” shelled Quantum Well. These structures show gain lifetimes of an amazing 5.1 ns, vastly outcompeting other colloidal NC structures, but this comes at the price of much lower intrinsic gain values. Finally, other reports have been made by Geiregat *et al.*¹⁶ of HgTe QDs, which show gain thresholds of $\langle N \rangle = 0.03$! This is explained by the fact that the optical gain in these materials is actually trap assisted, where essentially any injected carrier immediately inverts the system. This has the effect that there also are long gain lifetimes, but since it is a trap-assisted process, the density is unavoidably low, leading to very low intrinsic gain. However, this shows that doping NCs is a great way to reduce the threshold, and is shown in other studies as well. A couple examples are given by Geuchies *et al.*^{17,18}, where electrochemical doping of CdSe/CdS QDs and CdSe NPLs dramatically decreases the gain threshold. Characterising (g_i, τ_G, n_{th}) for a specific sample allows to catalog and easily

compare it to other colloidal NCs, and we like to define it as the “gain trifecta”, displayed in Figure 2.9b.

The current consensus is that the gain lifetime is the most important metric to optimize for good lasing devices, as evidenced by the work of Ahn *et al.*¹⁹, where large, graded shells (total diameter of 12.5 nm, as shown in Figure 1.2c) are used to increase the gain lifetime as much as possible. Because the active part of the NC is only the CdSe core, this inevitably leads to a large reduction in the intrinsic gain, which leads to large cavities needed for amplification.

2.4.3 Modelling of the Optical Gain in Colloidal Nanocrystals

In this Section the physics behind optical gain will be presented for two separate systems: one with clear strong confinement present in the system, and one without. The former means that size influences the optical properties. The latter means size has no influence, which basically comes down to optical gain in a bulk semiconductor.

2.4.3.1 Strong Confinement

Here, energy levels are well separated from each other due to confinement. Because of this, it is typical to present the amount of carriers as an average amount of excitons (or electron-hole pairs) per NC $\langle N \rangle$, which is calculated as the mean of a poissonian.

To explain the model, we will use a single-transition system. Assuming a transition between a g_e -fold degenerate upper state and g_h -fold lower state (which is the case for CdSe), we can express the absorbance based on the occupancy of both upper (N_e) and lower (N_h) as follows:

$$A(N_e, N_h) = \left(1 - \frac{N_e}{g_e}\right) \left(1 - \frac{N_h}{g_h}\right) \cdot A_0 \quad (2.4.5)$$

Where A_0 is the linear absorbance of the transition. If the states are not occupied, this expression equates to the linear absorbance. If they

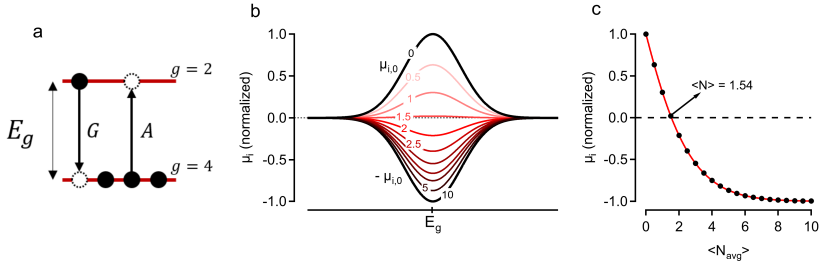


Figure 2.11: State filling shown for a $g_e = 2$ and $g_h = 4$ system, shown in (a). The intrinsic absorbance becomes negative for $\langle N \rangle = 1.54$. (b) The absorbance shown for various amounts of excitation. To fully invert the absorption, 10 excitons per NC are needed. (c) The absorbance as a function of excitons per NC. The threshold is found for $\langle N \rangle = 1.54$.

are maximally occupied, the expression becomes zero, indicating a full bleach. Similarly, we can express the stimulated emission of this transition as follows:

$$G(N_e, N_h) = \frac{N_e}{g_e} \cdot \frac{N_h}{g_h} \cdot A_0 \quad (2.4.6)$$

Which yields zero when the states are unoccupied, and A_0 for maximal occupation. The net absorbance of a single QD is the difference between these two expressions:

$$A(N_e, N_h) = A(N_e, N_h) - G(N_e, N_h) = \left(1 - \frac{N_e}{g_e} - \frac{N_h}{g_h}\right) \cdot A_0 \quad (2.4.7)$$

This expression can be extended for an ensemble of nanocrystals, containing on average $\langle N \rangle$ electron-hole pairs. If the ensemble contains $\langle N \rangle$ electron-hole pairs, then the probability of a single nanocrystal containing N electron-hole pairs follows a Poisson distribution $P(N, \langle N \rangle)$. The net absorbance of the ensemble is then found by summing over all possible occupancies:

$$A(\langle N \rangle) = \sum_{N=0}^{\infty} P(N, \langle N \rangle) \cdot \left(1 - \frac{N_e(N)}{g_e} - \frac{N_h(N)}{g_h}\right) \cdot A_0 \quad (2.4.8)$$

This expression allows us to find the required excitation to reach gain for a single transition. In our example where $(g_e, g_h) = (2, 4)$ the threshold

equals $\langle N \rangle = 1.54$, as shown in previous work¹². Here, N_e and N_h equal N before the full degeneracy is reached, and equal the degeneracy after they are completely filled. Redshifts, due to presence of charges, can lower this number.

2.4.3.2 Without Strong Confinement

When there is no strong confinement in the nanocrystal - when the diameter is sufficiently larger than the Bohr Diameter - bulk semiconductor physics can be used to explain the physics behind the material. The main difference between a Quantum Dot and a bulk semiconductor comes from the difference in the Density-Of-States (DOS), which for a QD is a discrete set of possible levels, while for bulk semiconductors it is a parabolic function of levels (see Figure 2.2). Other than that, the occupation is governed by Fermi-Dirac (FD) statistics. So we have a system of a Valence Band (VB) and Conduction Band (CB), separated by a bandgap (E_g). The FD occupation factor for electrons in the CB is defined as

$$f_c(E, E_F, T) = \frac{1}{1 + \exp\left(\frac{E - E_F}{k_B T}\right)} \quad (2.4.9)$$

Assuming a system in equilibrium (no injected carriers), $E_F = E_g/2$ (when choosing $E_{VB} = 0$). This distribution means that, for $T = 0$, the system is fully occupied below E_F , and empty above. This distribution is “smoothed” around E_F for $T > 0$, indicating the importance of temperature. When the system is *not* occupied with electrons, it is occupied with a hole. So we can define the hole FD occupation factor as

$$f_v(E, E_F, T) = 1 - f_c(E, E_F, T) = 1 - \frac{1}{1 + \exp\left(\frac{E - E_F}{k_B T}\right)} \quad (2.4.10)$$

$$= \frac{1}{1 + \exp\left(\frac{E_F - E}{k_B T}\right)} \quad (2.4.11)$$

This is the situation in equilibrium. Knowing the DOS (through the effective masses), the electron and hole distributions can be calculated

using these formulas. When charges are injected, the amount of electrons and holes will increase, with $n = p$ (considering only optical injection, which causes the creation of both an electron and a hole). This can be calculated through the change in Fermi Level, where for this situation the Quasi Fermi Level becomes different for electrons and holes separately. Knowing the injected electron density n , we know from bulk semiconductor physics that it is linked to the electron Quasi Fermi Level ($E_{F,e}$) by

$$n = N_{n,eff} \times F_{1/2} \left(\frac{E_{F,e} - E_g}{k_B T} \right) \quad (2.4.12)$$

with $N_{n,eff}$ the effective DOS at the band edge, defined as $N_{n,eff} = 2 \left(\frac{m_e^* k_B T}{2\pi\hbar^2} \right)^{3/2}$. $F_{1/2}$ is the Fermi-Integral, defined as

$$F_{1/2}(x) = \frac{1}{\Gamma(3/2)} \int_0^\infty \frac{t^{1/2}}{e^{1/2-x} + 1} dt \quad (2.4.13)$$

which cannot be inverted analytically. Many good numerical solutions exist and can be used to invert this relation to find the Quasi Fermi Level. Knowing the Quasi Fermi Level, the FD occupation can be calculated.

This exercise can be repeated for the holes. The differences come from the energy difference in the FD integral (the VB energy is set to zero), and the possible different band bending if the effective masses are different. For clarity later, it is useful to again translate the hole occupation to an electron occupation, which will *empty* the VB due to injected holes. Doing so, we end up with the Fermi Occupation Factors with injected carriers for the *electrons* in the CB and VB:

$$f_c(E, E_{F,e}, T) = \frac{1}{1 + \exp \left(\frac{E - E_{F,e}}{k_B T} \right)} \quad (2.4.14)$$

$$f_v(E, E_{F,h}, T) = \frac{1}{1 + \exp \left(\frac{E - E_{F,h}}{k_B T} \right)} \quad (2.4.15)$$

Which links back to population inversion: when the CB is filled, and the VB is not, and there are states available, there will be optical gain.

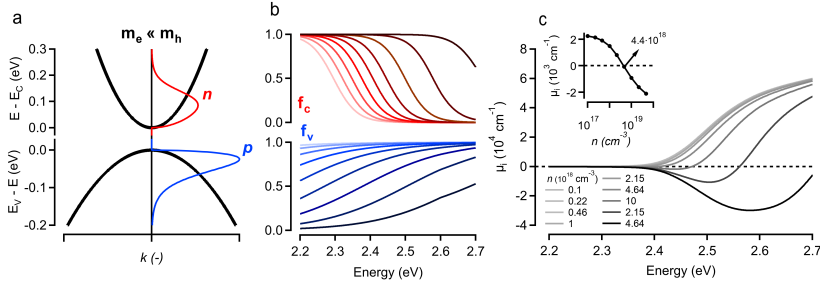


Figure 2.12: (a) Valence - and Conduction Bands example for a bulk material with $m_e = 0.2$ and $m_h = 0.7$ (wz-CdS). (b) FD occupation factors for different optical excitation powers. For low powers f_v is zero and f_c is zero, which reverses for powers. (c) The combination of the FD occupation factors leading to absorption for low power, and gain for higher powers. The used densities are shown here. The inset shows the intrinsic absorption as a function of optical power, with a gain threshold of $n_{th} = 4.4 \cdot 10^{18} \text{ cm}^{-3}$.

This argument can be condensed in the formula

$$g_i(E) = \mu_{i,0}(E, T) \times [f_c(E, E_{F,e}, T) - f_v(E, E_{F,h}, T)] \quad (2.4.16)$$

This model will be discussed in more detail in Chapter 5 and 6. An applied example is shown in Figure 2.12, where the effective masses of wz-CdS are used. A threshold density of $n_{thres} = 4.4 \cdot 10^{18} \text{ cm}^{-3}$ is found, which, for a 10 nm diameter NC, translates to $\langle N \rangle \approx 2.3$. It is important to note here that for particles without strong confinement, the carrier density is a more general unit to use than the average carriers per NC.

2.4.4 Ultrafast Photoluminescence

We can also measure time-resolved photoluminescence using an ultrafast method, called Transient Grating Photoluminescence Spectroscopy (TG-PLS). By employing optical delays, like with TA, similar time resolution can be reached here, although the setup is a bit different. An example setup is shown in Figure 2.13. Here, there is no probe necessary to measure for changes in the material since the signal is the PL from the sample

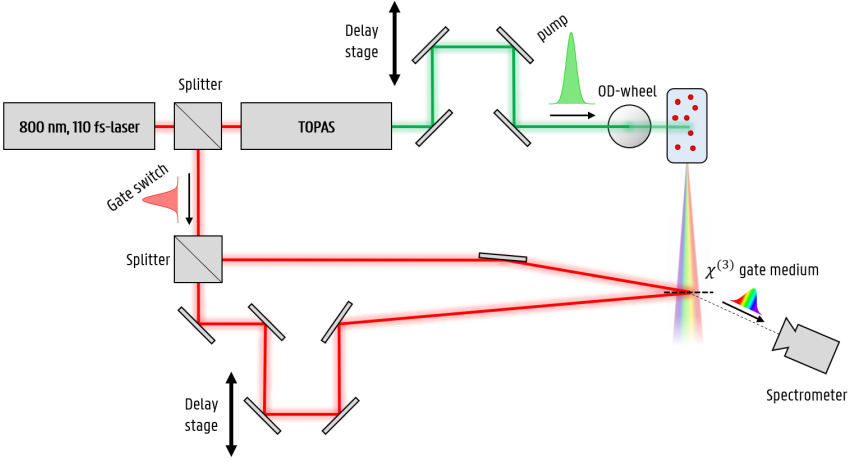


Figure 2.13: Schematic of the Ultrafast Photoluminescence setup used in this work.

itself. However, instead a “gate switch” signal is used that is split off from the 800 nm source, and then split up again to achieve two gate beams. By focusing these two together on the $\chi^{(3)}$ -medium a temporary grating (only lasts for the length of the gate beams, so around 100 fs) is created due to the Kerr effect. The delay used for one of the gate beams is to make sure they arrive at the same time, and can be used together with the angle between the two beams to determine the angle of refraction. The delay used for the pump beam is used to determine which time slice gets diffracted. In reality, the setup is more complicated with added lenses to achieve the high power densities necessary for the grating operation to work, and is adapted from Chen *et al.*²⁰.

It is worthwhile to briefly contrast a ΔA signal, as measured from Transient Absorption, to a Ultrafast Photoluminescence signal. In TA, the sum of the effects on the electrons and holes is probed: $n + p$. It is possible to look at these separately by looking, for example, at the signal of an intraband bleach in the conduction band, which does not rely on the amount of holes present. Contrary to this, for Ultrafast Photoluminescence, to see a signal both carriers need to be present: $n \cdot p$. This gives

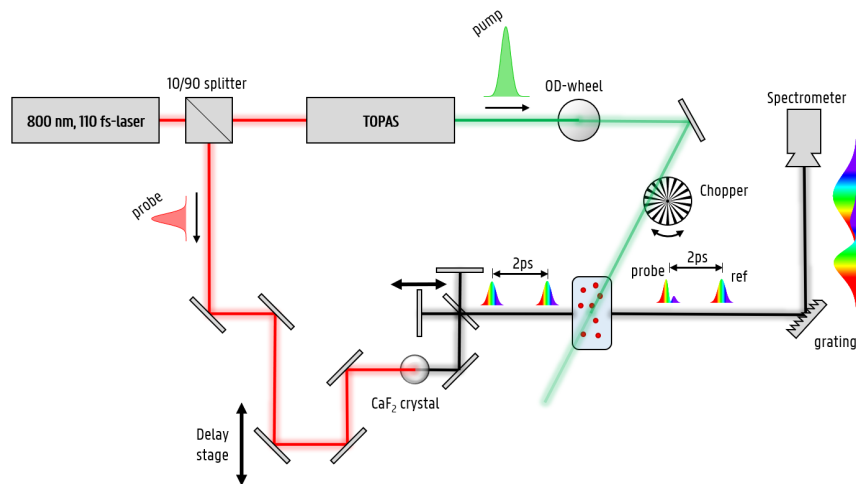


Figure 2.14: Schematic of the Frequency Domain Interferometry (FDI) setup used in this work.

us possibilities, to find temperatures of the carriers. This is discussed in detail in Chapter 6.

2.4.5 Ultrafast Phase Effects

Frequency Domain Interferometry (FDI) is a probe-pump-ref technique, similar to TA but with an added reference probe beam. The technique is sketched in Figure 2.14. The three beams interact with the sample, with the reference first (broadband), then the pump (fixed wavelength, with high intensity), and finally the probe. The time between the probe and reference is fixed to be 2 ps, but between the pump and probe the pump-probe delay can be swept and is referred to as τ . (naturally, this leads to a $2 - \tau$ difference between the reference and the pump beams. This small time difference between probe and reference is important, since behind the sample a grating is used to broaden the probe and reference beams, and the information from the measurement comes from the overlap between these two beams. This is an intrinsic downside to the FDI technique, since

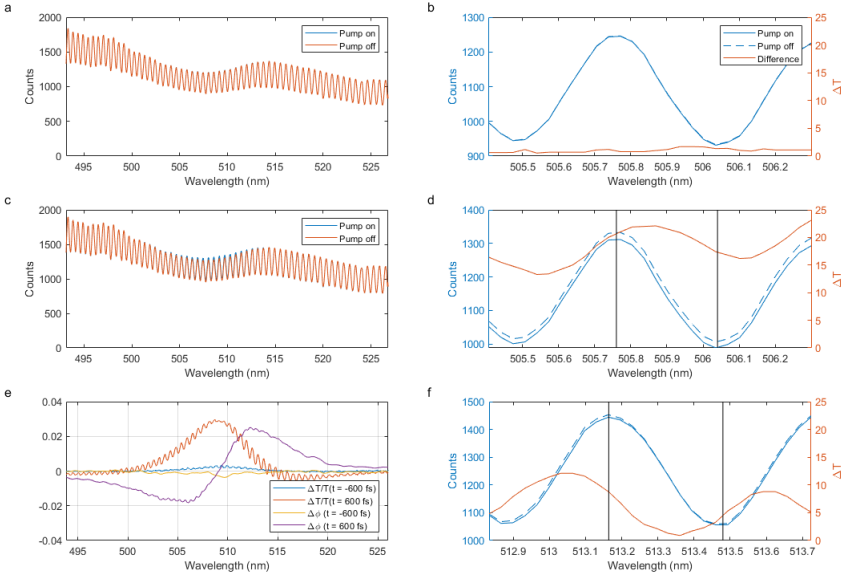


Figure 2.15: Example measurement of the FDI technique, showing various interferograms and the extracted phase change.

it limits the pump-probe delay that can be measured. TA does not have this limitation.

Assuming the pump is off, the probe and reference will give the exact same measured spectrum. The probe spectrum will however change when the pump is turned on, both the absorbance and the phase of the beam will change. This is in fact the same for TA, but there only the intensity for all wavelengths is measured. Because here the reference and probe beams are overlapped, an interference pattern will emerge, which will change depending on the pump intensity. This can be used to calculate back both the change in absorption and the change in phase due to excitation. These measurements are not done in-house, but in Victoria University of Wellington by our collaborators. Below some experimental details are given and comments regarding the accuracy.

The experimental FDI setup was built as a modification of a standard

transient absorption setup at Victoria University of Wellington.²¹ An example is shown in Figure 2.14. After the CaF₂ the probe is split and with a 50/50-splitter and the probe is delayed by 2 ps compared to the reference by using a Michelson Interferometer. After the sample, a grating is added to diffract the pulses, to cause an overlap between reference and probe. From the measured interferograms then the phase information can be calculated back.

To illustrate the method, some interferograms are shown in Figure 2.15, for ground state (pump off) and excited state (pump on). Figure (a) shows interferograms at -600 fs when the sample is in the ground and excited state, showing complete overlap, where (b) shows a zoom on two periods. The difference is nearly zero. Figure (c) shows the interferogram at +600 fs, where the intensity difference is now noticeable, as shown by the zoom in Figure (d) and (f). Finally, Figure (e) shows the extracted phase change after the Fourier retrieval algorithm for both times (-600 fs and +600 fs), together with the change in transmission.

This is shown for the case before excitation (Figures (a) and (b)) at -600 fs, and after excitation (Figures (c) and (d)).

Accuracy The accuracy of the FDI technique is dependent on several parameters. The first parameter is the time delay between the reference and probe pulse, which determines the period of the interference pattern. The second parameter is the spectral resolution of the spectrometer, which determines the number of pixels to capture a single period. The third is the stability of the optical system, determining the shot noise. To gain a better understanding of the noise level after the Fourier phase retrieval, we have analyzed 10 differential phase spectra before time-zero, shown in Figure 2.16. The individual spectra shown are a result of 3.000 ground and excited-state shots obtained in a single run. We have shown the change in the phase rather than the change in refractive index as the refractive index is calculated from the phase, wavelength and thickness of the sample. This shows that the retrieved differential phase has an averaged standard deviation of $2.9 \cdot 10^{-4}$.

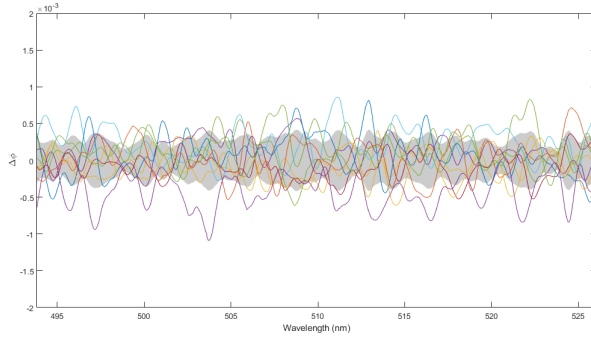


Figure 2.16: Error estimation of the differential phase spectrum. The lines show 10 differential phase spectra between -2 ps and -300 fs, where no signal is expected. The grey area indicates the standard deviation of the differential phase spectrum for these spectra at each wavelength. This shows an average standard deviation of $2.9 \cdot 10^{-4}$ for the retrieved phase.

The FDI technique is used in Chapter 7 to find phase differences induced by excitation directly, and will be compared to an indirect method by analyzing TA data. The limited time window in the FDI technique makes alternative methods to determine phase changes viable.

2.5 Thin Films of Colloidal Nanocrystals

Properties of colloidal NCs are typically studied in solution. Translating these properties to thin films is typically not such an easy task, but very necessary for going toward applications: for either making LEDs, photo-detectors, or lasers, we need to embed the NCs in a stack that allows us to direct the flow of the light. Different methods exist to tackle this crucial step, and pattern NC layers afterward. These methods range from very simple, often producing rough films, to complex but very well controlled films, and will be discussed in this section. Lift-off, a method to pattern NC films, will also be discussed here.

2.5.1 Film Deposition Methods

2.5.1.1 Drop-casting

By far the easiest way to make a thin film of colloidal NCs is by drop-casting: taking a certain volume of NC solution, simply dropping it on a substrate, and waiting for the solvent to dry out. These thin films can be made thick quite easily (more than a micron thick is feasible), since there is no loss of material, but they will also not be really uniform. Typically the solvent tends to dry on the outside first, giving rise to so called “coffee stain” layers (see also Figure 2.17a), where the film can be multiple microns thick while the center is much more thin, as shown in the work of Zavelani *et al.*²² with colloidal CdSe/CdS core/shell quantum rods. Here, a very small volume was deposited and only 10 nm thicknesses are found in the center, while at the edge the thickness ranges from 30 - 90 nm. Nevertheless, when thick layers are necessary and roughness is not of the highest importance, drop-casting can be used. Dropcasting is the easiest way to deposit a NC film, but the dirtiest. As such, this technique is not used often anymore for any type of application.

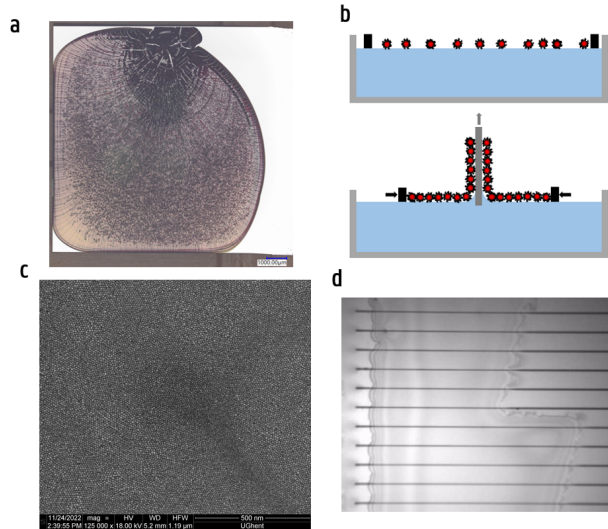


Figure 2.17: (a) Coffee stain effect from dropcasting and irregular drying of the film. (b) Langmuir-Blodgett deposition example. (c) Langmuir-Blodgett film of bulk CdS NCs as seen with SEM. (d) Inkjet printed trapezoid pattern on waveguides with thickness of 1 μm .

2.5.1.2 Spincoating

Spincoating is a technique where liquid is dropped on a substrate, but instead of waiting for the solvent to evaporate, the substrate is spun around with high rounds per minute (RPM) (1000-5000 RPM are typical values). Due to the centripetal force most of the liquid gets pushed off the substrate, resulting in a parabolic shaped layer where the center is quite flat and smooth. This technique is also used to deposit layers of photo or e-beam resist (see later).

Specifically for NCs, spincoating is the most often used technique for layers going from a couple of mono-layers to a relatively thick layer: limits are around 20-400 nm. The smoothness is definitely a step up compared to drop-casting, where here a 50 nm film typically has a thickness variation of ± 5 nm. But the downside is the loss of material, since you need

high concentration for a decent film thickness, and in the end most of the material is lost. A typical rule of thumb is that thickness scales proportional with the concentration of the NCs, and inversely proportional with the spinning speed. Going toward thicker films (> 200 nm) these proportionalities no longer hold and much higher concentrations are needed.

2.5.1.3 Langmuir-Blodgett Deposition

Langmuir-Blodgett deposition is a technique used to create near-perfect monolayers of NCs. The basis of this technique is the fact that due to the organic ligands being apolar (typically long organic molecules), they are not soluble in water. The setup is as follows: a basin is filled with water and a substrate is inserted vertically in it. Some of the NC containing sample is then deposited in this water: due to the insolubility, the NC “film” will spread out over the water layer. Then, the surface area of the water is decreased by slowly pushing the sidewalls in, pushing the NC film closer together. This is maintained until a pushback in the form of pressure is sensed on the sidewalls, meaning the NCs are pushed as close together as they can without starting to overlap. At this stage, the substrate is pulled out while continuously increasing the pressure on the sidewalls, this way the monolayer will be transferred onto the substrate. Details are shown in Figure 2.17b.

The advantage of this technique is that it can lead to very uniform monolayers (see Figure 2.17c)^{23,24}, but it is a very slow deposition method. Getting the NC sample in the right condition for good monolayer deposition is also difficult since too many or too few ligands can create sub-optimal films, and optimizing the surface tension is also necessary. For more deposition, the deposition can be repeated multiple times, every time depositing an additional monolayer

2.5.1.4 Inkjet Printing

Inkjet printing is a technique to locally deposit small droplets to form thin films only locally, similar to an inkjet printer for printing documents.

Precise control of the deposited volume (typically order of pico litres) determines the minimum printer feature size that can be made. The precise control has advantages that processing is no longer necessary, possibly destroying the NC layer (atleast when the NC deposition is the final processing step), and less material is wasted because the NCs are only deposited precisely where they are needed.

By using inkjet printing for colloidal nanocrystals, pixels have been demonstrated of 20 μm , by using 2 pL droplets²⁵, showing an impressive possible resolution of 1000 pixels-per-inch (PPI). The authors furthermore demonstrate a functional QLED display at 500 PPI. Important for making a good ink is the wettability of the surface, expressed through the inverse Ohnesorge number Z , which is defined as

$$Z = \frac{\sqrt{\gamma\rho d}}{\eta} \quad (2.5.1)$$

where γ is the ink surface tension, ρ is the density of the ink, η is the viscosity, and d is the nozzle diameter. A value of $1 < Z < 10$ leads to stable, separated droplets. The paper of Yang *et al.* discusses using a mixture of 5% octane and 95% cyclohexylbenzene (CHB) as an ideal ink. The addition of octane prohibits the “coffee stain” rings that appear for pure CHB, at 5% octane it is reported that the NC film is distributed nearly uniformly over the pixel. An example of an inkjet printed pattern can be seen in Figure 2.17d, where a trapezoidal pattern of NCs is printed on waveguides. It also shows the coffee stain effect on the edges, showing that optimisation could improve the uniformity of these types of deposited films.

2.5.2 Patterning NCs through Lift-off

A final and very precise deposition method for NCs is liftoff. This is done by doing either optical or e-beam lithography, but we will focus here on e-beam lithography due to its use in this work. With this technique, patterns with extremely small sizes can be made, for example Elsinger *et al.* have deposited PbS/CdS QD pillars with diameters of about 20 nm²⁶.

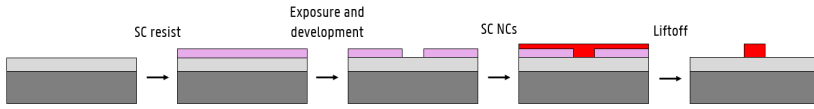


Figure 2.18: Liftoff process for colloidal NCs.

The size limitation depends also on the resist thickness and the e-beam alignment.

The liftoff process flow is shown in Figure 2.18. A different resist is used compared to regular ebeam lithography. The liftoff is performed in acetone typically, although Xie *et al.* showed that a ratio of 1:4 acetone/toluene gives ideal results²³, an apolar solvent that dissolves the NCs prevents immediate redeposition of the NCs somewhere on the substrate. Note that this was done specifically for monolayers of NCs. The shown process is on Silicon Oxide (SiO_x), but can be adapted to be performed on a Silicon Nitride (SiN_x) thin film instead, for instance, to later embed the NCs in a waveguide. Processing of NC waveguides is discussed in more detail in Chapter 3.

Bibliography

- ¹ Emile Drijvers, Jonathan De Roo, Pieter Geiregat, Krisztina Feher, Zeger Hens, and Tangi Aubert. Revisited wurtzite cdse synthesis: A gateway for the versatile flash synthesis of multishell quantum dots and rods. *Chemistry of Materials*, 28(20):7311–7323, 2016.
- ² Louis E Brus. Electron–electron and electron-hole interactions in small semiconductor crystallites: The size dependence of the lowest excited electronic state. *The Journal of chemical physics*, 80(9):4403–4409, 1984.
- ³ Dmitri V Talapin, Andrey L Rogach, Andreas Kornowski, Markus Haase, and Horst Weller. Highly luminescent monodisperse cdse and cdse/zns nanocrystals synthesized in a hexadecylamine- trioctylphosphine oxide- trioctylphosphine mixture. *Nano letters*, 1(4):207–211, 2001.
- ⁴ Sandrine Ithurria, MD Tessier, Benoit Mahler, RPSM Lobo, B Dubertret, and Al L Efros. Colloidal nanoplatelets with two-dimensional electronic structure. *Nature materials*, 10(12):936–941, 2011.
- ⁵ Zeger Hens and Iwan Moreels. Light absorption by colloidal semiconductor quantum dots. *Journal of Materials Chemistry*, 22(21):10406–10415, 2012.
- ⁶ Yera Ye Ussembayev, Zeger Hens, and Kristiaan Neyts. Contrasting anisotropy of light absorption and emission by semiconductor nanoparticles. *ACS Photonics*, 6(5):1146–1152, 2019.
- ⁷ Vadim A Markel. Introduction to the maxwell garnett approximation: tutorial. *JOSA A*, 33(7):1244–1256, 2016.
- ⁸ Ari Sihvola and Ismo V Lindell. Transmission line analogy for calculating the effective permittivity of mixtures with spherical multilayer scatterers. *Journal of electromagnetic waves and applications*, 2(8):741–756, 1988.

- ⁹ A Sihvola and IV Lindell. Polarizability and effective permittivity of layered and continuously inhomogeneous dielectric spheres. *Journal of electromagnetic waves and applications*, 3(1):37–60, 1989.
- ¹⁰ Arthur E Neeves and Meyer H Birnboim. Composite structures for the enhancement of nonlinear-optical susceptibility. *JOSA B*, 6(4):787–796, 1989.
- ¹¹ Bram De Geyter and Zeger Hens. The absorption coefficient of pbse/cdse core/shell colloidal quantum dots. *Applied Physics Letters*, 97(16):161908, 2010.
- ¹² S. Bisschop, P. Geiregat, T. Aubert, and Z. Hens. The Impact of Core/Shell Sizes on the Optical Gain Characteristics of CdSe/CdS Quantum Dots. *ACS Nano*, 12:9011–9021, 2018.
- ¹³ Pieter Schiettecatte, Zeger Hens, and Pieter Geiregat. A roadmap to decipher ultrafast photophysics in two-dimensional nanomaterials. *The Journal of Chemical Physics*, 2022.
- ¹⁴ Renu Tomar, Aditya Kulkarni, Kai Chen, Shalini Singh, Dries Van Thourhout, Justin M Hodgkiss, Laurens DA Siebbeles, Zeger Hens, and Pieter Geiregat. Charge carrier cooling bottleneck opens up nonexcitonic gain mechanisms in colloidal cdse quantum wells. *The Journal of Physical Chemistry C*, 123(14):9640–9650, 2019.
- ¹⁵ James Cassidy, Benjamin T Diroll, Navendu Mondal, David B Berkin-sky, Kehui Zhao, Dulanjan Harankahage, Dmitry Porotnikov, Reagan Gately, Dmitriy Khon, Andrew Proppe, et al. Quantum shells boost the optical gain of lasing media. *ACS nano*, 16(2):3017–3026, 2022.
- ¹⁶ Pieter Geiregat, Arjan J Houtepen, Laxmi Kishore Sagar, Ivan Infante, Felipe Zapata, Valeriia Grigel, Guy Allan, Christophe Delerue, Dries Van Thourhout, and Zeger Hens. Continuous-wave infrared optical gain and amplified spontaneous emission at ultralow threshold by colloidal hgte quantum dots. *Nature Materials*, 17(1):35–42, 2018.

- ¹⁷ Jaco J Geuchies, Baldur Brynjarsson, Gianluca Grimaldi, Solrun Gudjonsdottir, Ward Van Der Stam, Wiel H Evers, and Arjan J Houtepen. Quantitative electrochemical control over optical gain in quantum-dot solids. *ACS nano*, 15(1):377–386, 2020.
- ¹⁸ Jaco J Geuchies, Robbert Dijkhuizen, Marijn Koel, Gianluca Grimaldi, Indy Du Fossé, Wiel H Evers, Zeger Hens, and Arjan J Houtepen. Zero-threshold optical gain in electrochemically doped nanoplatelets and the physics behind it. *ACS nano*, 16(11):18777–18788, 2022.
- ¹⁹ Namyoungh Ahn, Young-Shin Park, Clément Livache, Jun Du, Kivanc Gungor, Jaehoon Kim, and Victor I Klimov. Optically excited lasing in a cavity-based, high-current-density quantum dot electroluminescent device. *Advanced Materials*, page 2206613, 2022.
- ²⁰ Kai Chen, Alex J Barker, Matthew E Reish, Keith C Gordon, and Justin M Hodgkiss. Broadband ultrafast photoluminescence spectroscopy resolves charge photogeneration via delocalized hot excitons in polymer: fullerene photovoltaic blends. *Journal of the American Chemical Society*, 135(49):18502–18512, 2013.
- ²¹ Ronnie R Tamming, Justinas Butkus, Michael B Price, Parth Vashishtha, Shyamal K K Prasad, Jonathan E Halpert, Kai Chen, and Justin M Hodgkiss. Ultrafast Spectrally Resolved Photoinduced Complex Refractive Index Changes in CsPbBr₃ Perovskites. *ACS Photonics*, 6:345–350, 2019.
- ²² Margherita Zavelani-Rossi, Maria Grazia Lupo, Roman Krahne, Liberato Manna, and Guglielmo Lanzani. Lasing in self-assembled microcavities of cdse/cds core/shell colloidal quantum rods. *Nanoscale*, 2(6):931–935, 2010.
- ²³ Weiqiang Xie, Raquel Gomes, Tangi Aubert, Suzanne Bisschop, Yunpeng Zhu, Zeger Hens, Edouard Brainis, and Dries Van Thourhout. Nanoscale and single-dot patterning of colloidal quantum dots. *Nano letters*, 15(11):7481–7487, 2015.

- ²⁴ Abdoulghafar Omari, Hiroyuki Shinci, Pieter Geiregat, Dries Van Thourhout, and Zeger Hens. Characterization of pbs/cds qdot absorption on soi waveguides. In *17th Annual Symposium of the IEEE Photonics Benelux Chapter*, pages 295–298. IEEE, 2012.
- ²⁵ Peihua Yang, Long Zhang, Dong Jin Kang, Robert Strahl, and Tobias Kraus. High-resolution inkjet printing of quantum dot light-emitting microdiode arrays. *Advanced Optical Materials*, 8(1):1901429, 2020.
- ²⁶ Lukas Elsinger, Ronan Gourgues, Iman E Zadeh, Jorick Maes, Antonio Guardiani, Gabriele Bulgarini, Sylvania F Pereira, Sander N Dorenbos, Val Zwiller, Zeger Hens, et al. Integration of colloidal pbs/cds quantum dots with plasmonic antennas and superconducting detectors on a silicon nitride photonic platform. *Nano letters*, 19(8):5452–5458, 2019.

Chapter 3

Integrated Photonics

3.1 Introduction

This Chapter will introduce basic concepts related to Integrated Photonics, starting from building blocks to the details regarding devices studied in this work.

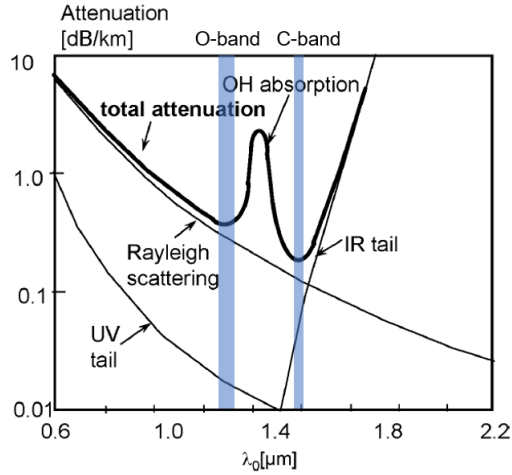


Figure 3.1: Attenuation in optical fibers by absorption and scattering¹.

3.2 Silicon Nitride Platform for Visible Photonics

Integrated Silicon Photonics started out in the near infrared range, specifically the O- (1260 - 1360 nm) and C-band (1530-1565 nm), see Figure 3.1. In these bands, the losses in fibers are the lowest, and typical telecom applications still operate around 1.55 μm because of this. At these wavelengths, the intrinsic losses will be the lowest (0.4 dB/km at 1.3 μm and 0.15 dB/km at 1.55 μm). The first steps to developing integrated photonics was as such to create Photonic Integrated Circuits (PICs) at these wavelengths, which was done through the Silicon-On-Insulator (SOI) platform. Here, silica (SiO_2) is grown on a silicon wafer, after which this wafer is flipped and bonded on a handle wafer. After this, most of the first wafer is removed by various methods, leaving a thin silicon layer behind, which after polishing is ready to be used. This layer can then be patterned to make waveguides and other optical components (see top of Figure 3.2 for the SOI platform).

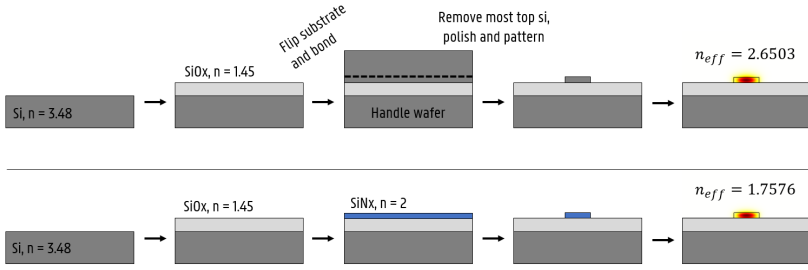


Figure 3.2: (top) SOI platform from starting Silicon wafer to finished waveguide with corresponding optical mode. (bottom) same for the SiNx platform.

Silicon has a bandgap of 1.12 eV, meaning it will start absorbing wavelengths shorter than $\sim 1.1 \mu\text{m}$. The SOI platform cannot be used in the visible region because of this. To move toward shorter wavelengths, the platform of Silicon Nitride (Si_3N_4 , SiNx) on SiOx is used (see bottom of Figure 3.2). Here, SiNx layers are grown directly on top of SiOx, on top of a silicon substrate. Silicon Nitride is an insulator which has low losses over the entire visible spectrum, the downside compared to silicon is the lower refractive index, which will lead to a smaller confinement. SiNx

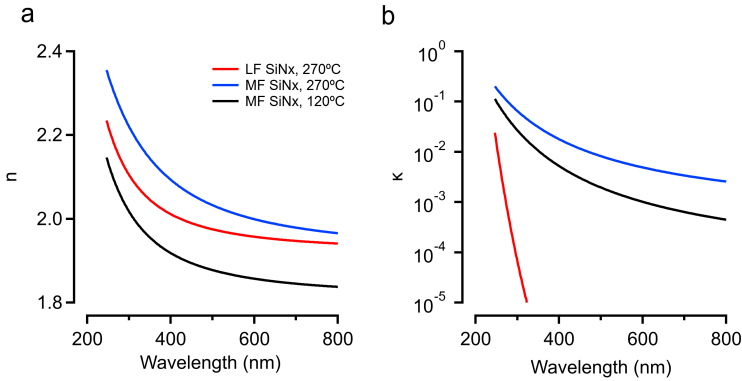


Figure 3.3: (a) Refractive index of various types of SiNx grown in-house. (b) Extinction coefficient of various types of SiNx grown in-house.

used in industry is typically grown using Low-Pressure Chemical Vapour Deposition (LPCVD), which operates at very high temperatures (800-900°), and has low deposition rates. This deposition leads to the lowest losses. However, for our specific case where NCs need to be embedded, these high temperatures are not an option. Instead, SiNx it is grown using Plasma Enhanced Chemical Vapour Deposition (PECVD). Here, we define high temperature deposition as deposition at 270°C, (HT-SiNx). Low temperature deposition is done at 120°C (LT-SiNx). Changing the plasma frequency from Low Frequency (LF-SiNx) to Mixed Frequency (MF-SiNx), or High Frequency (HF-SiNx) has consequences for the properties as well. It changes the refractive index, losses, density, adhesion and growth rate. Typically, LF-HT-SiNx has the lowest losses, see also Figure 3.3². State-of-the-art SiNx waveguides can achieve losses of ~ 5 dB/m. We can grow SiNx layers in-house that give losses < 1 dB/cm.

In this work we exclusively focus on the SiNx platform, and in the following Sections we will introduce some photonic components specifically designed on this platform.

3.3 Integrated Photonic Components

Components on PICs that guide, direct and filter light are discussed in this Section. These are typically referred to as “passive”, meaning they are ideally lossless, but in practice designed and fabricated to be as lossless as possible. Contrary to this there are active structures, which amplify light or actively manipulate light and will be discussed after the passive ones.

3.3.1 Passive Components

To understand Photonic Circuits we need to solve Maxwell Equations. For many cases, the refractive index is piecewise constant. Without going too much into detail, for this case the Maxwell Equations can be reduced to the scalar Helmholtz Equation:

$$\nabla^2\Psi(\vec{r}) + k_0^2n^2(\vec{r})\Psi(\vec{r}) = 0 \quad (3.3.1)$$

Where $\Psi(\vec{r}) = \Psi(x, y, z)$ can be any electric or magnetic field component. This equation can be solved for specific simple situations, or used in Finite-Difference Time-Domain (FDTD) software. Simply put, light will be localised or confined in a high-index medium. The strength of the confinement will depend on the index contrast, and the size of the high index material.

Passive structures will always be lossy, either due to absorption of a material, scattering or radiation. In general, losses are described by using the unit of dB/cm (or any kind of length unit). A loss of 3 dB/cm means that about half the optical power is lost in 1 cm, a typical value found in visible photonic waveguides.

3.3.1.1 Waveguides

A waveguide is one of the simplest but fundamental types of structures on a PIC. It is a rectangle patterned in a high index material to guide light

on-chip. Different types of waveguides exist: strip and photonic crystal waveguides are the most important ones in this work.

Choosing the propagation direction to be the z -direction, the refractive index can be written as $n(\vec{r}) = n(x, y)$. Eigenmodes of the waveguide are either propagating or evanescent waves, of which the transversal shape does not change during propagation. Because of the propagation in the z -direction, we know that

$$\vec{E}(\vec{r}) = \vec{e}(x, y) \cdot e^{-j\beta z} \quad (3.3.2)$$

$$\vec{H}(\vec{r}) = \vec{h}(x, y) \cdot e^{-j\beta z} \quad (3.3.3)$$

Where \vec{E}, \vec{H} are the electric and magnetic fields, respectively. Three parameters completely determine the solution to this problem. β , which is the propagation constant, $n_{eff} = \frac{\beta}{k_0}$, the effective refractive index, and $\epsilon_{eff} = n_{eff}^2$, the effective dielectric constant. Different solutions exist, a set of guided modes with discrete solutions for ϵ_{eff} , and a set of radiating modes which either are propagating or evanescent. These solutions are continuous in ϵ_{eff} . The guided modes are the ones that are localised in the high refractive index material of the structure. The higher the refractive index contrast, and the bigger the waveguide, the more guided modes will be “supported” by the waveguide. It can be seen as a “deeper and wider” potential well, when making the analogy to quantum mechanics. Any electric field can be described by taking linear combinations of the guided and radiating modes (they form a complete set).

Three types of guided modes exist, Transversal Electromagnetic plane wave (TEM) modes, where neither the electric and magnetic field exist in the direction of propagation. The other two are Transversal Electric (TE), and Transverse Magnetic (TM) modes, where the electric (magnetic) field does not exist in the axis of propagation, respectively (see Figure 3.4). One can design either thin or wide waveguides depending on if single-mode or multi-mode behaviour is desired.

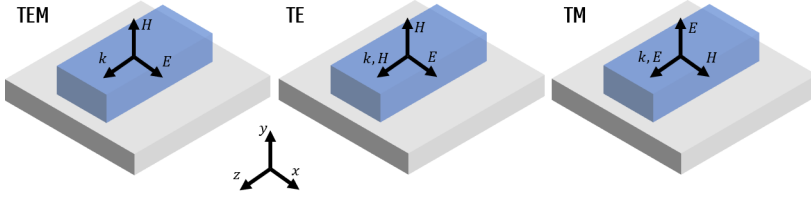


Figure 3.4: Different types of polarization in a waveguide.

3.3.1.2 Coupled Waveguides

Consider two z -invariant waveguides in close proximity to each other, where in each waveguide there is a dominant mode with propagation constant β_1 and β_2 , respectively. Due to the close proximity, we can look at the situation as the added waveguide being a perturbation on each other. Because of this, we can write the total field as

$$\Psi(x, z) = C_1(z)\psi_1(x) \cdot e^{-j\beta_1 z} + C_2(z)\psi_2(x) \cdot e^{-j\beta_2 z} \quad (3.3.4)$$

where $C_1(z)$ ($C_2(z)$) stand for the coupling from waveguide 1 to 2 (2 to 1), respectively. The z -dependence can be rewritten as $X_i(z) = C_i(z) \cdot e^{-j\beta_i z}$, which allows to re-write the equation as

$$\Psi(x, z) = X_1(z)\psi_1(x) + X_2(z)\psi_2(x) \quad (3.3.5)$$

Considering first the unperturbed situation, the modes of each waveguide separately satisfy

$$\frac{dX_i}{dz} = -j\beta_i X_i \Rightarrow X_i(z) = e^{-j\beta_i z} \quad (3.3.6)$$

If we now want to add a small perturbation, we need to add linear coupling terms κ :

$$\begin{cases} \frac{dX_1(z)}{dz} = -j\beta_1 X_1(z) - j(\kappa_{11} X_1(z) + \kappa_{12} X_2(z)) \\ \frac{dX_2(z)}{dz} = -j\beta_2 X_2(z) - j(\kappa_{21} X_1(z) + \kappa_{22} X_2(z)) \end{cases}$$

Without going into to much detail, if we assume a lossless situation, $X_1(0) = 1$ and $X_2(0) = 0$ (meaning only one mode is excited), we can

solve these equations to be

$$\begin{cases} X_1(z) = e^{-j\beta z} \cdot (\cos(\delta z) - j\frac{\Delta}{\delta} \sin(\delta z)) \\ X_2(z) = e^{-j\beta z} \cdot (-j\frac{\kappa_{21}}{\delta} \sin(\delta z)) \end{cases}$$

where

$$\begin{cases} \beta = (\beta_1 + \beta_2 + \kappa_{11} + \kappa_{22})/2 \\ \kappa = \sqrt{\kappa_{12}\kappa_{21}} \\ \Delta = (\beta_1 - \beta_2 + \kappa_{11} - \kappa_{22})/2 \\ \delta = \sqrt{\Delta^2 + \kappa^2} \end{cases}$$

Here, β can be seen as an average propagation constant of both modes, and Δ as the phase matching per length unit. If the two waveguides are identical, the situation becomes symmetric and $\beta_1 = \beta_2$, $\kappa_{11} = \kappa_{22}$ so there will be perfect phase matching and the mode will oscillate between the two waveguides. The other important parameter here is κ , the coupling strength, which will vary depending on the distance between the two waveguides. We can define the coupling length L_c as the length needed for maximal power exchange. For the phase matching case, this length is defined as

$$L_c = \frac{\pi}{2\kappa} \quad (3.3.7)$$

For every length L_c travelled, the power will be transmitted from one waveguide to the other. When there is no phase matching, but Δ is smaller than κ , the coupling length becomes

$$L_c = \frac{\pi}{2\delta} = \frac{\pi}{2\sqrt{\Delta^2 + \kappa^2}} \quad (3.3.8)$$

But the power will never be transmitted completely to the other waveguide. The maximum transmitted power is $\frac{\kappa^2}{\kappa^2 + \Delta^2}$. For a large phase mismatch, there will be no coupling between the waveguides. κ can be determined as a function of distance between waveguides through FDTD simulations. This coupled mode theory is relevant for designing ring resonators and various types of splitters, or directional couplers. Here, two coupled waveguides are designed such that a certain amount of power will

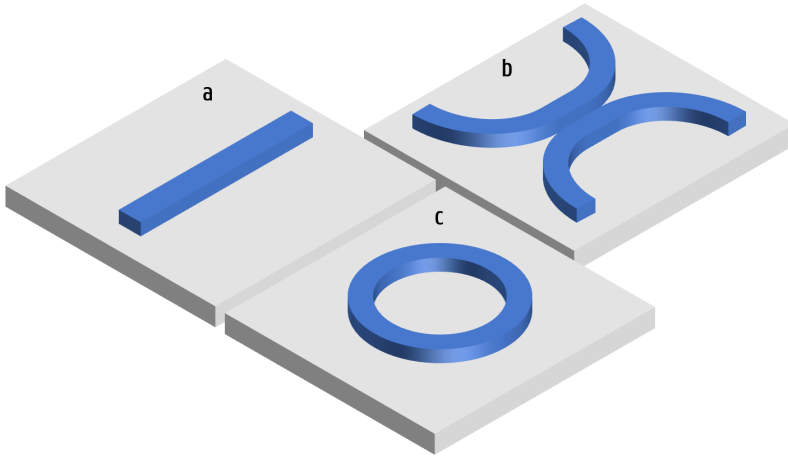


Figure 3.5: (a) Simple straight waveguide on SiNx. (b) Coupled waveguides. (c) Ring resonator.

be coupled from one to the other, which depends on the waveguide width, distance between the two, and the coupling length.

3.3.1.3 Ring Resonators

Ring resonators can be seen as waveguides that are curled up and attached to themselves, in principle becoming a waveguide with “infinite” length. When checking mode profiles for rings, it can be seen that the mode is pushed outwards due to the curvature. These additional losses typically referred to as the bending loss. A ring resonator can exist on its own, but there usually is a bus waveguide close to couple out some of the light of the resonating mode inside, either below or next to the ring. Due to the optical mode being localised on the edge of the ring, a ring and disk will optically behave the same.

Because the ring couples back to itself, it can be seen that only certain wavelengths will be allowed to exist inside: if there is a phase difference after a round-trip, there is destructive interference. For no phase differ-

ence, we find:

$$2\pi r n_{eff} = m\lambda_m \quad (3.3.9)$$

where any integer value of m will give a resonating mode. If r is very large, a ring resonator will as such support a dense spectrum of modes, which is quantified through the Free Spectral Range (FSR). The FSR is defined as the wavelength difference between two modes and is approximated in the case for constant refractive index, and when the FSR is small compared to the wavelength, as

$$\Delta\lambda_{FSR} = \frac{\lambda^2}{n_{eff} \cdot 2\pi r} \quad (3.3.10)$$

This is a simple example of a ring, but the same idea applies to any structure that reconnects on itself, like a so-called “race-track” resonator, for which we can generalize this formula to be $L \cdot n_{eff} = m\lambda_m$. Ring resonators are often used for filtering, where cascading multiple resonators can create circuits that do very precise filtering. Multiple resonators in series can also be used to make reflectors.

An important definition that can be made here is the Q -factor of a cavity, or in this specific case, of a ring resonator. It is defined as the ratio of the energy U stored in the cavity over the energy dissipated per optical cycle, multiplied with 2π :

$$Q = \left| \omega_c \frac{U(t)}{dU/dt} \right| \quad (3.3.11)$$

where ω_c is the frequency of the wave in the cavity. Solving this for $U(t)$ yields

$$U(t) = U_0 \cdot e^{-\frac{\omega_c \cdot t}{Q}} \quad (3.3.12)$$

Knowing that the energy in the cavity is proportional to the electric field squared ($U(t) \propto |E(t)|^2$), $E(t)$ can be written as

$$E(t) = E_0 \cdot e^{-\frac{\omega_c \cdot t}{2Q}} e^{-i\omega_c t} \quad (3.3.13)$$

with $E_0^2 = U_0$. If we Fourier Transform this equation, we get

$$E(\omega) = E_0 \cdot \frac{\omega_c/Q}{(\omega - \omega_c)^2 + (\omega_c/2Q)^2} \quad (3.3.14)$$

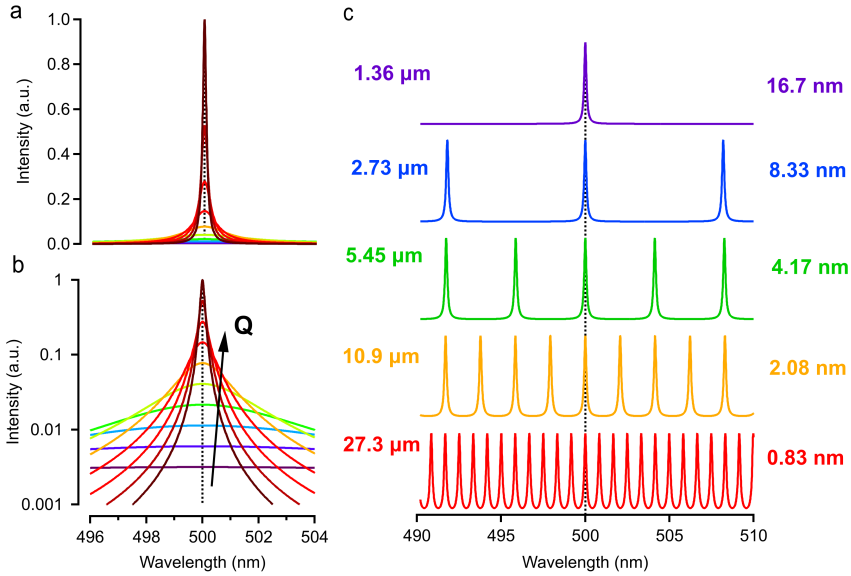


Figure 3.6: (a) Resonance for Q -factors going from 1 to 3200 with logarithmic spacing, where the radius is $1.36 \mu\text{m}$. (b) Same as (a) but the y-axis is logarithmic (c) Rings with different radii (shown on the left) and their corresponding FSR (right).

Showing that this is a Lorentzian distribution centered around ω_c and with width $\Delta\omega = \frac{\omega_c}{Q}$. From this, a more straightforward definition of the Q -factor can be found as

$$Q = \frac{\omega_c}{\Delta\omega} = \frac{E_c}{\Delta E} \approx \frac{\lambda_c}{\Delta\lambda} \quad (3.3.15)$$

where the last approximation holds if $\lambda_c \gg \Delta\lambda$. As such, when measuring the spectrum from a resonator, its Q -factor can be found by doing a Lorentzian fit of a peak. The more narrow, the higher the Q -factor will be. The Q -factor is an important metric for any type of cavity, not just a ring resonator. Some examples of resonators with different Q -factors are shown in Figure 3.6.

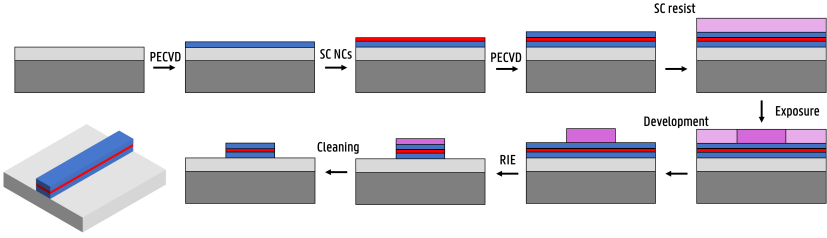


Figure 3.7: Process flow to make basic active waveguides with embedded NCs.

3.3.2 Active Components

Active photonic components will create, amplify or modulate an incoming light beam. These components are naturally more complicated, mainly due to the need for an external power source to achieve their purpose. For example: a modulator will need both an on-chip optical mode, and a signal to imprint on this mode. This signal can be created by using electrical or possibly optical signals. The same applies for any type of amplifier, the gain material in the amplifier will need to be put into population inversion to achieve amplification. In this Section, some of the active components used in this work are described.

3.3.2.1 Active Waveguides

It is possible to make waveguides active by embedding an active material (colloidal NCs) in a SiN_x waveguide (see Figure 3.7), or this process can be changed by overcoating the SiN_x with the active material instead (see Figure 3.8). Due to the typical lower refractive index of the NCs ($n \approx 1.65$) compared to SiN_x ($n \approx 2$), this will stretch the optical mode. If the NC layer is too thick, the mode will be pushed out in both the lower and upper layer of the SiN_x.

To grow these embedded NC waveguides, first LF SiN_x is grown because it usually has the lowest losses (usually about 100 nm). Next, the NCs are spincoated (about 50 nm), and to finalize the stack MF SiN_x is grown at 120°C. This lower temperature will lead to higher losses, but

is necessary to not destroy the NC layer during deposition. MF SiNx is chosen to have better adhesion on the NC layer. After building the stack, a lithography step is done to pattern the waveguides of desired width, and an etch is done. Usually, confinement achieved in NC layers through this method is 12-15%, which changes slightly by changing the thicknesses of the different layers, and the waveguide width. This flow is shown in Figure 3.7.

For the overcoated NC waveguides, the orders are reversed. After growing a (typically) thicker LF SiNx layer, the waveguides are patterned, after which the NCs are spincoated. This approach has the downside of having lower confinement because the NCs are not embedded, and that NCs are everywhere on the substrate (due to them not being etched), not only in the actual waveguides, further leading to lower confinement. Besides this, following this approach has the risk of the NCs not forming a smooth layer on top of the waveguide. The upside is that using the NCs is the final processing step, as such they will not be damaged because of PECVD or etching. If needed, they can still be protected from the environment (air, humidity) by spincoating photoresist on top or using non-invasive (or less invasive) SiOx deposition techniques, like using electron-beam deposition. It is important to note here that if the ratio of thicknesses between the SiNx – and NC layers is too large, then spincoating the NCs will not give a nice overcoating of the SiNx layer. Confinements here are about 5-10%.

A first experiment we can use these types of structures for is to check for amplification in a waveguide. Here, waveguides with NCs are patterned with a fixed width and changes in the length. A strong pump beam is used to excite the NCs, where a cylindrical lens is used to focus the beam in a stripe (on top of the waveguide). This excitation will lead to light amplification g_m , known as the modal gain, defined as the gain achieved in an actual waveguide. This can (and will be) coupled back to the intrinsic gain defined in Chapter 2 shortly. If the substrate is cleaved perpendicular to the propagation direction of the waveguides, we can measure the outcoupling light with a fiber from the side of the chip,

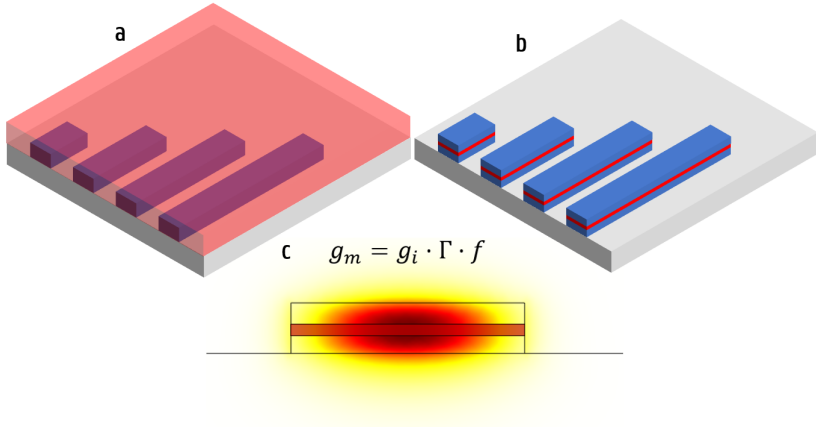


Figure 3.8: (a) LF SiNx waveguides patterned with various lengths, overcoated with NCs through spincoating. (b) LF SiNx/NC/MF SiNx waveguides, made by first growing the LF SiNx, followed by spincoating the NCs, and then the MF SiNx growth step. After making the full stack, the waveguides are patterned as before. (c) An optical mode profile for a NC layer between two SiNx layers. The confinement is calculated as the integrated electric field norm in the NC layer divided by the total electric field norm, in this case 13.5%.

which is called butt-coupling. The outcoupled intensity will be equal to

$$I = \int_0^L I_0 \times e^{g_m \cdot x} dx = I_0 \times \frac{e^{g_m \cdot L} - 1}{g_m} \quad (3.3.16)$$

Here, I is the summation of the light amplified over lengths $x \in [0, L]$.

Two types of measurements can be done with such samples:

1. *Power-in power-out* – Here, we focus on a single waveguide and measure the outcoupled light as a function of the used power of the incoming beam. By knowing the repetition rate of the laser, the beam size and the power used, we can determine a threshold for amplification P_{thres} (the necessary power to see the first amplification in the waveguide). If the full spectrum is measured a non-linear increase can be seen for a certain wavelength range, showing the ASE peak.

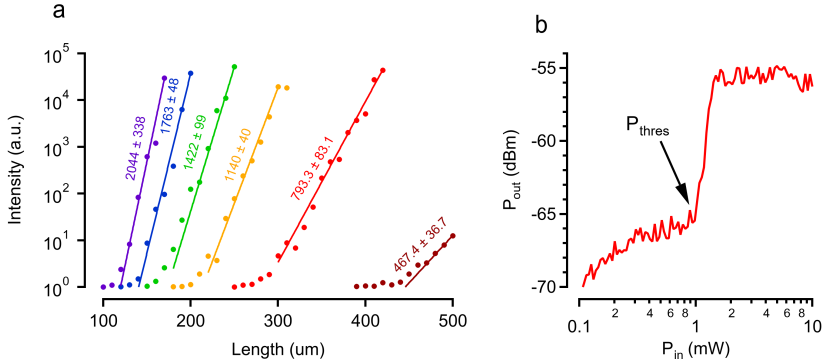


Figure 3.9: (a) Modal gain for various simulated gain values with background PL. From the slope of the exponential rise the modal gain can be determined. The error values of the fit are shown. (b) $P_{in} - P_{out}$ from a VSL measurement. The threshold power needed for gain can be determined here.

2. *Variable-Stripe-Length (VSL)* – For these experiments the pump power is kept fixed, and the length of the waveguide is changed. From the slope of the out coupled power as a function of the length, the modal gain g_m can be determined.

These two parameters, P_{thres} and g_m , are very useful to quantify whether or not a NC material is useful for lasing operation. They can also be coupled back to the threshold determined in solution (from TA experiments), and the modal gain can be coupled back to the intrinsic gain g_i through

$$g_m = g_i \cdot \Gamma \cdot f \quad (3.3.17)$$

where Γ is the confinement of the mode in the NC layer, and f is the volume fraction (typically about 40-50%, due to space being taken up by the ligands). This is shown in Figure 3.8c.

3.3.2.2 Fabry-Perot Lasers

In this Section, Fabry-Perot (FP) cavities and their corresponding lasers are discussed. They are one of the simplest cavities, and many concepts

defined here come back in later laser types. In the most abstract sense, a FP cavity is a cavity with a certain length L , which contains a gain medium with some modal gain g_m , and is surrounded by two mirrors with reflectivity R_1 and R_2 . In principle there does not have to be a gain medium in the entire cavity. Light can travel back and forth between the two mirrors and get amplified if (1) the round-trip corresponds to a phase shift of a multiple of 2π ($L = m \cdot \pi$, $m \in \mathbb{N}$), and (2) if the amplification overcomes the losses through the mirrors. This second requirement is known as the laser equation, given by

$$R_1 R_2 \cdot e^{2L \cdot g_m} = 1 \quad (3.3.18)$$

which states that if after a full round-trip, the power of the optical mode remains the same as it was originally, this is shown in Figure 3.10a. If the power becomes higher than one, exponential amplification occurs in the cavity, and if lower than one the mode decays in the cavity. In reality, the gain g_m is not fixed: due to amplification the gain in the medium will be lost. So when exciting the gain medium and a lasing mode starts to get amplified, a complex transient process occurs until Equation 3.3.18 is fulfilled and there is stable operation.

Losses can also be included in this Equation. Let us call α the loss due to some process, that which can be either absorption or scattering

$$R_1 R_2 \cdot e^{2L \cdot (g_m - \alpha)} = 1 \quad (3.3.19)$$

One could also define the net gain as the difference between the modal gain and the losses: $g = g_m - \alpha$ to go back to Equation 3.3.18. A typical value also defined is the “round-trip gain”, which would be the total gain from one round-trip, a dimensionless quantity: $g_{RT} = 2L \cdot (g_m - \alpha)$.

Figure 3.10b shows some situations where either $R_1 R_2 \cdot e^{2L \cdot (g_m - \alpha)}$ is larger or smaller than one, showing amplification of the power P in the cavity, the inset shows the periodicity of the amplification: losses when reflecting and exponential rise again while travelling in the cavity. Figure 3.10c shows the case where there is stability, and shows the outcoupled power for various reflection values R_1 (and the corresponding g necessary

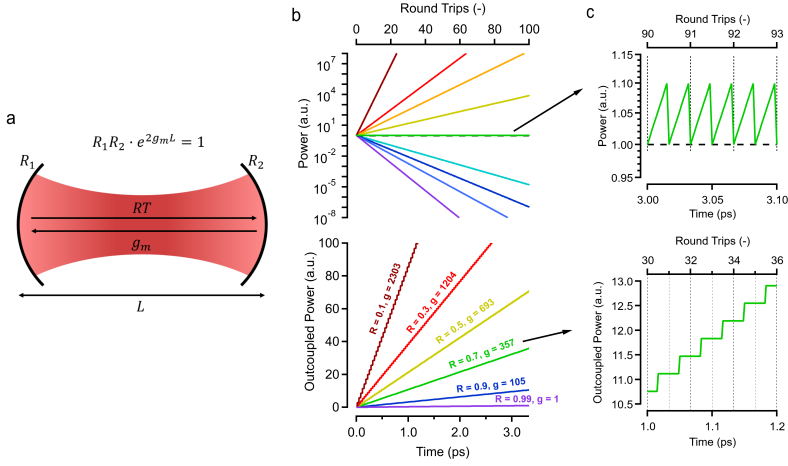


Figure 3.10: (a) Graphical depiction of a Fabry-Perot cavity. (b) The top shows mode amplification in a FP where $R_1 = R_2 = 0.9$ and the gain is changed. A gain of $g = 210$ is needed for stable operation (green curve). This is also shown in the top of Figure c. The bottom shows the outcoupled power for various values of R_1 , when $R_2 = 1$. The text on the lines shows the corresponding gain needed. The bottom of Figure c shows the stepwise outcoupled power (every round trip some power is added), for $R = 0.7$ and $g = 357$. All these examples have a cavity length of $L = 10 \cdot \lambda$, with $\lambda = 500$ nm.

to maintain stable operation) as a function of time, which can be measured in amount of Round Trips (RTs).

The mirrors here are quite abstract objects defined with a certain reflectivity. In the different laser types discussed below, they will be more practically defined.

3.3.2.3 Disk and Ring Lasers

Similar to the active waveguides, we can also make a ring resonator with embedded or overcoated NCs. Due to only certain wavelengths resonating (Equation 3.3.1.3) these structures can be turned into a laser. It is actually very similar to a passive ring resonator, but with gain in the ring. Here,

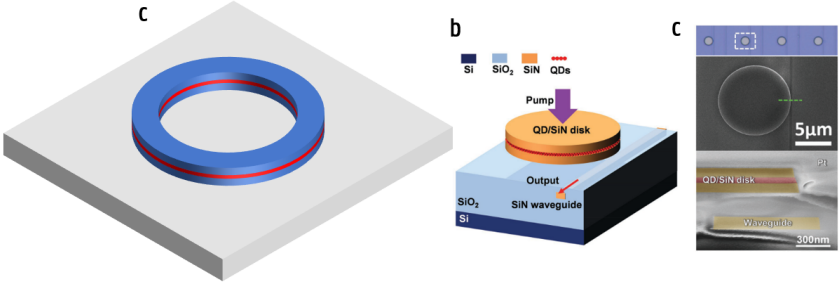


Figure 3.11: (a) Graphical depiction of an active ring resonator. (b) Structures as shown in Xie *et al.*³. A chip with embedded SiNx waveguides is made, afterward a SiNx/NC/SiNx stack is deposited on top. The structure is then finalized by etching the disk structures as shown. (c) Light of the whispering-gallery-mode is coupled to the embedded waveguide and measured through butt-coupling. (b) and (c) are taken from Xie *et al.*³.

the round-trip gain is defined as

$$g_{RT} = (g_m - \alpha) \cdot 2\pi r \quad (3.3.20)$$

For the case of a simple disk or ring. α is defined as the sum of all the losses (units of cm^{-1}). It will heavily impact the Q -factor of a disk laser. Lasing can be observed from the disk by measuring light that gets scattered perpendicular to the substrate, or by using a bus waveguide to couple out the light. In the case of Xie *et al.*³, first a substrate is made with some parallel SiNx waveguides, overgrown with SiOx. Afterward it is planarized and the SiNx disks with embedded CdSe/CdS QDs are grown on top (see Figure 3.11). Some of the light is coupled in the waveguide under the disks and this can be measured through butt-coupling. Using a waveguide underneath the disk allows to make it SiNx only, if a bus waveguide next to the ring would be used with the same processing flow, there would also be QDs inside. Since the optical mode is situated on the outside of the disk, there actually is little difference optically speaking between a disk and a ring unless the ring becomes too thin. Because of this there are some interesting possibilities processing wise, these are

discussed in Chapter 9.

3.3.2.4 Distributed Bragg Reflector Lasers

The Distributed Bragg Reflector (DBR) is built upon a periodic structure consisting of multiple layers, each characterized by its own refractive index. By carefully designing this structure, it becomes possible to create a highly efficient reflector for a specific wavelength.

To construct a reflector at a desired wavelength λ , a sequence of two layers with refractive indices n_L and n_H can be utilized. The thickness of each layer is determined to be $\lambda/4n_i$, where n_i corresponds to the refractive index of the respective layer. This particular configuration leads to constructive feedback for the reflected wave and destructive feedback for the transmitted wave.

Enhancing the reflectivity of the DBR can be achieved by adding multiple bilayers, as depicted in Figure 3.12c. This results in a stronger reflection, thereby effectively creating a highly efficient reflector within a specific range of wavelengths. The wavelength range for high reflection depends on the refractive index contrast $\Delta n = n_H - n_L$. A multiple of bi-layers will as such lead to a mirror.

Using two DBR mirrors with a cavity in between which has active material inside will lead to a laser cavity. The laser cavity length L has to be chosen such that $L = m \cdot \lambda/2$ with m an integer, to make sure the wavelength will resonate in the cavity. It can also be chosen very large so that the cavity supports many different modes, similar to the ring resonator.

We can make the DBR cavity in-plane, where typically the index contrast will be between SiNx ($n \approx 2$) and air ($n = 1$). The difficulty here lies with the fact that we are working in the visible, which leads to layers of thicknesses of around 100 nm, which is difficult to fabricate. Alternatively, we can use Vertical Cavity Surface Emitting Lasers (VCSELs), where layers are grown using PECVD or other deposition techniques, and the confinement will be out-of-plane in this case (hence the name, Surface Emitting Laser). For the cavity some spacer layer is typically grown, to

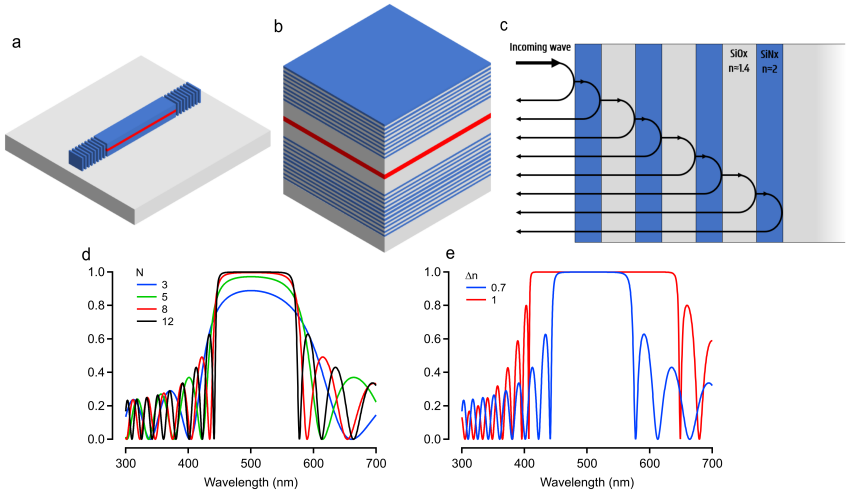


Figure 3.12: (a) In-plane DBR laser. (b) VCSEL type DBR laser. (c) Principle of a Distributed Bragg Reflector: constructive feedback for reflection, destructive feedback for transmission. (d) Reflection spectrum of a DBR mirror for increasing amount of bilayers, where the two materials are SiNx and SiOx ($n_{SiNx} = 2$ and $n_{SiOx} = 1.4$). (e) Reflectance spectrum of two DBR mirrors with changing refractive index contrast, between air and SiNx, and SiOx and SiNx, for 12 bilayers.

make sure maxima of the electric field exist in the cavity, where the mode is amplified. An advantage of VCSEL lasers is their large area, making very high output power lasers possible. Furthermore, they are cheap to produce, enabling their use in various consumer goods (like an optical mouse), and are easy to fiber couple. VCSEL lasers are very well explained using the Transfer Matrix Method (TMM), since they are usually multiple orders of magnitude larger in the plane than the thickness, allowing to use plane waves to describe them. Both these designs are shown in Figure 3.12.

3.3.2.5 1D Distributed Feedback Lasers

Distributed FeedBack (DFB) lasers also use periodicity for reflection, but the periodicity is situated in the active region itself. Here, we explain them

in a different manner: a periodic structure leads to conditions on the \vec{k} -vector due to translational symmetry. This reasoning is also applicable to DBR structures. The conditioning of the \vec{k} -vector can be used to create mirrors (amongst other things), and is also referred to as the Bragg Condition, defined as

$$\vec{k}_{out} = m \cdot \vec{K} + \vec{k}_{in} \quad (3.3.21)$$

where \vec{K} is the \vec{k} -vector of the lattice $|\vec{K}| = 2\pi/a$ (a is the period of the grating), and $m \in \mathbb{Z}$. This holds for the case of a 1D periodic structure, lets assume this is in the x -direction. If we have an incoming wave $|\vec{k}_{in}| = 2\pi/\lambda$ (the propagation is also in the x -direction), allowing us to assume a constant refractive index for simplicity (we come back to this later), and consider the situation for which $a = \lambda/2$, then we know

$$|\vec{K}| = \frac{2\pi}{a} = \frac{2\pi}{\lambda/2} = \frac{4\pi}{\lambda} = 2 \cdot |\vec{k}_{in}| \quad (3.3.22)$$

We can see that the Bragg Condition only imposes restrictions upon the \vec{k} -vector in the x -direction. If we draw the \vec{k} -vector diagram for this situation (see Figure 3.13), we can draw \vec{k}_{in} in the x -direction, and perpendicular we can draw lines with a spacing of $2 \cdot \vec{k}_{in}$. Then, the intersection between the circle with radius \vec{k}_{in} and the lines that are drawn are the allowed \vec{k}_{out} -vectors. Put it differently: $m \cdot \vec{K}$ ($m \in \mathbb{Z}$) can be added or subtracted to \vec{k}_{in} to make sure the periodicity of the structure is taken into account, and then a value for \vec{k}_z must be chosen such that $|\vec{k}_{in}|$ is conserved. The amount of times $m \cdot \vec{K}$ is added is the order of diffraction, $m = 1$ is the first order diffraction, $m = 2$ second order, and so on (can also be negative). Looking at Figure 3.13b, we can see for this particular case the only value for m that is allowed is -1 , meaning the light will be scattered back. This is referred to as a *first-order grating*, and will essentially operate as a mirror. A DBR can be explained with this exact formalism.

We can now also look at the situation where $a = \lambda$, here $\vec{K} = |\vec{k}_{in}|$. If we now look at the \vec{k} -diagram in this case, we see that more scattering directions are possible: back, but also up and down. Using this we can create a lasing cavity that shows emission perpendicular to the plane. This is referred to as a *second-order grating*.

It is also interesting to look at what happens if \vec{k}_{in} deviates from multiples of the grating vector \vec{K} . As can be seen from Figure 3.13b, for shorter wavelengths (higher energy) the circle becomes larger and scattering will no longer occur perpendicular to the plane. Instead, it will scatter *less* than 90° , and scatter slightly upward from the plane as well. Since there is no more feedback in this situation, the confinement will be weaker. Naturally, using an input \vec{k} -vector in the other direction will give a mirrored result, so there is symmetry in the system. Further deviating from the grating \vec{k} -vector will decrease the scattered angle even more. In the case of longer wavelengths, the situation will be similar but with a slight difference: the upward scattered waves will now be scattered with angles slightly *more* than 90° , and this is the only allowed diffraction order. It is possible to engineer a grating specifically to couple light out under a certain angle (perpendicular outcoupling also leads to backscatter, which ideally is avoided to have better outcoupling), typically this is done under 10° . Designing a grating this way gives rise to a so-called *grating coupler*.

As a final example we can also look at the case of a high-order grating, for example a 20th order $a = 10 \cdot \lambda$:

$$|\vec{K}| = \frac{2\pi}{a} = \frac{2\pi}{10 \cdot \lambda} = \frac{1}{10} \cdot \frac{2\pi}{\lambda} = \frac{1}{10} \cdot \vec{k}_{in} \quad (3.3.23)$$

We can see from the \vec{k} -diagram that the circle encompasses many vertical lines, and as such has many scattering directions.

For an actual practical application we have to correct for the medium, which will change the wavelength of the light in vacuum: $\lambda = \lambda_0/n_{eff}$. n_{eff} can be estimated through taking the geometric average of the refractive indices of the medium, although corrections on this will occur. For designing a DFB grating to operate at a specific wavelength, a sweep of period is done (either in simulation or experiment) to determine n_{eff} . This effective index will be influenced by the stack of materials and the index contrast, i.e. a SiNx grating overcoated with NCs (see Figure 3.13a) will have a lower index contrast than a air-clad grating. This change in refractive index will influence the angle of the various diffraction orders.

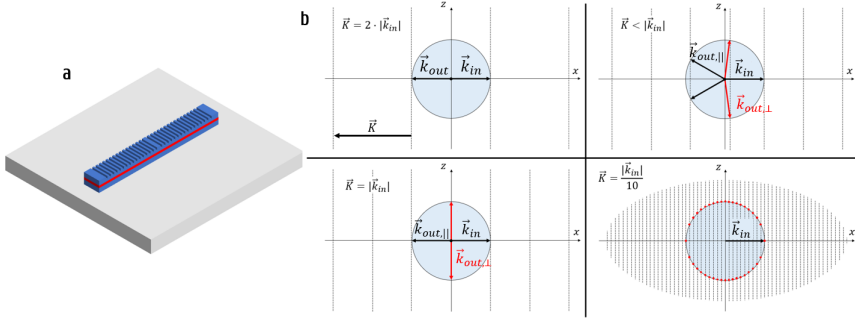


Figure 3.13: (a) 1D DFB laser structure with embedded NC layer. (b) \vec{k} -diagrams for various cases of gratings and values of \vec{k}_{in} .

The radius of the circle will become larger in the substrate than in the air above the grating. Since we are mostly interested in either backscattering, or perpendicular emission in this work, this added complexity changes little in the study.

Finally, it is worth noting that the examples explained here are for the case of an infinite grating: the emission angle for a 2nd order grating is theoretically zero degrees. For a finite crystal, there will be a certain emission cone which is dependent on the amount of periods of the grating. Furthermore, the Bragg Condition only gives information about which orders of diffraction are *allowed*. It is also possible to calculate the actual magnitude of the diffraction order, which can still become zero.

Like for the DBR laser, a cavity length L can be chosen such that either the DFB laser is single mode ($L = \lambda/2$), or multimode ($L = m \cdot \lambda/2$). This is also called a phase shifter. At UGent, work has been published on single mode DFB lasers using colloidal QDs, see Zhu *et al.*⁴.

3.3.2.6 2D Distributed Feedback Lasers

The same approach as above can be used to describe 2D DFB lasers, but here periodic symmetry exists in both the x - and y -dimension. In this case, we can write $\vec{K} = 2\pi/a_x + n \cdot 2\pi/a_y$, $(m, n) \in \mathbb{Z}$, and a_x, a_y the

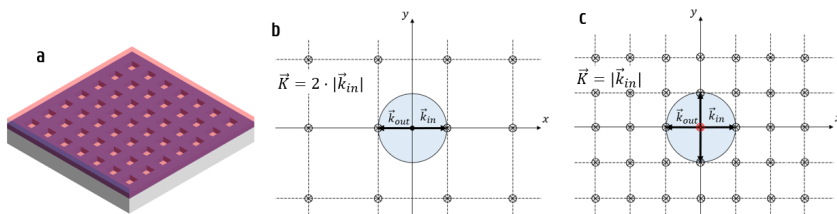


Figure 3.14: (a) 2D DFB laser structure with overcoated NC layer. (b) \vec{k} -diagram for a first order grating. (c) \vec{k} -diagram for a second order grating.

periodicity in the x - and y -direction, respectively. The added periodicity in the y -direction however does not impose much more difficulty: the same reasoning can be applied as before. If we choose $a_x = a_y = \lambda/2$ again like before, we see scattering can only happen backward. For $a_x = a_y = \lambda$, we can now scatter in six different directions instead of four in the 1D case. This becomes clear from looking at the \vec{k} -diagram. When changing the wavelength, at a certain size of the \vec{k} -sphere diagonal scattering will become possible, giving rise to more complex emission patterns.

3.3.2.7 Photonic Crystal Lasers

There is another, overarching way to explain the last three previous resonators, by looking directly again at the wave equation. Considering the 1D situation, and assuming $n(x)$ is periodic (as is the case for DBR, 1D and 2D DFB resonators), we can rewrite Eq. 3.3.1 as

$$-\frac{1}{n(x)^2} \frac{d^2}{dx^2} \Psi(x) = k_0^2 \Psi(x) \quad (3.3.24)$$

which writes it as an eigenvalue problem, where k_0^2 is the eigenvalue and $\Psi(x)$ is the eigenfunction of the linear operator $\frac{1}{n(x)^2} \frac{d^2}{dx^2}$. For a constant refractive index we can solve this to find plane waves

$$\Psi(x) = e^{-jkx} \quad (3.3.25)$$

with

$$k = \pm nk_0 = \pm n \frac{\omega}{c} \quad (3.3.26)$$

However, for a periodic refractive index, we know from the Bloch-Floquet theorem that there is a general solution of the shape

$$\Psi(x) = e^{-jkx} u_k(x) \quad (3.3.27)$$

where $u_k(x)$ is also a periodic function (same period as $n(x)$) and where, importantly, $k = nk_0$ no longer holds. Since $u_k(x)$ is periodic, we can determine its Fourier Series

$$u_k(x) = \sum_{l=-\infty}^{+\infty} a_l \cdot e^{-jlKx} \quad (3.3.28)$$

which, after using this definition in $\Psi(x)$

$$\Psi(x) = e^{-jkx} \left(\sum_{l=-\infty}^{+\infty} a_l \cdot e^{-jlKx} \right) = \sum_{l=-\infty}^{+\infty} a_l \cdot e^{-j(k+lK)x} \quad (3.3.29)$$

shows that the eigenvalue k is invariant under addition of lK with $l \in \mathbb{Z}$. This will add $l \cdot 2\pi$ to the phase, which becomes a factor of one. It is also invariant under a sign change $k \rightarrow -k$. Knowing this, we only need to look at values $k \in [0, \frac{K}{2}]$, also referred to as the Brillouin Zone. In other words: we can completely explain the behaviour in a periodic structure by using a superposition of plane waves with k -values between zero and $\frac{K}{2}$. The actual solution will depend on the shape of $n(x)$. A general shape of the dispersion relation $\omega(k)$ is that close to zero, the plane wave is very well approximated, but toward $\frac{K}{2}$ an anomaly will occur, where a gap will appear and a band of forbidden states arises. In the periodic structure, light with a frequency in this band is not allowed to appear or is attenuated. The size of this gap depends on the difference of the refractive index between the different layers, which can be directly translated to what was seen before with the DBR. By filling in Equation 3.3.29 into Equation 3.3.24, together with a Fourier Series expansion of the $n(x)^2$ function, the a_l factors can be determined.

These ideas can be generalised to 3D, where

$$\Psi_k(\vec{r}) = e^{-j\vec{k} \cdot \vec{r}} u_k(\vec{r}) \quad (3.3.30)$$

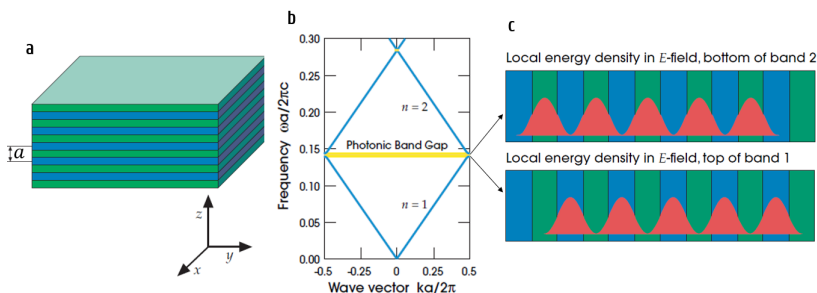


Figure 3.15: (a) 1D PhC example. (b) Calculated band diagram for this case. (c) Energy stored at the $\frac{ka}{2\pi} = 0.5$ point, for the two different bands. These images were taken from⁵.

The formalism outlined here is very similar to the derivation of energy bands for electrons in materials, specifically to explain band-gaps in a semiconductor. The similarity leads to the name of Photonic Crystals (PhCs), and the forbidden band of frequencies is often referred to as the *Photonic Bandgap*. Without going too much into detail, some basic characteristics of a 1D photonic crystal are discussed here to introduce relevant terminology. In Figure 3.15a, a DBR-type mirror is shown, which can be considered a 1D Photonic Crystal. By using numerical methods, the band diagram can be calculated, as shown in Figure 3.15b. This specific bandgap is when the contrast is made between a dielectricum with $\epsilon = 13$ ($n = 3.61$), and a dielectricum with $\epsilon = 12$ ($n = 3.46$). The band $n = 1$ is typically referred to as the dielectric band (corresponding to the higher refractive index material), and the band with $n = 2$ is called the air band (corresponding to the lower refractive index material). At the point where $\frac{ka}{2\pi} = 0.5$, a standing wave occurs for two different frequencies. For the frequency in the dielectric (air) band the bulk of the energy of the standing wave is stored in the layer with the highest (lowest) refractive index. This is shown in Figure 3.15c. These bandgaps can also be interpreted from the Section on DBR mirrors, where these are the frequencies for which there is perfect reflection.

This formalism is usually used in the context of 2D Photonic Crystals

(2D PhCs), similar to the 2D DFB lasers discussed. A specific cavity can be created by adding a defect (either a point or a line) in the crystal to locally confine the light. Since in Chapter 8 2D Photonic Crystal Lasers (also called Photonic Crystal Slabs) are used, they will be discussed here in more detail.

Photonic Crystal Slabs Let us first consider the case where the periodic structures stretch infinitely out of plane. The periodicity will impose restrictions on the \vec{k} -vector in the plane ($\vec{k}_{||}$), but not the one perpendicular to the plane (k_z). In general, a field F can be described then as

$$F_{(n,k_z,\vec{k}_{||})}(\vec{r}) = e^{i\vec{k}_{||}\cdot\vec{\rho}} e^{ik_z z} \vec{u}_{(n,k_z,\vec{k}_{||})}(\vec{\rho}) \quad (3.3.31)$$

where n is the band number, $\vec{\rho}$ the projection of \vec{r} in the xy -plane, and $u(\vec{\rho})$ the 2D equivalent of the general case described in Equation 3.3.30. When a mode only exists in-plane, i.e. $k_z = 0$, there is symmetry according to this plane: the mode does not change under reflections with respect to the xy -plane. Because of this, two distinct polarizations occur: TE modes have the magnetic field normal to the plane ($\vec{H} = H(\vec{\rho})\vec{z}$) and the electric field only in-plane ($\vec{E}(\vec{\rho})\cdot\vec{z} = 0$, \vec{z} is the unit vector for the z -axis). TM modes have the reverse. When considering a specific crystal, both of these polarizations can be calculated and sometimes a gap only appears for either. It is important to note that this symmetry, and as such the TE/TM splitting, only holds for an infinite 2D Photonic Crystal. For a realistic crystal, where it has only a certain thickness and is made on top of a certain substrate, this symmetry is broken and modes will only become “TE-like” or “TM-like”. Furthermore, for k -values that are too large in the z -direction, light will not be confined within the slab at all, and will as such not be affected by the periodicity of the crystal. For those k -values, the light will behave as plane waves.

An example of this is shown in Figure 3.16, where the band diagram is shown for both a crystal with dielectric pillars in air, and for dielectric “veins” with air holes. Here, a sweep of \vec{k} -values is done, going from the $(0,0)$ point (typically defined as Γ), to $(0, K/2)$ (or X point), to $(K/2, K/2)$

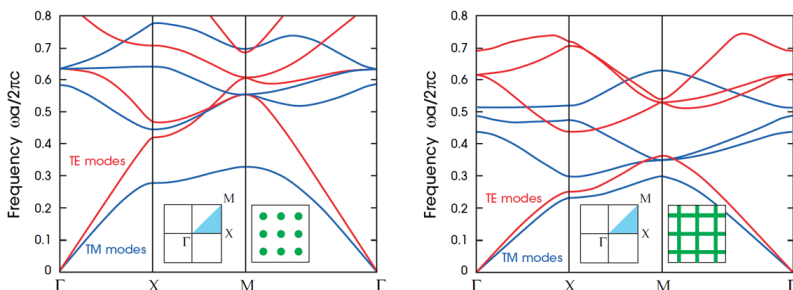


Figure 3.16: (a) Band diagram for a Photonic Crystal with dielectric columns (b) Band diagram for a Photonic Crystal with dielectric veins. Band diagrams taken from⁵.

(or M), and finally back to Γ . This is a typical Brillouin zone “walk” for photonic crystals with square-like symmetry.

One can see that for the dielectric pillars, a bandgap appears for the TM mode, while the dielectric veins show a bandgap for the TE mode. This can be explained by considering field discontinuities at the boundaries due to Maxwell’s equations. If we consider an (in-plane) interface between a high (ϵ_1) and low (ϵ_2) index material, then the energy density is given by $U_1 = \epsilon_1 |\vec{E}|^2$ before the interface and by $U_2 = \epsilon_2 |\vec{E}|^2$ after. TE modes only have in-plane electric field components, for which the boundary conditions state that $E_2 = \frac{\epsilon_1}{\epsilon_2} E_1$, from which follows that $U_2 = \frac{\epsilon_1}{\epsilon_2} U_1$. As such, the energy density will experience a discontinuous drop at the interface. For TM modes, where the electric field only exists perpendicular to the plane, it holds that $E_2 = E_1$, yielding $U_2 = \frac{\epsilon_2}{\epsilon_1} U_1$, which corresponds to a discontinuous jump in energy density. To summarize: for TM modes the energy density decreases at an interface where the dielectric constant decreases, and for TE modes the energy density increases at an interface where the dielectric constant decreases. Or put differently: a higher confinement can be reached for a TM mode when the dielectric is disconnected, whereas a higher confinement can be reached for a TE mode when the air is disconnected.

How can we use this argument to explain why TM gives a bandgap for

dielectric pillars and TE for dielectric veins? The dielectric pillar geometry is a geometry where the dielectric is disconnected, and the air is connected. The lower dielectric band will have the highest energy confinement when there are interfaces. The higher air band will have the highest energy confinement when there are no interfaces. The combination of these two effects causes the widest bandgap for the TM polarisation.

For the veins on the other hand the situation is flipped: this is a geometry where the dielectric is connected and the air is disconnected. Here, the lower dielectric band will favour energy confinement when there are no interfaces, and the higher air band will favour energy confinement when there are interfaces. This will favour TE polarisation. Following this train of thought, it can be seen that the duty cycle of the PhC will heavily impact the band-gap as well.

Photonic Crystals are quite complicated structures with various practical uses, although in general they are complex to make due to their demanding processing resolution requirements. Slight changes in periodicity can destroy the band gap, as they can be seen as “traps” inside the crystal, creating possible energy states in the forbidden zone. Nevertheless there is progress being made in the field of integrated Photonic Crystal lasers, as evidenced by some recent publications. Particularly the Noda group in Japan has quite some success with fabricating, measuring and understanding these lasers^{6,7}. Some concepts of Photonic Crystals will come back in Chapter 8.

3.3.2.8 Mach-Zehnder Interferometers

Contrary to the previous discussed active devices, a Mach-Zehnder-Interferometer (MZI) does not deal with light amplification, but with modulation. Consider a general modulator a black box with the input of a carrier and a bitstream, and as output the carrier with that bitstream imprinted on it (see Figure 3.17). A MZI is a device that can just do that, where the carrier signal is an electromagnetic wave and the bitstream is imprinted by turning off and on a voltage.

A MZI splits up a waveguide, as close to 50/50 as possible, and then

lets the light travel some distance (usually by curling up waveguides in spirals), before recombining the light again. The split up waveguides are typically referred to as the “arms” of the MZI. A MZI can be either symmetric (optical length is the same for both sides), or asymmetric (optical length is different). In practice, making a symmetrical MZI is rather difficult, since slight errors on the fabrication will introduce a phase shift anyway. Because of optical length differences, the two recombining arms of the MZI will have a phase shift $\Delta\phi$ (with ΔL_0 the *optical* length difference):

$$\Delta\phi = 2\pi \frac{\Delta L_0}{\lambda} \quad (3.3.32)$$

which shows that if the optical length is a multiple of the wavelength, there will be no phase shift. Assuming two incoming waves with intensity I_0 that recombine with a path difference of ΔL , we can show that

$$I = 2I_0 \left[1 + \cos \left(2\pi \frac{\Delta L_0}{\lambda} \right) \right] \quad (3.3.33)$$

meaning the waves will constructively interfere for multiples of the wavelength, and destructively interfere for multiples of half the wavelength.

This is the situation for the MZI at rest. By sweeping the wavelength, the length difference can be determined. To modulate the signal, some active material is added to one of the arms. Active meaning that the refractive index can somehow be controlled, like through applying a voltage over the material. An example of this is locally doping silicon, to turn it into a pn-junction. Through controlling the refractive index, one can control the difference in optical length ΔL between both arms. In this way, a voltage can be found to make sure the two arms will constructively interfere (giving a logical one), or destructively interfere (giving a logical zero). As such, a bitstream can be imprinted on a carrier wave. We can also define ΔL here as $\Delta L = (1 + \Delta n) \cdot \Delta L_0$.

Important metrics of modulators are switching speed, size, and losses. Switching speed is determined by how fast the active material reacts to the applied voltage, it will determine the max. bitrate that can be achieved with a modulator (typical metrics to define the switching speed are the

rise- and fall time). Size is a property mainly determined by a Figure of Merit (FOM) $V_\pi L_\pi$, the product between the voltage and length necessary to achieve a π -phaseshift (going from a logical one to zero). A material which refractive index is very sensitive to applied voltages (so: big refractive index shifts) can be short to still achieve a π -phaseshift. The smaller $V_\pi L_\pi$, the better (usually). Losses are due to not perfect 50/50 splitting, scattering in the waveguides or added absorption/scattering in the active material. Naturally, all these properties also influence one another.

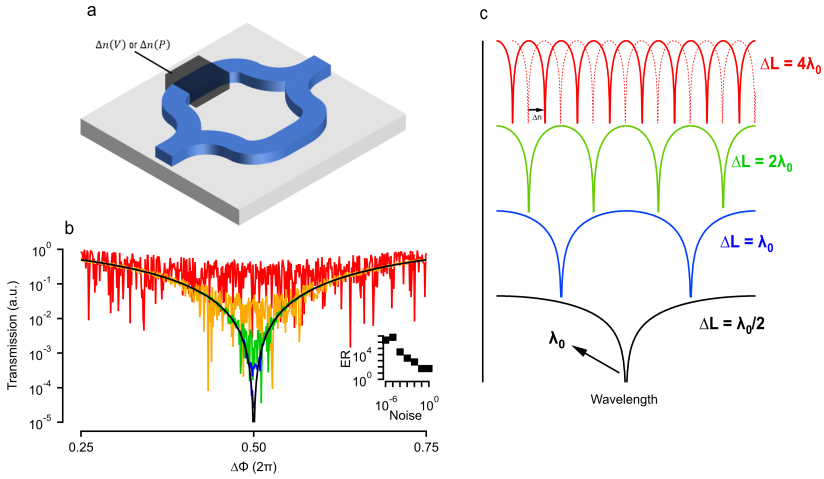


Figure 3.17: (a) Mach-Zehnder Interferometer. The black box denotes a material where the refractive index can be changed by applying a voltage or an optical power. (b) One period of a MZI shown for various values of noise, where the black line is the perfect case. Inset shows the Extinction Ratio (ER) vs. noise randomness. (c) Spectral behaviour of MZIs with various lengths. For the longest case (top), it is shown what effect changing the refractive index would have: shifting the spectrum.

Bibliography

- ¹ Roel Baets and G Roelkens. *Fotonica. UGent, February, 2004.*
- ² Weiqiang Xie, Yunpeng Zhu, Tangi Aubert, Steven Verstuyft, Zeger Hens, and Dries Van Thourhout. Low-loss silicon nitride waveguide hybridly integrated with colloidal quantum dots. *Optics Express*, 23(9):12152–12160, 2015.
- ³ Weiqiang Xie, Thilo Stöferle, Gabriele Raino, Tangi Aubert, Suzanne Bisschop, Yunpeng Zhu, Rainer F Mahrt, Pieter Geiregat, Edouard Brainis, and Zeger Hens. On-chip integrated quantum-dot–silicon-nitride microdisk lasers. *Adv. Mater.*, 29(16):1604866, 2017.
- ⁴ Yunpeng Zhu, Weiqiang Xie, Suzanne Bisschop, Tangi Aubert, Edouard Brainis, Pieter Geiregat, Zeger Hens, and Dries Van Thourhout. On-chip single-mode distributed feedback colloidal quantum dot laser under nanosecond pumping. *Acs Photonics*, 4(10):2446–2452, 2017.
- ⁵ John D Joannopoulos, Steven G Johnson, Joshua N Winn, and Robert D Meade. *Molding the flow of light. Princeton Univ. Press, Princeton, NJ [ua], 2008.*
- ⁶ Kyosuke Sakai, Eiji Miyai, Takui Sakaguchi, Dai Ohnishi, Takayuki Okano, and Susumu Noda. Lasing band edge identification for a surface-emitting photonic crystal laser. *IEEE Journal on Selected Areas in Communications*, 23(7):1335–1340, 2005.
- ⁷ T Inoue, M Yoshida, MD Zoysa, K Ishizaki, and S Noda. Design of photonic-crystal surface-emitting lasers with enhanced in-plane optical feedback for high-speed operation. *Optics Express*, 28(4):5050–5057, 2020.

Part II

Broadband Ultrafast Properties of Colloidal Nanocrystals

Chapter 4

Gain Through Core/Shell Quantum Dots with Thick CdS Shells

4.1 Introduction

The CdSe/CdS core/shell colloidal QD system is the workhorse of colloidal NC lasers. They are the most stable, have the most reliably engineered properties, and are absolutely the most studied. The state-of-the-art structure is already more complex with additional ZnS/ZnSe shelling, can include graded shells, but the foundations are still the CdSe/CdS system. The CdS shell is crucial in delocalizing the electron from the core, making Auger recombination less likely, and as such, increasing the gain lifetime. Besides this, it is also necessary for trap passivation: adding a shell massively increased the Quantum Yield, since the surface traps are mainly hole traps, and the hole remains localised to the core. This separates the holes from the traps. But essentially the optical properties of interest, such as light emission and amplification still originates from the core. Furthermore, in typical TA measurements, it is only the core that

gets excited, by using low enough energies that the CdS does not absorb the pump (>520 nm). Because of this, the absorption cross-section will be determined mainly by the core volume¹, where it is shown that actually the smallest shell diameter (or shell volume) is optimal because then the active material in the QD will be maximalised, while still passivating the surface. In this Chapter, we will look into increasing the spectral gain window by measuring the optical gain when the shell is excited, by using shorter wavelengths or higher energy photons as the excitation source, and looking into exciton densities exceeding the typical 2 by far. A perfect material to check optical gain from the shell transitions are the “Giant Shell Quantum Dots” (GSQDs) first reported by Di Stasio *et al.*² where multiple ASE peaks were found as a function of increasing the core size. Here, we take a more in-depth look in the gain metrics of the material via quantitative Transient Absorption Spectroscopy for both short (~ 5 ns) and long (up to 10 μ s) pump-probe delays, doing $k \cdot p$ calculations and extending the state-filling model explained in the introduction to multiple higher energy levels. An important factor here is the temperature, causing higher energy states to be occupied even without excitation. This direct measurement of the gain threshold through TA spectroscopy is coupled to a method to derive it from the gain lifetime, revealing the Auger Rate scales with $\langle N \rangle \cdot (\langle N \rangle - 1)$, in accordance with the work of Melnychuk *et al.*³.

This work is the result of a collaboration between teams at UGent, Departement of Chemistry and Photonics Research group, at Universitat Jaume I, Spain, Departement de Quimica Fisica i Analitica, and Politecnico di Milano, Italy, Istituto Italiano di Tecnologia. My personal contribution was conducting the high fluency TA measurements and analysis and adapting a state-filling model to incorporate multiple states allowing to use the $k \cdot p$ data in it.

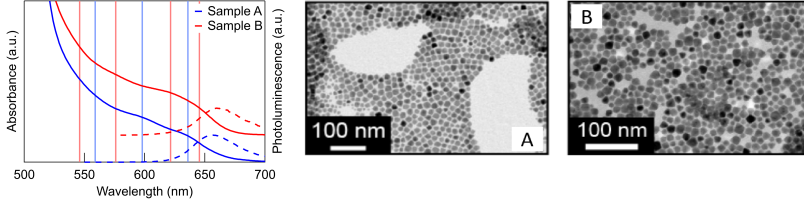


Figure 4.1: (left) Absorbance spectra of the two samples, with vertical lines indicating the different transitions as obtained from second-derivative analysis. PL spectra show a maximum at 657 nm and 661 nm, respectively. (right) TEM images of both Sample A and Sample B, taken from².

4.2 Material Description

For this study, we have investigated two samples of CdSe/CdS pure-phase wurtzite nanocrystals with a thick CdS shell. The first has a 4.1 nm CdSe core and an overall diameter of 15.0 nm (15 Mono Layers (ML) CdS shell, sample A), the second has a 7.5 nm core and an overall diameter of 13.5 nm (8.6 ML CdS shell, sample B). Associated transmission electron microscope images, absorbance and PL spectra were reported previously². The samples have a band gap at 636 nm and 646 nm, respectively (Figure 4.1). Using second-derivative analysis of the absorption spectrum⁴, we can discern up to three (sample A) and four (sample B) transitions. These transitions yield, as discussed by Di Stasio *et al.*² Amplified Spontaneous Emission (ASE) resulting in an ASE spectrum that extends from the CdSe core to the CdS shell band edge (Table 4.1).

	Sample A		Sample B	
	Absorbance (nm)	ASE (nm)	Absorbance (nm)	ASE (nm)
1st peak	636	623	646	648
2nd peak	598	568	622	612
3rd peak	559	523	576	566
4th peak	—	—	546	538

Table 4.1: Spectral position of the transitions in the absorbance and (reported²) ASE spectra. All ASE peaks are blue shifted compared with the corresponding absorbance peaks.

4.3 Energy Level Calculations

To gain further insight into this optical behavior, we performed $k \cdot p$ band structure calculations, for a series of nanocrystals with fixed CdSe/CdS diameter of 15 nm, and for two additional CdSe/CdS that match the geometry of our experimental samples A and B. We calculated the electron and hole states within a wurtzite description. Electron states were described with a single-band effective mass Hamiltonian, for the hole states we used Chuangs six-band Hamiltonian^{5,6}. Coupling between heavy hole, light hole and split-off subbands was hence taken into account, along with a finite band offset between core and shell. As compared to cubic and quasi-cubic Hamiltonians, the wurtzite model provides a more accurate description of the density of hole states, which are significantly influenced by band coupling. Strain and piezoelectricity⁷ were not considered here, and parameters used for the wurtzite description are given in Appendix B. The motivation for these choices is not given here since the $k \cdot p$ simulations were not done by me personally, but more details are given in Appendix B. We first considered nanocrystals with fixed overall (i.e. core plus shell) diameter $D_{cs} = 15$ nm (similar to the experimental samples) and variable core diameter D_c (Figure 4.2a). Calculations show that electron $1S_e$ and $1P_e$ energy levels are considerably split, by 80 meV or more across the entire range (Figure 4.2b). Remarkably, despite the large CdS shell yielding a 15 nm overall diameter, the $1P_e$, $2S_e$ and $1D_e$ levels are also clearly split, even though they lie above the conduction band offset and are de-localized over the entire core/shell nanocrystal (Figure B.5) for most core diameters.

The hole energy levels on the other hand are much more closely spaced (Figure 4.2c). A first band of states is formed by the $1S_{3/2}$ and $1P_{3/2}$ states. Due to the crystal field of the wurtzite lattice, the four-fold degenerate $1S_{3/2}$ hole state ($F = 3/2$, $F_z = \pm 3/2, \pm 1/2$) splits into a ground state doublet with $F_z = \pm 3/2$ and an excited state with $F_z = \pm 1/2$. The former (latter) has predominant heavy hole (light hole) character. Interestingly, for the experimental nanocrystals used (Figure 4.2d, Figure

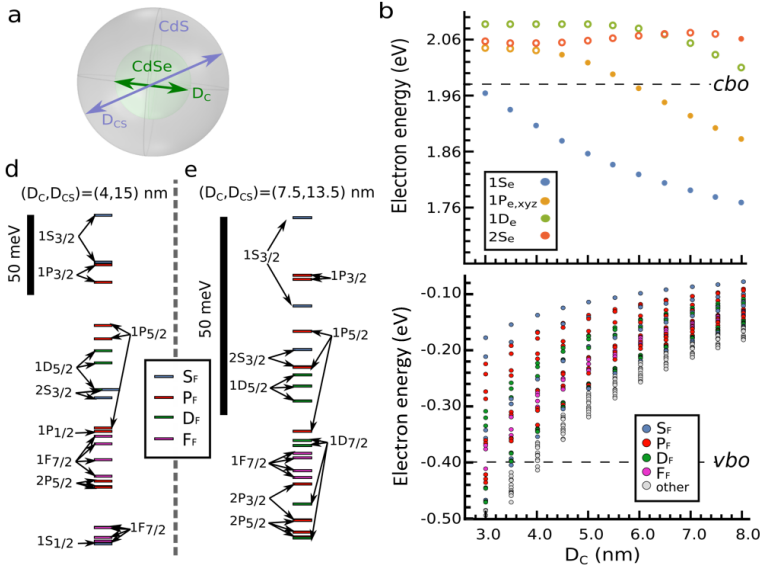


Figure 4.2: Calculated energy levels of wurtzite CdSe/CdS nanocrystals as a function of core diameter. (a) Sketch of the heterostructure under study. (b) Electron states, for which solid dots (empty circles) denote electron states with most of its charge density in the core (shell). (c) Hole states. (d,e) Zoom of hole states for sample A and B, respectively. In b and c, energies are referred to the top of the CdSe valence band (in bulk), the dot color indicates the lowest envelope angular momentum, and the dashed line represents the bulk conduction (cbo) and valence (vbo) band offset.

4.2e), these states lie within 42 meV and 23 meV for sample A and B, respectively, implying that these are thermally occupied at room temperature. For sample B, a second band of thermally accessible hole energy levels formed by $1P_{5/2}$ and $2S_{3/2}$ states can be identified, lying around 29-38 meV below the ground state.

The spectral position of optically allowed transitions between these states and the respective $1S_e$ and $1P_e$ electron states was subsequently calculated. We have to remark that these do not exactly match experimental values, as we did not include electron-hole Coulomb interactions in the band structure calculations. Rather than evaluating the exact Cou-

lomb energy for the whole band of excited states, which would require massive configuration interaction calculations, we added a fixed shift to the calculated transitions, of 177 meV and 20.5 meV for sample A and B, respectively, to match the experimental $1S_e - 1S_{3/2}$ transition. All the results are shown in the tables below for Sample A and B.

Hole level	Energy (eV)	Delta (meV)	Occ (%)	Hole level	Energy (eV)	Delta (meV)	Occ (%)
1S _{3/2}	-0.137691727	0	24.17	1P _{1/2}	-0.272921558	-135.2298311	0.13
1S _{3/2}	-0.137664364	0.02736247	24.20	1F _{7/2}	-0.276039296	-138.3475695	0.11
1S _{3/2}	-0.166944896	-29.25316891	7.74	1F _{7/2}	-0.276052179	-138.3604519	0.11
1S _{3/2}	-0.166951986	-29.26025885	7.74	1F _{7/2}	-0.280694169	-143.002442	0.09
1P _{3/2}	-0.168680323	-30.98859587	7.24	1F _{7/2}	-0.280695763	-143.0040361	0.09
1P _{3/2}	-0.168690163	-30.99843601	7.24	1F _{7/2}	-0.290730662	-153.0389353	0.06
1P _{3/2}	-0.179572331	-41.88060391	4.74	1F _{7/2}	-0.290739271	-153.0475447	0.06
1P _{3/2}	-0.179597488	-41.90576166	4.73	1F _{7/2}	-0.300977692	-163.2859651	0.04
1P _{5/2}	-0.206606952	-68.91522494	1.65	1F _{7/2}	-0.300980289	-163.2885619	0.04
1P _{5/2}	-0.20662968	-68.93795372	1.65	2P _{5/2}	-0.304058538	-166.3668116	0.04
1P _{5/2}	-0.215016652	-77.32492518	1.19	2P _{5/2}	-0.304058958	-166.3672315	0.04
1P _{5/2}	-0.215023833	-77.33210667	1.19	2P _{5/2}	-0.307502749	-169.811022	0.03
1D _{5/2}	-0.222429906	-84.73817967	0.89	2P _{5/2}	-0.307511312	-169.8195848	0.03
1D _{5/2}	-0.222438648	-84.74692151	0.89	2P _{5/2}	-0.307897051	-170.2053248	0.03
1D _{5/2}	-0.230073228	-92.38150091	0.66	2P _{5/2}	-0.307914778	-170.223051	0.03
1D _{5/2}	-0.230077505	-92.38577809	0.66	1D _{7/2}	-0.333037849	-195.3461227	0.01
1D _{5/2}	-0.246801879	-109.1101519	0.35	1D _{7/2}	-0.333038598	-195.3468713	0.01
1D _{5/2}	-0.246815012	-109.123285	0.35	1D _{7/2}	-0.333155912	-195.4641852	0.01
2S _{3/2}	-0.246822764	-109.1310374	0.35	1D _{7/2}	-0.333171114	-195.4793868	0.01
2S _{3/2}	-0.246833174	-109.1414474	0.35	1D _{7/2}	-0.339321937	-201.6302102	0.01
2S _{3/2}	-0.251891359	-114.199632	0.28	1D _{7/2}	-0.339343473	-201.6517468	0.01
2S _{3/2}	-0.251915478	-114.2237514	0.28	1D _{7/2}	-0.341606008	-203.9142818	0.01
1P _{5/2}	-0.270769876	-133.0781495	0.14	1D _{7/2}	-0.34161193	-203.9202034	0.01
1P _{5/2}	-0.270787978	-133.0962515	0.14	1S _{1/2}	-0.343323619	-205.6318926	0.01
1P _{1/2}	-0.272912828	-135.2211009	0.13	1S _{1/2}	-0.34333237	-205.6406436	0.01

Table 4.2: Calculated hole levels for sample A.

4.3. Energy Level Calculations

Hole level	Energy (eV)	Delta (meV)	Occ (%)	Hole level	Energy (eV)	Delta (meV)	Occ (%)
$1S_{3/2}$	-0.079607541	0	9.72	$1D_{7/2}$	-0.136626781	-57.01924006	1.06
$1S_{3/2}$	-0.079635851	-0.028310485	9.71	$1D_{7/2}$	-0.137891853	-58.28431201	1.01
$1P_{3/2}$	-0.094345469	-14.73792875	5.48	$1D_{7/2}$	-0.137898641	-58.29110004	1.01
$1P_{3/2}$	-0.09437333	-14.7657898	5.47	$1F_{7/2}$	-0.139889261	-60.28172078	0.93
$1P_{3/2}$	-0.095415027	-15.80748646	5.25	$1F_{7/2}$	-0.139898792	-60.29125152	0.93
$1P_{3/2}$	-0.095429197	-15.82165658	5.25	$1F_{7/2}$	-0.141039873	-61.43233278	0.89
$1S_{3/2}$	-0.102218882	-22.61134131	4.03	$1F_{7/2}$	-0.141062439	-61.4548985	0.89
$1S_{3/2}$	-0.10222388	-22.61633972	4.03	$1F_{7/2}$	-0.144337442	-64.72990132	0.78
$1P_{5/2}$	-0.108687753	-29.08021249	3.13	$1F_{7/2}$	-0.144346553	-64.7390121	0.78
$1P_{5/2}$	-0.108712579	-29.10503849	3.13	$1F_{7/2}$	-0.146092578	-66.48503751	0.73
$2S_{3/2}$	-0.113359005	-33.75146397	2.61	$1F_{7/2}$	-0.146095305	-66.48776464	0.73
$2S_{3/2}$	-0.113377883	-33.77034229	2.61	$2P_{3/2}$	-0.147736277	-68.12873673	0.69
$2S_{3/2}$	-0.11777295	-38.16540934	2.20	$2P_{3/2}$	-0.147739734	-68.13219294	0.69
$2S_{3/2}$	-0.117773935	-38.16639488	2.20	$1D_{7/2}$	-0.152860629	-73.25308792	0.56
$1P_{5/2}$	-0.117913491	-38.30595023	2.19	$1D_{7/2}$	-0.152868416	-73.26087492	0.56
$1P_{5/2}$	-0.117917557	-38.31001635	2.19	$2P_{3/2}$	-0.156936768	-77.3292276	0.48
$1D_{5/2}$	-0.11983383	-40.22628907	2.03	$2P_{3/2}$	-0.156961122	-77.35358103	0.48
$1D_{5/2}$	-0.119850273	-40.24273243	2.03	$2P_{5/2}$	-0.157078637	-77.47109673	0.48
$1D_{5/2}$	-0.122691622	-43.08408108	1.82	$2P_{5/2}$	-0.157099141	-77.49160058	0.48
$1D_{5/2}$	-0.122709598	-43.10205736	1.82	$2P_{5/2}$	-0.160054822	-80.44728157	0.42
$1D_{5/2}$	-0.126523373	-46.91583218	1.57	$2P_{5/2}$	-0.16007127	-80.46372973	0.42
$1D_{5/2}$	-0.126545394	-46.93785298	1.56	$2P_{5/2}$	-0.161289171	-81.68163053	0.40
$1P_{5/2}$	-0.134243738	-54.63619694	1.16	$2P_{5/2}$	-0.161295234	-81.68769361	0.40
$1P_{5/2}$	-0.134253886	-54.64634566	1.16	$1D_{7/2}$	-0.16154626	-81.93871906	0.40
$1D_{7/2}$	-0.1366086	-57.00105952	1.06	$1D_{7/2}$	-0.161554385	-81.94684433	0.40

Table 4.3: Calculated hole energy levels for sample B.

Electron Level	Energy (eV)	Δ (meV)	$E_g + \Delta$	Electron Level	Energy (eV)	Δ (meV)	$E_g + \Delta$
1Se	0.24601		1.97601	1Se	0.11916		1.84916
1Pe(y)	0.38082	134.81	2.11082	1Pe(x)	0.24302	123.86	1.97302
1Pe(x)	0.38082	134.81	2.11082	1Pe(y)	0.24302	123.86	1.97302
1Pe(z)	0.38083	134.82	2.11083	1Pe(z)	0.24303	123.87	1.97303
2Se	0.39328	147.27	2.12328	1De(xz)	0.37982	260.66	2.10982
1De(x ² -y ²)	0.42791	181.90	2.15791	1De(yz)	0.37983	260.67	2.10983
1De(xy)	0.42792	181.91	2.15792	1De(xy)	0.37983	260.67	2.10983
1De(yz)	0.42793	181.92	2.15793	1De(x ² -y ²)	0.37983	260.67	2.10983
1De(xz)	0.42794	181.93	2.15794	1De(z ²)	0.37985	260.69	2.10985
1De(z ²)	0.42795	181.94	2.15795	2Se	0.43821	319.05	2.16821
1Fe	0.47818	232.17	2.20818	1Fe	0.49897	379.81	2.22897
1Fe	0.47819	232.18	2.20819	1Fe	0.49897	379.81	2.22897
1Fe	0.4782	232.19	2.20820	1Fe	0.49898	379.82	2.22898
1Fe	0.4782	232.19	2.20820	1Fe	0.49898	379.82	2.22898
1Fe	0.47822	232.21	2.20822	1Fe	0.49899	379.83	2.22899
1Fe	0.47823	232.22	2.20823	1Fe	0.499	379.84	2.229
1Fe	0.47826	232.25	2.20826	1Fe	0.49902	379.86	2.22902
2Pe	0.49213	246.12	2.22213	2Pe	0.52606	406.9	2.25606
2Pe	0.49215	246.14	2.22215	2Pe	0.52607	406.91	2.25607
2Pe	0.49221	246.20	2.22221	2Pe	0.5261	406.94	2.2561

Table 4.4: Calculated electron energy levels for sample A (left) and B (right).

4.4 Transient Absorption Spectroscopy Measurements

4.4.1 Low Fluency Measurements

In order to understand the gain in the material, we first performed Transient Absorption Spectroscopy, in a time domain extending from femto- up to microseconds. Samples were excited with a 355 nm nanosecond pulse for which the TA was collected for a pump-probe delay of up to 10 μ s. For the shorter time delays (up to 3 ns), samples were excited with a 400 nm femtosecond pulse, both exciting well within the CdS shell. In Figure 4.3, for sample A, both maps were normalized at 1 ns in order to reconstruct the entire decay. The excitation fluency was kept at 65 μ J/cm², for which we excite on average $\langle N \rangle \approx 1.6$ excitons per nanocrystal. We observed a broad bleach band consisting of several transitions, which all have a TA bleach that extends into the microsecond time domain (Figure 4.3b). Independent of the wavelength interval that we probed, all transitions have a similar long-lived decay constant (Figure 4.3c), which also matches well with the photoluminescence decay. Note that an initial fast relaxation (2 ps time range) is observed for the 470-500 nm interval, with a similar rise time for the remaining spectral range below the CdS band edge. It reflects hot carrier relaxation to the CdS band edge⁸. A similar long lifetime is observed for all states that are probed in sample B (Figure 4.3d-e).

A Stark shift (for example due to trapped charges) is expected to induce an asymmetric bleach signal with strong photo-induced absorption⁹ which we do not observe, we can rule it out as the origin of these long-lived features. Hence they can be ascribed to state filling of different excited electron and hole levels.

Resulting transition wavelengths and associated thermal occupancy of the respective hole levels are compared to the TA spectrum collected at 1 ns in Figure 4.4, with all calculated transitions shown in Appendix B. The results demonstrate that indeed, a broad range of transitions, spanning the region between the CdSe and CdS band edge, are governed by thermally

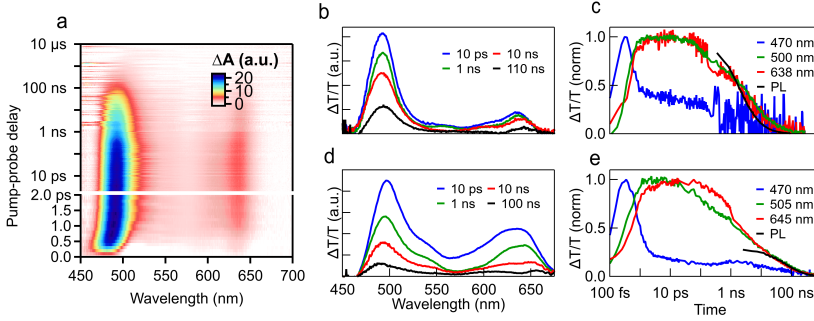


Figure 4.3: (a) TA map for sample A, using a pump fluency of $65 \mu\text{J}/\text{cm}^2$, constructed from fs and ns TA spectra. (b) $\Delta T/T$ spectra at different time intervals for sample A, demonstrating broadband, long-lived TA relaxation. (c) Sample A decay traces for the TA bleach features are similar across the spectrum, and agree with the PL decay (black line). (d)-(e) $\Delta T/T$ spectra at different delay times and decay traces for sample B, showing similar behavior.

occupied S - and P -hole states. In line with earlier TA experiments of the Houtepen group¹⁰ in high-quality CdSe/CdS nanocrystals also holes contribute to the TA bleach spectrum, hence the thermal occupation of excited hole states between the CdSe and CdS band gap is expected to yield long-lived bleach features, in agreement with experimental data. With a valence band offset between CdSe and CdS of about 440 meV, the close spacing of hole states is dictated predominantly by the large diameter of the CdSe core, showing the importance of increasing the latter to obtain the unique features described above. For sample A, we also observe a bleach feature around 600 nm that cannot be explained by the hole occupancy, however, this wavelength range corresponds to transitions involving the $1S_e$ electron state (Figure 4.4a, grey bars, with arbitrary height). Similar transitions appear for sample B around 635 nm. The highly occupied hole states are marked in bold.

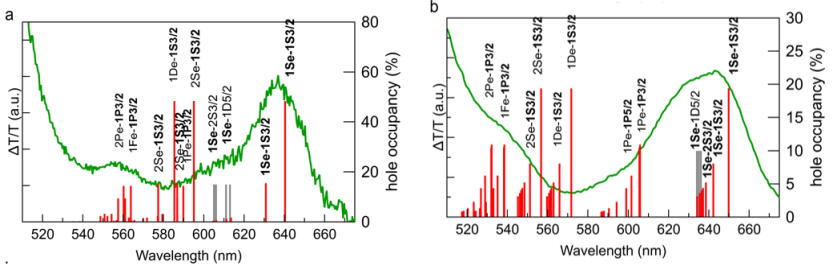


Figure 4.4: Calculated transitions and fractional hole occupancy (red bars) for sample A (a) and B (b), compared to the experimental TA spectrum collected at 1 ns (green). Additional calculated transitions associated with the $1S_e$ electron state are marked with grey bars (arbitrary height).

4.4.2 High Fluency Measurements

With this detailed understanding of the CdSe/CdS giant-shell band structure and TA lifetimes in the CdSe/CdS band edges spectral range, we progressed to higher pump fluency, focusing now on femto- to nanosecond TA to investigate the gain dynamics. We measured the differential absorption ΔA at varying fluency, from which we calculated the gain G as $-(\Delta A + A_0)$, with A_0 the linear absorbance. The region of positive gain is then plotted in a gain map. Figure 4.6a shows a typical example, for sample A, measured at a pump fluency of 1.7 mJ/cm^2 , corresponding to an exciton density of $\langle N \rangle = 18$. The maps are then time-integrated over the full time domain (up to 3 ns) to construct the gain spectrum. Figures 4.6b-4.6c show the gain spectra for sample B, and Figures 4.6d-4.6e for sample A. Notice that an impressive gain band of up to 200 nm wide can be obtained, spanning essentially the entire spectral region between the CdSe and CdS band gaps. While the gain spectrum is blue shifted from the fundamental absorption gap, the wide spectral range obtained can be attributed to the ability of our CdSe/CdS to display gain even at exciton densities approaching $\langle N \rangle = 200$ for the highest pump fluency, suggesting that the large-core, giant-shell CdSe/CdS heterostructure can accommodate a high carrier density, although the question now becomes

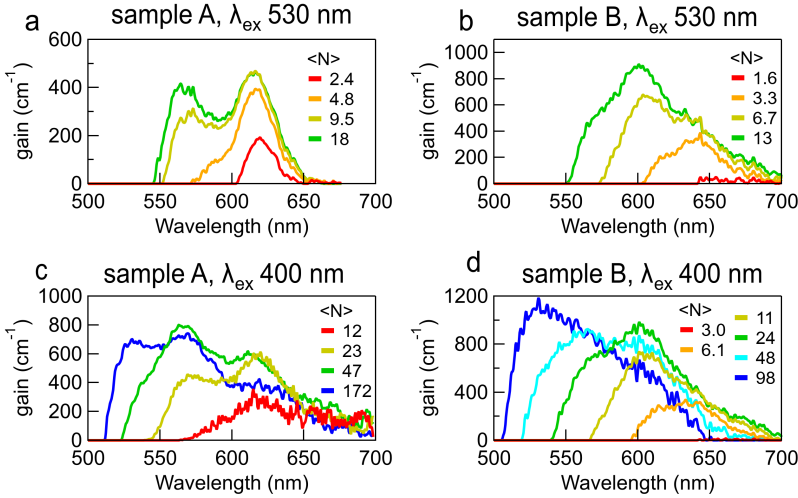


Figure 4.5: Intrinsic gain spectra collected at 3 ps for sample A (panels (a) and (b)), and sample B (panels (c) and (d)).

whether these charges can still be considered separated excitons or just a free $e - h$ plasma. At the same time, due to the giant-shell motif, the gain coefficient in the CdSe spectral region remains modest compared to literature values obtained on CdSe/CdS¹. Depending on the excitation conditions the band edge gain coefficient at 3 ps is about 400-465 cm⁻¹ and 465-580 cm⁻¹ for sample A and B, respectively (Figure 4.5), while CdSe/CdS with a thin shell showed values up to 2800 cm⁻¹. For higher-energy states, the gain coefficient does increase further, reaching 690 cm⁻¹ and 1090 cm⁻¹ at 530 nm for sample A and B, respectively. This decrease in gain amplitude can be understood purely from a volume based perspective, where having a small core/shell volume ratio translates to a small amount of active material.

Next, the experimental gain spectra are compared to the spectral positions of the ASE peaks (Table 4.1, Figure 4.6, black vertical lines). Clearly, the spectral features observed in the gain spectra agree well with the spectral position of the ASE peaks. In addition, we can now also assign the

states that pertain to these features. For this, we calculated the expected transition wavelength of the different states using the $k \cdot p$ band structure (Figure 4.6, grey vertical lines, and Appendix B for all transitions and wavelengths). Again, we applied a fixed red shift, of 137 meV and 26.4 meV for sample A and B, respectively, to match calculated transitions with the experimental band edge gain peaks. Focusing first on the large-core sample B (Figures 4.6b-4.6c), comparison of computational and experimental data shows that a continuous gain spectrum can indeed be obtained due to the high number of electron/hole states with transitions between the CdSe and CdS band gap. A more careful inspection shows that states which line up with the ASE/gain peaks correspond to transitions involving the $1S_e$, $1P_e$, $1D_e$ and $1F_e$ electron states, respectively. More specifically, they are due to the transitions $1S_e - 1S_{3/2}$, the $1P_e - 1P_{3/2} - 1P_e - 1P_{5/2}$ manifold, $1D_e - 1S_{3/2} - 1D_e - 1S_{5/2}$ manifold, and $1F_e - 1P_{3/2}$, with possible contribution from the $2P_e - 1P_{3/2} - 1P_e - 1P_{5/2}$ manifold for the latter, as these are closely spaced with the former. For sample A, a similar picture arises, yet assignment of the final ASE transition around 520 nm (Figure 4.6d) remains more ambiguous, possibly due to the fact that we do not take the additional blue shift due to multiexciton repulsions into account in our $k \cdot p$ calculations. Indeed, this results in an experimental ASE transition which is not superposed on the corresponding $1F_e - 1P_{3/2}$ transition as in the case of sample B, as this is calculated to lie around 550 nm. Note also that the gain spectra show additional features not perceived in the ASE spectra² for instance around 590 nm and 540-550 nm. However, the absence of ASE for sample A at these wavelengths might simply be due to mode competition between the different ASE modes.

Regarding the gain threshold, for sample B, when using 530 nm excitation (Figure 4.6b) to avoid nonradiative carrier losses due to surface trapping, the band edge gain develops with an onset of about $\langle N \rangle = 1 - 2$ excitons per nanocrystal, in line with earlier results on CdSe/CdS nanocrystals with a thinner CdS shell¹. The excited-state gain bands develop around $\langle N \rangle = 3$ excitons for the second band, and at $\langle N \rangle = 7 - 13$ for the

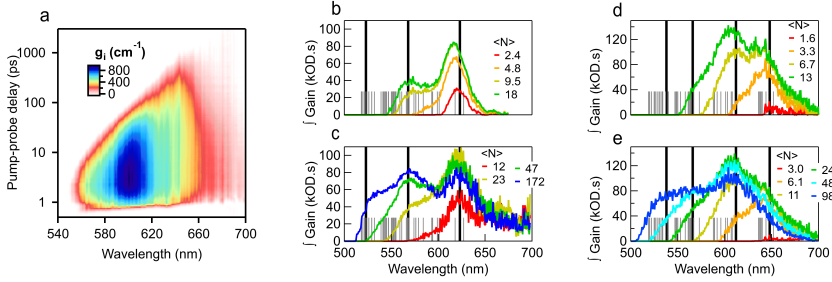


Figure 4.6: (a) TA gain map for sample A, obtained with a pump fluency of 1.7 mJ/cm². (b) Time-integrated gain spectra (i.e. the spectral region that does not show gain is set to zero), exciting sample B at 530 nm. The pump fluency has been converted to a number of excitons per nanocrystal, via the linear absorption cross section. Vertical black lines correspond to the ASE peak wavelengths, see Table 4.1. Vertical grey lines correspond to the calculated transitions. (c) When exciting sample B at 400 nm, a similar result is obtained, yet at higher exciton density. Due to the higher excitation photon energy, a fourth gain peak appears at the highest fluencies. (d)-(e) Similar results are obtained for sample A.

third gain band. Sample A shows a similar behavior (Figure 4.6d). These values are small considering the high degeneracy of the hole states, and suggest that exceeding population inversion of the corresponding electron levels is sufficient to obtain gain. When extending the pump wavelength from 530 nm to 400 nm and thus exciting primarily the CdS shell, for sample B (Figure 4.6c) the exciton density for a similar gain threshold is about twice the number required when pumping the CdSe core with 530 nm excitation. In addition, the fourth gain peak appears when the exciton density exceeds $\langle N \rangle = 24$. In the small-core sample A, the core-to-total nanocrystal volume ratio is significantly larger (1:49, compared to 1:6 for sample B), and as a result, while the same features can be observed, the exciton densities required to achieve gain using a 400 nm pump wavelength are significantly higher (Figure 4.6d), likely due to increased carrier trapping and nonradiative losses at the CdS surface¹¹.

To understand this threshold behaviour, we first measured the gain threshold by independent means. Starting with sample B, in Figure 4.7a

we plot contours of the gain threshold for varying pump fluency in a time-wavelength map, using a 530 nm pump wavelength. This representation reveals that, once the maximal gain is reached, the gain lifetime τ_G , i.e. the time delay at a given wavelength for which net stimulated emission turns into net absorption, is largely independent of the pump fluency. Maximum values lie around $\tau_{G,XX} = 650$ ps for the band edge gain. This gain lifetime is more than an order of magnitude shorter than the biexciton lifetime of $\tau_{XX} = 33$ ns estimated from the fluorescence decay time via $\tau_{XX} = \tau_X/4$,¹² allowing us to conclude that the gain lifetime is limited by nonradiative Auger recombination and not by its intrinsic radiative rate.

While ample literature is available that discusses the influence of the nanocrystal volume and the CdSe/CdS interface on the Auger rate k_{AR} ¹²⁻¹⁵, less is known about the scaling of k_{AR} with electron and hole density. Recently however, Philbin and Rabani^{16,17} showed that electron-hole correlations should not be neglected when calculating k_{AR} in weakly to moderately confined systems including CdSe/CdS nanocrystals, leading to an Auger rate that does not scale with $\langle N \rangle^2 \cdot (\langle N \rangle - 1)$, but as $k_{AR} \propto \langle N \rangle \cdot (\langle N \rangle - 1)$. Since we can assume that τ_G is inversely proportional to k_{AR} as discussed above, the lifetime spectrum can be converted to a gain threshold spectrum using this relation, since

$$\tau_G^{-1} \propto \langle N \rangle \cdot (\langle N \rangle - 1) \quad (4.4.1)$$

Knowing this, when we fix the biexciton gain threshold $\langle N_{XX} \rangle$ to 1.6 as given by the direct gain threshold measurement, and the associated biexciton gain lifetime $\tau_{G,XX}$ to 650 ps as given by the gain lifetime measurement, Equation (1) gives us the threshold for any given wavelength $\langle N(\lambda) \rangle$ from the gain lifetime $\tau_G(\lambda)$ as a solution of:

$$\frac{\langle N(\lambda) \rangle \cdot (\langle N(\lambda) \rangle - 1)}{\langle N_{XX} \rangle \cdot (\langle N_{XX} \rangle - 1)} \cdot \frac{\tau_{G,XX}}{\tau_G(\lambda)} \quad (4.4.2)$$

In Figure 4.7b, we compare the direct measurement of $\langle N \rangle$, extracted from an interpolation of the fluency dependent measurements of Figure

4.6b (red markers), and $\langle N \rangle$ obtained from the gain lifetime using the trace collected at highest fluency in Figure 4.7a and Equation 4.4.2 (blue markers). A remarkable agreement is observed, highlighting both that the gain is Auger-limited, and, more importantly, that a measurement of the gain lifetime provides a powerful method to understand the exciton density at which gain develops for different wavelengths and associated electronic states. Sample A, which has a maximal gain lifetime $\tau_{G,XX} = 495$ ps with a corresponding gain threshold $\langle N_{XX} \rangle = 1.6$, shows a similar result (Figure 4.7c-4.7d).

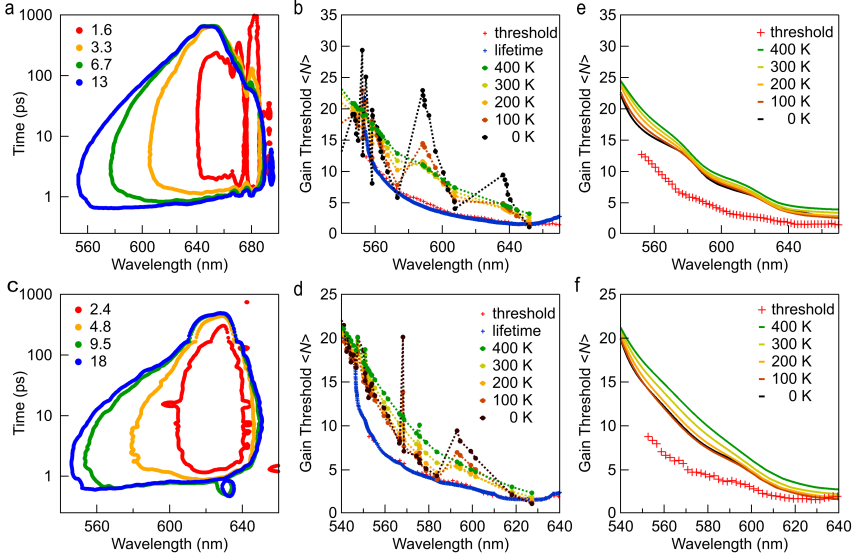


Figure 4.7: (a) Gain lifetime spectra for sample B, plotted as contours of the gain threshold in a time-wavelength map, using an excitation wavelength of 530 nm. The legend indicates the corresponding average number of excitons per nanocrystal. (b) Gain threshold spectrum obtained from direct measurement of the threshold using varying fluency (red markers), and as calculated from the gain lifetime at highest fluency (blue markers). Black, brown, orange, yellow and green traces show the gain threshold calculated from the $k \cdot p$ energy levels, at various temperatures. Due to thermal occupation of excited hole states at elevated temperature, a smoothed curve is obtained. (c)-(d) Same data for sample A. (e) Gain threshold spectra at varying temperature of sample B, calculated assuming a 75 meV line broadening for each transition. Data are compared to the experimental gain threshold (red markers). (f) Same data for sample A.

4.5 State Filling

4.5.1 Explanation of the Model

To model the gain threshold, a state-filling model is used with as input the calculated energy levels from the $k \cdot p$ analysis. This state-filling model is based on previous work by Bisschop *et al.*¹ where only the band gap transition is considered. Here, we have extended this model for a multilevel system, only possible due to the $k \cdot p$ calculations, and added temperature as a parameter.

To extend the model for a multilevel system with several allowed transitions, we consider first the situation at 0 K, that is, electron and hole states are sequentially filled in order of increasing energy. Here, the system consists of a series of electron and hole levels, N_e^i and N_h^j , each having their respective degeneracy. Based on selection rules, only certain transitions $A_{i \rightarrow j}(\langle N \rangle)$ are allowed, and we can calculate the absorbance for these transitions as:

$$A_{i \rightarrow j}(\langle N \rangle) = \sum_{N=0}^{\infty} P(N, \langle N \rangle) \cdot \left(1 - \frac{N_e^i(N)}{g_e^i} - \frac{N_h^j(N)}{g_h^j} \right) \cdot A_{0, i \rightarrow j} \quad (4.5.1)$$

Instead of applying this equation just once as is done for the band gap transition, in the multilevel system with n transitions, we calculate the corresponding gain threshold n times. Each of these transitions and corresponding threshold is then linked to a specific energy or wavelength, using the transition energies obtained via the $k \cdot p$ calculations (see Appendix B), finally yielding a threshold spectrum as shown in Figure 4.7.

4.5.2 Adding the Temperature

For the situation at 0 K, the levels will fill up in order of their respective energies (e.g. first the 1S-level, then the 1P-level, etc). Adding temperature as a parameter will change this, as thermal redistribution of electron and holes between closely-spaced states has to be taken into account. The probability of this is given by a Fermi-Dirac distribution. The first task is

to find the quasi-Fermi level to normalize the carrier distribution, which is done by solving the following equation for E_F numerically, where we sum over all energy states:

$$\langle N \rangle = \sum_i \frac{g_i}{1 + \exp\left(\frac{E_i - E_F}{kT}\right)} \quad (4.5.2)$$

Next, the occupancy of each state can be determined for a given number of electron-hole pairs $\langle N \rangle$. For the formula above for the absorbance, the only difference is the addition of the temperature as a parameter for the state filling, e.g. $N_e^i(N)$ becomes $N_e^i(N, T)$

$$N_e^i(N, T) = \frac{g_i}{1 + \exp\left(\frac{E_i - E_F}{kT}\right)} \quad (4.5.3)$$

A similar formula holds for the hole states. As a result, the filling of states is no longer step-wise, but becomes smoother at higher temperatures. As a check, filling at 0 K in the formula above yields indeed the case again of step-wise filling. An example of this is shown in Figure 4.8, for the two first electron and hole levels.

To further show that the filling depends on the temperature, Figure 4.9 shows the occupancy of all levels under consideration in our calculations, stacked on top of each other. Again, at 0 K levels fill up step-wise, while at 300 K, higher-excited states are occupied before full occupancy of lower-lying states is reached.

4.5.3 Applying the model to the $k \cdot p$ calculations

Finally, to consolidate the experimental results, we can model the gain threshold for the different calculated electronic states. As we know from the low-fluency TA spectroscopy, lowest-lying hole states are thermally occupied at room temperature, which is why temperature was added as a parameter. Based on the number of carriers in the system and the temperature, the occupancy of the energy levels was calculated for both electrons and holes by applying the appropriate Poisson and Fermi-Dirac

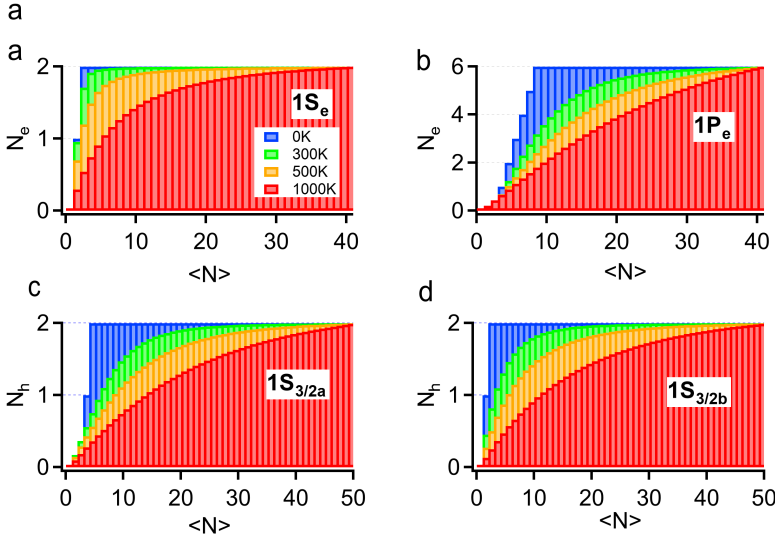


Figure 4.8: State-filling of the first two electron levels ($1S_e$ and $1P_e$) for sample A with a small core, at three different temperatures: 0 K (blue), 500 K (green) and 1000 K (red). At 0 K, we clearly see that the first and second electron first occupy the $1S_e$ state, and the $1P_e$ state only starts to fill from the third electron onward. Increasing the temperature on the other hand yields a more gradual filling of the different states.

statistics. Using these occupancies, we calculated the gain threshold for every transition, and together with the associated wavelength, reconstructed a discrete threshold spectrum. The latter is shown in Figure 4.7b and Figure 4.7d, for sample B and A, respectively. Focusing on sample B, initially, at 0 K we obtained the case of pure sequential state filling, with a band edge gain threshold starting at 1.15 excitons, in line with earlier results¹. At shorter wavelengths, the gain threshold rapidly increases due to the presence of higher excited hole states, after which another low-lying threshold is observed around 610 nm, here associated with the $1P_e - 1P_{3/2}$ transition. The pattern of increasing and decreasing threshold then repeats again. At higher temperatures however, here simulated between 100 K and 400 K, we observe less variations in the calculated curves,

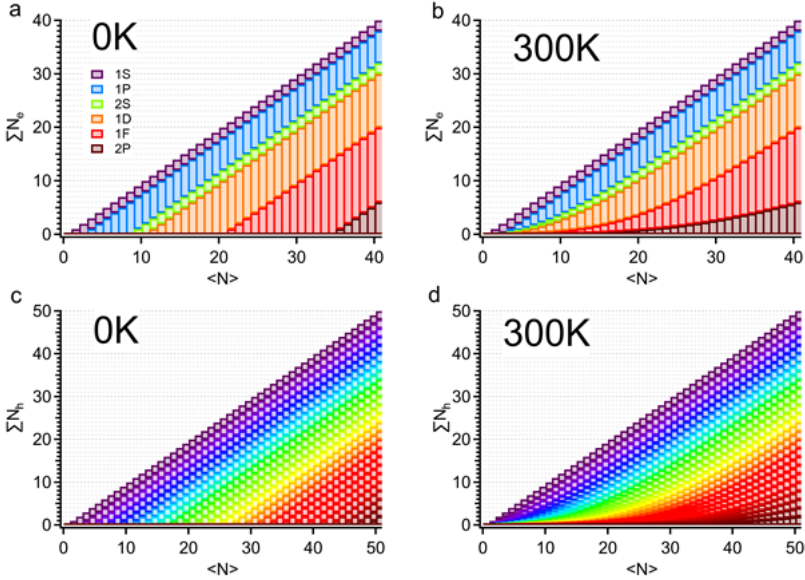


Figure 4.9: State-filling for all levels, for sample A with a small core. The respective occupation is shown as a function of the total number of electron-hole pairs. Compared with the sequential state filling calculated at 0 K, at 300 K the higher-energy states become occupied before full occupancy of lower-lying states is reached. (a)-(b) Case of electrons, (c)-(d) case of holes. Note the larger number of hole states included in the calculations compared to the number of electron states.

due to thermal occupancy of holes in excited states. In particular, transitions associated with the lowest $1S_{3/2}$ hole state, for sample B around 650 nm, see an increase of the threshold due to a relative depletion of the hole state induced by thermal redistribution of holes over different states, while the states at slightly shorter wavelength see a strong decrease of the threshold by thermal filling of the associated hole states, leading to a more efficient population inversion for these transitions than expected from pure sequential state filling. While we acknowledge that absolute values of the calculated threshold still remain about a factor of two higher than experimental data, the gradual increase of the gain threshold toward shorter wavelength is in line with the experimental observations. Hence,

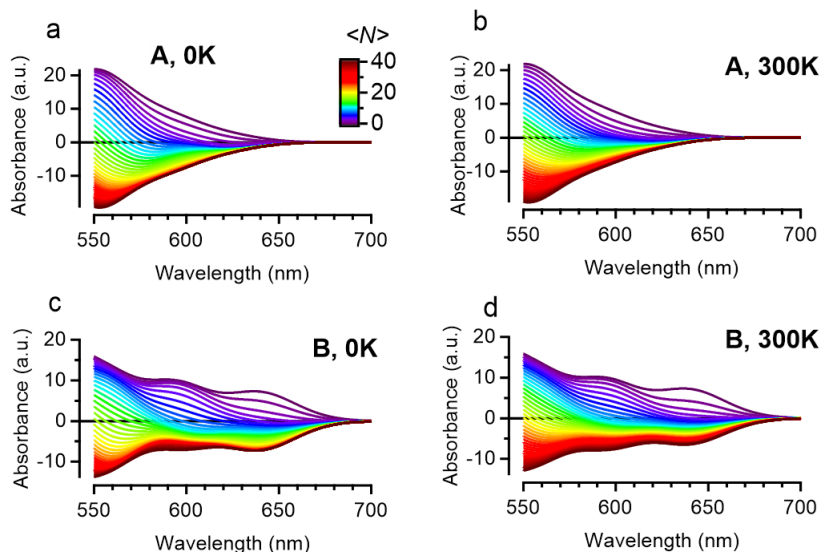


Figure 4.10: a) Calculated nonlinear absorption spectrum for sample B as a function of number of excitons, by assigning to each transition a Gaussian line width of 75 nm. Each transition is then assigned a value (oscillator strength) of +1 when it is empty, scaling down to -1 when it is fully occupied. The distribution of electrons and holes over the different energy levels is done as before for the discrete energy levels (cfr. above). The gain threshold is then determined for each wavelength as the number of excitons for which the spectrum transgresses from absorption (positive absorbance) to gain (negative absorbance). b) Same data for sample A.

at a small cost of increasing the gain threshold at the band edge, where hole states are depleted by thermal excitation, we can strongly reduce the gain threshold at higher energies by taking advantage of the same thermal excitation of holes into higher-excited states. Sample A shows similar behaviour. Second, as we also know that the nanocrystal ensemble exhibits absorption features that are broadened at room temperature, also the influence of line broadening was assessed. To do so, a line width of 75 meV was assigned to each transition, in accordance with the line width of the emission peak (Figure B.1). Following the approach of Bisschop et al¹ based on the occupation of the electron and hole levels, an amplitude

can be assigned to the transition (i.e. completely empty levels yield and amplitude of +1, completely filled levels yield -1). Summing up all these Gaussians yields a nonlinear absorption spectrum that depends on the number of excitons in the system $\langle N \rangle$ (see also Figure 4.10). We then derived the gain threshold spectrum by determining, for each wavelength, the number of excitons for which the spectra pass from absorption into gain. The results are shown in Figure 4.7e (sample B) and Figure 4.7f (sample A), respectively. Interestingly, line broadening leads to a further smoothening of the gain threshold spectra, here already observed at relatively lower temperature compared to the calculation using discrete energy levels. While further work remains to be done to carefully disentangle both effects, we conclude that thermal occupation of holes should not be neglected when analyzing gain in colloidal nanocrystals, yet homo- and/or heterogeneous line broadening of the transitions can to a certain extent mask its effect.

4.6 Conclusions

Combined experimental and computational work has revealed that thermal occupation of excited hole states in CdSe/CdS giant-shell nanocrystals with a large core has a profound effect on both the excited-state bleach dynamics and the gain thresholds. The $k \cdot p$ calculations demonstrate that due to reduced quantum confinement in such CdSe/CdS nanocrystals, a large number of hole states is thermally accessible at room temperature, leading to long-lived bleach features in the transient absorption spectra. At the same time, the thermal occupation of these states, together with a sufficiently long band edge gain lifetime approaching the nanosecond regime, yields a continuous, broadband gain spectrum up to 200 nm wide, spanning the entire spectral region between the CdSe and the CdS band edge. The gain threshold for the associated transitions, assigned again via $k \cdot p$ calculations, increases gradually with decreasing wavelength. This was confirmed by independently converting the gain lifetime into a gain threshold, assuming that the gain lifetime is limited by Auger recombination, and modeled by taking thermal occupancy of hole states into account in a state-filling model for the gain. Our results show that relaxing quantum confinement and therefore reducing the energetic spacing between the different hole states can lead to low-threshold broadband gain, and underline the role that temperature plays in such photophysics. The generality of the approach implies that it can be readily extended to future understanding of gain dynamics in similar colloidal nanocrystal systems, based for instance on III-V or perovskite semiconductors.

Gain in these materials has decent values in terms of intrinsic gain, lifetime and threshold. We suggest here that the gain first develops in the shell, the carriers relax to the band edge of the core, going from green shell gain to red core gain. An alternative way of looking at this system is by considering the shell to be the gain medium of choice: a bulk semiconductor (the shell), with a trap in the center (core), “destroying” the optical gain, because the holes get localised in the core. Seeing already optical gain in the TA, and ASE in previous work¹⁸ toward the green part

of the spectrum, while having such a big “trap state” in the nanocrystal, begs for further investigation: what if we now get rid of this trap state, by exchanging it to a wz-CdS core, essentially ending up with a huge CdS nanocrystal. What would the gain in such a system be like? Are the physics behind such systems dramatically different than quantum confined systems? Are they actually useful at all? These questions are tackled in the next Chapter, where exactly these types of materials are studied: core only, bulk CdS nanocrystals.

Bibliography

- ¹ S. Bisschop, P. Geiregat, T. Aubert, and Z. Hens. The Impact of Core/Shell Sizes on the Optical Gain Characteristics of CdSe/CdS Quantum Dots. *ACS Nano*, 12:9011–9021, 2018.
- ² Francesco Di Stasio, Anatolii Polovitsyn, Ilaria Angeloni, Iwan Moreels, and Roman Krahne. Broadband amplified spontaneous emission and random lasing from wurtzite cdse/cds "giant-shell" nanocrystals. *Acs Photonics*, 3(11):2083–2088, 2016.
- ³ Christopher Melnychuk and Philippe Guyot-Sionnest. Multicarrier dynamics in quantum dots. *Chemical Reviews*, 121(4):2325–2372, 2021.
- ⁴ Rolf Koole, Guy Allan, Christophe Delerue, Andries Meijerink, Daniël Vanmaekelbergh, and Arjan J Houtepen. Optical investigation of quantum confinement in pbse nanocrystals at different points in the brillouin zone. *Small*, 4(1):127–133, 2008.
- ⁵ SL Chuang and CS Chang. kp method for strained wurtzite semiconductors. *Physical Review B*, 54(4):2491, 1996.
- ⁶ Josep Planelles, F Rajadell, and Juan I Climente. Hole band mixing in cds and cdse quantum dots and quantum rods. *The Journal of Physical Chemistry C*, 114(18):8337–8342, 2010.
- ⁷ Carlos Segarra, Juan I Climente, Anatolii Polovitsyn, Fernando Rajadell, Iwan Moreels, and Josep Planelles. Piezoelectric control of the exciton wave function in colloidal cdse/cds nanocrystals. *The Journal of Physical Chemistry Letters*, 7(12):2182–2188, 2016.
- ⁸ Maria Grazia Lupo, Fabio Della Sala, Luigi Carbone, Margherita Zavelani-Rossi, Angela Fiore, Larry Luer, Dario Polli, Roberto Cingolani, Liberato Manna, and Guglielmo Lanzani. Ultrafast electron-hole dynamics in core/shell cdse/cds dot/rod nanocrystals. *Nano letters*, 8(12):4582–4587, 2008.

-
- ⁹ Alexander W Achtstein, Anatol V Prudnikau, Maxim V Ermolenko, Leonid I Gurinovich, Sergey V Gaponenko, Ulrike Woggon, Alexander V Baranov, Mikhail Yu Leonov, Ivan D Rukhlenko, Anatoly V Fedorov, et al. Electroabsorption by 0d, 1d, and 2d nanocrystals: A comparative study of cdse colloidal quantum dots, nanorods, and nanoplatelets. *ACS nano*, 8(8):7678–7686, 2014.
- ¹⁰ Gianluca Grimaldi, Jaco J Geuchies, Ward Van Der Stam, Indy Du Fossé, Baldur Brynjarsson, Nicholas Kirkwood, Sachin Kinge, Laurens DA Siebbeles, and Arjan J Houtepen. Spectroscopic evidence for the contribution of holes to the bleach of cd-chalcogenide quantum dots. *Nano letters*, 19(5):3002–3010, 2019.
- ¹¹ S Christodoulou, G Vaccaro, V Pinchetti, F De Donato, JQ Grim, A Casu, A Genovese, G Vicidomini, A Diaspro, S Brovelli, et al. Synthesis of highly luminescent wurtzite cdse/cds giant-shell nanocrystals using a fast continuous injection route. *Journal of Materials Chemistry C*, 2(17):3439–3447, 2014.
- ¹² Wan Ki Bae, Lazaro A Padilha, Young-Shin Park, Hunter McDaniel, Istvan Robel, Jeffrey M Pietryga, and Victor I Klimov. Controlled alloying of the core–shell interface in cdse/cds quantum dots for suppression of auger recombination. *ACS nano*, 7(4):3411–3419, 2013.
- ¹³ Young-Shin Park, Jaehoon Lim, Nikolay S Makarov, and Victor I Klimov. Effect of interfacial alloying versus ”volume scaling” on auger recombination in compositionally graded semiconductor quantum dots. *Nano letters*, 17(9):5607–5613, 2017.
- ¹⁴ István Robel, Ryan Gresback, Uwe Kortshagen, Richard D Schaller, and Victor I Klimov. Universal size-dependent trend in auger recombination in direct-gap and indirect-gap semiconductor nanocrystals. *Physical review letters*, 102(17):177404, 2009.
- ¹⁵ JI Climente, JL Movilla, and J Planelles. Effect of interface alloying and band-alignment on the auger recombination of heteronanocrystals. *Journal of Applied Physics*, 111(4):043509, 2012.

- ¹⁶ John P Philbin and Eran Rabani. Electron–hole correlations govern auger recombination in nanostructures. *Nano Letters*, 18(12):7889–7895, 2018.
- ¹⁷ John P Philbin and Eran Rabani. Auger recombination lifetime scaling for type i and quasi-type ii core/shell quantum dots. *The journal of physical chemistry letters*, 11(13):5132–5138, 2020.
- ¹⁸ Francesco Di Stasio, Anatolii Polovitsyn, Ilaria Angeloni, Iwan Moreels, and Roman Krahné. Broadband amplified spontaneous emission and random lasing from wurtzite CdSe/CdS ”giant-shell” nanocrystals. *ACS Photonics*, 3(11):2083–2088, 2016.

Chapter 5

Bulk CdS Colloidal Nanocrystals

5.1 Introduction

As discussed in Chapter 2, colloidal NCs for optical gain have been studied since the year 2000. Since then, a plethora of materials with various geometries and levels of have been added to the library of colloidal nanocrystals that show optical gain, ever improving the gain metrics with respect to gain magnitude (g_i), lifetime τ_G and threshold n_{th} . Ranging from CdSe/CdS core/shell QDs¹, dot-in-rods², and CdSe Quantum Wells³. At this point, the oldest system, that of CdSe/CdS core/shell QDs are still ahead in the race in terms of closest to a functional, room-temperature operated, electrically injected laser. However, these QDs are engineered in such a complex way that there is not any more room for improvement on the QD level. Other materials always seem to fall into the same trap: for stability and increased lifetimes (suppressed Auger), gain magnitude must be sacrificed. Optimisation always leads to longer lifetimes and lower threshold, but also lower gain magnitude, not completing our gain trifecta of parameters.

In this Chapter, an alternative material system is presented: weakly confined bulk NCs (8-12 nm diameter), applied to CdS. Although perhaps surprising, considering the tendency of the field to go toward confinement, we present here that the lack thereof actually becomes advantageous for optical gain. We present a full description of the material starting from synthesis, but with a heavy focus on the non-linear photo-physics through Transient Absorption Spectroscopy. The results show a remarkable gain metric combination, providing record high material gain values up to 50.000 cm^{-1} and a 3 ns gain lifetime limited by a radiative recombination process. Combined with a sub-unity gain thresholds, equivalent to $2 \cdot 10^{18} \text{ cm}^{-3}$, this gain trifecta outcompetes all known inorganic colloidal materials. Next, we show that this combination of groundbreaking optical gain metrics can be understood, and quantitatively modelled, using a framework of bulk semiconductor physics, yet only by including a strong band gap renormalization of up to 84 meV. Such highly desired redshifts outpace known shifts in quantum confined QDs with an order of magnitude. Opposed to these well-studied confined systems, where the redshift is a result from unbalanced attractions/repulsions of multi-excitons, in our bulk-like NCs these renormalizations originate from electrostatic screening effects. Such photo-physics was hereto unobserved in solution processable nanomaterials.

These samples were synthesized by Margarita Samoli and Ali Khan, where I performed TA measurements and created the model to explain the physics governing the optical gain. The Ultrafast PL measurements were done by Isabella Wagner.

5.2 Material Description

Differently sized wurtzite (wz) CdS NCs were synthesized using a continuous injection procedure in the range from 8 to 12 nm and characterized accordingly, see below. In what follows, we focus on the 12.0 nm NCs, unless mentioned otherwise. In Figure 5.1a, the absorption spectrum is shown together with the photoluminescence spectrum. The absorption spectrum A_0 is normalized to represent the intrinsic absorption coefficient $\mu_{i,0}(\lambda)$.⁴ The inset shows a tauc fit to determine the bandgap. Figure 5.1b shows the wz-CdS sizing curve together with our samples.⁵ Beyond the Bohr diameter of *ca.* 6 nm⁶, we observe a flat dispersion leveling off at the bulk gap (517 nm), indicating that our particles are bulk-like and at best subject to weak confinement. The inset shows a transmission electron microscopy (TEM) image of the mono-disperse particles with 12.0 \pm 2 nm average size. Figure 5.1c shows the PL decay fitted to a triple exponential decay. The fastest component, which we assign to a non-radiative trapping process, has a decay rate $k_1 = 0.33 \text{ ns}^{-1}$ ($\tau_1 = 3.0 \text{ ns}$)⁷. While a triple exponential fitting seems a lot to explain a decay over two decades, adding a third exponential was crucial to explain the full decay behaviour. This added longer component has only a slight impact on the shortest component, which is the one of interest in this study. The uncertainties on the fitting parameters gives confidence that the fit is robust.

$$y = y_0 + A_1 \times e^{-k_1 \cdot (t-t_0)} + A_2 \times e^{-k_2 \cdot (t-t_0)} + A_3 \times e^{-k_3 \cdot (t-t_0)} \quad (5.2.1)$$

	A (a.u.)	$\sigma(\mathbf{A})$	k (ns ⁻¹)	$\sigma(\mathbf{k})$	τ (ns)
Exp 1	1.04488	0.00527	0.33	0.00751	3
Exp 2	0.11541	0.00364	0.023593	0.00166	42.4
Exp 3	0.046793	0.0014	0.0034558	0.000156	289.3

Table 5.1: PL lifetimes fits

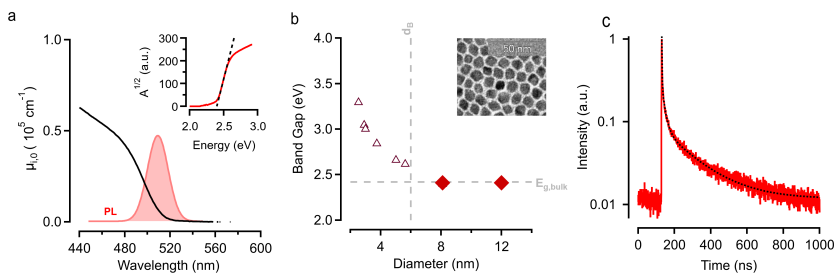


Figure 5.1: (a) Linear absorption (black), represented as the intrinsic absorption coefficient $\mu_{i,0}$, and the spontaneous photoluminescence (PL) after 400 nm excitation. The inset shows a tauc fit to determine the bandgap. (b) Sizing curve of wz-CdS (empty triangles) from Maes *et al.* combined with the band gap energy/size pairs (red diamonds) for our bulk-like CdS NCs.⁵ The vertical dashed line indicates the Bohr diameter (5.6 nm) and the horizontal dashed line shows the bulk band gap of wz-CdS (2.398 eV; 517 nm). Inset shows a transmission electron microscope (TEM) image of the 12.0 ± 2 nm wurtzite (wz) CdS NCs. (c) The PL lifetime, with a triple exponential fit.

5.2.1 Synthesis

5.2.1.1 Materials and Precursors

Cadmium oxide (CdO, 99.999%), sulfur powder (S, 99%), and trioctylphosphine (TOP, 97%) were purchased from Strem Chemicals. 1-octadecene (ODE, 90%) and oleic acid (OA, 90%) were purchased from Sigma Aldrich and used as-received without further purification. A Cadmium-oleate (0.5 M) solution is prepared as follows. 0.642 g CdO powder (5 mmol), 5 mL of oleic acid and 5 mL of ODE were added into a 25 mL three-necked flask. The mixture was then heated up to 120°C under vacuum and kept there for 30 minutes. Next the flask was heated to 300°C under N₂ flow and kept for 5 min at that temperature. A transparent product forms, that is then cooled to 120°C and kept under vacuum for 30 minutes to remove the water. Thereafter the obtained cadmium oleate solution (0.5 M) was cooled to room temperature and stored in N₂ atmosphere. A TOPS (0.5 M) solution is prepared as follows. 2.5 mL of ODE and 2.5 mL of TOP were added to S powder (0.080 g; 2.5 mmol) and the solution was stirred at 120°C for 30 minutes under N₂ to obtain TOPS.

The stock solutions were stored in a sealed vial under a N₂ atmosphere.

5.2.1.2 Synthesis Protocols

In a 25 mL three necked round bottom flask 8 mL of ODE was loaded and heated to 120°C under vacuum and kept for 30 minutes. Then the flask was filled with N₂ and heated to 300°C. Cadmium oleate solution was mixed with equimolar amount of TOPS solutions and injected to the preheated ODE at the rate 2 mL/hour. The injection time was adjusted in order to synthesize CdS NCs of different sizes. For example, to synthesize 12 nm CdS NCs, 2 mL of cadmium oleate and 2 mL of TOP-S solutions were mixed together and injected in 2 hours. After cooling the flask to room temperature, the CdS NCs were precipitated with 2-propanol and redispersed in toluene. Next, size selective precipitation was used to remove small NCs.

5.2.2 Intrinsic Absorption

To calculate the intrinsic absorbance, we start from the dielectric constants of wurtzite CdS from Adachi *et al.*⁸, for a wavelength of 300 nm. Due to the asymmetric nature of the crystal and the random orientation, we can average out the dielectric constant for electrical fields parallel and perpendicular to the *c*-axis

$$\tilde{\epsilon} = \frac{1}{3} \cdot \underbrace{(6.663 + 3.623i)}_{E \perp c} + \frac{2}{3} \cdot \underbrace{(6.601 + 3.466i)}_{E \parallel c} = 6.6217 + 3.5183i \quad (5.2.2)$$

From which we can calculate the intrinsic absorbance

$$\mu_i = \frac{2\pi}{\lambda n_s} \cdot \text{Im}(\tilde{\epsilon}) \cdot |f_{LF}|^2 \quad (5.2.3)$$

Where n_s the refractive index of the solvent, λ the wavelength at which we calculate the intrinsic absorbance (here we will use 300 nm, as stated above), and $|f_{LF}|^2$ the squared local-field factor, defined as (assuming here spherical particles):

$$f_{LF} = \frac{3 \cdot \tilde{\epsilon}}{\tilde{\epsilon} + 2 \cdot \epsilon_s} \quad (5.2.4)$$

With ϵ_s the dielectric constant for toluene, we find a value for the intrinsic absorbance

$$\mu_i(300 \text{ nm}) = 1.82 \cdot 10^5 \text{ cm}^{-1} \quad (5.2.5)$$

Knowing that at short wavelengths the absorbance spectrum becomes size independent, we can use this value to determine the wavelength-dependent intrinsic absorbance

$$\mu_i(\lambda) = \frac{A_0(\lambda)}{A_0(300 \text{ nm})} \cdot \mu_i(300 \text{ nm}) \quad (5.2.6)$$

5.2.3 Cross-section

From the intrinsic absorbance we can find the absorption cross section σ

$$\sigma(\lambda) = \mu_i(\lambda) \times V_{NC} \quad (5.2.7)$$

Depending on the excitation wavelength, it is necessary to correct the cross-section. This is only necessary if there is a significant change in absorption at the excitation wavelength: the higher in energy the less this correction will do. For example, later TA data with an excitation at 485 nm is shown, here this correction is necessary.

$$\sigma'(\lambda) = \sigma(\lambda) \times \left(1 + \frac{A(\lambda) - A_0(\lambda)}{A_0(\lambda)} \right) \quad (5.2.8)$$

The 485 nm excitation measurement shows corrections of more than 10% on the fluence.

5.2.4 Structural Characterisation

TEM images with their corresponding histograms are shown in Figure 5.2. X-Ray Diffraction (XRD) is also shown, with clear indication of the wurtzite structure of the discussed particles.

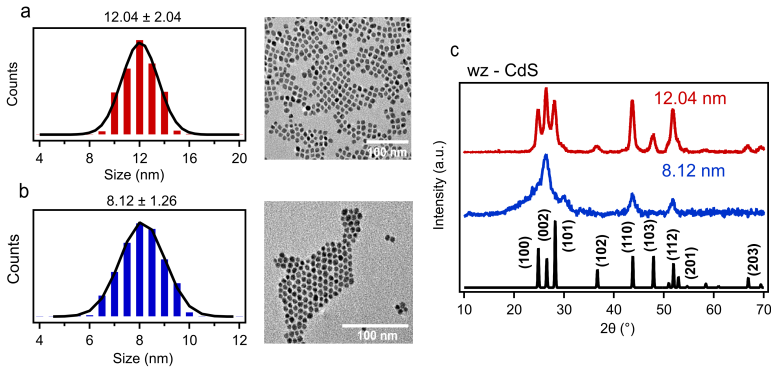


Figure 5.2: TEM of the 12.0 nm (a) and 8.1 nm (b) nanocrystals. XRD is shown in (c), showing wurtzite phase.

5.3 Gain Measurements in gCdS

We have performed TA measurements by using 485 nm excitation and 400 nm excitation, to look into the difference between off-resonant (400 nm) and more or less resonant excitation (485 nm).

Figure 5.3a shows a 2D map of g_i measured on 12.0 nm CdS NCs, here limited to $g_i > 0$, for photo-excitation at 400 nm creating $n = 5.3 \cdot 10^{19} \text{ cm}^{-3}$. Shown together with the linear coefficient $\mu_{i,0}$, it becomes clear that the material gain in CdS shows a combination of remarkable features. For this pair density, g_i extends from 460 nm to close 560 nm, extending on the long wavelength side far beyond the range of the linear absorption which drops to zero beyond the bulk band gap (517 nm). Moreover, g_i remains positive for a timespan close to the limit of our experiment, *i.e.* 3 ns. The gain magnitude is also very large compared to the intrinsic absorption at corresponding wavelengths, a point we will come back to further. Fluence dependent g_i maps contain all the information we need to analyze the gain trifacta, but are complex to understand. Therefore, we proceed to slice the data accordingly to obtain spectra (Figures 5.3b,c)

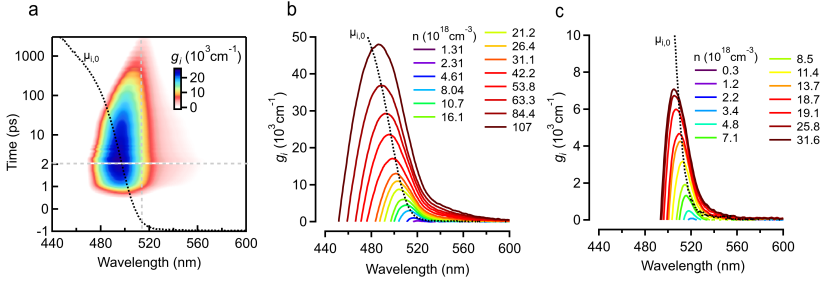


Figure 5.3: (a) False color map of the material gain $g_i(\lambda, t) > 0$ after photo-excitation with 400 nm creating a carrier density $n = 5.38 \cdot 10^{19} \text{ cm}^{-3}$. The dotted black line indicates the linear intrinsic absorption spectrum. (b) Material gain g_i at 3 ps time delay for pumping at 400 nm and (c) 485 nm, for increasing carrier density n .

and dynamics (Figure 5.4) for increasing carrier densities n .

In Figure 5.3b, g_i spectra at 3 ps after increasing photo-excitation with 400 nm are shown. A net gain window opens up near the band gap at $n \approx 10^{18} \text{ cm}^{-3}$, only to increase, without any signs of saturation, to nearly 50.000 cm^{-1} at shorter wavelengths. The gain simultaneously also red-shifts away from the linear absorption, showing net stimulated emission at wavelengths where there is no linear absorption, being from 520 nm to 600 nm. Such gain coefficients outpace 0D systems ($< 3000 \text{ cm}^{-1}$)¹, leaving only CdSe nanoplatelets as closest second ($< 20.000 \text{ cm}^{-1}$)⁹. Figure 5.3c shows g_i spectra, again at 3 ps, yet after 485 nm pumping. Again a gain window opens when the density increases above *ca.* $3 \cdot 10^{18} \text{ cm}^{-3}$, eventually stretching over a range from 490 nm to 560 nm. The gain does saturate across the entire spectrum, most likely due to a bleaching absorption cross section at the pump wavelength, peaking at 7000 cm^{-1} and thereby still outcompeting any known 0D QD material.

Figure 5.4 shows the dynamics of the material gain at the band gap after 400 nm (Figure 5.4a) and 485 nm (Figure 5.4b), excitation. We observe persisting gain ($g_i > 0$) up to 2.9 ns both for resonant (485 nm) and hot (400 nm) excitation. We define this time window as the gain lifetime $\tau_G = 2.9 \text{ ns}$. This multi-nanosecond lifetime matches state-of-art

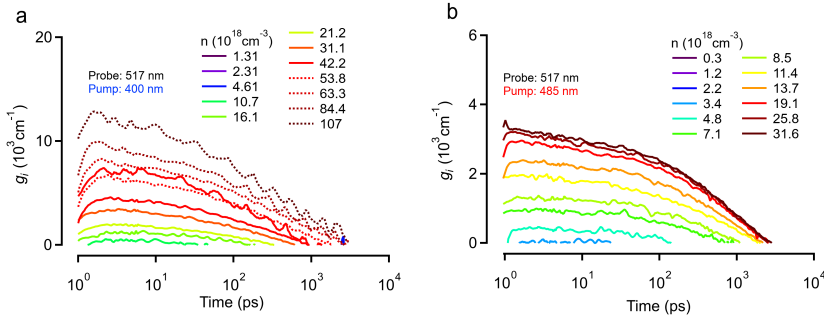


Figure 5.4: Dynamics of the material gain $g_i(t)$ at the band gap (517 nm) after photo-excitation with (a) 400 nm and (b) 485 nm, for similar carrier densities as Figure 5.3b,c. A consistent gain lifetime of 3 ns is found.

lifetimes observed in alloyed shell CdSe/CdS¹⁰ or surface quantum well systems¹¹, both made using more complex synthetic procedures.

A similar analysis is done on the 8.1 nm CdS sample, see Figure 5.5. The same bandgap of around 2.4 eV is found, and very similar gain properties (with excitation at 400 nm) as shown in Figure 5.5. We see comparable lifetimes and thresholds (Figure 5.5b,c), however there seems to be quite a difference in gain magnitude, where the bigger sample shows up to five times higher magnitude for similar power densities. This can be related to an older, less optimized synthesis protocol which leads to higher trapping. This is supported by the QY, which is lower in this particular sample (about 1%) compared to the bigger NCs (where typically 5-10% is found). In principle, there should be no difference regarding gain since both samples exceed the Bohr diameter.

These disruptive optical gain parameters show no signs of saturation in the hereto difficult blue-green spectral region for colloidal gain materials. Record gain magnitudes ($> 50.000 \text{ cm}^{-1}$), multi-nanosecond gain lifetimes capped by radiative processes and low gain thresholds ($< 10 \text{ } \mu\text{J}/\text{cm}^2$) are obtained in concert for the first time.

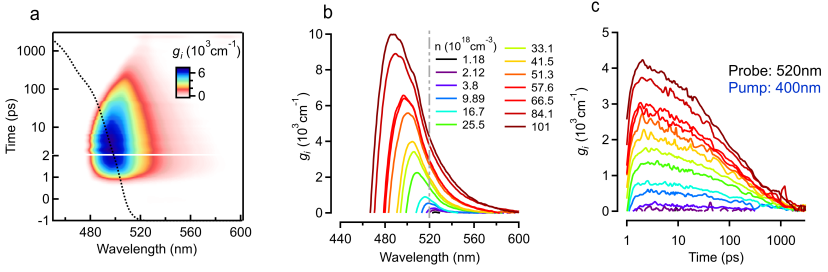


Figure 5.5: TA measurements of the 8.1 nm CdS NC sample. The false color map in Figure (a) is taken at $n = 5.13 \cdot 10^{19} \text{ cm}^{-3}$.

5.4 Modelling of the Material

The remarkable gain metrics raise an intriguing question: how can these parameters be explained? Due to the large diameter, we opted to try modelling the material using bulk semiconductor physics, where strong confinement is no longer present.

5.4.1 Bulk Gain Model

Bulk optical gain is mediated by classical state-filling of continuous energy bands, which in turn is dictated by Fermi-Dirac statistics defined by a carrier temperature T and density n . Any spectral shifts occur through a mechanism of band gap renormalization, a point we will discuss further below. In what follows, we assume that the band structure of CdS can be described by a single valence and a single conduction band, be it with different curvature, see Figure 5.7a. As was already discussed in Chapter 2, we can model our material with bulk semiconductor gain using Equation 2.4.16:

$$g_i(E) = \mu_{i,0}(E, T) \times [f_c(E, E_{F,e}, T) - f_v(E, E_{F,h}, T)] \quad (5.4.1)$$

State filling after strong excitation will lead to a population inversion

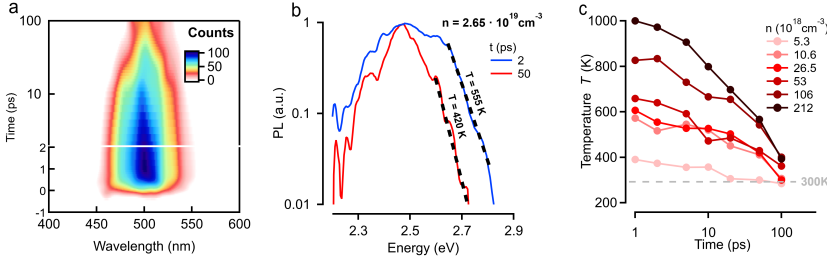


Figure 5.6: (a) 2D time-wavelength map of transient PL after photo-excitation with 400 nm. (b) Example of slices for two different pump-probe delays, where the fit using Equation 5.4.2 is used. (c) Carrier temperature T for different time delays and select carrier densities

where $f_v < f_c$ at a given energy E . Since we know n from the experimental conditions, only the carrier temperature T remains an adjustable parameter for now. However, T can also be extracted from transient optical experiments. Here, we propose to use femtosecond photoluminescence spectroscopy (PL)¹², which was explained in Chapter 2. One can directly obtain T from fitting PL spectra to:¹³

$$PL(E) \propto \sqrt{E - E_g} \times e^{-\frac{E - E_g}{k_B T}} \quad (5.4.2)$$

This will be discussed in much more detail in Chapter 6. Figure 5.6a shows a 2D map of the PL for photo-excitation at 400 nm creating $n = 2.65 \cdot 10^{19} \text{ cm}^{-3}$. Taking horizontal slices at certain times (Figure 5.6b), we can extract PL spectral shapes and fit Equation 5.4.2 to obtain T as function of time at varying pump power, see Figure 5.6c. The observation of pro-longed overheating of the carrier gas is in line with several other reports on phonon bottlenecks in polar semiconductors.^{3,14–16} With the experimental input for both n and T , we can in principle model the full gain spectrum using Equation 2.4.16. Figure 5.7b shows the result of such a prediction for a scenario after 485 nm excitation, grey dashed line, in comparison to the experimental spectrum (solid red line). The model reproduces the experimental shape but misses the low energy gain and,

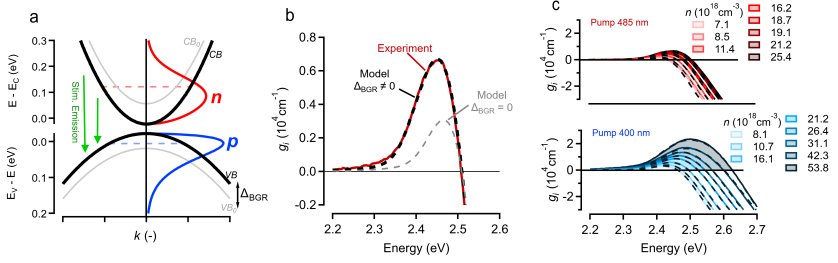


Figure 5.7: (a) Quantitative Bulk Gain Model (a) A single valence band and conduction band (black) are shown, together with the calculated electron (red, n) and hole (blue, p) densities. Green arrows indicate radiative recombination through spontaneous or stimulated emission. (b) Material gain spectrum with (dashed grey) $n = 1.79 \cdot 10^{19} \text{ cm}^{-3}$ and $T = 440 \text{ K}$ without band gap renormalization (BGR). Dashed black line adds a BGR of 45 meV. Solid red line indicates experimental data. (c) Excellent correspondence is found between experiment (solid) and model (dashed) using only Δ_{BGR} as freely adjustable parameter for both (top) 485 nm and (bottom) 400 nm pump.

more importantly, severely underestimates the peak value. To improve the model, we proceed to include a spectral shift, which in the context of bulk semiconductors is often referred to as a band gap renormalization (BGR), here labeled Δ_{BGR} :

$$g_i(E, n, T) = \mu_{i,0}(E - \Delta_{BGR}) \cdot (f_c(E, n, T) - f_v(E, n, T)) \quad (5.4.3)$$

Using $\Delta_{BGR} = 45 \text{ meV}$, the dashed black line in Figure 5.7b shows a perfect match with the experimental gain spectrum on all fronts. In fact, using Δ_{BGR} as the only freely adjustable parameter, we can quantitatively reproduce all the g_i spectra both for 400 nm (Figure 5.7c, top) and 485 nm (Figure 5.7c, bottom).

This procedure is done for multiple pump powers, always at the pump-probe delay of 3 ps, to assure that the carriers have decayed to the band edge. The results are shown in Table 5.2 and Figure 5.8. From Figure 5.8 it can be seen that the used carrier density value for the fit is consistently

p400			p485		
$n(10^{18} \text{ cm}^{-3})$	T(K)	$\Delta_{BGR}(\text{meV})$	$n(10^{18} \text{ cm}^{-3})$	T(K)	$\Delta_{BGR}(\text{meV})$
16.2	400	40	9.6	330	26
18	410	40	12.1	360	32
22.4	440	47	15.5	380	39
28.2	470	52	18.6	400	43
33	500	55	20	410	45
37.5	500	60	22.1	430	45
45.7	550	60	23.1	440	45
50.3	460	70	23.9	440	45

Table 5.2: Bulk gain fit results.

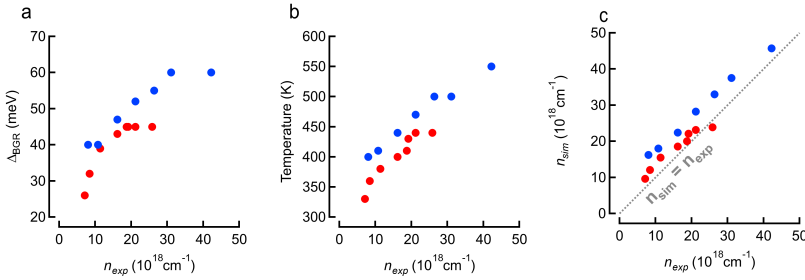


Figure 5.8: The fit parameters used to achieve the fits in Figure 5.7c. They are also displayed in Table 5.2.

higher compared to the experimentally measured value, possibly pointing to an inaccuracy in the power measurement.

5.4.1.1 Band Gap Renormalisation

Clearly, the BGR is the main driver for the remarkable gain magnitudes observed. The concept of a shrinking band gap under strong photo-excitation is not so very different from the observed bi-exciton shifts in confined QDs in terms of spectral imprint, *i.e.* an energy shift of the excited state absorption spectrum^{1,17}, yet the origins are quite different.

Where in confined systems exciton-exciton interactions are dictated by repulsions and attractions between negative and positive charges^{17,18}, the nature of the bulk BGR effect is found mainly in a self-energy correction due to increased screening of charges in the plasma state formed at high carrier density.¹⁹ To the best of our knowledge, the latter has not been observed yet in solution processable nano-materials, yet it clearly proves to be of extreme value. Indeed, the BGR pushes the window of stimulated emission away from the linear absorption, effectively shifting the large oscillator strength of high energy transition towards the band gap. Such spectral redshifting was shown to be beneficial already for strongly confined CdSe/CdS QDs, yet the largest shifts observed here (84 meV) exceed typical bi-exciton red-shifts (1 - 5 meV) observed confined systems by an order of magnitude.^{1,20} Following the works of Trankle²¹ and Dneprovskii¹⁹, the band gap renormalization in 3D systems can be written down as:

$$\frac{\Delta_{BGR}}{R_X} = \left(\frac{n}{n_M(T)} \right)^{1/2} - 2 = \alpha^{-1/2} \left(\frac{n}{T} \right)^{1/2} - 2 \quad (5.4.4)$$

where $R_X = 28$ meV is the bulk exciton binding energy of wz-CdS²², and n_M is the Mott density which is given in the classical limit as:¹⁹

$$n_M = \alpha T = 0.028 \times \epsilon_{CdS} \times \frac{k_B T}{R_X a_B^3} \quad (5.4.5)$$

where T is the temperature in K, $\epsilon_{CdS} = 8.6$ is the static dielectric constant of wz-CdS, and $a_B = 5.8$ nm is the Bohr radius. The proportionality constant α amounts to $3.7 \cdot 10^{15} \text{ cm}^{-3} \text{ K}^{-1}$.

Figure 5.9a shows the theoretical prediction together with the experimental values obtained from best fits to the gain spectra. A good correspondence across the entire density range is found for both pump scenarios, indicating that our bulk approximation extended with BGR effects provides a suitable quantitative framework to understand the remarkable gain bandwidth, shape and magnitude.

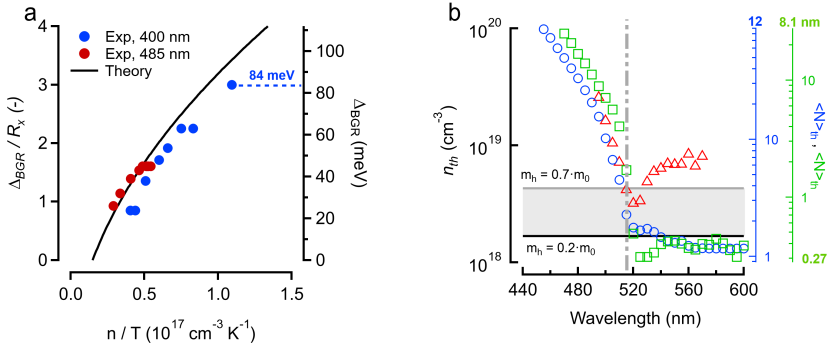


Figure 5.9: (a) Obtained Δ_{BGR} values, both absolute (right axis) and normalized to the bulk exciton binding energy of wz-CdS $R_X = 28$ meV (left axis), from full spectrum fits for increasing carrier density in the case of 400 nm (blue markers) and 485 nm (red markers) pumping. Solid black line is a parameter-free theoretical prediction, see main text. The Δ_{BGR} reaches a value of 84 meV without clear signs of saturation. (b) Minimum carrier density required to reach transparency $g_i = 0$, called the threshold density n_{th} , as function of wavelength for pumping at 485 nm (red markers) and 400 nm (blue markers), for the 12.0 nm NCs. Green markers show the result for the 8.1 nm NCs. Vertical axes on the right indicate the same densities reported as absolute number of electron-hole pairs $\langle N \rangle$ per NC. Horizontal lines indicate the theoretically predicted threshold range using heavy and light-hole effective masses $m_{LH,HH}$.

Gain Threshold Given the excellent match of bulk modeling for the g_i spectra, we now focus on understanding the threshold in a similar framework. Looking back at Figures 5.3b,c, the threshold density n_{th} required to achieve transparency ($g_i = 0$) depends strongly on the probe wavelength. Figure 5.9b summarizes these findings for the 8.1 and 12 nm NCs, showing that the lowest density required to achieve transparency around the band gap is $3 \cdot 10^{18} \text{ cm}^{-3}$. We observe an increase in the threshold density going towards shorter wavelengths, but at longer wavelengths the 400 nm pump produces a sizably lower gain threshold opposed to the 485 nm case. The lowest value for n_{th} corresponds to $n_{th} = 1.1 \cdot 10^{18} \text{ cm}^{-3}$, equivalent to a single electron-hole pair on average, $\langle N \rangle = 1$, for the 12.0 nm NCs. Remarkably however, as the 8.1 nm NCs show a similar gain threshold density, this implies a lower $\langle N \rangle = 0.27$

absolute number per NC required for optical gain. This number corresponds to a scenario where only 1 out of 3 NCs needs to be excited to reach transparency, a regime denoted earlier in literature as 'single exciton gain' in the context of strongly confined NCs.¹⁷

Within a bulk picture, one can analytically calculate the threshold in the absence of spectral shifts²³

$$n_{fc} \approx 1.5 \times \left(\frac{M}{m_r}\right)^{3/4} \times \left(\frac{2\pi m_r k_B T}{h^2}\right)^{3/2} \quad (5.4.6)$$

Using average effective masses for heavy-holes and electrons ($m_h; m_e$) = (0.7/0.3; 0.19)^{8,24}, the sum mass $M = m_e^* + m_h^*$ and the reduced mass $m_r = 0.15$. We find a good correspondence with the experimental thresholds for both the 8.1 and 12.0 nm NCs, see horizontal lines for varying hole masses in Figure 5.9b. The latter are different in volume by a factor of 3, which confirms that the density is what dictates gain, not the absolute number of carriers per NC. The lower threshold values compared to the bulk model at longer wavelengths are due to the beneficial effect of band gap renormalization. Finally, we should note that the threshold energy flux at 400 nm corresponds to only 9 $\mu\text{J}/\text{cm}^2$, a number which is on par with best results for solution processable materials in the blue-green, such as perovskites and nanoplatelets and various other colloidal gain media in the red part of the spectrum.^{25,26}

5.4.2 Second order recombination

To understand the final unique gain metric of CdS NCs, being the long multi-nanosecond gain lifetime, we have to focus on the limiting recombination dynamics of the charge carriers themselves. Again using the notion of bulk photo-physics, these dynamics can be described using the generic rate equation:

$$-\frac{dn}{dt} = k_1 n + k_2 n^2 + k_3 n^3 \approx k_1 n + k_2 n^2 \quad (5.4.7)$$

where the rates k_i each relate to a specific physical process. In the bulk approximation, k_1 refers to a linear charge trapping mechanism. The

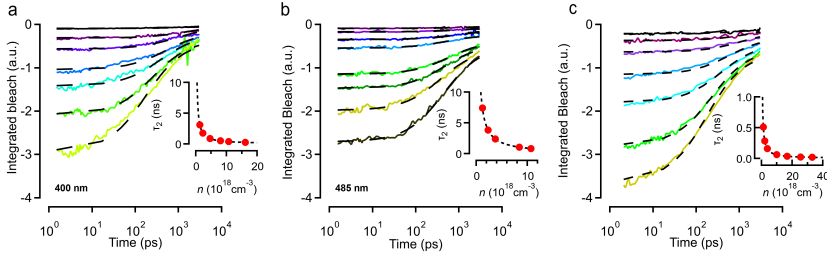


Figure 5.10: Recombination dynamics of charge carriers in CdS NCs tracked by the integrated bleach around the band gap region (420 nm - 600 nm, colored traces) for the 12.0 nm sample (a) 400 nm and (b) 485 nm, and for the 8.1 nm sample (c). Global fits using a mixed first and second order recombination model are indicated by dashed black lines. The insets show the predicted two-body lifetime $\tau_2 = 1/k_2 n_0$, where n_0 is the initial charge density and k_2 is the second order recombination constant from the global fit.

second order recombination constant k_2 relates to a radiative electron-hole pair recombination event $R \propto n \times p = n^2 = p^2$. One can assign a lifetime to the two-body recombination process using the initial carrier density n_0 : $\tau_2 = \frac{1}{k_2 n_0}$, which is of course density dependent. Finally, k_3 relates to non-radiative Auger recombination, which is a three-particle process. The lifetime associated with Auger processes can be written as $\tau_{Auger} = \frac{1}{k_3 n^2}$.²⁷ Fitting the full rate equation is tedious as no analytical solution is available, but we can make the following assumptions. We assume that trapping is fluence independent and fix $k_1 = 0.33 \text{ ns}^{-1}$ in the fit to the value obtained from the PL lifetime fit, see Figure 5.1c. At the carrier densities of $10^{18} - 10^{20} \text{ cm}^{-3}$ used in this work, the Auger timescale in bulk CdS is expected to be 0.1 to 1 microsecond based on $k_{3,bulk} = 10^{-30} \text{ cm}^6 \text{ s}^{-1}$.²⁷ This is far slower than our time-window and we can assume that Auger processes are in fact inefficient for these particle sizes. This allows us to ignore the cubic term in Equation 5.4.7, which leaves us with a mixed first and second order process, for which an analytical solution exists:

$$n(t) = \frac{k_1 n_0}{e^{k_1 t} (k_2 n_0 + k_1) - k_2 n_0} \quad (5.4.8)$$

To avoid the influence of spectral shifts and to capture all charges, including those in higher energy states, we integrate the bleach data from 420 to 600 nm, which results in a series of time-dependent integrated bleach curves plotted for both 400 nm and 485 nm pumping in Figure 5.10a,b. Fitting these traces using a global fit procedure, where n_0 and k_1 are known, we obtain the dashed lines in Figures Figure 5.10a,b which clearly provide a good description of carrier recombination. The global fit produces $k_{2,400} = 2.44 \cdot 10^{-10} \text{ cm}^3\text{s}^{-1}$ and $k_{2,485} = 1.13 \cdot 10^{-10} \text{ cm}^3\text{s}^{-1}$. The same can be done for the 8.1 nm sample, shown in Figure 5.10c, which yields $k_{2,400} = 1.96 \cdot 10^{-10} \text{ cm}^3\text{s}^{-1}$, comparable to the 12.0 nm NCs. Using the fact that the k_2 process is the limiting factor for sustaining net optical gain, we can estimate the gain lifetime τ_G as the time it takes to annihilate n_{thr} , as determined above, for example at 485 nm:

$$\tau_{G,485} = \frac{1}{k_{2,485} n_{th}} = 2.9 \text{ ns} \quad (5.4.9)$$

After this timescale, the density is annihilated to the level of a single excitation. For such a scenario, we know that the cap is coincidentally also set at 3 ns by the non-radiative decay k_1 . As such, our gain lifetime is capped by a radiative electron-hole recombination, not by fast Auger, as in strongly confined systems. When considering high density operation, such as in lasers or high brightness LEDs, the fact that carrier recombination is dictated by a radiative loss channel is intrinsically different from confined QD technology where Auger recombination limits the light output.

5.5 Conclusions

Our results present a paradigm shift in the quest for efficient solution processable inorganic gain materials, pointing towards weak confinement as the best regime for realizing efficient and broadband optical gain. The impressive metrics, combining excellent results for the full gain trirecta, can be explained quantitatively using a bulk physics model with strong band gap renormalization, a hereto unobserved bulk physics phenomenon for solution processable semiconductors.

The large material gain and long gain lifetime will reduce Joule heating in electrically pumped QD laser devices by reducing required layer thickness for net gain, leading to a lower electrical resistance, and by lowering the current densities required for transparency. The disruptive gain coefficients can finally also tackle sizeable and inevitable metal losses, allowing also for more flexible optical designs for electrically pumped QD laser diodes. And finally, the increased radiative rate at high densities allows for very bright emitting diodes. The discussion of these materials and their use in devices is continued in Chapter 8.

Bibliography

- ¹ S. Bisschop, P. Geiregat, T. Aubert, and Z. Hens. The Impact of Core/Shell Sizes on the Optical Gain Characteristics of CdSe/CdS Quantum Dots. *ACS Nano*, 12:9011–9021, 2018.
- ² Margherita Zavelani-Rossi, Maria Grazia Lupo, Roman Krahne, Liberato Manna, and Guglielmo Lanzani. Lasing in self-assembled microcavities of cdse/cds core/shell colloidal quantum rods. *Nanoscale*, 2(6):931–935, 2010.
- ³ Renu Tomar, Aditya Kulkarni, Kai Chen, Shalini Singh, Dries Van Thourhout, Justin M Hodgkiss, Laurens DA Siebbeles, Zeger Hens, and Pieter Geiregat. Charge carrier cooling bottleneck opens up nonexcitonic gain mechanisms in colloidal cdse quantum wells. *J. Phys. Chem. C*, 123(14):9640–9650, 2019.
- ⁴ Zeger Hens and Iwan Moreels. Light absorption by colloidal semiconductor quantum dots. *Journal of Materials Chemistry*, 22(21):10406, 2012.
- ⁵ Jorick Maes, Lieve Balcaen, Emile Drijvers, Qiang Zhao, Jonathan De Roo, André Vantomme, Frank Vanhaecke, Pieter Geiregat, and Zeger Hens. Light Absorption Coefficient of CsPbBr₃ Perovskite Nanocrystals. *J. Phys. Chem. Lett.*, 9:3093–3097, 2018.
- ⁶ M Thambidurai, N Muthukumarasamy, S Agilan, N Murugan, S Vasantha, R Balasundaraprabhu, and TS Senthil. Strong quantum confinement effect in nanocrystalline cds. *Journal of materials science*, 45(12):3254–3258, 2010.
- ⁷ Nader Ghobadi. Band gap determination using absorption spectrum fitting procedure. *International Nano Letters*, 3(1):1–4, 2013.
- ⁸ S. Adachi. *Optical Constants of Crystalline and Amorphous Semiconductors*. Springer Science, 1999.

- ⁹ Pieter Geiregat, Renu Tomar, Kai Chen, Shalini Singh, Justin M Hodgkiss, and Zeger Hens. Thermodynamic Equilibrium between Excitons and Excitonic Molecules Dictates Optical Gain in Colloidal CdSe Quantum Wells. *J. Phys. Chem. Lett.*, 10(13):3637–3644, 2019.
- ¹⁰ Jaehoon Lim, Young-Shin Park, and Victor I. Klimov. Optical gain in colloidal quantum dots achieved with direct-current electrical pumping. *Nature Materials*, 17(November):42–49, 2017.
- ¹¹ James Cassidy, Benjamin T. Diroll, Navendu Mondal, David B. Berkinsky, Kehui Zhao, Dulanjan Harankahage, Dmitry Porotnikov, Reagan Gately, Dmitriy Khon, Andrew Proppe, Mounqi G. Bawendi, Richard D. Schaller, Anton V. Malko, and Mikhail Zamkov. Quantum Shells Boost the Optical Gain of Lasing Media. *ACS Nano*, 16(2):3017–3026, 2022.
- ¹² Kai Chen, Joseph K. Gallaher, Alex J. Barker, and Justin M. Hodgkiss. Transient Grating Photoluminescence Spectroscopy: an Ultrafast Method of Gating Broadband Spectra. *J. Phys. Chem. Lett.*, 5(10):1732–1737, 2014.
- ¹³ I. Pelant and J. Valenta. *Luminescence Spectroscopy of Semiconductors*. 2012.
- ¹⁴ Philipp Sippel, Wiebke Albrecht, Johanna C Van Der Bok, Relinde J A Van Dijk-moes, Thomas Hannappel, Rainer Eichberger, and Daniel Vanmaekelbergh. Femtosecond Cooling of Hot Electrons in CdSe Quantum-Well Platelets. *Nano Letters*, 15(4):2409–2416, 2015.
- ¹⁵ Ye Yang, David P. Ostrowski, Ryan M. France, Kai Zhu, Jao van de Lagemaat, Joseph M. Luther, and Matthew C. Beard. Observation of a hot-phonon bottleneck in lead-iodide perovskites. *Nature Photonics*, (October):1–7, 2015.
- ¹⁶ Carmelita Rod  , Bastiaan B. V. Salzmann, Isabella Wagner, Yera Ussembayev, Kai Chen, Justin M. Hodgkiss, Kristiaan Neyts, Iwan

- Moreels, Daniel Vanmaekelbergh, and Pieter Geiregat. Stimulated emission through an electron-hole plasma in colloidal cdse quantum rings. *Nano Letters*, 21(23):10062–10069, 2021. doi: 10.1021/acs.nanolett.1c03501.
- ¹⁷ Victor I Klimov, Sergei a Ivanov, Jagjit Nanda, Marc Achermann, Ilya Bezel, John a McGuire, and Andrei Piryatinski. Single-exciton optical gain in semiconductor nanocrystals. *Nature*, 447(7143):441–6, may 2007.
- ¹⁸ Pieter Geiregat, Arjan Houtepen, Yolanda Justo, Ferdinand C. Grozema, Dries Van Thourhout, and Zeger Hens. Coulomb shifts upon exciton addition to photoexcited PbS colloidal quantum dots. *The Journal of Physical Chemistry C*, 118(38):22284–22290, sep 2014.
- ¹⁹ V S Dneprovskii, V I Klimov, and M G Novikov. Dynamics and mechanisms of recombination of electron-hole plasma and high-density excitons in CdS and CdSe. *Sov. Phys. JETP*, 3(September 1991):468–478, 1991.
- ²⁰ M Pietryga, Young-shin Park, Jaehoon Lim, Andrew F Fidler, Wan Ki Bae, Sergio Brovelli, and Victor I Klimov. Spectroscopic and Device Aspects of Nanocrystal Quantum Dots. *Chemical Reviews*, 116:10513–10622, 2016.
- ²¹ B. Tränkle, H. Leier, A. Forchel, H. Haug, C. Ell, and G. Weimann. Dimensionality Dependence of the Band-Gap Renormalization in Two- and Three Dimensional Electron-Hole Plasmas. *Physical Review Letters*, 58(4), 1987.
- ²² H. Saito and E.O. Göbel. Picosecond spectroscopy of highly excited Cds. *Physical Review B*, 31(4):2360–2369, 1985.
- ²³ K. Asano and T. Yoshioka. Exciton-Mott Physics in Two-Dimensional Electron-Hole Systems: Phase Diagram and Single-Particle Spectra. *J. Phys. Soc. Jpn.*, 82:084702, 2014.

- ²⁴ M. Cardona. Band Parameters Of Semiconductors with Zincblende, Wurtzite and Germanium Structure. *J. Phys. Chem. Solids*, 24:1543–1555, 1963.
- ²⁵ Yemliha Altintas, Kivanc Gungor, Yuan Gao, Mustafa Sak, Ulviyya Quliyeva, Golam Bappi, Evren Mutlugun, Edward H. Sargent, and Hilmi Volkan Demir. Giant Alloyed Hot Injection Shells Enable Ultra-low Optical Gain Threshold in Colloidal Quantum Wells. *ACS Nano*, 13(9):10662–10670, 2019.
- ²⁶ Brandon R Sutherland and Edward H Sargent. Perovskite photonic sources. *Nature Publishing Group*, 10(5):295–302, 2016.
- ²⁷ Christopher Melnychuk and Philippe Guyot-Sionnest. Multicarrier dynamics in quantum dots. *Chemical Reviews*, 121(4):2325–2372, 2021.

Chapter 6

Carrier Temperature in Bulk Nanocrystals

6.1 Introduction

In recent years, many exciting high quality direct gap semiconductors have been prepared through advances in bottom-up wet chemical synthesis. In particular weakly confined nano-materials, such as bulk-like halide perovskite films¹ and II-VI Cd-based NCs^{2,3}, but also quasi-2D nanoplatelets⁴, have shown great potential for solution processable lasers and photo-voltaics (PV)⁵.

The distribution of charge carriers over the semi-discrete, often even nearly continuous, energy spectrum in such materials is a key parameter to evaluate and optimize their performance in many studies and is dictated by the temperature of the electron and/or hole gas T after photo-excitation. For example in the context of hot carrier solar cells, the extraction of carriers with excess energy is desired. In such cases, it is paramount to know the effect of composition (hybrid, fully inorganic, ...) and shape (nanoscale, bulk, ...) of the semiconductor on both the efficiency of generating hot charges and the timescales on which they cool

down or transfer. A case example in the past years is that of halide - perovskite semiconductors, where several groups have shown that the A-site cation has a critical role in slowing down carrier relaxation, highlighting for example differences between MAPbBr_3 and CsPbBr_3 . Other reports showed that also the B-site can be of importance, showing a sizable cooling bottleneck in CsSnBr_3 .^{6,7} For applications involving optical gain, such as lasers, the balance between stimulated emission and absorption is heavily affected by the carrier temperature. Indeed, high temperatures imply a strongly diluted occupation of the band edge states leading to problems in sustaining the required population inversion.

Using ultrafast optical spectroscopy methods, such as transient absorption (TA)⁸⁻¹³ and, less used, ultrafast broadband photoluminescence (PL)^{14,15}, researchers have attempted to extract the carrier temperature and use it to understand the photo-physics in low and high carrier density scenarios. Often, these procedures rely on a simple exponential fit of the high energy tail of the transient signal, be it luminescence or transient absorption. However, much ambiguity remains in which method now yields a consistent temperature, how to reliably extract it under certain approximations and under which circumstances these all-optical methods would even agree. Here, we show that the applicability of each method depends on the symmetry of the semiconductor's band structure. In band-symmetric semiconductors with reasonably equal masses for electrons and holes, such as halide perovskites, both TA and PL agree on carrier temperature and even a simple exponential tail-fit approximation is arguably correct. However, in asymmetric band scenarios, such as very common II-VI or III-V materials, PL is a much more reliable technique, in particular at high carrier temperatures where single exponential tail fitting of TA drastically overestimates carrier temperatures. Our theoretical modelling also shows how both methods can be made to yield a correct temperature given an adaptation of the widely used Boltzmann tail fitting procedure.

The theoretical derivation discussed in this Chapter was done by me, together with the acquisition and analysis of the TA data shown about CdS NCs. The Ultrafast PL was done by Isabella Wagner.

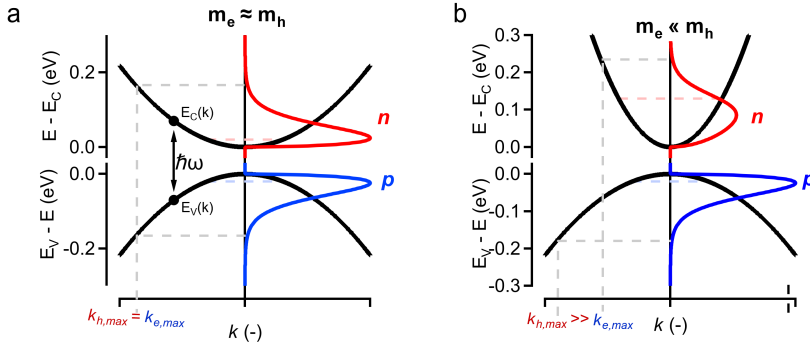


Figure 6.1: Conduction and valence bands of an symmetric (a, $m_e = m_h$) and asymmetric (b, $m_e < m_h$) energy band situation, showing in parallel the electron (red, $n(E)$) and hole (blue, $p(E)$) distribution functions. Horizontal axis shows the maximum k vector of occupied electron (red) and hole (blue) states.

6.2 Carrier Temperature

Before we start out how to extract a carrier temperature from ultrafast optical experiments, we should first rationalize what temperature imparts on a semiconductor's properties and how this affects our measurements. Figure 6.2a shows how the temperature T of charge carriers affects their distribution $n(E, T)$ over the energy level spectrum of a semiconductor, here represented by a parabolic energy band. Low temperatures tend to focus photo-excited charges in the lower energy states, whereas higher temperatures spread them out over the energy level ladder given by the density of states $g(E)$. The spreading is controlled by the temperature through the statistical Fermi-Dirac distribution $f(E, E_{F,n})$, resulting for electrons (“e”) in:

$$n(E, T) = f_e(E, E_F, T) \times g_e(E) \quad (6.2.1)$$

A similar expression can be written for holes (“h”). If one could meas-

ure the full extent of this charge carrier distribution $n(E, T)$ and know $g(E)$ in advance, it should be possible to obtain the desired temperature T . Knowledge of $g(E)$ boils down to the effective mass of the band, which is often well-known for electrons but less so for holes. The question thus shifts to how we can measure $n/p(E, T)$ using optical methods. When photo-exciting a semiconductor using light, both electrons and holes are produced. These each have their own energy level spectrum (Density Of States) and associated carrier distribution $n(E, T)$ and $p(E, T)$. Figures 6.1a and 6.1b show such an example for a band symmetric (6.1a, $m_e^* < m_h^*$) and band-asymmetric (6.1b, $m_e^* = m_h^*$) case. Any optical method will probe these distributions simultaneously, either as a sum $n+p$, in transient absorption experiments, or a product $n \times p$, in luminescence experiments. Indeed, in TA experiments, a bleach $\Delta A(E)$ of the probe absorption is observed as soon as carriers block an optical transition by Pauli blocking (state filling) after an initial excitation event. This means that either an electron or a hole can cause a signal, making a TA signal sensitive to $n+p$, see Figure 6.2b. Clearly, even if no electrons are present at high k -values, a probe beam can still detect the presence of the spread out holes at higher cut-off energies. In ultrafast photo-luminescence experiments (PL), the sample is excited with a short light pulse and the (spontaneously) emitted light after electron-hole pair recombination is proportional to the product $n \times p$, see Figure 6.2b, thereby requiring the presence of both charges in a vertical transition. This implies that a much narrower spread in k -values is obtained, as shown in Figure 6.2b.

Finally, neither TA nor PL have direct access to either n or p . To tackle this problem, one often uses a shortcut based on the assumption that the Fermi-Dirac distribution approximates a much simpler Boltzmann expression ($\propto e^{-\frac{E}{kT}}$) and that the density of states $g(E)$ flattens off at high energy, an approach we will refer to further as the “Boltzmann tail approximation” (BTA). Indeed, this approximates $n(E, T)$ as a decaying single exponential function whose slope is proportional to $1/T$. Based on this, the extrapolation is made that both TA and PL signals at high energy reveal the temperature by a simple slope fit. However, it is math-

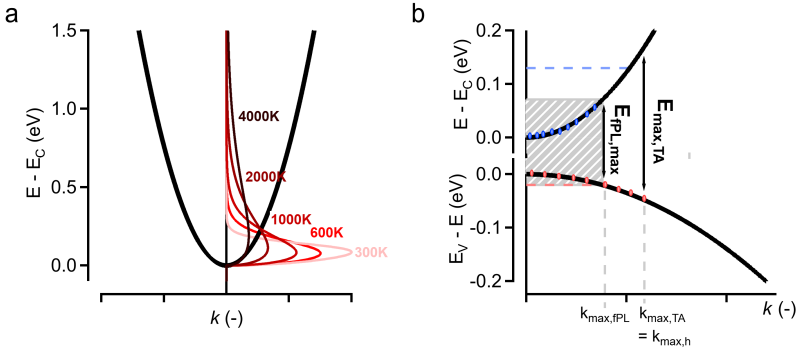


Figure 6.2: (a) Carrier distribution functions $n(E)$ for different carrier temperatures T from 300 to 4000K for a parabolic energy band. (b) Energies probed by transient luminescence (PL) and transient absorption (TA), and the associated maximum k -vectors. Note that for this band-asymmetric situation with heavier hole mass (smaller curvature), the holes extend much further in k -values.

ematically clear that a product $n \times p$ or a sum $n + p$ can never yield the same approximation. Second, it remains very unclear how an asymmetry in the density of states for electrons and holes would impact these approximation since in both experiments the probe or emitted PL is a result of a joint density of states.

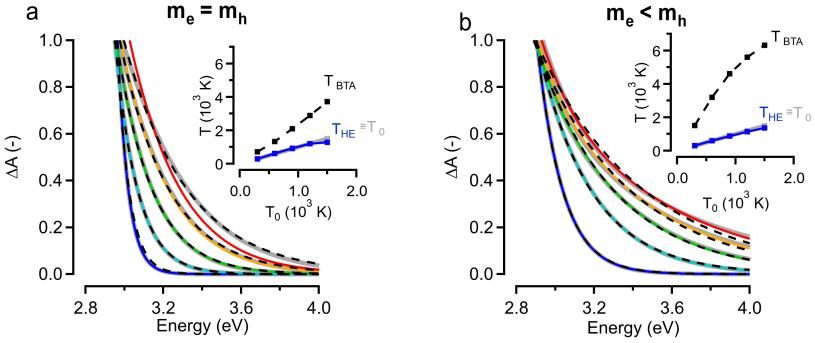


Figure 6.3: Theoretical predictions of transient absorption (TA) for equal masses $m_e^* = m_h^*$ (a), and different masses $m_e^* < m_h^*$, based on exact model (color traces), the high energy limit of these exact models (HE) and the often used simplified Boltzmann tail approximation (BTA). The insets show the input temperatures for the exact model T_0 , as the x -axis, and the extracted temperature from the HE (blue, solid) and BTA (black, dashed) fits. For the equal masses, a factor two in temperature difference can be seen.

6.3 Model Derivation

In this Section, we attempt to derive a method to extract the temperature based on the model discussed in Section 2.4.3.2, for both TA and PL data.

6.3.1 Temperature from Change in Absorption

As previously discussed, A can be written as

$$A(E, E_{F,h}, E_{F,e}, T) = A_0(E, T) \times [f_v(E, E_{F,h}, T) - f_c(E, E_{F,e}, T)] \quad (6.3.1)$$

where $f_v(E, E_{F,h}, T)$, $f_c(E, E_{F,e}, T)$ are defined as

$$f_c(E, E_{F,e}, T) = \frac{1}{1 + \exp\left(\frac{E_C(k) - E_{F,e}}{k_B T}\right)} \quad (6.3.2)$$

$$f_v(E, E_{F,h}, T) = \frac{1}{1 + \exp\left(\frac{E_V(k) - E_{F,h}}{k_B T}\right)} \quad (6.3.3)$$

which are the occupation chances of electrons in the conduction - and valence band respectively, where the dispersion relations of $E_C(k)$ and $E_V(k)$ were filled in. They are energy dependent through the carrier momentum k . We can calculate the quasi fermi levels back from the carrier density n . The selection rule for an absorption event is that there cannot be any momentum change when absorbing a photon with frequency ω , so the relationship $\hbar\omega = E = E_C(k) - E_V(k)$ holds (as shown in Figure 6.1a), with

$$E_C(k) = E_g + \frac{\hbar^2 k^2}{2m_e^*} \quad (6.3.4)$$

$$E_V(k) = -\frac{\hbar^2 k^2}{2m_h^*} \quad (6.3.5)$$

where m_e^* and m_h^* are the effective masses of the electrons and holes, respectively. From this we can calculate

$$E = E_g + \frac{\hbar^2 k^2}{2m_e^*} + \frac{\hbar^2 k^2}{2m_h^*} = E_g + \frac{\hbar^2 k^2}{2m_r} \quad (6.3.6)$$

with m_r the reduced effective mass $\left(\frac{1}{m_e^*} + \frac{1}{m_h^*}\right)^{-1}$. Solving this for k , we get

$$k_0 = \sqrt{\frac{2m_r}{\hbar^2}(E - E_g)} \quad (6.3.7)$$

Where k_0 is the k -value for which an optical transition of energy E can occur. Combining the selection rules with the FD occupation factors, we find

$$f_c(E, E_{F,e}, T) = \frac{1}{1 + \exp\left(\frac{E_g + \frac{\hbar^2 k_0^2}{2m_e^*} - E_{F,e}}{k_B T}\right)} \quad (6.3.8)$$

$$= \frac{1}{1 + \exp\left(\frac{E_g + \frac{m_r}{m_e^*}(E - E_g) - E_{F,e}}{k_B T}\right)} \quad (6.3.9)$$

$$f_v(E, E_{F,h}, T) = \frac{1}{1 + \exp\left(\frac{-\frac{\hbar^2 k_0^2}{2m_h^*} - E_{F,h}}{k_B T}\right)} \quad (6.3.10)$$

$$= \frac{1}{1 + \exp\left(\frac{-\frac{m_r}{m_h^*}(E - E_g) - E_{F,h}}{k_B T}\right)} \quad (6.3.11)$$

If we now approximate these FD distributions for the high energy tail by Boltzmann distributions, we find

$$f_c(E, E_{F,e}, T) \approx C_C(E_{F,e}, T) \times \exp\left(-\frac{E - E_g}{\frac{m_e^*}{m_r} k_B T}\right) \quad (6.3.12)$$

$$= C_C(E_{F,e}, T) \times \exp\left(-\frac{E - E_g}{\tau_e}\right) \quad (6.3.13)$$

$$f_v(E, E_{F,h}, T) \approx 1 - C_V(E_{F,h}, T) \times \exp\left(-\frac{E - E_g}{\frac{m_h^*}{m_r} k_B T}\right) \quad (6.3.14)$$

$$= 1 - C_V(E_{F,h}, T) \times \exp\left(-\frac{E - E_g}{\tau_h}\right) \quad (6.3.15)$$

where τ_i is defined as $\frac{m_i^*}{m_r} k_B T$ for $i = e, h$. The pre-factors are defined as (although these can be seen as independent fitting parameters, see later)

$$C_C(E_{F,e}, T) = \exp\left(\frac{E_{F,e} - E_g}{k_B T}\right) \quad (6.3.16)$$

$$C_V(E_{F,h}, T) = \exp\left(-\frac{E_{F,h}}{k_B T}\right) \quad (6.3.17)$$

This we can use to approximate the high energy tail of $A(E, E_{F,e}, E_{F,h}, T)$

$$A(E, E_{F,e}, E_{F,h}, T) = A_0(E) \times \left[1 - C_V(E_{F,h}, T) \times \exp\left(-\frac{E - E_g}{\tau_h}\right) - C_C(E_{F,e}, T) \times \exp\left(-\frac{E - E_g}{\tau_e}\right) \right] \quad (6.3.18)$$

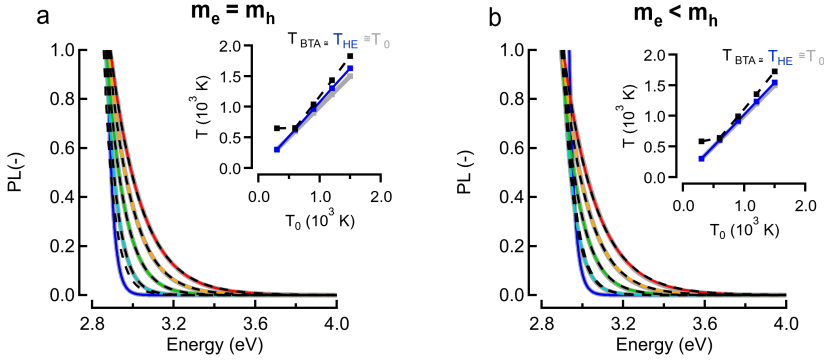


Figure 6.4: Theoretical predictions of photoluminescence (PL) for equal masses $m_e = m_h$ (a), and different masses $m_e < m_h$, based on exact model (color traces), the high energy limit of these exact models (HE) and the often used simplified Boltzmann tail approximation (BTA). The insets show the input temperatures for the exact model T_0 , as the x -axis, and the extracted temperature from the HE (blue, dashed) and BTA (black, dashed) fits. A good match is found between all three.

If we define $\Delta A(E, T) = A(E, T) - A_0(E)$, we can also find

$$\Delta A(E, E_{F,e}, E_{F,h}, T) = -A_0(E) \times \left[C_V(E_{F,h}, T) \times \exp\left(-\frac{E - E_g}{\tau_h}\right) + C_C(E_{F,e}, T) \times \exp\left(-\frac{E - E_g}{\tau_e}\right) \right] \quad (6.3.19)$$

6.3.2 Temperature from Ultrafast Luminescence

We start from the idea that PL is the product of the Density of States with the FD distributions of the conduction and valence bands

$$PL(E, E_{F,e}, E_{F,h}, T) = g_{eh}(E) \cdot f_c(E, E_{F,e}, T) \cdot (1 - f_v(E, E_{F,h}, T)) \quad (6.3.20)$$

where $g_{eh}(E)$ is proportional with $\sqrt{E - E_g}$, and (f_c, f_v) are defined as before. $(1 - f_v(E, E_{F,h}, T))$ here denotes the chance of the valence band not being occupied with an electron (so: occupied with a hole).

The same selection rule for the transition applied from before, which is

$$\hbar\omega = E = E_C(k) - E_V(k) = E_g + \frac{\hbar^2 k^2}{2m_e^*} + \frac{\hbar^2 k^2}{2m_h^*} = E_g + \frac{\hbar^2 k^2}{2m_r} \quad (6.3.21)$$

We can solve this to k to find

$$k_0 = \sqrt{\frac{2m_r}{\hbar^2}(E - E_g)} \quad (6.3.22)$$

for this k value, defined as k_0 , a transition is allowed with energy E . We can use this in the FD distributions:

$$f_c(E, E_{F,e}, T) = \frac{1}{1 + \exp\left(\frac{E_g + \frac{\hbar^2 k_0^2}{2m_e^*} - E_{F,e}}{k_B T}\right)} \quad (6.3.23)$$

$$= \frac{1}{1 + \exp\left(\frac{E_g + \frac{m_r}{m_e^*}(E - E_g) - E_{F,e}}{k_B T}\right)} \quad (6.3.24)$$

$$1 - f_v(E, E_{F,h}, T) = 1 - \frac{1}{1 + \exp\left(\frac{-E_{F,h} - \frac{\hbar^2 k_0^2}{2m_h^*}}{k_B T}\right)} \quad (6.3.25)$$

$$= 1 - \frac{1}{1 + \exp\left(\frac{-E_{F,h} - \frac{m_r}{m_h^*}(E - E_g)}{k_B T}\right)} \quad (6.3.26)$$

$$= \frac{1 + \exp\left(\frac{-E_{F,h} - \frac{m_r}{m_h^*}(E - E_g)}{k_B T}\right) - 1}{1 + \exp\left(\frac{-E_{F,h} - \frac{m_r}{m_h^*}(E - E_g)}{k_B T}\right)} \quad (6.3.27)$$

$$= \frac{1}{1 + \exp\left(\frac{E_{F,h} + \frac{m_r}{m_h^*}(E - E_g)}{k_B T}\right)} \quad (6.3.28)$$

Now we can start approximating:

$$f_c(E, E_{F,e}, T) \approx C_C(E_{F,e}, T) \times \exp\left(-\frac{E - E_g}{\tau_e}\right) \quad (6.3.29)$$

$$1 - f_v(E, E_{F,h}, T) \approx C_V(E_{F,h}, T) \times \exp\left(-\frac{E - E_g}{\tau_h}\right) \quad (6.3.30)$$

So we finally end up with

$$PL(E, E_{F,e}, E_{F,h}, T) = C_C \cdot C_V \cdot \sqrt{E - E_g} \cdot \exp\left(-\frac{E - E_g}{\tau_e}\right) \cdot \exp\left(-\frac{E - E_g}{\tau_h}\right) \quad (6.3.31)$$

$$= C_C(E_{F,e}, T) \cdot C_V(E_{F,e}, T) \cdot \sqrt{E - E_g} \cdot \exp\left(-\frac{E - E_g}{\tau_r}\right) \quad (6.3.32)$$

where $\tau_r = \left(\frac{1}{\tau_e} + \frac{1}{\tau_h}\right)^{-1}$, which can be solved to become, perhaps surprisingly:

$$\tau_r = \frac{\tau_h + \tau_e}{\tau_h \tau_e} \quad (6.3.33)$$

$$= \frac{\frac{m_h^*}{m_r} + \frac{m_e^*}{m_r}}{\frac{m_h^*}{m_r} \cdot \frac{m_e^*}{m_r}} \times k_B T \quad (6.3.34)$$

$$= \frac{m_h^* + m_e^*}{m_h^* \cdot m_e^*} \cdot \frac{1}{m_r} \times k_B T \quad (6.3.35)$$

$$= k_B T \quad (6.3.36)$$

So we obtain:

$$PL(E, E_{F,e}, E_{F,h}, T) = C_C(E_{F,e}, T) \cdot C_V(E_{F,h}, T) \times \sqrt{E - E_g} \cdot \exp\left(-\frac{E - E_g}{k_B T}\right) \quad (6.3.37)$$

We can combine the product of the two pre factors $C(E_{F,e}, E_{F,h}, T) = C_C(E_{F,e}, T) \cdot C_V(E_{F,h}, T)$.

It is clear from this derivation that the PL case is easier to fit: the exponential simplifies to a single Boltzmann without any additional factors in the exponent, contrary to the transient absorption case.

6.3.3 Comparison

For TA we found:

$$\Delta A(E, E_{F,e}, E_{F,h}, T) = -A_0(E) \times \left[C_V(E_{F,h}, T) \times \exp\left(-\frac{E - E_g}{\tau_h}\right) + C_C(E_{F,e}, T) \times \exp\left(-\frac{E - E_g}{\tau_e}\right) \right] \quad (6.3.38)$$

and for PL:

$$PL(E, E_{F,e}, E_{F,h}, T) = C(E_{F,e}, E_{F,h}, T) \times \sqrt{E - E_g} \cdot \exp\left(-\frac{E - E_g}{k_B T}\right) \quad (6.3.39)$$

Comparing this to the very commonly used Boltzmann Tail Approximation (BTA), where both the TA and PL signals in the high energy limit are approximated as a single exponential:

$$f(E) \propto e^{-\frac{E}{k_B T}} \quad (6.3.40)$$

We can see that for TA the BTA approach is particularly problematic since a sum of two exponentials is obtained in reality. Only if the masses of electrons and holes are equal does one obtain a single exponential profile at high energy, a point we will come back to further. PL is rather insensitive to this problem and always yields a single exponential decay at high energy with a direct scaling to temperature of the slope. Other than that, the lack of the DOS pre-factor inclusion in the modelling (for bulk systems a square root factor), is also problematic.

Figures 6.3 and 6.4 show a series of theoretical calculations of the high energy TA (6.3) and PL signals (6.4) for both a band-asymmetric (left, $m_e^* = m_h^* = 0.2m_0$) and band-symmetric semiconductor (right, $m_e^* = 0.2m_0$; $m_h^* = 0.7m_0$). First, the full model with a given input temperature T_0 is presented without any approximations (colored traces) as a representation of the actual TA/PL signals. Then, we apply our high energy limit (HE) model, Equations (6.3.38, 6.3.39) to this data (grey traces) and obtain T_{HE} , shown in the insets. Finally, we simply fit a

single exponential (dashed black line) to obtain the “Boltzmann tail approximation” (BTA) often used in literature, giving a temperature T_{BTA} .

Clearly, PL is very insensitive to the way the spectra are fitted, yielding a consistent temperature throughout, which was expected based on the theoretical considerations above. TA however is more problematic, always overestimating the actual temperature in the BTA approximation. Based on Equation 6.3.38 it is clear why this happens for the band - asymmetric case as we force a single exponential decay onto a double-exponential function.

6.4 High Energy Limits

The previous Section shows that PL is superior in extracting temperatures from ultrafast data. But the question remains whether we can find something by performing tail fittings for TA data. To do this, it is worthwhile to look at the derived formula for TA, Equation 6.3.38, in more detail. Specifically, at the C_V and C_C pre-factors. In the next Section, we will look into the ratio of these pre-factors, after which we can then compare the approximated fits to the full model.

6.4.1 About C_C and C_V

As a reminder, C_C and C_V are defined as

$$C_C(E_{F,e}, T) = \exp\left(\frac{E_{F,e} - E_g}{k_B T}\right) \quad (6.4.1)$$

$$C_V(E_{F,e}, T) = \exp\left(-\frac{E_{F,h}}{k_B T}\right) \quad (6.4.2)$$

To find the relationship between these two pre-factors we need to find the quasi Fermi levels:

$$E_{F,e} = k_B T \cdot F_{1/2}^{-1}\left(\frac{n}{N_{e,eff}}\right) + E_g \quad (6.4.3)$$

$$E_{F,h} = -k_B T \cdot F_{1/2}^{-1}\left(\frac{n}{N_{h,eff}}\right) \quad (6.4.4)$$

Where the Fermi-Dirac integral cannot be solved analytically, and $N_{i,eff}$ is given by $2\left(\frac{m_i^* k_B T}{2\pi\hbar^2}\right)^{3/2}$ but can be approximated in two regimes:

$$F_{1/2}(\eta) = \begin{cases} e^\eta & \eta \ll -1 \\ \frac{4}{3} \left(\frac{\eta^3}{\pi}\right)^{1/2} & \eta \gg -1 \end{cases}$$

Which each can be inverted to find

$$F_{1/2}^{-1}(\nu) = \begin{cases} \ln(\nu) & \nu \ll e^{-1} \\ \left[\frac{9\pi}{16} \cdot \nu^2\right]^{1/3} & \nu \gg e^{-1} \end{cases}$$

We can take a look at each of these cases separately.

$$6.4.1.1 \quad \nu \gg e^{-1} \Rightarrow \frac{n}{N_{i,eff}} \gg e^{-1}$$

The simplest case, since the logarithm and exponential cancel each other out. This holds for low carrier densities.

$$E_{F,e} = k_B T \cdot \ln \left(\frac{n}{N_{e,eff}} \right) + E_g \quad (6.4.5)$$

$$E_{F,h} = -k_B T \cdot \ln \left(\frac{n}{N_{h,eff}} \right) \quad (6.4.6)$$

From which we can find $C_C(E_{F,e}, T)$ and $C_V(E_{F,h}, T)$

$$C_C(E_{F,e}, T) = \exp \left(\frac{k_B T \cdot \ln \left(\frac{n}{N_{e,eff}} \right) + E_g - E_g}{k_B T} \right) \quad (6.4.7)$$

$$= \exp \left[\ln \left(\frac{n}{N_{e,eff}} \right) \right] \quad (6.4.8)$$

$$= \frac{n}{N_{e,eff}} \quad (6.4.9)$$

and

$$C_V(E_{F,h}, T) = \exp \left(\frac{k_B T \cdot \ln \left(\frac{n}{N_{h,eff}} \right)}{k_B T} \right) \quad (6.4.10)$$

$$= \exp \left[\ln \left(\frac{n}{N_{h,eff}} \right) \right] \quad (6.4.11)$$

$$= \frac{n}{N_{h,eff}} \quad (6.4.12)$$

Filling in the definition of $N_{i,eff}$ and dividing the two pre-factors, we get

$$\frac{C_C}{C_V} = \left(\frac{m_h^*}{m_e^*} \right)^{3/2} \quad (6.4.13)$$

showing that the ratio becomes independent of (n, T) .

6.4.1.2 $\nu \ll e^{-1} \Rightarrow \frac{n}{N_{i,eff}} \ll e^{-1}$

Here the solution is not quite so elegant, and we are in the high density regime

$$E_{F,e} = k_B T \cdot \left[\frac{9\pi}{16} \left(\frac{n}{N_{e,eff}} \right)^2 \right]^{1/3} + E_g \quad (6.4.14)$$

$$E_{F,h} = -k_B T \cdot \left[\frac{9\pi}{16} \left(\frac{n}{N_{h,eff}} \right)^2 \right]^{1/3} \quad (6.4.15)$$

Which we again fill in in the definition of the pre-factors

$$C_C(E_{F,e}, T) = \exp \left(\frac{k_B T \cdot \left[\frac{9\pi}{16} \left(\frac{n}{N_{e,eff}} \right)^2 \right]^{1/3} + E_g - E_g}{k_B T} \right) \quad (6.4.16)$$

$$= \exp \left(\left[\frac{9\pi}{16} \left(\frac{n}{N_{e,eff}} \right)^2 \right]^{1/3} \right) \quad (6.4.17)$$

$$= \exp \left(\left[\frac{9\pi}{64} \cdot n^2 \right]^{1/3} \cdot \frac{2\pi\hbar^2}{m_e^* k_B T} \right) \quad (6.4.18)$$

and

$$C_V(E_{F,h}, T) = \exp \left(\frac{k_B T \cdot \left[\frac{9\pi}{16} \left(\frac{n}{N_{h,eff}} \right)^2 \right]^{1/3}}{k_B T} \right) \quad (6.4.19)$$

$$= \exp \left(\left[\frac{9\pi}{16} \left(\frac{n}{N_{h,eff}} \right)^2 \right]^{1/3} \right) \quad (6.4.20)$$

$$= \exp \left(\left[\frac{9\pi}{64} \cdot n^2 \right]^{1/3} \cdot \frac{2\pi\hbar^2}{m_h^* k_B T} \right) \quad (6.4.21)$$

Before dividing the two pre-factors, we can define $c = \left[\frac{9\pi}{64} \right]^{1/3} \cdot \frac{2\pi\hbar^2}{k_B}$ for ease of notation. When we divide the two factors we get

$$\frac{C_C(E_{F,e}, T)}{C_V(E_{F,h}, T)} = \exp \left(c \cdot \frac{n^{2/3}}{T} \times \left[\frac{1}{m_e^*} - \frac{1}{m_h^*} \right] \right) \quad (6.4.22)$$

Here we see that the pre-factors become temperature and carrier density dependent. Interestingly, in the limit where the effective masses become equal, this ratio becomes one, meaning the ratio of C_V and C_V becomes independent of (n, T) . Similarly, the denominator in both exponentials become $2k_B T$. We could already see this in Figure 6.3a, where $m_e^* = m_h^*$.

We can check the limits of the different regions for both electrons and holes. The limit is

$$\frac{n_{thr}}{N_{i,eff}} \approx e^{-1} \quad (6.4.23)$$

which we can rewrite as

$$n_{thr} = e^{-1} \cdot 2 \left(\frac{m_i^* k_B T}{2\pi\hbar^2} \right)^{3/2} \quad (6.4.24)$$

We can calculate this limit for both the electrons and holes. Due to the typically higher mass of the holes, the threshold density will be higher and as such the independence will hold for larger carrier densities for the holes specifically. Of course, for the actual temperature fit, the constant ratio will hold only up until one of the two pre-factors become carrier density dependent.

These results can be summarised in Figure 6.5. (a) shows the exact ratio (full lines) and the two approximations (constant low limit, which is around 6.5 for our used masses, and coloured dashed lines for the high limit). (b) shows the change in threshold carrier density as a function of temperature for electrons (red), holes (blue) and also the crossing point between low and high limit (black). The latter case is when the two limits equal each other. In general we can conclude here that for a reasonable carrier density ($n = 10^{20} \text{ cm}^{-3}$ is about the maximum) the lower limit applies. Using this approximation, we can rewrite ΔA

$$\Delta A(E, T) = -A_0(E) \cdot C \times \left[(m_e^*)^{3/2} \times \exp\left(-\frac{E - E_g}{\tau_h}\right) + (m_h^*)^{3/2} \times \exp\left(-\frac{E - E_g}{\tau_e}\right) \right] \quad (6.4.25)$$

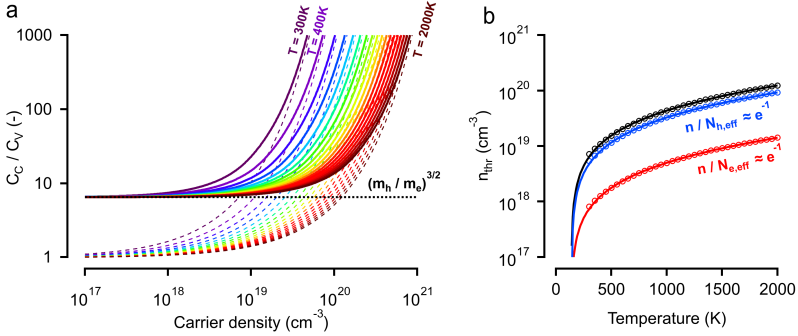


Figure 6.5: (a) Ratio of the pre-factors of the two exponentials derived from the TA temperature fitting. (b) the threshold for the two regimes as a function of the temperature. Masses used here are $m_e^* = 0.2m_0$ and $m_h^* = 0.7m_0$.

6.4.2 Exponential Decays

The pre-factor only gives part of the image, since the slopes of both the electron and hole exponentials will be scaled according to the τ_i factor. For the case that $m_e^* < m_h^*$, we can see that the electron exponential will decay much quicker although it has a higher weight. This can be seen in Figure 6.6, where the sum of exponentials is shown and it is clear that there are two different regimes. For this specific case, mostly the hole exponential will in fact be relevant in our fitting region, despite its lower weight. In fact, in general, it will always be the species with the highest mass that will become dominant for high energies. For the general case we can look at the tipping point E_{thr} where the two exponentials become equal to each other (and as such for energies higher than this value the hole exponential will be the dominant decay):

$$C_C(E_{F,e}, T) \times \exp\left(-\frac{E_{thr} - E_g}{\tau_e}\right) = C_V(E_{F,h}, T) \times \exp\left(-\frac{E_{thr} - E_g}{\tau_h}\right) \quad (6.4.26)$$

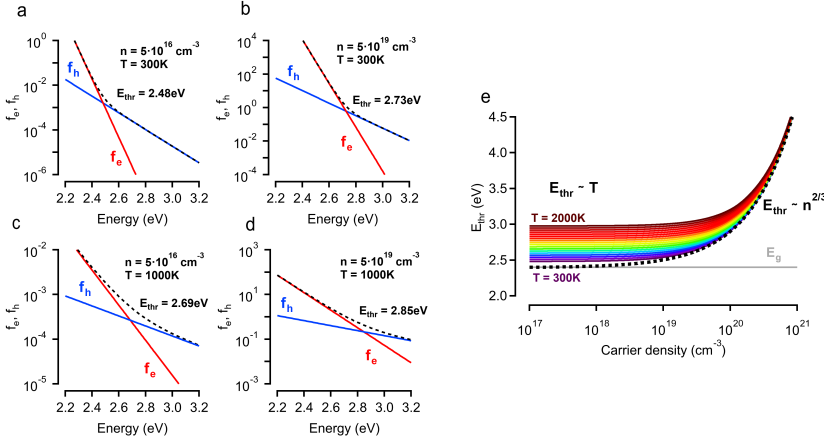


Figure 6.6: (a)-(d) magnitude of each of the exponentials for 4 different combinations, low/high temperature and carrier density. (e) E_{thr} as a function of the carrier density and plotted for a range of temperatures. The dotted line shows the high density limit.

This can be solved for E_{thr}

$$E_{thr} = E_g + \frac{m_h^* + m_e^*}{m_h^* - m_e^*} \cdot kT \times \ln \left(\frac{C_C(E_{F,e}, T)}{C_V(E_{F,h}, T)} \right) \quad (6.4.27)$$

Which will only depend linearly on the temperature for the low density regime

$$E_{thr} = E_g + \frac{m_h^* + m_e^*}{m_h^* - m_e^*} \cdot kT \times \frac{3}{2} \cdot \ln \left(\frac{m_h^*}{m_e^*} \right) \quad (6.4.28)$$

and will become temperature independent for the high density regime

$$E_{thr} = E_g + \frac{m_h^* + m_e^*}{m_h^* - m_e^*} \cdot kT \times \left(c \cdot \frac{n^{2/3}}{T} \times \left[\frac{1}{m_e^*} - \frac{1}{m_h^*} \right] \right) \quad (6.4.29)$$

$$= E_g + \left(\frac{9\pi}{64} \right)^{1/3} \cdot \frac{2\pi\hbar^2}{m_r} \cdot n^{2/3} \quad (6.4.30)$$

We can see that the second, electron related, exponential will decay much quicker although it has a higher initial weight, as is shown in Figure 6.6a. As a result, the fits at high energy are dominated by holes (or more

general: the highest mass carrier), and can be fitted starting from E_{thr} with:

$$\Delta A(E, T) \approx -\sqrt{E - E_g} \cdot C \times \exp\left(-\frac{E - E_g}{\tau_h}\right) \quad (6.4.31)$$

Looking back at Figure 6.2b, this is exactly what we expected since holes spread out much more in momentum space resulting in their sole contribution to the TA signal at high probe photon energies.

From this, we can deduce that in practical terms, if we choose the lower limit of the fit well (high enough) then we can fit the TA data with a single exponential. Interestingly, the low carrier regime effect also scaled with the difference between the effective masses of electrons and holes, so if they become equal the effect disappears. This means that for equal masses and low carrier densities, the “high energy tail” actually already starts at the bandgap.

Despite the large window where a single exponential fit is applicable, it should be emphasized that to obtain the correct temperature from a fit to TA spectra in the case of band-asymmetry, one clearly has to know very precisely the masses of the charge carriers involved. This is typically quite problematic for holes. Even if the masses, or energy band curvatures, are reasonably well known around the band gap, the non-parabolic and multi-band nature complicates the assignment of a single “mass” at higher energies. Unfortunately, this is exactly the regime where the temperature fitting analysis is performed. On the other hand, knowing what we have deduced we can actually estimate the hole mass based on Equation 6.3.38, by assuming that for long pump-probe delays, the sample is back at room temperature.

Even if the masses of both bands are equal, one has to thread with caution even though Equation 6.3.38 greatly simplifies, given $\tau_p = \tau_c = 2k_B T$ and $C_C = C_V$ as shown above, to the form:

$$\Delta A \approx -\sqrt{E - E_g} \cdot C \times \exp\left(-\frac{E - E_g}{2kT}\right) \quad (6.4.32)$$

Whereas this is indeed a single exponential, the slope is now dictated by

$2k_B T$, not $k_B T$, an observation that is retrieved in the inset of Figure 6.3a.

6.4.3 Experimental Results

To cross check our model with experiments, we proceed to analyse the TA and PL of a bulk-like system with direct gaps: CdS, for which $m_e^* < m_h^*$.

Figure 6.7 shows the experimental data obtained in a TA (Figure 6.7a) and PL (Figure 6.7b) experiment after 400 nm excitation of 12.0 nm CdS NCs creating a charge carrier density $n = 5.4 \cdot 10^{19} \text{ cm}^{-3}$. Using the BTA approximation fit, we obtain very high carrier temperatures that exceed even room temperature after 3 ns as indicated by the dashed color lines. This is clearly not very physical, but not unexpected based on our theoretical analysis. Indeed, a single exponential fit will overestimate the temperature with a factor of $\frac{m_h^*}{m_r}$. Rescaling this temperature to the actual temperature requires knowledge of the hole mass as indicated by Equation 6.4.31. As we do not know the exact hole mass, we decide to force the temperature at 3 ns to 300 K, which in turn gives us the actual hole mass. Values between 0.22 and 0.29 m_0 are obtained, see Figure 6.7c, which indicate more contribution from light holes. Importantly, the initial carrier temperatures are significantly reduced compared to the BTA approximation.

The PL data are fitted using Equation 6.3.39 and the extracted temperatures are shown in Figure 6.7d. Similar temperatures to the TA fitting with our expanded model are obtained, indicating that a simple exponential fit to TA data is indeed dramatically overestimating the temperature.

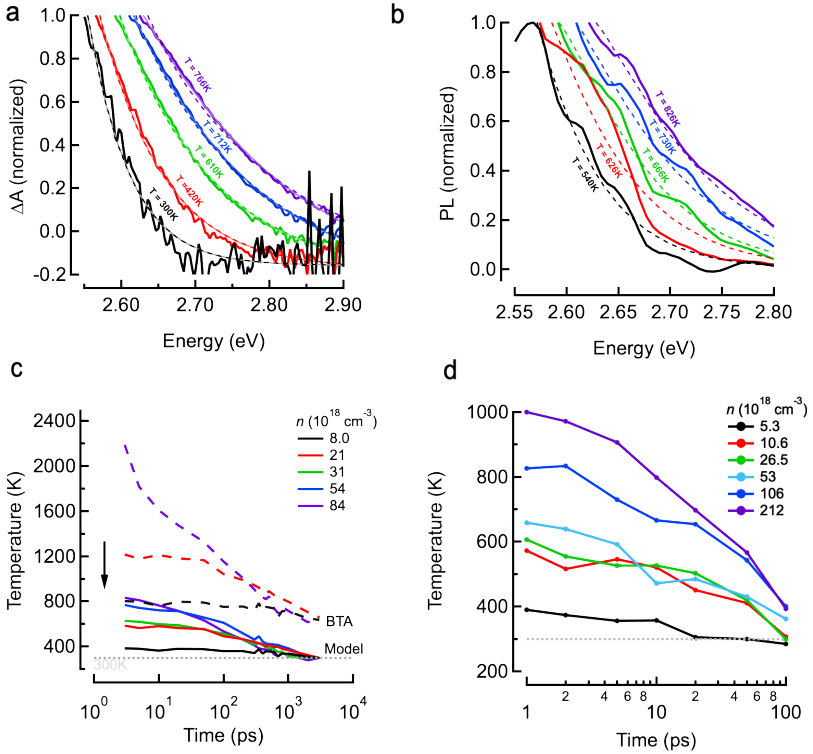


Figure 6.7: Experiments on 12.0 nm CdS NCs. (a) Normalized TA traces $\Delta A(E)$ at varying time delays after photo-excitation with 400 nm (3.1 eV) creating $n = 5.4 \cdot 10^{19} \text{ cm}^{-3}$. (b) Similar experiment but now collecting the transient photo-luminescence. (c) Extracted carrier temperature from the TA traces in (a) using the BTA approximation (dashed) lines and the adapted model (solid lines). (d) Extracted temperature from fits to the PL slopes in (b).

6.5 Conclusions

Our results show that a correct determination of the carrier temperature is best done via transient photoluminescence methods. If transient absorption is used, one should proceed with caution taking the curvatures of the energy bands explicitly into account. Only in the case of band-symmetric semiconductors can one use a simple single exponential decay at high energy to extract temperatures, but also in those cases a correct interpretation of the slope is necessary.

Applying these fits to more material systems would be a good next step. Specifically the case of equal masses, since there the Equations simplify quite a bit. A good material system for this are perovskites, where the effective masses are typically equal^{16,17}. Besides this, it is also possible to adapt the fits for other geometries, by changing the DOS pre-factor (here always a square root factor was used). For example, using the input of the $k \cdot p$ calculations in Chapter 4, a DOS function can be derived. With this, from the TA high energy tails also a temperature could be found.

Bibliography

- ¹ Qing Zhang, Qiuyu Shang, Rui Su, T Thu Ha Do, and Qihua Xiong. Halide perovskite semiconductor lasers: materials, cavity design, and low threshold. *Nano Letters*, 21(5):1903–1914, 2021.
- ² Weiqiang Xie, Yunpeng Zhu, Suzanne Bisschop, Tangi Aubert, Zeger Hens, Dries Van Thourhout, and Pieter Geiregat. Colloidal Quantum Dots Enabling Coherent Light Sources for Integrated Silicon-Nitride Photonics. *IEEE J. Sel. Top. Quant.*, 23(5):1–13, 2017.
- ³ Namyoung Ahn, Young-Shin Park, Clément Livache, Jun Du, Kivanc Gungor, Jaehoon Kim, and Victor I Klimov. Optically excited lasing in a cavity-based, high-current-density quantum dot electroluminescent device. *Advanced Materials*, page 2206613, 2022.
- ⁴ Joel Q Grim, Sotirios Christodoulou, Francesco Di Stasio, Roman Krahne, Roberto Cingolani, Liberato Manna, and Iwan Moreels. Continuous-wave Biexciton Lasing at Room Temperature Using Solution-Processed Quantum Wells. *Nat. Nanotechnol.*, 9:891–895, oct 2014.
- ⁵ Martin A Green, Anita Ho-Baillie, and Henry J Snaith. The emergence of perovskite solar cells. *Nature photonics*, 8(7):506–514, 2014.
- ⁶ Sachin Dev Verma, Qifei Gu, Aditya Sadhanala, Vijay Venugopalan, and Akshay Rao. Slow carrier cooling in hybrid pb-sn halide perovskites. *ACS Energy Letters*, 4(3):736–740, 2019.
- ⁷ Linjie Dai, Zeyu Deng, Florian Auras, Heather Goodwin, Zhilong Zhang, John C. Walmsley, Paul D. Bristowe, Felix Deschler, and Neil C. Greenham. Slow carrier relaxation in tin-based perovskite nanocrystals. *Nature Photonics*, 15(9):696–702, 2021.
- ⁸ Junsheng Chen, Maria E. Messing, Kaibo Zheng, and Tonu Pullerits. Cation-dependent hot carrier cooling in halide perovskite nanocrystals. *Journal of the American Chemical Society*, 141:3532–3540, 2019.

- ⁹ M Price, J Butkus, T Jellicoe, A Sadhanala, A Briane, J Halpert, K Broch, J Hodgkiss, R Friend, and F Deschler. Hot Carrier Cooling and Photo-induced Refractive Index Changes in Organic-Inorganic Lead Halide Perovskites. *Nat. Commun.*, 6(May):1–8, 2015.
- ¹⁰ M. Li, S. Bhaumik, T. W. Goh, M. S. Kumar, N. Yantara, M. Gratzel, S. Mhaisalkar, N. Mathews, and T. C. Sum. Slow cooling and highly efficient extraction of hot carriers in colloidal perovskite nanocrystals. *Nature Communications*, 8:14350–14350, 2017. NULL.
- ¹¹ Jianfeng Yang, Xiaoming Wen, Hongze Xia, Rui Sheng, Qingshan Ma, Jincheol Kim, Patrick Tapping, Takaaki Harada, Tak W. Kee, Fuzhi Huang, Yi-Bing Cheng, Martin Green, Anita Ho-Baillie, Shujuan Huang, Santosh Shrestha, Robert Patterson, and Gavin Conibeer. Acoustic-optical phonon up-conversion and hot-phonon bottleneck in lead-halide perovskites. *Nature Communications*, 8:14120–14120, 2017.
- ¹² Paris Papagiorgis, Loredana Protesescu, Maksym V. Kovalenko, Andreas Othonos, and Grigorios Itskos. Long-lived hot carriers in formamidinium lead iodide nanocrystals. *The Journal of Physical Chemistry C*, pages acs.jpcc.7b02308–acs.jpcc.7b02308, 2017.
- ¹³ Jianhui Fu, Qiang Xu, Guifang Han, Bo Wu, Cheng Hon Alfred Huan, Meng Lee Leek, and Tze Chien Sum. Hot carrier cooling mechanisms in halide perovskites. *Nature Communications*, 8(1), 2017.
- ¹⁴ H. Zhu, Kiyoshi Miyata, Yongping Fu, Jue Wang, Prakriti P. Joshi, Daniel Niesner, Kristopher W. Williams, Song Jin, and X. Y. Zhu. Screening in crystalline liquids protects energetic carriers in hybrid perovskites. *Science*, 353(6306):1409–1413, 2016.
- ¹⁵ Jia Wei Melvin Lim, Yue Wang, Jianhui Fu, Qiannan Zhang, and Tze Chien Sum. Spotlight on hot carriers in halide perovskite luminescence. *ACS Energy Letters*, 7(2):749–756, 2022.
- ¹⁶ Pieter Geiregat, Jorick Maes, Kai Chen, Emile Drijvers, Jonathan De Roo, Justin M. Hodgkiss, and Zeger Hens. Using Bulk-like Nanocrys-

- tals To Probe Intrinsic Optical Gain Characteristics of Inorganic Lead Halide Perovskites. *ACS Nano*, 12(10):10178–10188, 2018.
- ¹⁷ Gurivi Reddy Yettapu, Debnath Talukdar, Sohini Sarkar, Abhishek Swarnkar, Angshuman Nag, Prasenjit Ghosh, and Pankaj Mandal. Terahertz conductivity within colloidal cspbbr3 perovskite nanocrystals: remarkably high carrier mobilities and large diffusion lengths. *Nano letters*, 16(8):4838–4848, 2016.

Chapter 7

Transient Phase Effects in Colloidal Nanocrystals

Injecting carriers changes the absorbance of a material, which can be measured through TA spectroscopy. This has been discussed in previous Chapters. Here, we turn toward an other effect that introducing carriers can have: changing the refractive index. These two effects are closely linked, and from one the other can be determined. This is done through the Kramers-Krönig relation applied to the dielectric function, which is possible since it is an analytic function. For colloidal nanocrystals this is linked through the Maxwell-Garnett Effective Medium Approach. By an iterative method, the dielectric function that reproduces the absorption spectrum can be reproduced. This has already been demonstrated in previous work^{1,2}, for the steady-state dielectric function of Quantum Dots, and is expanded upon here for ultrafast effects and different geometries.

Understanding phase effects in photonic devices is crucial both for (a) making devices that use phase effects, like modulators, and (b) understanding the possible resonance shifts that can occur in lasers. From the dielectric function, the refractive index can be calculated of intrinsic colloidal nanocrystals, from which phase effects in devices can be derived.

After describing the used method, it is applied to 2D 4.5 ML CdSe colloidal Quantum Wells, to the CdSe/CdS core/shell QDs, and to the bulk CdS NCs. These results, achieved through modelling, are then compared to direct experimental methods to determine the phase change in colloidal nanocrystals, femtosecond Frequency Domain Interferometry (FDI).

The derivations performed in this Chapter were done by me, based on earlier work. The NPLs used were provided to me by Shalini Singh and Renu Tomar, and the CdSe/CdS QDs and CdS NCs by Margarita Samoli. The FDI measurements were done by Ronnie Tamming.

7.1 Definitions

This work uses many different parameters with different subscripts, we have summarized all these in Table 7.1.

Symbol	Quantity	SI units
$\tilde{\epsilon}$	Intrinsic complex dielectric function	
ϵ_R	Intrinsic real part of dielectric function	
ϵ_I	Intrinsic imaginary part of dielectric function	
$\tilde{\epsilon}_0$	Intrinsic linear complex dielectric function	
$\epsilon_{R,0}$	Intrinsic linear real part of dielectric function	
$\epsilon_{I,0}$	Intrinsic linear imaginary part of dielectric function	
$\epsilon_{R,bulk}$	Real part of dielectric function of a bulk semiconductor	
$\epsilon_{I,bulk}$	Imaginary part of dielectric function of a bulk semiconductor	
ϵ_s	Dielectric function of solvent	
ϵ_m	Dielectric function of medium	
\tilde{n}	Intrinsic complex refractive index	
n	Intrinsic real refractive index	
k	Intrinsic extinction coefficient	
\tilde{n}_0	Intrinsic linear complex refractive index	
n_0	Intrinsic linear real refractive index	
k_0	Intrinsic linear coefficient	
n_{bulk}	Refractive index of a bulk semiconductor	
k_{bulk}	Extinction coefficient of a bulk semiconductor	
n_s	Refractive index of solvent	
n_m	Refractive index of medium	
μ_i	Intrinsic absorption coefficient	m^{-1}
$\mu_{i,0}$	Intrinsic linear absorption coefficient	m^{-1}
A	Absorbance	
L_i	Depolarization factor ($i = x, y, z$)	
$f_{LF,i}$	Local field factor ($i = x, y, z$)	
V	Volume of particle	m^3
σ_a	Absorption cross-section	m^{-2}
f_{osc}	Oscillator strength of the bandgap	
$f_{osc,0}$	Linear oscillator strength of the bandgap	
$\mu_{i,gap}^*$	Integrated intrinsic absorption coefficient of the bandgap	m^{-1}
$\mu_{i,gap}^0$	Integrated intrinsic linear absorption coefficient of the bandgap	m^{-1}
$\Delta\phi$	Change in phase	
f	Volume fraction of the nanoparticle in the solvent	

Table 7.1: Definitions of parameters used in this work.

7.2 Iterative Algorithm

The procedure to extract the refractive index from a linear absorption spectrum uses both the Maxwell-Garnett (MG) effective medium theory and the Kramers-Krönig relations (KK-relations), and is based on previous work by Moreels *et al.*² and Alvas-Santos *et al.*¹, which we generalise here for anisotropic particles.

The MG relation links the intrinsic absorption μ_i of a composite to the the complex valued dielectric function $\tilde{\epsilon} = \epsilon_R + i \cdot \epsilon_I$ of the dispersed semiconductor. The expression for μ_i in the MG model is given as follows:

$$\mu_i = \frac{2\pi}{\lambda n_s} |f_{LF}|^2 \epsilon_I \quad (7.2.1)$$

Using a KK relation, one could trace the latter back to ϵ_R if the μ_i spectrum is known experimentally and obtain the full dielectric function $\tilde{\epsilon} = \epsilon_R + i \cdot \epsilon_I$ and hence refractive index $\tilde{n} = \tilde{\epsilon}^{1/2}$. A complication arises due to the dependence of the local field factor $|f_{LF}|$ on both ϵ_R and ϵ_I of the nanoparticle. The latter makes a direct inversion of Equation 7.2.1 from absorption to ϵ_I impossible. So an iterative procedure must be used, and is derived below.

7.2.1 Maxwell Garnet Effective Medium

As mentioned before, MG effective medium theory states that the intrinsic absorption coefficient can be calculated analytically as (here for a general case):

$$\mu_i = \frac{2\pi}{\lambda n_s} \left(\frac{1}{3} |f_{LF,x}|^2 + \frac{1}{3} |f_{LF,y}|^2 + \frac{1}{3} |f_{LF,z}|^2 \right) \epsilon_I \quad (7.2.2)$$

with the local field factors $f_{LF,i}$ defined as:

$$f_{LF,i} = \frac{\epsilon_s}{\epsilon_s + L_i \cdot (\tilde{\epsilon} - \epsilon_s)} \quad (7.2.3)$$

where $\tilde{\epsilon} = \epsilon_R + i \cdot \epsilon_I$ and $\epsilon_s = n_s^2$, the dielectric constant of the solvent, which is assumed constant in the region of interest. The L_i factor is called

a depolarization factor. We approximate the nanoparticles as ellipsoids (the validity of this approximation is discussed later), allowing to calculate the L factors using the following integral, taking L_z as an example:³

$$L_z = \int_0^\infty \frac{abc}{2(s+c^2)^{3/2}(s+a^2)^{1/2}(s+b^2)^{1/2}} ds \quad (7.2.4)$$

with a, b, c half the length of the nanoparticle in the x, y, z -directions, respectively. The other depolarization factors can be found by cyclic permutation of this integral.

We can also calculate the cross-section from the intrinsic absorption by using

$$\sigma_a(\lambda) = \mu_i(\lambda) \times V \quad (7.2.5)$$

7.2.2 Kramers-Krönig Relations

To find a connection between ϵ_R and ϵ_I , the following KK-relation is used

$$\epsilon_R(\omega) = 1 + \frac{2}{\pi} \int_0^\infty \frac{\omega' \epsilon_I(\omega')}{\omega'^2 - \omega^2} d\omega' \quad (7.2.6)$$

from which is clear that if ϵ_I is known for the entire frequency range, ϵ_R can be calculated. Since the actual data is discrete and as a function of the wavelength this integral will be changed to a sum, and we will sum over wavelengths instead of the frequency using $\omega = \frac{2\pi c}{\lambda}$, with c the speed of light. This allows to rewrite Equation 7.2.6 as:

$$\epsilon_R(\lambda_j) = 1 + \frac{2}{\pi} \sum_{k \neq j} \frac{\lambda_j^2 \Delta\lambda}{\lambda_k (\lambda_j^2 - \lambda_k^2)} \epsilon_I(\lambda_k) \quad (7.2.7)$$

where the $k = j$ term is omitted to avoid infinite values. If a constant step is assumed, we can write $\lambda_j = j\Delta\lambda$ and $\lambda_k = k\Delta\lambda$ (an important note about this will be made later), which can be inserted into (7.2.7) to get to:

$$\epsilon_{R,j} = 1 + \frac{2}{\pi} \sum_{j \neq k} \frac{j^2}{k(j^2 - k^2)} \epsilon_{I,k} \quad (7.2.8)$$

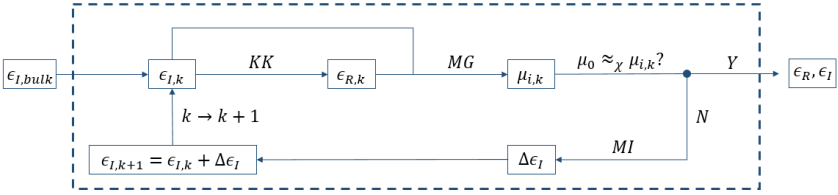


Figure 7.1: Schematic of the applied procedure. KK: Kramers-Krönig relation, MG: Maxwell-Garnett effective medium theory, MI: Matrix Inversion.

For this expression a matrix formalism can easily be used with $\vec{\epsilon}_R$ and $\vec{\epsilon}_I$ as column vectors (similarly, μ_i and the Local Field factors will also become vectors due to this discretization):

$$\vec{\epsilon}_R = 1 + \frac{2}{\pi} \mathbf{A} \cdot \vec{\epsilon}_I \quad (7.2.9)$$

with

$$[\mathbf{A}]_{j,k} = \begin{cases} \frac{j^2}{k(j^2 - k^2)} & k \neq j \\ 0 & k = j \end{cases} \quad (7.2.10)$$

An important note has to be made going from Equation 7.2.7 to Equation 7.2.8. The constant step also assumes that the summation starts from a wavelength of zero, which naturally is not the case for an actual absorption measurement. To account for this, for higher energies than the experiment provides (or shorter wavelengths) the values for the bulk material can be used

$$\epsilon_I(E > E_0) = \epsilon_{I,bulk}(E) \quad (7.2.11)$$

where E_0 is the photon of the highest energy for which the absorption is measured, taken here as 4 eV. Going to higher photon energies above 4 eV, a Drude model can be used:¹

$$\epsilon_I(E > E_{Drude}) = \frac{a}{E(E^2 + b^2)} \quad (7.2.12)$$

with a and b chosen such that the sum rule $\int_0^\infty E\epsilon_I(E)dE = (\pi/2)E_p^2$ is valid¹ where E_p is the bulk plasmon energy.

Looking back now to (7.2.8), it can be rewritten as

$$\epsilon_R(j) = 1 + \frac{2}{\pi} \left(\sum_{j \neq k} \frac{(\lambda_0 + j)^2}{(\lambda_0 + k)[(\lambda_0 + j)^2 - (\lambda_0 + k)^2]} \epsilon_I(\lambda_0 + k) + \sum'_{j \neq k} \frac{j^2}{k(j^2 - k^2)} \epsilon_I(k) \right) \quad (7.2.13)$$

where the first summation can be looked at as a new \mathbf{A} -matrix multiplied with the $\vec{\epsilon}_I$ -vector now only running over the absorption spectrum range and the bulk data (λ_0 is the first actual data point from the experiment), and the second sum includes all wavelengths that contribute from the Drude model and the bulk data. This contribution can be stored in a single vector \vec{v} , since the different data points do not influence each other (ϵ_I is fixed in this region). This leads to the KK-relation that can be used

$$\vec{\epsilon}_R = 1 + \frac{2}{\pi} (\mathbf{A} \cdot \vec{\epsilon}_I + \vec{v}) \quad (7.2.14)$$

7.2.3 Complete Procedure

If we now start from a trial function $\vec{\epsilon}_{I,bulk}$, it is possible to calculate a trial function $\vec{\epsilon}_{R,bulk}$ by applying (7.2.14), and then these can be inserted into (7.2.2) to calculate $\vec{\mu}_{bulk}$, which naturally will be different from the experimental μ_i . Expanding (7.2.2) with $\vec{\epsilon}_I = \vec{\epsilon}_{I,bulk} + \Delta\vec{\epsilon}$ and $\vec{\epsilon}_R = \vec{\epsilon}_{R,bulk} + \Delta\vec{\epsilon}$, it can be expressed as follows

$$\vec{M} = \mathbf{C} \cdot \Delta\vec{\epsilon}_I + \mathbf{D} \cdot \Delta\vec{\epsilon}_R \quad (7.2.15)$$

with

$$\vec{M} = \vec{\mu}_i - \sum_{n=x,y,z} \vec{\mu}_{i,n}^{(0)} \quad (7.2.16)$$

$$[\mathbf{C}]_{j,k} = \begin{cases} \sum_{n=x,y,z} \mu_{i,n}^{(0)}(j) \left(I_n^{(1)}(j) + \frac{1}{\epsilon_{I,bulk}(j)} \right) & j = k \\ 0 & j \neq k \end{cases} \quad (7.2.17)$$

$$[\mathbf{D}]_{j,k} = \begin{cases} \sum_{n=x,y,z} \mu_{i,n}^{(0)}(j) R_n^{(1)}(j) & j = k \\ 0 & j \neq k \end{cases} \quad (7.2.18)$$

where the $\vec{R}_n^{(1)}$ and $\vec{I}_n^{(1)}$ factors are defined as follows

$$\vec{R}_n^{(1)} = -\frac{|\vec{f}_{LF,n}^{(0)}|^2}{\epsilon_s^2} 2L_n (\epsilon_s + L_n \cdot (\vec{\epsilon}_{R,bulk} - \epsilon_s)) \quad (7.2.19)$$

$$\vec{I}_i^{(1)} = -\frac{|\vec{f}_{LF,n}^{(0)}|^2}{\epsilon_s^2} 2L_n^2 \vec{\epsilon}_{I,bulk} \quad (7.2.20)$$

where the zero-order absorption and local field factors are found by inserting the trial functions directly into Equation 7.2.2 and Equation 7.2.3. Note that $[\mathbf{C}]_{j,k}$ becomes infinite when $\epsilon_{I,bulk} = 0$

Since the vector \vec{v} does not change, the KK-relation between $\Delta \vec{\epsilon}_I$ and $\Delta \vec{\epsilon}_R$ becomes $\Delta \vec{\epsilon}_R = (2/\pi) \mathbf{A} \cdot \Delta \vec{\epsilon}_I$, which can be inserted into Equation 7.2.15 to get a direct link between $\vec{\mu}_i$ and $\Delta \vec{\epsilon}_I$:

$$\Delta \vec{\epsilon}_I = [\mathbf{C} + (2/\pi) \mathbf{D} \cdot \mathbf{A}]^{-1} \cdot \vec{M} \quad (7.2.21)$$

then, by again applying the KK-relation $\Delta \vec{\epsilon}_R$ can be found and the new $\vec{\epsilon}_R$ and $\vec{\epsilon}_I$ can be calculated, which will in the next step replace $\epsilon_{R,bulk}$ and $\epsilon_{I,bulk}$. By now using these to calculate a new $\vec{\mu}_0$ we can repeat the process, until $\vec{\mu}_0 \approx_\chi \vec{\mu}_i$, which means that the difference between $\vec{\mu}_i$ and $\vec{\mu}_0$ is smaller than χ (χ chosen arbitrarily).

After calculating (ϵ_R, ϵ_I) , we can find the refractive index and extinction coefficient by using

$$n = \sqrt{\frac{|\vec{\epsilon}| + \epsilon_R}{2}} \quad (7.2.22)$$

$$k = \sqrt{\frac{|\vec{\epsilon}| - \epsilon_R}{2}} \quad (7.2.23)$$

Using these formulas we can determine the ‘‘intrinsic’’ refractive index, when space would be fully occupied with nanocrystals.

7.3 Phase shift Calculation of Composite Media

The refractive index changes calculated through application of the KK-based algorithm present us with the change of the platelet's refractive index. However, nanoplatelets will always be used in the context of a composite medium with volume fraction f , either as a colloidal dispersion ($f \ll 1$) or a close-packed film ($f \approx 1$). The composite medium's "effective" (subscript m) dielectric function for a certain polarization direction $n = x, y, z$ can be written as:

$$\epsilon_{n,m} = \epsilon_s \frac{\epsilon_s + [L_n \cdot (1 - f) + f](\tilde{\epsilon}_n - \epsilon_s)}{\epsilon_s + L_n \cdot (1 - f)(\tilde{\epsilon}_n(\lambda) - \epsilon_s)} \quad (7.3.1)$$

where L_n is again the depolarization factor and using the fact that the nanoparticles are randomly oriented, the actual dielectric function becomes:

$$\epsilon_m = \frac{1}{3} \cdot [\epsilon_{x,m} + \epsilon_{y,m} + \epsilon_{z,m}] \quad (7.3.2)$$

Combining Equation 7.3.2 and Equation 7.2.22 we can find n_m of the composite medium, which allows us to get a theoretical value for the expected phase shift under certain excitation.

Finally, we then can find the change in refractive index by extracting the refractive index without excitation: $\Delta n_m(\lambda, t) = n_m(\lambda, t) - n_{0,m}(\lambda)$. The phase change can then be found:

$$\Delta\phi = \Delta n_m(\Delta n, n_s, f) \times \frac{2\pi}{\lambda} L \quad (7.3.3)$$

where L is the cuvette length. This phase change can be directly compared to the Frequency Domain Interferometry data. Only by going through this procedure do we find a perfect match between the KK algorithm and the measurement.

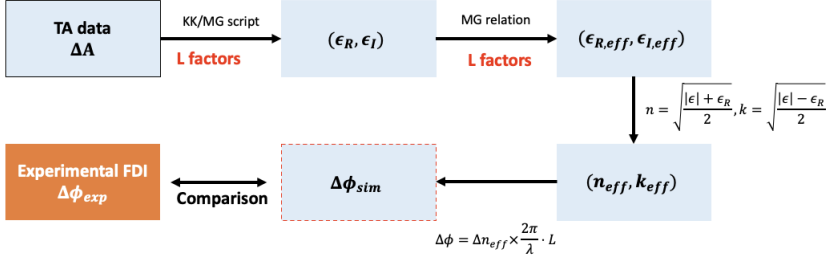


Figure 7.2: Schematic describing KK algorithm approach to obtain an effective medium phase change which can be compared to the experimental FDI output.

7.4 4.5ML CdSe Colloidal Quantum Wells

The algorithm is first used on 4.5ML CdSe nanoplatelets. Their strong anisotropy and high size selectiveness leads to very strong excitonic peaks, which will also translate to strong phase effects. In the next Section, the material is discussed, together with TA data and the found transient phase effects.

7.4.1 Material Description

Synthesis of 4.5 ML platelets 4.5 monolayer CdSe nanoplatelets were synthesized according to literature procedures and carried out by degassing cadmium myristate (0.34 g), Se (24 mg) and ODE (25 mL) in a three necked flask in vacuum and backfilling with N_2 .^{4,5} To this solution, 0.08 g of cadmium acetate was added at 205 °C when the solution turned yellow. Next, the solution was heated at 240 °C for 10 minute and 1.6 g of cadmium oleate in ODE was added at end. Samples were washed with a hexane/ethanol mixture. For spectroscopy, the CdSe platelets were dispersed in a transparent solvent (hexane) to achieve optical densities of 0.1 at the first heavy-hole exciton transition (510 nm). The photoluminescence quantum yield was determined using an integrating sphere after

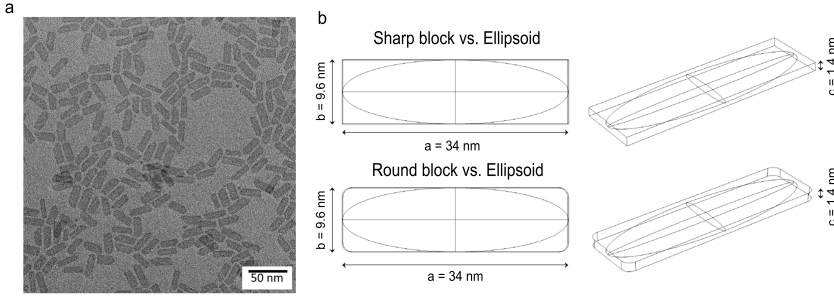


Figure 7.3: (a) TEM imaging showing the $34 \times 9.6 \text{ nm}^2$ nanoplatelets used in this work. (b) Dimensions of the simulated shapes for the local field factors.

CW photo-excitation at 400 nm.

7.4.2 Intrinsic Absorption Coefficient

To use the algorithm we need to calculate the intrinsic absorption coefficient at short wavelengths, where we assume it is the same as for bulk CdSe. Knowing this we can rescale the entire absorption spectrum to the intrinsic value.

Focusing on 300 nm, we can use tabulated values for the dielectric function of CdSe $(7.4 + 8.2 \cdot i)^6$ and the refractive index of hexane, $n_s = 1.405$. Finally, taking the dimensions of the platelets into account ($a = 17 \text{ nm}$; $b = 4.8 \text{ nm}$; $c = 0.68 \text{ nm}$), we can calculate the different factors leading to μ_i at 300 nm. The depolarization factors are calculated as:

$$\begin{aligned}
 L_z &= \int_0^\infty \frac{a^3 r R}{2(s + r^2 a^2)^{3/2} (s + a^2)^{1/2} (s + R^2 a^2)^{1/2}} ds = 0.8648 \\
 L_y &= \int_0^\infty \frac{a^3 r R}{2(s + a^2)^{3/2} (s + R^2 a^2)^{1/2} (s + r^2 a^2)^{1/2}} ds = 0.0181 \quad (7.4.1) \\
 L_x &= \int_0^\infty \frac{a^3 r R}{2(s + R^2 a^2)^{3/2} (s + r^2 a^2)^{1/2} (s + a^2)^{1/2}} ds = 0.1171
 \end{aligned}$$

where $r = c/a$ and $R = b/a$. The local field factors are obtained as: $(f_{LF,x}; f_{LF,y}; f_{LF,z}) = (0.71; 0.95; 0.20)$. This leads to an average local

field factor $f_{LF} = \frac{1}{3} \times (f_{LF,x}^2 + f_{LF,y}^2 + f_{LF,z}^2)$ of 0.482. The validity of these approximated depolarisation factors is checked below. Combining the above, we find:

$$\mu_{i,0}(300 \text{ nm}) = 5.9 \times 10^5 \text{ cm}^{-1} \quad (7.4.2)$$

One can translate this μ_i to different wavelengths by means of the linear absorption spectrum A_0 : $\mu_{i,0}(\lambda) = \mu_{i,0}(300 \text{ nm}) \times \frac{A_0(\lambda)}{A_0(300 \text{ nm})}$. Now we can also translate this into an absorption cross section using the previously mentioned relation $\sigma_a(\lambda) = \mu_i(\lambda) \times V$:

$$\begin{aligned} \sigma_{300} &= 5.9 \cdot 10^5 \text{ cm}^{-1} \times 446.5 \cdot 10^{-21} \text{ cm}^3 = 2.7 \cdot 10^{-13} \text{ cm}^2 \\ \sigma_{400} &= 1.8 \cdot 10^5 \text{ cm}^{-1} \times 446.5 \cdot 10^{-21} \text{ cm}^3 = 7.9 \cdot 10^{-14} \text{ cm}^2 \end{aligned} \quad (7.4.3)$$

One can also determine μ_i experimentally by measuring the UV/VIS spectrum of a dispersion of NPLs and normalizing the spectrum to the volume fraction determined separately by a combination of microscopy (TEM) and elemental analysis (ICP). This was done by Achtstein *et al.* who found excellent correspondence with the bulk approximation route outlined above.³ As such, we can confidently state that we know the intrinsic absorption coefficient spectrum of our CdSe NPLs.

7.4.2.1 Exact vs. approximated depolarisation factors

In this work we use the ellipsoid approximation of the nanoplatelets to calculate their depolarization factors, since there is a simple analytical formula for this case, see Equation 7.4.1. Here, we are going to compare the local field factors following from that approach, to those calculated with a numerical method but with a more exact shape.^{7,8}

We chose to calculate the local field factors both for a sharp and rounded block, with the same parameters as the ellipsoid ($34 \times 9.6 \times 1.36 \text{ nm}^3$), see Figure 7.3. The local field factors are also numerically calculated for the ellipsoid. The results are summarized in Table 7.2. First of all, we can

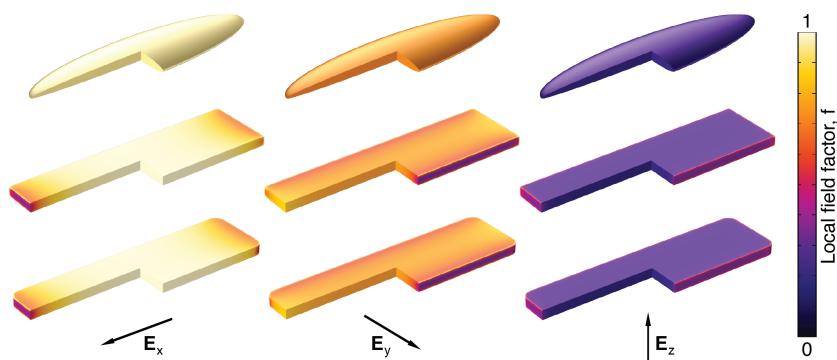


Figure 7.4: Local field factor distribution for various shapes: (top) ellipsoid, (middle) sharp edged beam and (bottom) round edged beam. The columns refer to different orientations of the electric field.

	$f_{LF,x}$	$f_{LF,y}$	$f_{LF,z}$	$\frac{1}{3} \cdot \sum f_{LF,n} ^2$
ellipsoid (analytical)	0.95	0.71	0.2	0.4822
ellipsoid (numerical)	0.951	0.705	0.204	0.481
block (sharp)	0.917	0.687	0.223	0.4542
block (rounded)	0.916	0.686	0.222	0.453

Table 7.2: Summarized results of the local field factors.

see that the numerical method shows us very similar results as the analytical formula. If we compare the ellipsoid values to sharp and rounded block for example, we see only a couple of percent of difference.

If we look at the distribution of the local field factors through the shape we do see clear differences (see Figure 7.4): they are constant for the ellipsoid but vary for the blocks, mostly toward the edges. However, if we get the average local field factor by integration over the total volume, these very local fluctuations wash out. This shows that the ellipsoidal approximation is a valid concept to calculate the depolarization factors.

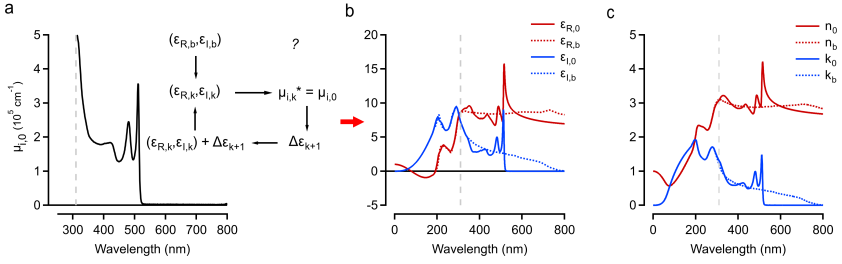


Figure 7.5: Steady state complex refractive index of CdSe NPLs (a) The ground state absorption spectrum plotted as the intrinsic absorption coefficient $\mu_{i,0}$. Inset shows a summary of the iterative procedure used to translate the $\mu_{i,0}$ spectrum into the permittivity function $\tilde{\epsilon}_0$, which is shown in (b). Dotted lines indicate the bulk dielectric function of CdSe. (c) Calculated complex linear refractive index $\tilde{n}_0 = n_0 + i \cdot k_0$ of the NPLs from the permittivity function in (b). The (complex) bulk CdSe refractive index is shown in dotted lines as reference. The vertical grey dashed line indicate the 4 eV point from which the dielectric function is assumed bulk-like towards shorter wavelengths.

7.4.3 Refractive Index in Ground State

Knowing the linear intrinsic absorption spectrum of the CdSe NPLs, the depolarisation factors, and the dielectric function of bulk CdSe (as a guess), we can in a first step calculate the linear dielectric function for this material, which will lead to the linear refractive index and extinction coefficient. The results of this calculation are shown in Figure 7.5. The actual calculation is made above 300 nm, for shorter wavelengths or higher energies it is assumed that the dielectric function is similar to bulk CdSe. These results are in agreement with Zhang *et al.*⁹, who have done ellipsometry on thin films of CdSe NPLs.

Convergence The convergence process is shown in Figure 7.6, where every correction on ϵ_I is divided by two to show the convergence more clearly. As can be seen, after the first step the shape of ϵ_I already resembles that of the absorbance spectrum very well.

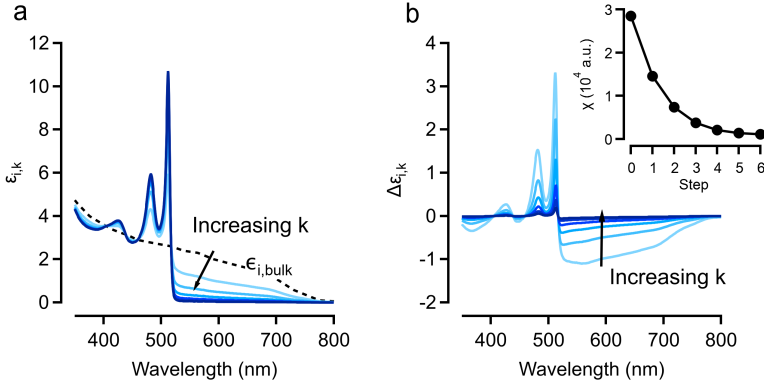


Figure 7.6: (a) ϵ_I after the k -th step in the procedure. (b) The correction on ϵ_I for every step k . The inset shows the error after step k . Note that every correction is divided by two to more clearly show the convergence process.

7.4.4 Refractive Index under Excitation

7.4.4.1 TA data

With the linear dielectric function in hand, we can also apply the algorithm to the non-linear absorbance $A(\lambda, t) = (A_0(\lambda) + \Delta A(\lambda, t))$, normalised to $\mu_i(\lambda, t)$, found through Transient Absorption Spectroscopy. This will yield us the non-linear dielectric function and refractive index, which can be related to the phase-change induced due to high carrier densities. The algorithm is applied for every pump-probe delay separately and then put back into the same data format as a TA map for easy comparison. An example of a TA map used is shown in Figure 7.7. This map is measured with $\langle N \rangle \approx 110$.

Focusing first on the $\mu_i(\lambda, t)$ input, we show in Figure 7.7 (second from top) a summary of the fluence dependence at 3 ps in the visible and near-infrared part of the spectrum. Similar to the observations of Tomar *et al.*, we observe an increased saturation of the HH/LH absorption.¹⁰ The absorbance also turns negative, indicating the occurrence of net optical gain.¹⁰⁻¹² Interestingly, the “deep” bleach in the TA map translates to

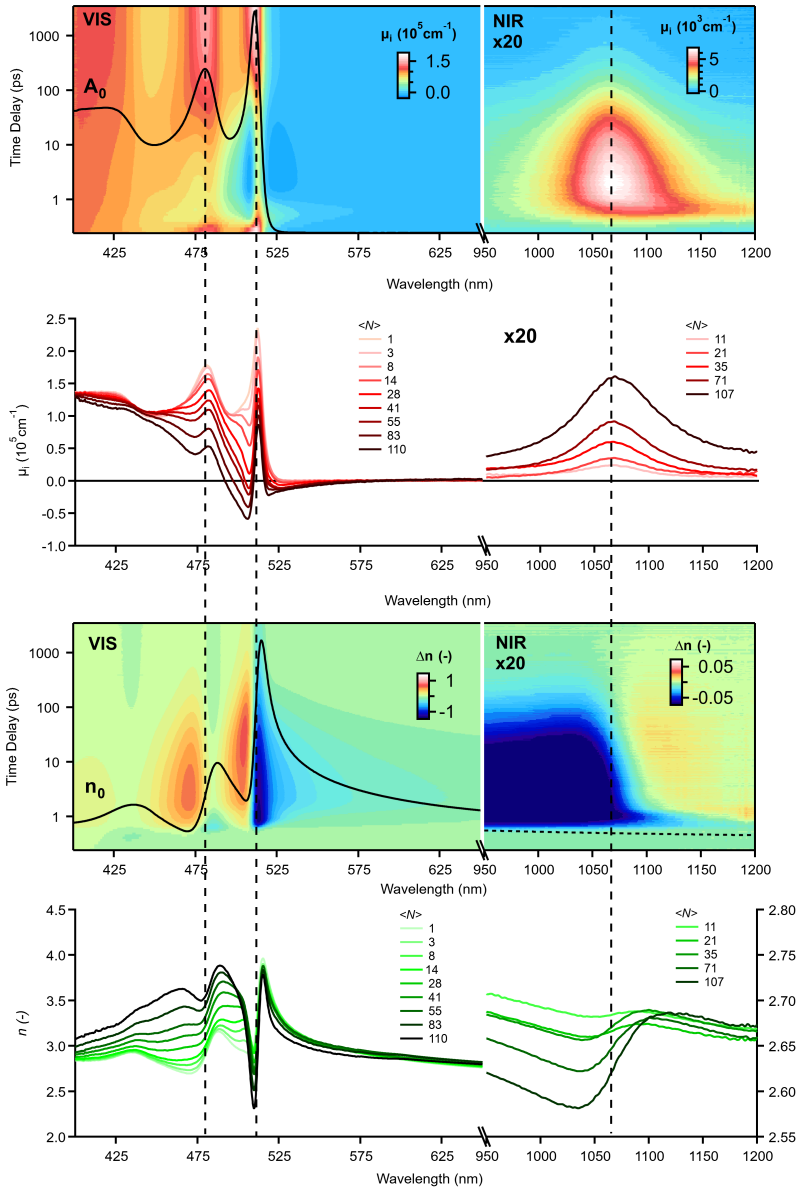


Figure 7.7: Overview of $\mu_i(\lambda, t)$ non-linear absorption spectroscopy. (Top) False color map of μ_i across the visible and near-infrared spectrum (Second from top) Slices of the color maps at 3 ps for increasing fluence, expressed as average number of absorbed photons per NPL, $\langle N \rangle$ (Third from top) Refractive Index map generated through the script (Bottom) Refractive index Slices of the color maps at 3ps for increasing fluence, expressed as average number of absorbed photons per NPL.

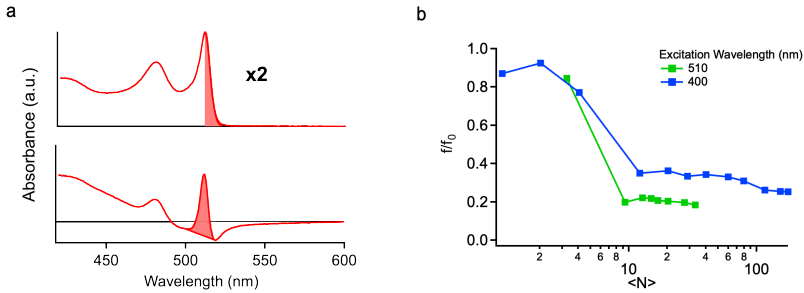


Figure 7.8: (a) Integration of the absorbance spectrum, specifically the heavy-hole exciton absorption shown for both the linear absorption A_0 , giving rise to f_0 (top, here half of the peak is integrated and multiplied by 2) and an excited state spectrum A (bottom), giving rise to $f(\langle N \rangle)$. Due to the presence of charge carriers, it is clear that the HH-exciton absorption / oscillator strength collapses, and this collapse is displayed in (b), again for both off-resonant (blue) and resonant (green) excitation, by means of the ratio f/f_0 . The collapse is more abrupt, and stronger for the resonant excitation scenario.

a very broad effect in the Transient Refractive Index (TRI) map. This effect can be used for our advantage in integrated devices. In the near-infrared, we observe the clear emergence of the well-defined intra-band transition (IB). As confirmed by Diroll *et al.* we can assign this feature to an electron-related intra-band transition.¹³

Figure 7.7 (third from top) shows the calculated map of $\Delta n = n - n_0$, *i.e.* the change of the real part of the refractive index of the NPLs, together with n_0 , the linear refractive index (black line), for $\langle N \rangle = 110$, equivalent to a surface density of $4.5 \times 10^{13} \text{ cm}^{-2}$. We observe a clear connection to the bleach features of Figure 7.7 (second from top) as derivative signatures are observed around the HH and LH exciton positions (485 nm / 512 nm, dashed lines in Figure 7.7 in the visible). Extending into the near-infrared, a sizeable modulation is also observed around IB (dashed line in this NIR). Moreover, a broad sub - band gap modulation is observed in the region of 550 - 950 nm, where no steady state absorption is present.

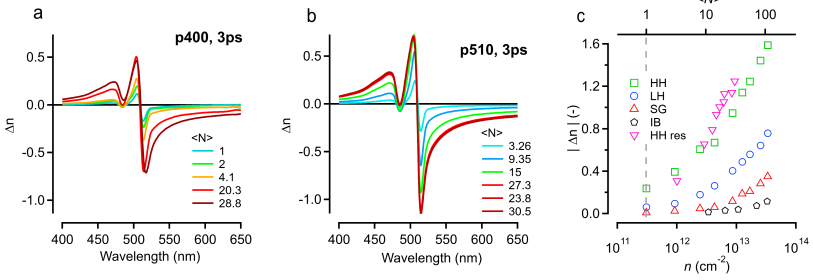


Figure 7.9: Modulation of the refractive index Δn plotted for off-resonant (a) and on-resonance (b) around the HH resonance. The value at 513 nm is plotted on a log scale in (c) to emphasize the resonant pump experiment (pink triangles, right).

7.4.4.2 Oscillator Strength

We integrated the absorbance spectrum around the HH resonance ($\mu_{i,gap}$), which is related to the oscillator strength as follows¹⁴:

$$f_{osc} = \frac{2V_{pl}\epsilon_0 n_s m_e}{e\pi\hbar|f_{LF}|^2} \mu_{i,gap} \quad (7.4.4)$$

Since everything in this expression remains fixed under excitation besides the integrated absorbance of the band gap $\mu_{i,gap}$, the ratio of the oscillator strengths of steady state ($f_{osc,0}$) and excited state (f_{osc}) becomes

$$\frac{f_{osc}}{f_{osc,0}} = \frac{\mu_{i,gap}^*}{\mu_{i,gap}^0} \quad (7.4.5)$$

7.4.4.3 Resonant excitation

Besides this high energy excitation, we also investigated resonant excitation to investigate the effect of temperature on the modulation. We have studied these effects in detail, finding charge cooling bottlenecks at high $\langle N \rangle$.¹⁰ To study the effect on the NPLs refractive index modulation, we performed additional TA experiments using a resonant pump at 510 nm. The latter provides a scenario where no excess energy is left to the charges.

We observe a slightly stronger modulation when pumping on-resonance (510 nm), see Figure 7.9b.

We understand this as follows. The index modulation in essence originates from the collapse of the exciton absorption lines. Their saturation (or bleaching) gives rise to ΔA which in turn results in Δn via the KK-relations. A stronger saturation under resonant pumping would hence lead to a stronger index modulation. This is exactly what is observed when looking at the oscillator strength, as obtained from the linear and transient absorbance (see Figure 7.9a), of the HH-exciton transition. Figure 7.9b shows that the oscillator strength decreases faster for increasing density when pumping resonantly.

7.4.4.4 Polarized Excitation

Besides resonant pumping, we have also looked into polarised excitation. This is of importance due to the anisotropic nature of the NPLs. We proceeded to investigate the effect of the polarization of pump and probe on the final response. Experiments were carried out in co-polarized (xx) and counter-polarized (xy) linear polarization settings for pump-probe respectively. As we observe in Figure 7.10 below, no sizable difference is obtained between both experiments, nor in the kinetics, nor in the shape of the spectrum, and this for both the visible and near-infrared spectrum. If the ΔA data is exactly the same between both polarization sequences, so will the Δn .

7.4.4.5 Discussion

We note that our model yields the modulation of the NPL refractive index and is as such an intrinsic change at the level of the nanoparticle. To directly compare this to the phase shift of the FDI experiments, we need to calculate the effect of a change in the NPL refractive index Δn on the whole composite medium (solvent, NPLs) measured using FDI. Figure 7.11 (left) shows the comparison between the experimental FDI phase change (red) and the phase change obtained from our algorithm

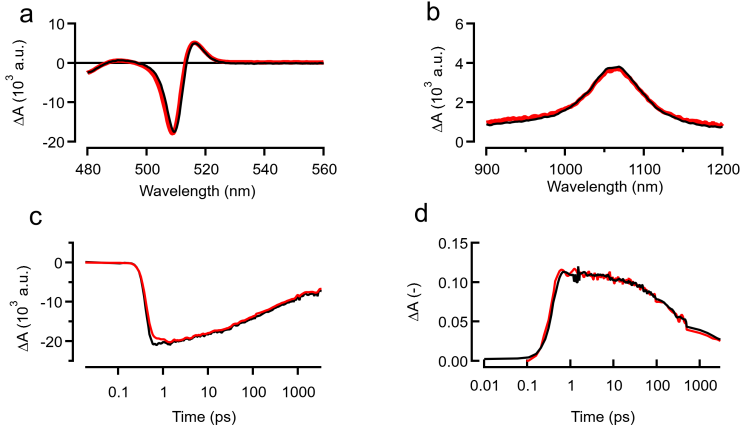


Figure 7.10: Polarization contrast for 400 nm pump and co (black) and cross (red)-polarized probe (a,b) ΔA spectrum around the (a) HH-resonance and (b) intraband transition at 3 ps for crossed (xy) and co (xx) polarized pump-probe sequences. (c) Kinetics for both polarization sequences at the (c) HH resonance and (d) intraband transition.

approach. Both the magnitude, the sharp derivative shape figures around the HH/LH resonances and the sub-gap modulation of the phase shift are retrieved quantitatively. This excellent match again confirms that we can use the iterative algorithm presented earlier to obtain the absolute (and transient) refractive index (changes) reliably.

Having confirmed the KK approach, we proceed in Figures 7.7(c,d) to show the spectra of Δn at 3 ps for increasing carrier densities. Figure 7.9 shows the fluence scaling at select wavelengths: at the HH resonance (510 nm, $n_0 = 3.45$), at the LH resonance (485 nm, $n_0 = 3.2$), sub-band gap (600 nm, $n_0 = 2.9$) and at the near-infrared intra-band transition (IB, 1050 nm, $n_0 = 2.7$). We observe above-unity modulation at high exciton density for HH, corresponding to $\Delta n/n_0 > 0.3$. Tomar *et al.* showed that optical gain occurs in that spectral range so clearly these modulations will affect cavity design for lasers based on these materials.¹⁵ On the LH resonance, the modulation is equally intense leveling off at around

$\Delta n \approx 1$. For the sub-gap modulation at *e.g.* 600 nm, a maximum relative change $\Delta n/n_0 = 0.13$ is observed.

It is worthwhile to compare the values of index modulation obtained to literature reports on 2D systems, such as epitaxial quantum wells or TMDs.^{16–18} Typical refractive index changes are limited to 0.01 for off-resonance and to 0.1 for on-resonance modulation for carrier densities generated electrically close to 10^{13} cm^{-2} . For our experimental scenario NPLs offer stronger modulations at comparable surface density and even exceed epitaxial 2D materials for resonant modulations. The work of Park *et al.* showed that decreasing quantum well thickness down to *ca.* 7 nm improves the modulation depth at fixed carrier density, an effect ascribed to the increased excitonic character of the band edge transitions. The even stronger modulation observed here for the extremely thin 1.37 nm CdSe quantum wells fits within that concept, indicating the importance of excitonic effects.

Rapid multi-exciton recombination will quench the modulation,¹⁹ yet Figure 7.9 shows that even for regimes of single excitations per sheet (vertical dashed line) $\langle N \rangle \ll 1$, or sheet densities below 10^{11} cm^{-2} , a sizeable modulation is achievable. Figure 7.11 shows the full kinetics at the same select wavelengths as Figure 7.9 for a fluence creating $\langle N \rangle = 110^{12}$,^{19–21}. Based on the $1/e^2$ limit, shown as the horizontal dashed line in Figure 7.11, modulations should be feasible at a rate close 3.5 GHz (285 ps) across a wide spectral window.

7.4.5 Verification through FDI Measurements

Finally, to check the found refractive index changes, the 4.5 ML CdSe NPLs were measured in FDI, as described in Section 2.4.5. To compare the measurement to our simulated refractive index change, first some post-processing of data must be done as shown in Figure 7.2 and a $\Delta\phi_{sim}$ can be determined. This is plotted against the FDI data, shown in Figure 7.11a, showing excellent agreement, confirming that the performed simulations are correct.

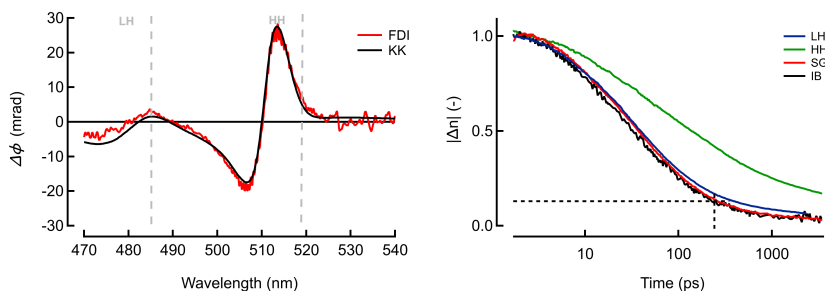


Figure 7.11: (Left) calculated phase change through excitation, overlaid with phase change measured through FDI with excellent agreement. (Right) normalised refractive index change dynamics, useful to calculate possible fastest switching speed. Shown for 4 different wavelength regions of interest.

7.5 Transient Phase Effects in Colloidal CdSe/CdS Quantum Dots

The protocol described above was developed specifically to look at 4.5ML CdSe NPLs, but considering the maturity of the CdSe/CdS core/shell system it is useful to also apply it to these types of NCs. These NCs are more mature in use in photonic devices (cleaner films, more stable operation), and would give opportunities regarding possible use in modulators. Although the protocol is already defined above, slight changes will have to be made which will be discussed when needed. Besides that, we will just stick to describing the data.

7.5.1 Material Description

Typical CdSe/CdS QDs are used with core diameters of about 4 nm, and total diameters of about 7.3 nm. These were shown by Bisschop *et al.*²² to have the best gain metrics, and as such are the typical NCs used in our devices. These are made by using the flash synthesis developed by Drijvers *et al.*²³. Here, a synthesis is used that grows highly luminescent

and multishelled heterostructures. The synthesis is described in Chapter 2.

7.5.2 Intrinsic Absorption Coefficient

We can again determine the intrinsic absorption coefficient. Flash synthesized CdSe/CdS core/shell QDs have a wurtzite phase instead of cubic for the CdSe NPLs, so we need to average the dielectric function over both directions.

$$\epsilon_{CdSe} = \frac{1}{3} \cdot (7.987 + i \cdot 6.211) + \frac{2}{3} \cdot (6.906 + i \cdot 7.288) = 7.27 + i \cdot 6.93 \quad (7.5.1)$$

$$\epsilon_{CdS} = \frac{1}{3} \cdot (6.663 + i \cdot 3.623) + \frac{2}{3} \cdot (6.601 + i \cdot 3.466) = 6.62 + i \cdot 3.52 \quad (7.5.2)$$

By using the protocol to determine the intrinsic absorbance from a multilayered QD system (see Section 2.3.4), we can determine the intrinsic absorbance, using depolarisation factors of $\frac{1}{3}$ for all directions:

$$\mu_{i,0}(300 \text{ nm}) = 1.84 \cdot 10^5 \text{ cm}^{-1} \quad (7.5.3)$$

It must be noted that besides using the intrinsic absorbance at one wavelength to rescale the absorption spectrum, we actually use ϵ_I over the entire spectrum as (1) the initial guess for the dielectric function, and (2) as the pinned bulk values in the wavelength region where there is no data available. In principle, we need to first determine the bulk dielectric function of a CdSe/CdS system (with a specific core/shell structure), in a colloidal dispersion. To make things a bit easier, we choose to just average the bulk dielectric functions of CdSe and CdS based on the volume:

$$\epsilon_I(\lambda) = \frac{V_{core}}{V_{core} + V_{shell}} \times \epsilon_{I,CdSe}(\lambda) + \frac{V_{shell}}{V_{core} + V_{shell}} \times \epsilon_{I,CdS}(\lambda) \quad (7.5.4)$$

which will not be very accurate close to the band gap, but the higher the energy is (or the shorter the wavelength) this approximation becomes better. Indeed, by approximating like this we find an intrinsic absorbance at 300 nm of $1.91 \cdot 10^5 \text{ cm}^{-1}$, which is less than 5% off the calculation above.

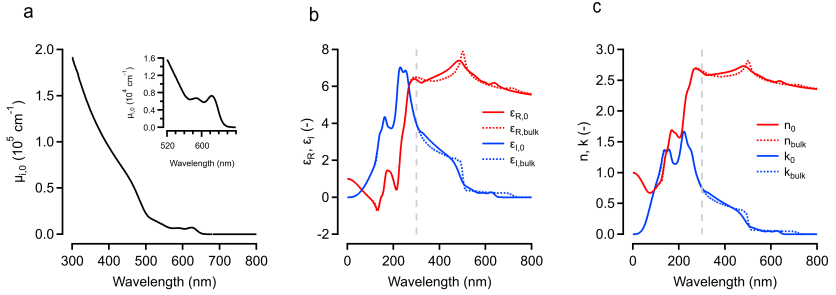


Figure 7.12: (a) Intrinsic Absorbance of CdSe/CdS core/shell QDs, with the inset showing a zoom in around the band gap. (b) (ϵ_I, ϵ_R) of CdSe/CdS (full lines), compared to bulk (dotted lines). (c) (n, k) of CdSe/CdS (full lines), compared to bulk (dotted lines).

7.5.3 Refractive Index in Ground State

Applying the adapted protocol gives us the results shown in Figure 7.12. There are still modifications on the dielectric function due to the confinement, but they are much less drastic compared to the NPL case. This is due to the less pronounced resonances that are seen here. The step-like behaviour that can be seen in the bulk spectra are due to the CdSe dielectric function that starts to contribute. It is worth repeating that in this wavelength region, the averaging method used to calculate the dielectric function is not accurate, only at shorter wavelengths it becomes a decent approximation.

7.5.4 Refractive Index under excitation

Some results of applying the protocol to TA data is shown in Figure 7.13. Similar to the NPLs, we can describe excitations in these QDs as average amount of excitons per dot considering we are in the quantum confinement regime. As discussed in previous chapters, the expected amount of excitons needed for transparency is $\langle N \rangle \approx 1.54$, which indeed we can see in Figure 7.13c). Again, we see that the much less sharp features, caused

by (1) inhomogeneous broadening due to size dispersion, and (2) the much higher excitonic binding energy in 2D materials compared to 0D, yield not as drastic changes in the excited absorption spectrum. This undoubtedly will also translate to less sharp features in the refractive index spectrum, which we indeed see in Figure 7.13d.

Here we can see intrinsic refractive index changes of less than 0.2 maximum, which, however, seem to saturate for certain excitation strengths in the sub-gap region. This makes sense considering the levels in the QD are filled for a certain amount of excitation. This sub-gap region is ideal for modulation since there is no absorption here (this is discussed in more detail in Chapter 10). The strongest effects occur not at the 1S and 1P exciton (around 620 and 580 nm, respectively), but about 20 nm redshifted compared to that. This is especially visible in the Δn map shown in Figure 7.13b, where the 1S exciton at 620 nm shows barely any change (especially for lower excitation powers).

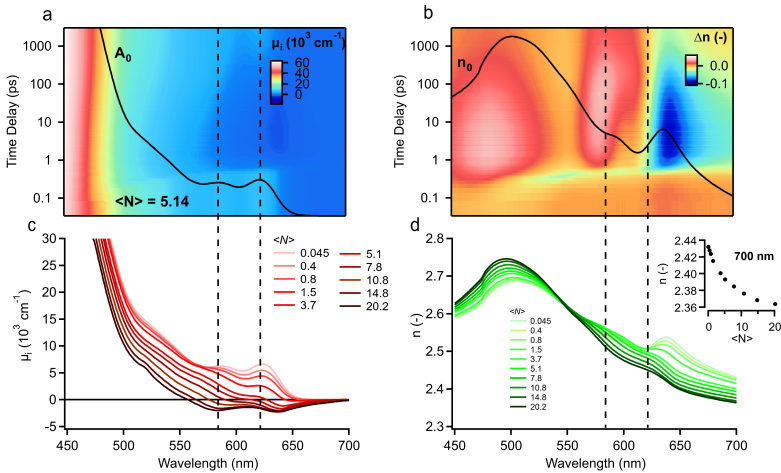


Figure 7.13: (a) Absorption map under excitation, with $\langle N \rangle = 5.18$. (b) Δn map found from transforming the map shown in (a). (c) Absorption under various amounts of excitation, at a pump probe delay of 3 ps. (d) Refractive index under various amounts of excitation, at a pump probe delay of 3 ps. The inset shows the refractive index as a function of the excitation power, at 700 nm.

7.6 Transient Phase Effects in bulk CdS colloidal NCs

As a final material, it is worth looking into the bulk CdS NCs and the changes in refractive index that can be seen here. Due to the extremely high ΔA changes measured in TA, it is probable to think that this will give rise to very large Δn shifts as well.

7.6.1 Material Description

As the material synthesis is already discussed thoroughly in Section 5.2.1, we just repeat here that these are bulk-like CdS NCs, with wurtzite phase, with diameters of about 12 nm (larger than the Bohr diameter of around 6 nm).

7.6.2 Intrinsic Absorption Coefficient

Since this system only contains a single material, we can relatively simply determine the intrinsic absorption at 300 nm. We can simply re-use the values from Equation 7.5.2. From this, we can then calculate

$$\mu_{i,0}(300 \text{ nm}) = 1.82 \cdot 10^5 \text{ cm}^{-1} \quad (7.6.1)$$

where again depolarisation factors of $\frac{1}{3}$ in every direction are used.

7.6.3 Refractive Index in Ground State

Applying the protocol yields the results shown in Figure 7.14. Perhaps unsurprisingly, it is only a slight modification of the bulk CdS properties, mainly close to the band edge. The inset in Figure 7.14a shows the absorption near the band edge, where slight bumps can be seen: either due to (1) just noise, or (2) a small amount of tiny CdS particles present in the sample, where there still is confinement present. These bumps would then correspond to the exciton energy of that small subset of particles. This effect is the reason why there are small changes near the bandgap.

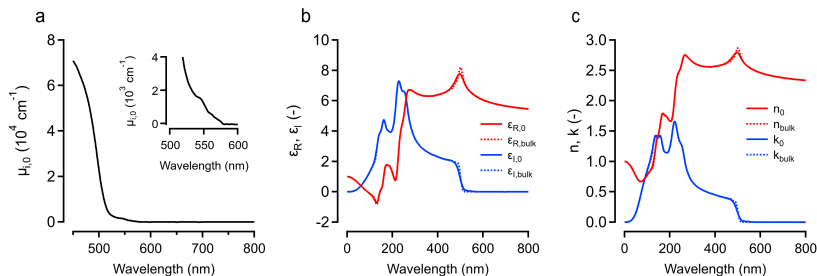


Figure 7.14: (a) Intrinsic Absorbance of bulk CdS NCs. The inset shows a zoom around the band gap, showing small bumps, probably due to a small subset of NCs that are still showing confinement. (b) (ϵ_I, ϵ_R) of bulk CdS NCs (full lines), compared to bulk (dotted lines). (c) (n, k) of bulk CdS NCs (full lines), compared to bulk (dotted lines).

This is noticeable for all four properties (ϵ_I, ϵ_R) (Figure 7.14b) and (n, k) (Figure 7.14c).

7.6.4 Refractive Index under Excitation

Looking at the TA data in Figure 7.15, we see, as shown before, the typical relatively featureless spectrum in Figure 7.15c, as also discussed in Chapter 5. This translates to Figure 7.15, where changes are seen of up to 0.5, much larger than the CdSe/CdS case. Here, the sub-gap changes to the refractive index seem to behave quite linearly as a function of the excitation (the inset is at 600 nm). This corresponds well to the absorption spectra as well, where seemingly it is possible to dump an infinite amount of charges into the system and gain will keep building up.

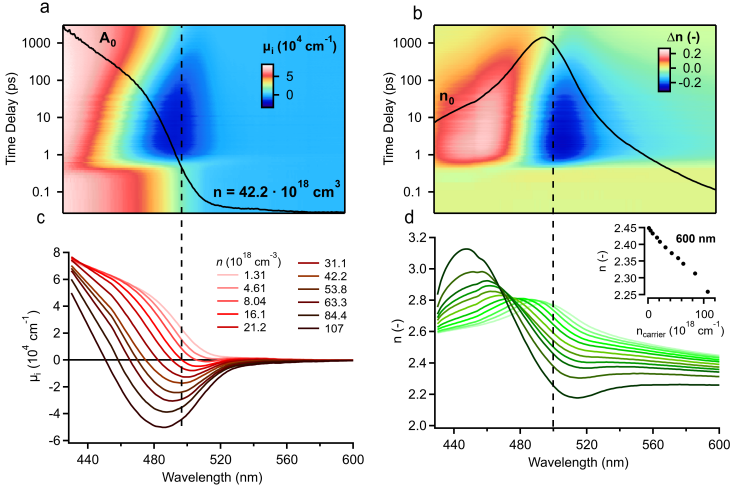


Figure 7.15: (a) Absorption map under excitation, with $\langle N \rangle = 5.18$. (b) Δn map found from transforming the map shown in (a). (c) Absorption under various amounts of excitation, at a pump probe delay of 3 ps. (d) Refractive index under various amounts of excitation, at a pump probe delay of 3 ps. The inset shows the refractive index as a function of excitation strength at 600 nm, showing linear behaviour.

7.7 Conclusions

In this Chapter, a framework is presented that can be used for colloidal NCs of random geometry, which can calculate intrinsic refractive indices for materials in rest. This framework can also be used on materials that are being optically excited. This was cross-checked by doing direct phase change measurements on the 4.5 ML CdSe NPLs, and showed that the framework works as expected. In principle, this could be routinely used on ΔA data to find the complementary Δn data, as shown by its use on the two other data sets presented (CdSe/CdS QDs, CdS bulk NCs). This allows for immediate characterisation of the colloidal NC in question for possible use as either light emitters or modulators. The latter is something that as of yet has not been shown for colloidal NCs, and is discussed further in Chapter 10.

Bibliography

- ¹ Marcelo Alves-Santos, Rosa Di Felice, and Guido Goldoni. Dielectric Functions of Semiconductor Nanoparticles from the Optical Absorption Spectrum: The Case of CdSe and CdS. *J. Phys. Chem. C*, 114(9):3776–3780, mar 2010.
- ² Iwan Moreels, Guy Allan, Bram De Geyter, Ludger Wirtz, Christophe Delerue, and Zeger Hens. Dielectric Function of Colloidal Lead Chalcogenide Quantum Dots Obtained by a Kramers-Krönig Analysis of the Absorbance Spectrum. *Phys. Rev. B*, 81(23):1–7, jun 2010.
- ³ Alexander W. Achtstein, Andrei Schliwa, Anatol Prudnikau, Marya Hardzei, Mikhail V. Artemyev, Christian Thomsen, and Ulrike Woggon. Electronic Structure and Exciton-Phonon Interaction in Two-Dimensional Colloidal CdSe Nanosheets. *Nano Lett.*, 12(6):3151–3157, 2012.
- ⁴ S. Ithurria, M. D. Tessier, B. Mahler, R. P. S. M. Lobo, B. Dubertret, and Al. L. Efros. Colloidal Nanoplatelets with Two-Dimensional Electronic Structure. *Nat. Mater.*, 10(10):1–6, oct 2011.
- ⁵ Shalini Singh, Renu Tomar, Stephanie ten Brinck, Jonathan De Roo, Pieter Geiregat, Jose C. Martins, Ivan Infante, and Zeger Hens. Colloidal CdSe Nanoplatelets, a Model for Surface Chemistry/Opto-Electronic Property Relations in Semiconductor Nanocrystals. *J. Am. Chem. Soc.*, 140:13292–13300, 2018.
- ⁶ S. Adachi. *Optical Constants of Crystalline and Amorphous Semiconductors*. Springer Science, 1999.
- ⁷ Yera Ye Ussembayev, Zeger Hens, and Kristiaan Neyts. Contrasting anisotropy of light absorption and emission by semiconductor nanoparticles. *ACS Photonics*, 6(5):1146–1152, 2019.

-
- ⁸ Yera Y Ussembayev, Natalia K Zawacka, Filip Strubbe, Zeger Hens, and Kristiaan Neyts. Waveguiding of photoluminescence in a layer of semiconductor nanoparticles. *Nanomaterials*, 11(3):683, 2021.
- ⁹ Zitong Zhang, Yi Tian Thung, Xiaoxuan Chen, Lin Wang, Weijun Fan, Lu Ding, and Handong Sun. Study of Complex Optical Constants of Neat Cadmium Selenide Nanoplatelets Thin Films by Spectroscopic Ellipsometry. *J. Phys. Chem. Lett.*, 12:191–198, 2021.
- ¹⁰ Renu Tomar, Aditya Kulkarni, Kai Chen, Shalini Singh, Dries Van Thourhout, Justin M Hodgkiss, Laurens DA Siebbeles, Zeger Hens, and Pieter Geiregat. Charge carrier cooling bottleneck opens up nonexcitonic gain mechanisms in colloidal cdse quantum wells. *J. Phys. Chem. C*, 123(14):9640–9650, 2019.
- ¹¹ Joel Q Grim, Sotirios Christodoulou, Francesco Di Stasio, Roman Krahné, Roberto Cingolani, Liberato Manna, and Iwan Moreels. Continuous-wave Biexciton Lasing at Room Temperature Using Solution-Processed Quantum Wells. *Nat. Nanotechnol.*, 9:891–895, oct 2014.
- ¹² Pieter Geiregat, Dries Van Thourhout, and Zeger Hens. A bright future for colloidal quantum dot lasers. *NPG Asia Materials*, 11(1):41, 2019.
- ¹³ Benjamin T. Diroll, Menglu Chen, Igor Coropceanu, Kali R. Williams, Dmitri V. Talapin, Philippe Guyot-Sionnest, and Richard D. Schaller. Polarized Near-infrared Intersubband Absorptions in CdSe Colloidal Quantum Wells. *Nat. Comm.*, 10(1):1–9, 2019.
- ¹⁴ Pieter Geiregat, Carmelita Rodá, Ivo Tanghe, Shalini Singh, Alessio Di Giacomo, Delphine Lebrun, Gianluca Grimaldi, Jorick Maes, Dries Van Thourhout, Iwan Moreels, et al. Localization-limited exciton oscillator strength in colloidal cdse nanoplatelets revealed by the optically induced stark effect. *Light: Science & Applications*, 10(1):1–11, 2021.
- ¹⁵ Jianfeng Yang, Xiaoming Wen, Hongze Xia, Rui Sheng, Qingshan Ma, Jincheol Kim, Patrick Tapping, Takaaki Harada, Tak W. Kee,

- Fuzhi Huang, Yi-Bing Cheng, Martin Green, Anita Ho-Baillie, Shujuan Huang, Santosh Shrestha, Robert Patterson, and Gavin Conibeer. Acoustic-optical phonon up-conversion and hot-phonon bottleneck in lead-halide perovskites. *Nature Communications*, 8:14120–14120, 2017.
- ¹⁶ S. H. Park, J. F. Morhange, A. D. Jeffery, R. A. Morgan, A. Chavez-Pirson, H. M. Gibbs, S. W. Koch, N. Peyghambarian, M. Derstine, A. C. Gossard, J. H. English, and W. Weigmann. Measurements of Room-Temperature Band-Gap-Resonant Optical Nonlinearities of GaAs/AlGaAs Multiple Quantum Wells and Bulk GaAs. *Appl. Phys. Lett.*, 52(15):1201–1203, 1988.
- ¹⁷ E. Garmire. Resonant Optical Nonlinearities in Semiconductors. *IEEE J. Sel. Top. Quant.*, 6(6):1094–1110, 2000.
- ¹⁸ Yiling Yu, Yifei Yu, Lujun Huang, Haowei Peng, Liwei Xiong, and Linyou Cao. Giant Gating Tunability of Optical Refractive Index in Transition Metal Dichalcogenide Monolayers. *Nano Lett.*, 17:3613–3618, 2017.
- ¹⁹ Qiuyang Li and Tianquan Lian. Area- and Thickness-Dependent Biexciton Auger Recombination in Colloidal CdSe Nanoplatelets: Breaking the Universal Volume Scaling Law. *Nano Lett.*, 17:3152–3158, 2017.
- ²⁰ Lucas T Kunneman, Juleon M Schins, Silvia Pedetti, Hadrien Heuclin, Ferdinand C Grozema, Arjan J Houtepen, Benoit Dubertret, and Laurens D A Siebbeles. Nature and Decay Pathways of Photoexcited States in CdSe and CdSe/CdS Nanoplatelets. *Nano Lett.*, 14(12):7039–7045, 2014.
- ²¹ Matthew Pelton. Carrier Dynamics, Optical Gain, and Lasing with Colloidal Quantum Wells. *J. Phys. Chem. C*, 122:10659–10674, 2018.
- ²² S. Bisschop, P. Geiregat, T. Aubert, and Z. Hens. The Impact of Core/Shell Sizes on the Optical Gain Characteristics of CdSe/CdS Quantum Dots. *ACS Nano*, 12:9011–9021, 2018.

- ²³ Emile Drijvers, Jonathan De Roo, Pieter Geiregat, Krisztina Feher, Zeger Hens, and Tangi Aubert. Revisited wurtzite cdse synthesis: A gateway for the versatile flash synthesis of multishell quantum dots and rods. *Chemistry of Materials*, 28(20):7311–7323, 2016.

Part III

Colloidal Nanocrystals in Integrated Photonic Devices

Chapter 8

Lasers with Bulk CdS Nanocrystals

In Chapter 5, we have shown the very promising TA data of bulk CdS NCs. The gain metrics are impressive: comparable to state-of-the-art thresholds, very strong intrinsic gain factors (up to 50000 cm^{-1}), and very long gain lifetimes ($> 3 \text{ ns}$). In this Chapter, we try to capitalize on these results by showing that this translates to good properties on-chip, by first showing amplification (through measuring ASE), and lasing.

Showing ASE is the first step in this process, since it demonstrates amplification on-chip, is a good first check of the film quality, and the films are easy to make. Second, lasing is demonstrated, where it was opted to go for a Photonic Crystal slab design. These types of structures are first simulated in various ways to understand the underlying lasing mechanism, and then measurements are shown. This choice of design was made because of simplicity in processing, since the NC spincoating could be done at the end. This was expected to give a film of comparable quality as the ASE case. Furthermore, the superb resolution of e-beam lithography makes these types of designs viable. Measurements are performed both with femtosecond and nanosecond excitation, showing lasing

with low threshold and decent Q -factors.

Samples used in this Chapter were designed, fabricated and measured by me, together with the simulations performed. The NCs were provided by Margarita Samoli.

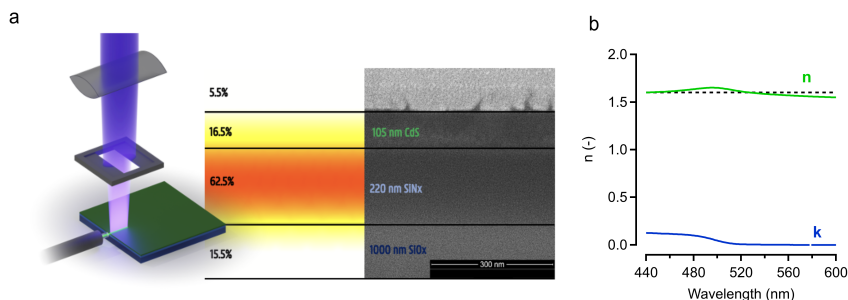


Figure 8.1: Amplifying Spontaneous Emission (ASE) in Thin Films (a) Cross section and optical mode calculations of the nitride/NC stacks used. Schematic also shows the ASE and variable stripe length method. (b) Estimation for n and k based on simulations done in Chapter 7.

8.1 Amplified Spontaneous Emission in Bulk CdS thin films

Sample substrates are 1 μm thick SiO_x on Si. First, 220 nm of LF-HT-SiN_x is grown. On this, the CdS NCs are spincoated, a layer of 105 nm. The cross-section can be seen in Figure 8.1a, together with a simulated mode profile. Using a cylindrical lens and a slit, the 400 nm excitation source is focused into a well defined and uniform pump spot. The emission is captured from the side with a fiber, and sent to a spectrometer, as also shown in Figure 8.1a.

To measure ASE, the area is kept constant and the power is gradually increased, and the result is displayed in Figure 8.2a. A clear threshold is observed for ASE around 500 nm, and then at higher power a secondary ASE lobe can be seen around 480 nm. In total, ASE can be observed in a spectral range going from 530 to 460 nm. A clear threshold of $n = 8.9(1) \cdot 10^{18} \text{ cm}^{-3}$ is observed for the main ASE lobe (blue, Figure 8.2b, which shows the integrated intensity of this lobe). Interestingly, a secondary lobe (purple, Figure 8.2b) with a threshold of $n = 2.8(3) \cdot 10^{19} \text{ cm}^{-3}$ appears as well. This measurement already shows contrast to ASE in

other colloidal NC systems¹: the emission does not seem to saturate, nor does it produce typical narrow ASE lines. It however does strengthen our view put forward first in Chapter 5: that of a bulk NC model where there is only weak confinement. The high DOS available allows us to keep injecting more and more carriers, leading to the very high gain magnitudes needed for such strong and broad amplification. The double-lobe that is seen is unexpected, and probably has to do with complex underlying dynamics such as competition between stimulated emission and carrier cooling in the NCs due to pulsed excitation. An interesting future experiment that could be performed here is measuring the ASE as a function of time, to see whether there is a spectral shift in the gain. The gain could first arise in the blue region and then shifts towards the green region, as is seen in the TA data, where the blue gain is relatively short-lived. Similarly, the ASE could be observed under nanosecond or CW excitation to check for differences. The two lobes were not seen in the TA data, the gain builds up for all wavelengths in the gain band at the same time. Interestingly, this did occur in the CdSe/CdS GSQD TA data discussed in Chapter 4, where the broadness is more continuous. More data is needed to fully understand these dynamics. Finally, the extreme increase in signal (5 orders of magnitude) is again different than typical confined colloidal NC systems, where it is typically around 1-2 orders of magnitude. This can again be understood through the high gain coefficient, but also the fact that the limiting dynamic process is radiative recombination (k_2), which only speeds up light emission at higher density opposed to non-radiative Auger in confined systems.

A second measurement with (almost) the same setup is the VSL experiment, see Figure 8.3, where now the power is kept constant and the stripe length is varied. The intensity will increase as a function of the stripe length, and by using Equation 3.3.16

$$I = I_0 \times \frac{e^{g_m \cdot L} - 1}{g_m} \quad (8.1.1)$$

a value for g_m can be found, the modal gain in the film. These values can be rescaled to the intrinsic gain by using the confinement in the NC layer

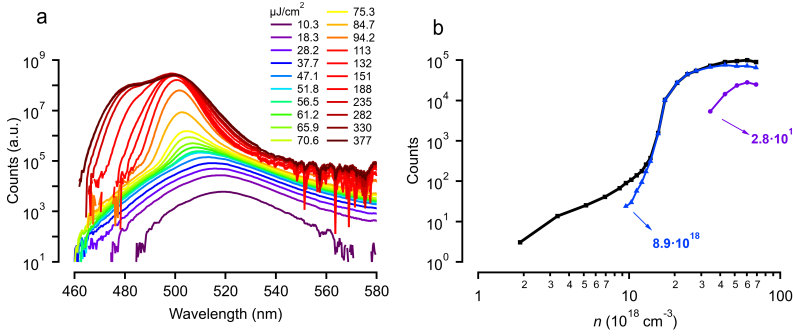


Figure 8.2: (a) ASE spectra at fixed stripe length of 3 mm using 400 nm pumping. We observe both a strong supra-linear increase and sizable broadening of the collected luminescence to a double peak structure. (b) Integrated counts of the total spectrum (black) and the separate ASE_n features (blue, purple), showing clear threshold behaviour, indicated by blue and purple arrows. Horizontal axis is expressed as created carrier density n .

and the volume fraction ($g_m = g_i \cdot \Gamma \cdot f$), and compared to the TA data in Figure 5.3b and 5.3c, with comparable, albeit a bit lower, intrinsic gain values. These lower values can probably be explained by scattering in the film. To determine the confinement, a mode simulation is carried out and the confinement is found to be 16.5% in the CdS NC layer. The index used for the CdS BNCs is calculated from the bulk refractive index of wz-CdS, and estimated from $r_{core} = 6$ nm (leading to V_{core}), with a total radius of $r_{tot} = 7$ nm (V_{tot}), to account for the ligand shell also, which has a refractive index of $n_{lig} = 1.5$ (organics). Then, the refractive index of the nanocrystal can be calculated as

$$n_{NC}(\lambda) = \frac{V_{core}}{V_{tot}} \cdot n_{CdS} + \frac{V_{tot} - V_{core}}{V_{tot}} \cdot n_{lig} \quad (8.1.2)$$

From this, estimating a 50% packing, the refractive index of the film is found

$$n_{film} = 0.5 \cdot n_{NC} + 0.5 \cdot 1 \quad (8.1.3)$$

which is shown in 8.1b. In the simulations, an average flat index of 1.6 is used. The intrinsic gain is calculated based on the results, and shown in

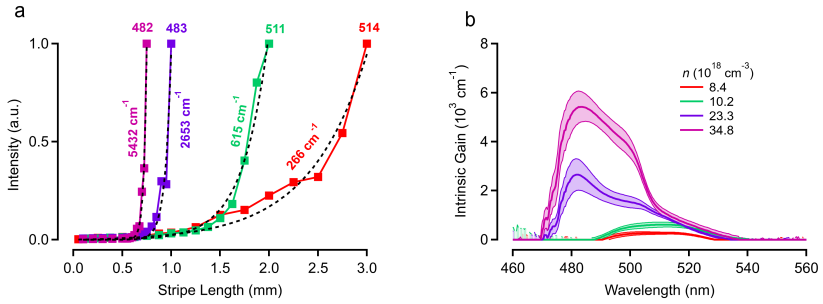


Figure 8.3: (a) Variable stripe length measurements at different wavelengths (472, 473, 503 and 504 nm) at fixed pump power (shown in 8.3b) showing supra-linear increase with increasing amplifier length. Dashed lines indicate fits to extract the material gain coefficients. (b) VSL spectrum showing the extracted intrinsic gain versus wavelength at different carrier densities.

Figure 8.3b as a function of wavelength, with the thin lines showing the errors on the fit. In Figure 8.3a, the gain of the strongest wavelength is shown.

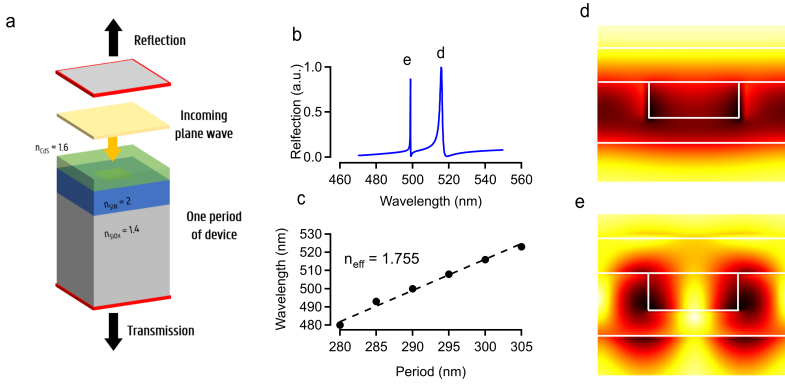


Figure 8.4: Schematic and some results of the 2D DFB simulations. (a) Shows a unit cell of the device. An incoming plane wave on the structure is shown, with a reflection monitor on the top, and transmission monitor on the bottom. (b) Shows the reflectance spectrum for a device with a period of 300 nm. (c) Shows the lowest resonance seen in the reflection spectrum as a function of period, and the extracted proportional constant n_{eff} . (d) and (e) show cross sections in the middle of the period for the mode at 515 nm and 498 nm, displaying the electric field intensity. These both show that the mode is confined mostly within the SiNx layer and the NCs in the hole.

8.2 Photonic Crystal Slab Lasers

To demonstrate lasing, we opted for a Photonic Crystal (PhC) slab design since previous work in the field has shown lasing with similar geometry², and such geometries are relatively easy to process. The gratings can be made and afterward NCs can be spincoated on top. Before discussing the experimental results from these devices, it is worth discussing the theoretical background in more detail of such structures, to understand the underlying optical mechanism.

8.2.1 Simulating PhC Lasers

To understand PhC lasers based on bulk colloidal NCs, four types of simulations are done (1) a full 3D simulation of a single period, with an incoming plane wave from the top, effectively considering these structures

as a reflector, (2) a 1D PhC structure with dipole sources in every period, (3) a 2D PhC structure with dipole sources in every period, and (4) full bandstructure simulations of the device. The first simulation type already gives some basic insight into the reflection/transmission spectrum of such devices, but for thorough understanding regarding the far field, Q -factor, and electric/magnetic field distributions, the latter simulations will be more useful. After this discussion, the results of the different lasers are shown. The dimensions used in the simulations are based on a FIB cross-section of an actual device: the SiNx thickness is 150 nm, with a 90 nm CdS layer on top which fills the holes nicely. The etch depth of the holes is also 90 nm.

8.2.1.1 Single Period with Incoming Plane Wave

First, a single period is simulated using Lumerical, where we use a unit cell with periodic boundary conditions (see Figure 8.4a), in a full 3D simulation. In the z -direction, a Perfectly Matched Layer (PML) is used, which is a numerical “perfect absorber”. Physically it can be interpreted as the light passing it escaping toward infinity. This PML boundary is placed a couple of wavelengths away from the structure. This type of boundary is typically used when a periodic boundary is not used in the following simulations. We use an incoming plane wave and check the transmission and reflection of the structure of varying grating period. The duty cycle of the structures is 50% and the thicknesses used are coupled back from the FIB cross-section, as stated above. Results are shown in Figure 8.4a and b. Besides the longest wavelength resonance, interestingly, we can also observe a secondary much sharper resonance. Looking into detail at how the mode looks here by taking a cross-section, we see that the first resonance (d) is much more uniformly spread over the SiNx layer and within the hole filled with nanocrystals. The other, sharper resonance (e) shows that the mode mostly exists in the interface between these two layers.

This simulation was mostly done to check the influence of the period on the resonance wavelength. A clear influence is found, where the pro-

portionality constant can be found through the Bragg Condition of a 2nd order grating: $\lambda_{Bragg} = n_{eff} \cdot \Lambda$, where Λ is the period. This formula is used in Figure 8.4c, where an effective index of 1.755 is found for the longest wavelength mode. For a more in-depth study, we turn to the simulations described in the next Sections.

8.2.1.2 1D PhC Devices

In this Section, a 1D DFB or PhC slab is simulated. Here, there is only periodicity in one direction instead of the two directions in the actual device. As was discussed already in Chapter 3, in the Section on 1D and 2D DFB gratings, they are very similar. The simulated geometry is shown in Figure 8.5a, with the different layers, monitors and locations of the electromagnetic sources. The structure is a simple 2nd order grating, so the grating will scatter upward and sideward. The 2D nature means that the structure stretches out infinitely out of the screen.

Linking the photonic bandstructure to the \vec{k} -diagram is no trivial thing. The first order diffraction occurring in a 2nd-order grating explains why there is upward scattering in these types of gratings, as explained in Section 3.3.2.7. Since $\vec{k} = 2\pi/\lambda$ we are in the Γ point, but in the second band (see in Figure 3.15b on the right, $\omega a/2\pi c \approx 0.62$). In principle, we do not require a bandgap in these structures, but we do require the dispersion relation to become flat, which translates to the mode being a standing wave, or the in-plane group velocity going to zero. There is no restriction on \vec{k} in the z -direction. As such, in the Γ -point, the mode cannot travel in-plane, but can still travel out of plane, like we can find from applying the Bragg Condition. This is explored more in-depth in the final simulation, where the band diagrams are discussed.

Similar to the simulations in the previous Section, the geometry parameters are chosen based on the FIB cross-sections of the actual device. The period here is fixed at 300 nm, since the effect of changing the period is already discussed in the previous Section, and the duty cycle is chosen as 50%. As sources, magnetic dipoles are used which are placed at the antinode position in the Photonic Crystal layer periodically and perpen-

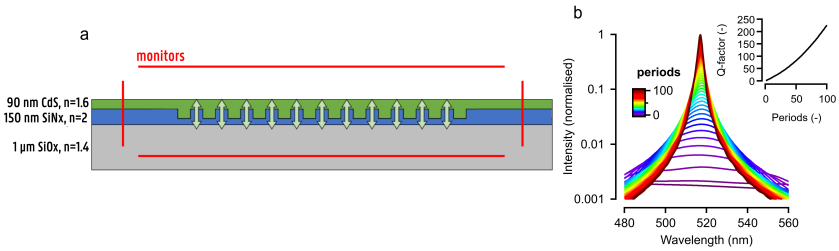


Figure 8.5: (a) The geometry for the 1D PhC simulations. The layer thicknesses are shown on the left, the different monitors are shown in red (although the one above the device is the main one of interest), and the magnetic dipole sources are shown in green. The gratings are etched 90 nm deep. (b) The intensity going through the top monitor for increasing amount of periods, going from 1 to 101. The inset shows the Q -factor.

dicular to the surface, to specifically excite the TE modes, as discussed in Chapter 3 in the Section on Photonic Crystals. Multiple monitors are placed around the device, with the one on top being the most important since we are interested in surface emission. It is placed about one wavelength above the NC layer. We will investigate the resonant wavelength and its associated Q -factor, and the Far-Field (FF) pattern of these structures.

The transmission through the top monitor is shown in Figure 8.5b, for increasing amounts of periods. Clearly a sharper resonance starts to appear, for a period of 300 nm it converges to about 517 nm. The sharpness keeps increasing, and as such so does the Q -factor, reaching values of almost 250. Besides the amount of periods, the SiNx thickness and etch depth can be tuned for optimal Q -factor.

In Figure 8.6a, the FF pattern is shown for all different wavelengths, showing clearly much stronger emission for 517 nm, where the resonance wavelength is (see Figure 8.5b). However, contrary to what would be expected because of the \vec{k} -diagram, this emission is *not* occurring at an angle of zero degrees. Two clear lobes can be seen, at around $\pm 1.4^\circ$. This is explained after discussing the FF patterns.

In Figure 8.6b, the same FF patterns are shown but normalised for

each wavelength. This shows that moving away from the resonance point, the angle will indeed start changing according to the \vec{k} -diagram, and this is symmetric for shorter and longer wavelengths. The symmetry is broken around 432 nm, because a secondary (TE) mode starts contributing, although from Figure 8.6a we know that not much light gets coupled into this mode, or rather, not much light of this mode couples out perpendicular to the surface. The light that does couple out has an almost equally small angle ($\pm 1.1^\circ$). Only in a very small spectral range this mode is dominant. Both these maps are simulations with 51 periods. Figure 8.6c shows the normalised emission at the resonance wavelength of 517 nm, for a different amount of periods. The log scale indicates that a big decrease in angle is achieved by adding more periods, but the destructive interference at zero degrees never disappears. As can be seen from Figure 8.7b, the y -component (upward component) of the electric field (which is the only component, due to TE polarisation) is anti-symmetric. This antisymmetry is typical for the lasing mode in a DFB laser^{3,4}. This is because the $+x$ and $-x$ travelling waves that comprise the standing wave have equal intensity but opposite sign, causing them to destructively interfere in the y -direction, which inhibits vertical emission. This, however, only holds for an infinite crystal. For realistic, finite crystals the field distribution antisymmetry is broken near the boundary of the device, although remaining perfect in the center. From the Near-Field (NF) pattern shown in Figure 8.6c bottom, the emitted power (Poynting vector) of the resonant mode through the monitor above the device is zero for $x = 0$ and grows larger to the sides. As such, the confinement within the crystal is really strong for this particular mode, with the boundary causing some radiant emission, leading to a very narrow lasing mode. The FF pattern can be calculated from the NF pattern, through the fourier transform. This emission from the sides of the device will cause slight deviations from zero-angle emission. The anti-symmetry of the mode is crucial to understand the mechanism behind confinement and perpendicular emission in these types of devices.

Looking at Figure 8.7a, the previous results are summarized: the red

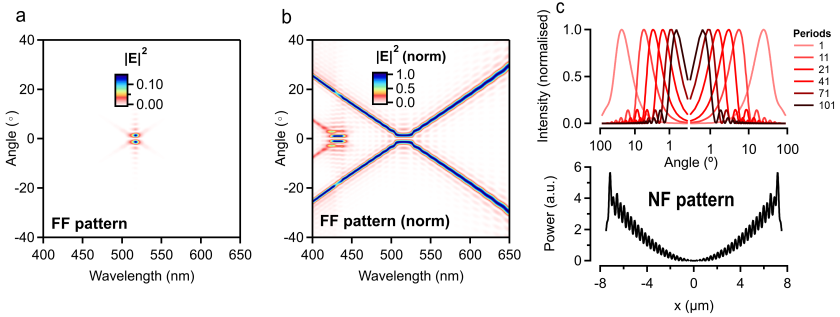


Figure 8.6: (a) Far-field pattern simulated for 51 periods. (b) Same as (a), but normalised for every wavelength, showing the dominant emission angle for every wavelength more clearly. Note that around 440-450 nm, a secondary mode becomes dominant. (c) FF pattern at 517 nm for a different amount of periods, showing the decrease of the emission cone for increasing number of periods, showing that there is no emission for zero degrees (top), NF pattern for 51 periods, showing barely any transmitted power from the center (bottom).

curve shows the max angle (calculated from the origin to the strong first lobe) as a function of the amount of periods, and the blue curve shows the found Q -factor. The Q -factor is found by doing Lorentzian fits on the data from Figure 8.5b, as demonstrated in the inset of Figure 8.7a, showing the inverse proportional relationship between the emission angle and the Q -factor.

Figure 8.7b shows the electric in-plane component for the fundamental mode (the other field components are zero), showing a clear standing wave pattern and the TE polarisation (expected because of the magnetic dipole sources). The black lines drawn over the distributions denote the outline of the SiNx grating, showing here three periods of the PhC. It can be seen that the electric field is at its maximum at the edges of the hole. This electric field distribution looks quite similar to the electric field found from the previous simulations, shown in Figure 8.4e, interestingly enough. The fact that multiple extrema are found per period is because this is a 2nd-order grating (one period corresponds to a full wavelength, as is shown in Figure 8.7b). Finally, in Figure 8.7c, the effect of changing the duty cycle

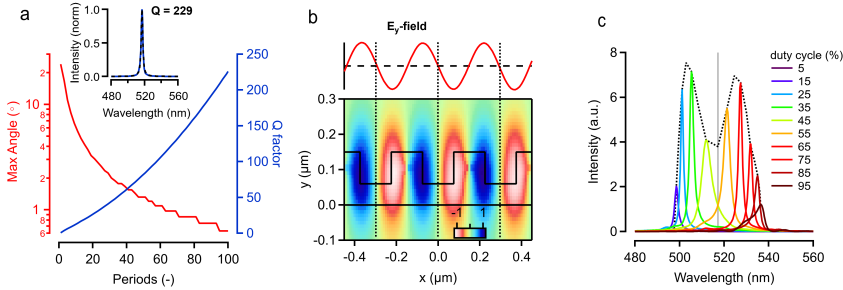


Figure 8.7: (a) The maximum angle for increasing the amount of periods (red, left), and the Q -factor found from a lorentzian fit from the data in Figure 8.5b. (b) E_y -field shown at the fundamental mode (517 nm), in the middle of the cavity, showing clear anti-symmetry. The zero amplitude in the center of the hole of the grating leads to no perpendicularly outcoupled light. Toward the outside of the grating, this anti-symmetry is broken, causing perpendicular outcoupling to occur at the edges of the device. (c) Spectrum shown for various duty cycles, with the black dashed line showing the maximum for every simulated duty cycle.

is shown by showing the perpendicular emission for different duty cycles. The wavelength shift can be interpreted as the gradual change in effective index: for the low duty cycle there is only a small pillar of SiNx, while the high duty cycle only has a small hole filled with NCs. The gradual increase of SiNx will lead to an increase of the effective index, and as such shift the lasing mode to longer wavelengths.

8.2.1.3 2D PhC Devices

With some basic insight from the 1D PhC, we can take a look at the 2D PhC devices. In principle, these are just two 1D PhCs perpendicular on each other in the plane, and we will see that many things do come back from the 1D case. In Figure 8.8a, the simulated device is shown. The geometry is the same as for the 1D PhCs, except now there is periodicity in both the x and y direction. The thicknesses remain the same, with a 150 nm SiNx layer with 90 nm etched holes, and overcoated with a 90 nm CdS film. The monitor of interest is placed about one wavelength above

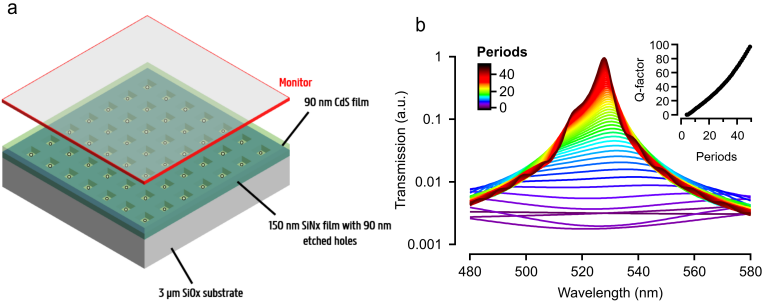


Figure 8.8: (a) Geometry of the 2D PhC device. The green dots are the placed magnetic dipoles in the etched SiNx holes, and a monitor is placed above the entire device, to capture the emitted light. (b) Shows the transmitted light for various wavelength, and for an increasing amount of periods. The inset shows the found Q -factor.

the CdS layer. Magnetic dipoles again are placed in the middle of the etched hole (see the light green dots in Figure 8.8a). The period is again 300 nm, and the duty cycle here is chosen to be 40%, which was chosen such that the holes matched well with the mesh, to reduce computation time.

Figure 8.8b shows the transmission through the top monitor for increasing the amount of periods, here with a maximum amount of 50 periods, and the inset shows the extracted Q -factor from a Lorentzian fit, showing comparable results to the 1D case (bearing in mind that we only have half the period range). A noticeable difference with the 1D case however is the added bumps in the spectra, maybe indicating some weak Fabry-Perot cavity formation in-plane due to putting the boundary layer too close, although this needs to be investigated further. The resonant mode is also red-shifted, possibly due to the change in duty cycle, or a change in the effective refractive index. If one would calculate the geometric average of the refractive index over one period of the device in the 1D case, the formula would be

$$n_{eff} = \frac{d_{etch}}{d_{tot}} \cdot ((1 - dc) \cdot n_{SiNx} + dc \cdot n_{CdS}) + \left(1 - \frac{d_{etch}}{d_{tot}}\right) \cdot n_{SiNx} \quad (8.2.1)$$

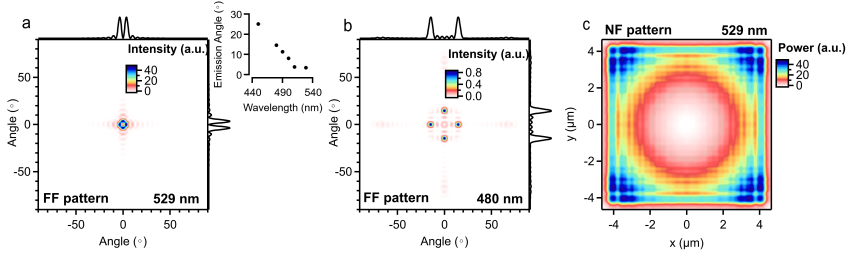


Figure 8.9: (a) Far field pattern at the fundamental mode, showing a ring-shaped pattern. The cross-sections at zero degrees for x and y are shown outside of the image. (b) Far field pattern at a higher energy (480 nm), showing that emission at higher energies corresponds to emission with at an angle. The inset between (a) and (b) shows the emission angle for various wavelengths. (c) The Near Field pattern for the fundamental mode, showing that most of the emission comes from the edge of the device.

which for a duty cycle of 50% would get $n_{eff} = 1.88$. For the 2D case, the geometric average would be

$$n_{eff} = \frac{d_{etch}}{d_{tot}} \cdot ((1 - dc^2) \cdot n_{SiNx} + dc^2 \cdot n_{CdS}) + \left(1 - \frac{d_{etch}}{d_{tot}}\right) \cdot n_{SiNx} \quad (8.2.2)$$

yielding a value of $n_{eff} = 1.94$. The higher effective index would red-shift the spectra. Factoring in the lower duty cycle, it will be red-shifted even more (doing the same calculation with 40% gives $n_{eff} = 1.96$).

Looking at the FF patterns in Figure 8.9a and b, we again see a similar splitting as in the 1D case, where the fundamental mode seems to give more of a ring shaped pattern. This is a typical FF pattern, also reported in literature both in simulation studies^{5,6} and measured on actual devices^{3,7}. Comparing to the 1D case, we again see that there is a splitting between the two maxima of emission. This mode is anti-symmetric (Figure 8.10a), allowing us to use the same explanation as for the 1D case: anti-symmetry leads to destructive interference which does not allow any vertical outcoupling, but the finiteness of the crystal breaks this perfect anti-symmetry, causing upward emission from the edges of the device. In Figure 8.9c the NF pattern is again shown, showing zero

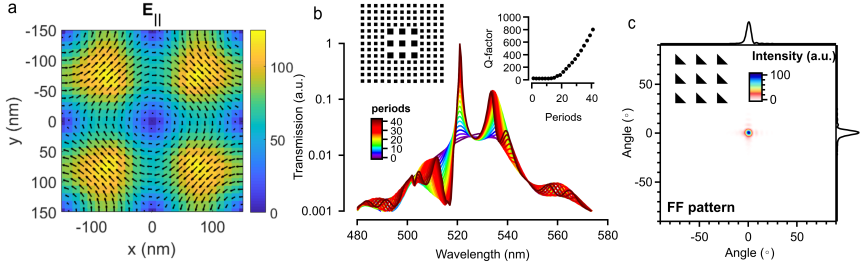


Figure 8.10: (a) In-plane E-field for the fundamental mode, showing a zero in the middle of the period, and anti-symmetry with respect to x and y -axis. (b) Transmission for a heterogeneous PhC cavity, for a fixed $n_{in} = 20$ and increasing n_{out} . The inset shows the Q -factor, showing a steep ramp up starting from about $n_{out} = 15$. (c) FF pattern for a PhC structure with triangles instead of squares. Breaking the symmetry leads to a single lobed, albeit a bit skewed, pattern.

intensity in the center. This then leads to ring shaped FF patterns. Taking slices both for the angle in the x -direction and y -direction both give the same FF pattern as shown in the 1D case. The inset between Figure 8.9a and b shows the emission angle for different wavelengths, showing, as expected from the \vec{k} -diagram, that for shorter wavelengths the emission will come out of the device under an angle.

In Figure 8.10a, the in-plane electric field is shown, corresponding to TE polarization (out-of-plane electric field is close to zero). The x -component of the electric field is anti-symmetric with respect to mirroring on the x -axis, and the y -component with respect mirroring on the y -axis. The field becomes zero at the middle of the period (center of the hole) and at the edges.

The found Q -factors, both for 1D and 2D gratings, is not exceptionally high. This is because of radiative emission out of plane (both up- and downward), and leakage to the sides. To avoid the latter, a 1st order grating can be added on the outside of this 2nd order grating, forming a “heterogeneous Photonic Crystal Cavity”, or even a “core/shell Photonic Crystal Cavity”. To show that this would already quite drastically improve the confinement, in Figure 8.10b the spectra are shown for a system

which has 20 2nd order periods, with an increasing amount of 1st order periods, showing much more narrow emitting lines. There is a mode splitting, due to resonances in-plane being confined within a Fabry-Perot cavity in both x and y direction: $a \cdot n_{in} \cdot n_{eff} = m \cdot 2\pi$ (n_{in} is the amount of periods of the 2nd order grating) has to hold. This is just a first quick demonstration of how these cavities, made to demonstrate lasing, can be quite easily improved. Considering the PhC band diagram, the combination of these two crystals means that the Γ -point of the 2nd-order grating has to lie somewhere in the bandgap of the 1st-order grating, as is discussed also by Inoue *et al.*⁸. This would achieve perfect reflection of this mode, back into the 2nd-order cavity.

This splitting could be resolved by adding some distance d on both sides of the 2nd-order grating without any structure, just the plain slab, such that the requirement $(2d + a \cdot n_{in}) \cdot n_{eff} = m \cdot 2\pi$ corresponds to the exact center wavelength of choice. Nevertheless, by increasing n_{in} , unavoidably multimode behaviour will start occurring due to this in-plane confinement. To limit this, an option is to *decrease* the amount of 2nd-order periods and increase the amount of 1st-order periods even more: increasing confinement with a smaller total device size. This will yield high Q -factor cavities, but the far-field pattern will become more broad. An optimisation of this is beyond the scope of this study.

Besides optimizing the cavity, controlling the far-field pattern is also favourable: typically, a single-lobed emission cone would be preferable to this ring shaped pattern observed here. To do so this anti-symmetry, causing the perpendicular emission to be forbidden, must be broken. This can be achieved by manipulating the unit cell of the device, and changing the symmetry of it, as is explained by Wang *et al.*⁵. Breaking the symmetry leads to a higher overlap between the hole and the in-plane electric fields, yielding more efficient upward scattering. As an example of this, a far-field pattern was generated where the periodic square holes were exchanged for a triangular pattern, see Figure 8.10c. This already shows single-lobed emission.

8.2.1.4 Photonic Bandstructure Simulations

To conclude the simulation part, it is worthwhile taking a look into the photonic bandstructure of these devices. Here, we move back to simulating a single period of the structure, with Bloch Boundary Conditions. This boundary condition adds a phase every time the waves cross a boundary, determined by an imposed \vec{k} -value. For example, when crossing the boundary in the x -direction:

$$\vec{E}_{x,min} = e^{i \cdot a \cdot k_x} \times \vec{E}_{x,max} \quad (8.2.3)$$

$$\vec{E}_{x,max} = e^{-i \cdot a \cdot k_x} \times \vec{E}_{x,min} \quad (8.2.4)$$

Previously, magnetic dipole sources are placed periodically within the structure to excite specifically the optical mode of interest. Here, a dipole cloud is used to excite as many modes as possible. The same geometry as before is used, with a layer of 150 nm of SiNx, a 90 nm hole with a duty cycle of 60%, which is filled with NCs, and is overcoated with a layer of 90 nm of NCs.

By then sweeping over \vec{k} -values for the boundary condition, the resonating modes can be determined and their respective frequencies. Plotting then the found resonances for the chosen \vec{k} -values will yield the photonic bandstructure. As for choosing \vec{k} -values, typically a sweep is done from $\Gamma - X - M - \Gamma$, like in Figure 3.16. However, for our specific situation where we are interested in surface emission in a 2nd-order grating, it is preferable to look at $M - \Gamma - X$, since then the point of interest is in the middle, like typically done in literature^{5,8} on Photonic Crystal Surface Emitting Lasers. Indeed, at Γ , the in-plane wave-vector is zero, meaning there is a standing wave in-plane, and travelling can only occur out of plane. As such, it is worth investigating the field distributions of the various frequencies found at the Γ -point. We can relate this to the mode found in the previous simulations, as evidenced by the sharp emission peak upward.

There, however, is not just a single frequency that exists at the Γ -point. Typically, multiple bands are found with either a maximum or a

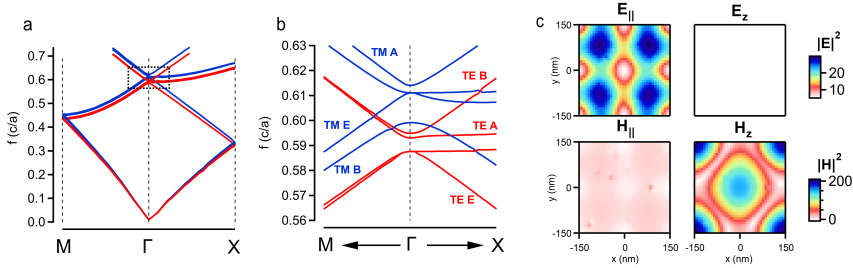


Figure 8.11: (a) Bandstructure of the discussed structure, going from $M - \Gamma - X$. TE bands are shown in red and TM bands in blue. The black box drawn around Γ_1 shows where the zoom is for (b). (b) Zoom in around Γ_1 , showing a (small) bandgap for TE, and none for TM. (c) The electric and magnetic fields for the fundamental TE mode at Γ (the black dot in (b)). This clearly shows that the in-plane electric fields is much stronger than the out-of-plane, and the reverse is true for the magnetic fields.

minimum at Γ . These extrema correspond to flat dispersion, meaning the group velocity of the mode is zero, again leading to a standing wave. This is a typical property of photonic crystals, called “slow light”⁹. The band gap specifically is of less importance in the specific application envisioned in this Chapter, we are mainly concerned with which optical modes are allowed at this Γ -point, and as such showing a zero group velocity. Through these bandstructure simulations, we can identify the different allowed frequencies at Γ and discuss their respective Q -factor. With this information, we can then start labelling different experimentally found lasing modes, as there is not always just a single lasing mode, especially at higher excitation powers. It is worth repeating here that the information found from these simulations give us the *possible* resonances. In an actual laser, the combination of the Q -factor and the available gain over the spectrum will determine which of these possible resonances will start lasing.

Figure 8.11 shows the simulated bandstructure. in Figure 8.11a a wide range is shown, while Figure 8.11b a more zoomed-in picture is shown around the Γ -point and frequencies of interest ($f_{norm} = 0.56 - 0.63$), corresponding to the wavelength range of 476-535 nm. The TE bands are coloured red, and the TM bands blue. Due to the asymmetry in the

structure (because of the SiOx substrate), there is some slight mixing of the modes, and they are typically referred to as “TE-like” or “even-like”, or “TM-like” or “odd-like” in literature¹⁰. The even or odd refers to the symmetry with respect to the z -axis. This mixing is typically less than a percent, and the mode can be determined by checking the field components (TE will have mainly E_x , E_y and H_z , while TM will mainly have H_x , H_y and E_z). This is demonstrated in Figure 8.11c, for the lowest frequency resonance. The in-plane amplitude is shown (left) vs. the out-of-plane amplitude, with the same scaling. For both electric- (top row) and magnetic- (bottom row) fields. From this, we can clearly deduce that this particular mode is TE-like. The same can be repeated for the different modes, allowing us to assign the different bands to TE or TM. From the zoomed in banddiagram, we can assign various “band gaps” in these systems which, again, have little meaning considering we are interested in the modes at the Γ -point itself, no the frequencies between. The fact that the dispersion relation becomes flat will allow resonances to appear as well for TM modes.

From the band diagram, we can find eight bands, typically denoted with the names provided in Figure 8.11. These are names typically used in literature, assigned based on the in-plane field distributions¹¹. Although there are eight bands, The E_1 and E_2 modes become degenerate at the Γ -point. Both these E modes are symmetric with respect to the x or y axis, leading to a superposition. This leaves us with six wavelengths through $c = \lambda \cdot f$, which are categorised in Table 8.1. This shows that, for this particular structure, the TE modes are at longer wavelength, or lower energy. Furthermore, as already discussed, these show anti-symmetric fields in-plane, leading to the upward scattering being forbidden. Because of this, the mode is well confined and the Q -factor will be high, hence why this mode is typically the one that lases and is the one most thoroughly studied in the previous Sections. This is very clearly seen from Table 8.1, where the Q -factor is shown. A very large discrepancy can be seen between the E and A/B modes respectively. It is worth noting that these Q -factors found from these simulations are not reliable: to accurately determine

Mode	f (c/a)	Wavelength (nm)	Confinement (%)	Q-factor
TE E	0.5863	511.7	22.9	229
TE A	0.5922	506.6	37.2	$4.7 \cdot 10^8$
TE B	0.5950	504.2	39.0	$4.7 \cdot 10^9$
TM B	0.5996	500.3	28.6	$2.8 \cdot 10^9$
TM E	0.6122	490.0	28.4	3169
TM A	0.6163	486.8	37.3	$4.3 \cdot 10^8$

Table 8.1: Found bands for our structure, with their corresponding mode type and frequency at the Γ_1 -point.

a Q-factor, the mode must at least significantly decay in the simulation timeframe. Due to the very long photon lifetime, this timeframe must be very long. The values are mostly presented to showcase the difference between the modes that have anti-symmetric in-plane fields (A and B) vs. the modes that do not have these anti-symmetric in-plane fields (E). It is worth noting here that these Q-factors are extracted for “infinite” devices. In a more realistic finite device, we would go back to more reasonable values, as found in Figure 8.10. Finally, the confinement in the NC layer is also shown. The overlap between the in-plane field and the NC layer will depend on the optical mode, which will have an effect on the modal gain achievable in the device.

Each of these six modes are candidates for possible lasing operation. An explanation to which of these will operate the most efficiently is given in the work by Sakai *et al.*⁶, specifically for the TE modes. Here, it is stated that the E mode will be more leaky because the mode is symmetric, allowing for efficient vertical outcoupling. The Γ -point for the B-band specifically will also be less confined due to the flat dispersion relation toward the X-point, allowing photons to couple easier to different k -values (this does not correspond to the extracted Q-values from our simulations, further showing that these are not completely accurate). This leaves the A band as the prime lasing candidate. And indeed, from experiments where a resonator is pumped “cold” (below lasing threshold), photon lifetimes, or Q-factors, can be found where the A-band is superior. However, when looking into the symmetry of the fields for our specific simulation, we find

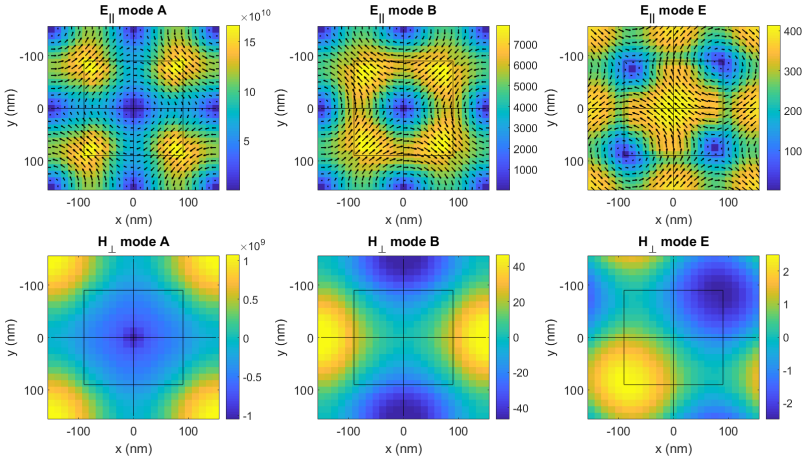


Figure 8.12: Different in-plane electric- (top) and magnetic- (bottom) fields for the three different TE modes. From left to right: TE A, TE B and TE E. For the TM modes, the electric and magnetic field distributions will be swapped.

that the in-plane electric field is anti-symmetric for all four A/B modes, see Figure 8.12. Here, the in-plane fields clearly show that mirroring over x will mirror E_x , and the same holds for mirroring over y . The symmetry planes are shown in black. In the work of Jin *et al.*³ on 1D gratings, an alternative explanation is given through the overlap between the grating periodicity and the optical mode. This also relates to the anti-symmetry or symmetry of the mode, but gives us a less strict criterion on which to evaluate the effectiveness of the vertical outcoupling.

The band structure will change depending on the duty cycle, and the shape of the unit cell. This will shift the different frequencies or wavelengths at the Γ -point. Because of this, the effect on the six modes was checked by changing the duty cycle from 10% to 90%, as shown in Figure 8.13. The duty cycle is defined as the size of the hole, so higher duty cycle will lead to more NCs in the device. The lower index will shift the modes toward shorter wavelengths, as can be seen in Figure 8.13a. Interestingly, the distance between the modes does change, specifically the modes do come closer together for larger duty cycles. This is also found in

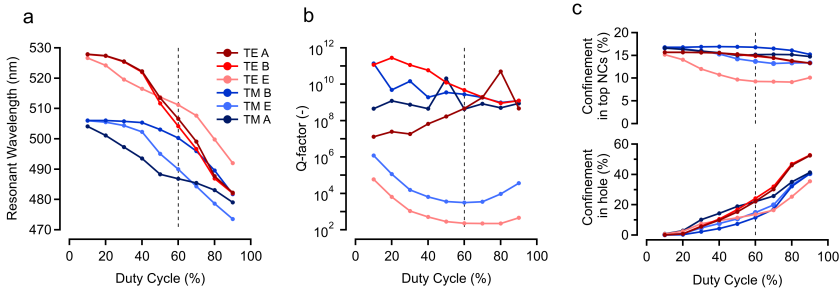


Figure 8.13: Effect of changing the duty cycle on the device. (a) Changes on the resonant wavelength of the six modes. (b) Effect on the Q-factor. (c) Effect on the confinement, both in the hole and in the NC layer on top of the grating. The black dashed line shows the device for which the bandstructure was simulated.

the work of Yokoyama *et al.*¹¹. Figure 8.13b shows the Q-factor for changing duty cycle, with a clear separation between the A/B modes and the E modes. The A/B Q-factors do not show any clear behaviour, probably due to inaccuracy of these determined Q-factors as explained earlier. The E bands do show a clear minimum, and an upward trend when going to small duty cycles. Finally, the confinement both in the hole and the top NC layer is shown. Naturally, when increasing the hole size the confinement in the NCs will go up, independent of mode type. The confinement effect on the mode in the top NC layer is quite independent of the duty cycle.

Depending on the gain material specifically TE or TM modes only will be excited (for example, in the work of Jin *et al.* they only discuss TE modes because the device has an active layer of MQWs). In our case, where the gain material is symmetric, both modes should resonate, and the resonating modes will mainly depend on the overlap between the gain bandwidth and the specific mode, together with the Q-factor. Finally, the best resonance does not necessarily lead to the strongest lasing mode: gain magnitude will influence this as well. This approach at least allows us to determine, for a specific lasing structure, the different resonances that exist and allows us to identify the different lasing peaks that appear.

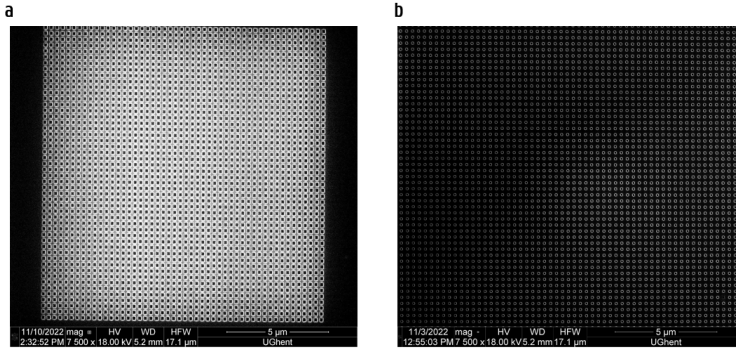


Figure 8.14: FIB images of two 2D PhC cavities (a) 280 nm period, with 60% duty cycle. (b) 300 nm period, with 30% duty cycle.

8.2.2 Photonic Crystal Slab Lasers with bulk CdS NCs

The starting substrates are the same as for the ASE measurements, although with a thicker oxide layer of 3 μm to ensure good mode confinement in the top layers. Again, SiNx is grown using PECVD, in this case 150 nm. With electron beam lithography, the holes of the grating can be patterned. Gratings are made with a wide range of periods to ensure lasing operation in the gain window. After the grating etch, the NCs are spincoated with a thickness of about 90 nm above the SiNx. The holes are filled with NCs, and a smooth layer with an additional 90 nm thickness is created over the SiNx layer. This can be seen in Figure 8.15a, where we show a FIB cross-section of one of the periods, together with a mode simulation in the middle of the structure. These structures are measured by excitation under an angle, and the emission is measured perpendicular to the surface. Some SEM images taken of the total devices are shown in Figure 8.14, showing very uniform gratings.

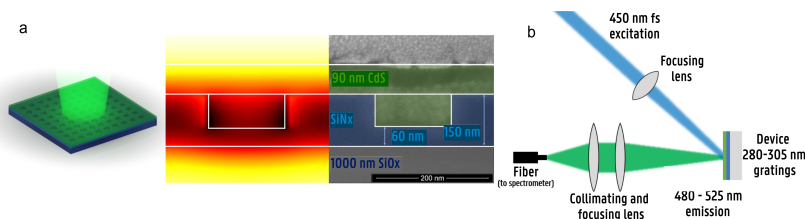


Figure 8.15: (a) Schematic of the NC covered 2D grating etched into silicon nitride grown on silicon oxide. The pitch Λ determines the grating resonance. (b) The experimental setup used for the measurements.

8.2.2.1 Laser Measurements

Lasing with Femtosecond Excitation The measured devices are shown in Figure 8.15a, where the values used in the simulations can be seen: a CdS NC layer with a thickness of 90 nm, on top of a 150 nm SiNx layer with 90 nm etched holes. The periods are swept from 280 to 305 nm, in steps of 5 nm. The structures are excited using a 450 nm femtosecond laser using a $100 \times 100 \mu\text{m}$ spot size, the setup is shown in Figure 8.15b. The vertically emission is collimated, and then focused on a fiber which goes to a spectrometer.

The results are shown in Figure 8.16, where the lowest threshold device is shown in Figure 8.16e. With a period Λ of 300 nm, the light emitted is centered at 517 nm and increases supra-linear with in excitation fluence for over 3 orders of magnitude. A clear threshold at $17 \mu\text{J}/\text{cm}^2$ is observed (see inset) while at high fluence the emission does not show strong saturation as observed typically for other colloidal NC lasers. The latter can again be assigned to the increased radiative rate at high density, opposed to Auger losses in confined colloidal NC lasers taking over at high pump fluence. By varying the period, we can obtain similar lasing action across the 490 - 520 nm window, albeit with increasing threshold fluence going into the blue. This is expected given the gain threshold is lowest for the band gap region, see Figure 5.3b-c, where the BGR is dominant. The spectra of the largest period samples also display a second mode which is

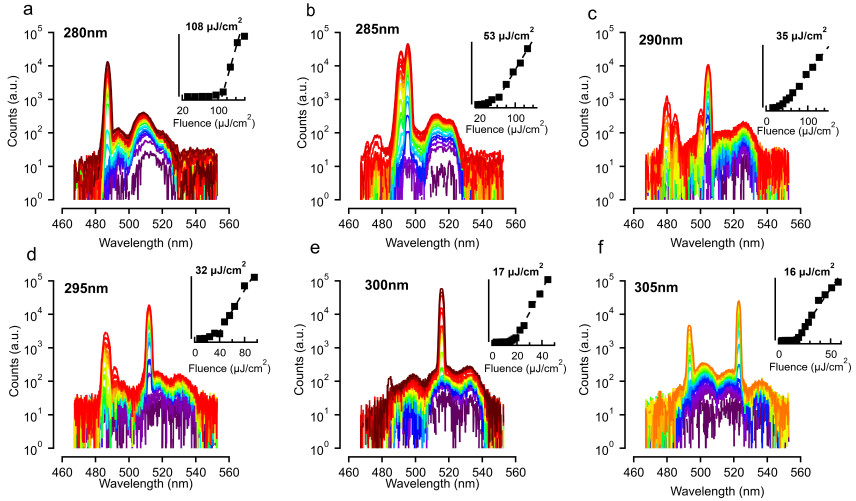


Figure 8.16: Measurements of six different devices with periods going from 280 - 305 nm. The insets show the determined threshold fluences.

much less confined in the NC layer, yet due to the high gain coefficients obtained in CdS across the spectrum, they can also start lasing.

The results are combined in Figure 8.17a, where the top figure shows the transmission gathered from Section 8.2.1.1, the middle figure shows the normalised lasing peaks for the six different devices, and the bottom figure shows the measured thresholds. The resonance as a function of the period is shown in Figure 8.17b, and compared to the resonances found from the simulations. Using the Bragg expression we can find the effective index, which shows excellent agreement between the simulation and the experiment. Finally, in Figure 8.17c, a measurement with a higher resolution grating is shown to estimate the linewidth of the lasing line, the FWHM is around 0.4-0.5 nm, shown in the inset. The Q -factor is also found from a Lorentzian fit, which can be used to estimate the losses. In a laser, the losses come either from scattering or absorption. Considering that the system is showing optical gain, we can neglect the absorption part and say the losses are purely due to scattering. In reality, this over-

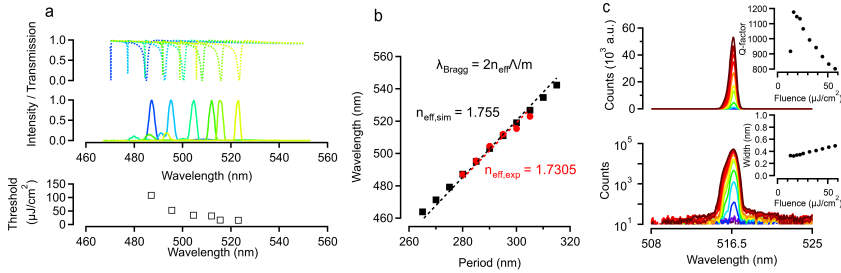


Figure 8.17: (a) Grating spectra (top) calculated using an index for the CdS of 1.6 (estimated through the simulations performed in Chapter 7, see Figure 8.1b). and matching experimental spectra (middle). Bottom graph shows the thresholds for each device. (b) Comparison between the extracted effective index of the experiment (red) and simulation (black), with excellent agreement. (c) Measurement of the device with a period of 300 nm, with a higher resolution grating, to show the width of the lasing peak, shown both in linear (top) and log scale (bottom). The insets show the Q -factor from a Lorentzian fit (top), and the FWHM (bottom).

estimates the scattering losses and underestimates the absorption most likely. The Q -factor can be linked to the losses α through¹²

$$\alpha = \frac{2\pi n_{\text{eff}}}{Q\lambda} \quad (8.2.5)$$

Using the effective indices found in Figure 8.17b ($n_{\text{eff}} = 1.7305$), a Q -factor ranging from 800 to 1200 yields losses $\alpha = 263 - 175 \text{ cm}^{-1}$. Which can be contributed purely to scattering, but, as mentioned, absorption can also play a role here. Due to the femtosecond excitation the NCs only stay in population inversion for a short time, and most likely the mode is attenuated at least partly due to re-absorption after all the gain is gone. This tends to cause lasers with femtosecond excitation to have broader linewidths than nanosecond or continuously excited lasers.

To check the FF pattern experimentally, the fiber to collect the emission can be swapped with a CCD camera. The measured pattern (as a function of distance in x, y) can be translated to a divergence angle based on the distance between the sample and the CCD. A ring-shaped pattern is found, an excellent agreement with the simulation work, see Figure 8.18.

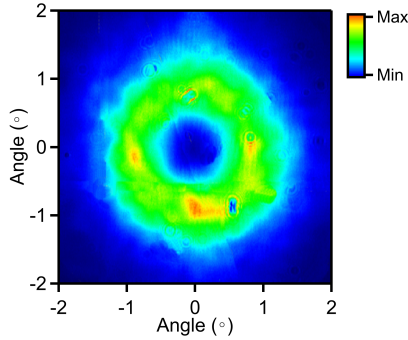


Figure 8.18: Measured FF pattern of the PhC lasers.

The divergence angle found further corresponds to the amount of periods used in this particular device (100×100 periods).

Lasing with Nanosecond Excitation Finally, these devices were also measured with a nanosecond excitation source, with pulses of 7 ns wide at 355 nm. The repetition rate of the laser was 100 Hz. The setup to do this looks very similar to the femtosecond setup shown in Figure 8.15a, but with a different spectrometer of lower quality (Thorlabs Compact CCD Spectrometer, CCS100/M), and naturally a different excitation laser. These measurements were performed more as a quick check than a thorough study. Nevertheless, nice lasing operation was found with threshold fluence around $100 \mu\text{J}/\text{cm}^2$ was found for the best devices, significantly lower than the values reported with the colloidal CdSe/CdS QDs by Zhu *et al.*¹³ or Xie *et al.*¹². This is done even without optimizing the devices, suggesting that much improvement is still possible. The width of the lasing modes is smaller compared to the femtosecond excitation, which we attribute to the mode reaching stability during excitation, since the excitation pulse here is longer than the gain lifetime.

Figure 8.19a shows lasing peaks of three different devices. In Figure 8.19b the spectra are shown below and above threshold (the peak at 532 nm seen in the graph below threshold is the first harmonic of the excita-

tion laser). Finally, in Figure 8.19, the threshold and the corresponding CW power is shown (calculated through dividing the fluence by the pulse length), where the two devices more to the green show thresholds of $100 \mu\text{J}/\text{cm}^2$, corresponding to $14 \text{ kW}/\text{cm}^2$ of CW power. These values are much lower than other reported colloidal QD based devices, which creates exciting prospects.

Since nanosecond excitation inevitably also introduces a higher thermal load (not to mention the fact that these devices were excited with a 355 nm excitation laser source), destruction of the CdS film due to heating was considered an issue. These measurements are performed in air, without any sort of cooling. Over time, destruction of the film occurred. Earlier devices using CdSe/CdS QDs, where red lasing was demonstrated, did show stable operation with SiNx on top, showing possible pathways for more stable operation. What is important to say here is that for higher repetition rates the device does break down significantly faster, showing that heat does become a problem. The measurements shown here are done at a repetition rate of 100 Hz, and the spectrometer integrates for a second (meaning only 100 pulses can saturate the detector). Increasing the repetition rate to 1 kHz, leads the sample to break down much faster (more than ten times faster as one would expect). We think this is due the sample not being able to cool down completely in one millisecond, leading to an ever increasing temperature, and as such a quicker breakdown.

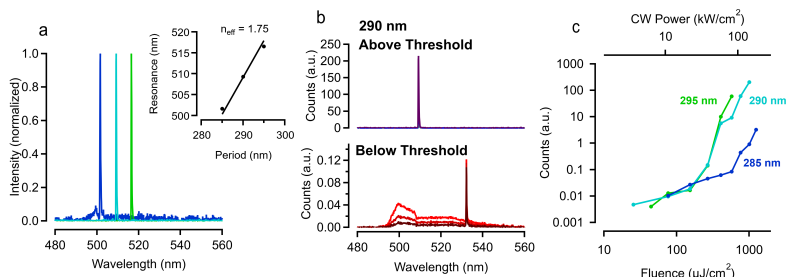


Figure 8.19: Nanosecond excitation lasing measurements. (a) Normalised spectra shown for various periods. The inset shows the fitted spectrum width of the lasing mode at 518 nm. (b) The resonant wavelength for various periods, showing that there are three different effective indices that come into play here. (c) Measured intensity for 2000 seconds, where a new measurement was done every 25 seconds, showing decay of the lasing line.

8.3 On-Chip Optical Gain in other Bulk Nanocrystals

Besides seeing lasing in the bulk CdS NCs, the same concept has been applied to other bulk NCs. The study of CdS is the most advanced, but it is worth sharing that the principles of bulk NC lasing at least translate to other materials. CdSe and ZnSe will briefly be shown here.

8.3.1 CdSe ASE and Lasing

Through a similar synthesis as for the CdS bulk NCs, bulk wz-CdSe can also be made. From TA measurements however it can be seen that the results are not as impressive: the intrinsic gain is comparable in size to CdSe/CdS core/shell QDs, but the gain lifetimes are lower (800 ps^{14}). Although disappointing, this can be explained through the much weaker binding energy in CdSe compared to CdS (about half as strong binding¹⁵). Knowing what we know from the bulk model, this will massively decrease the band-gap-renormalisation effect, yielding much lower optical gain.

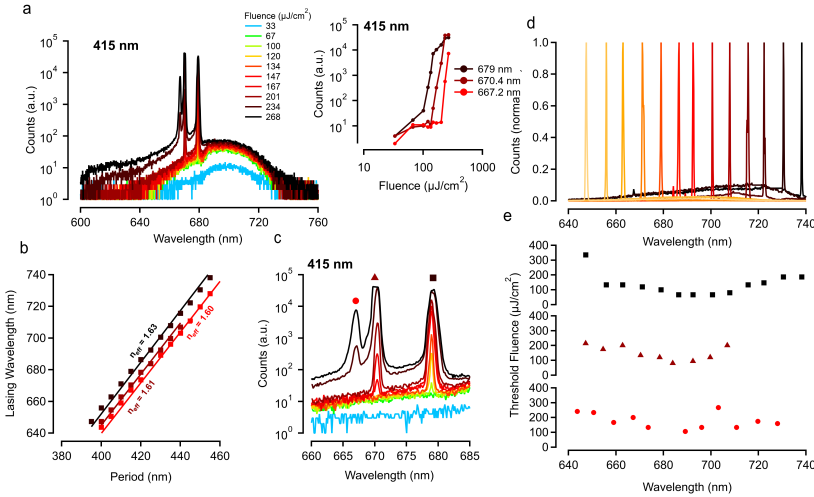


Figure 8.20: (a) Spectra on a device with a period of 415 nm, coated with bulk CdSe NCs. The inset shows the thresholds of the three different lasing modes (b) Effective index extraction for the three different modes. (c) Zoom in of the three modes. The objects above the peaks assign the thresholds used in (e). (d) Normalised lasing peaks over an impressive 100 nm bandwidth. (e) Thresholds for all devices, for all three modes.

Nevertheless, the fact that there is optical gain was observed through TA, we tried to see lasing, using the same type of structures as for the CdS NCs, but with larger periods to account for the different spectral window. In Figure 8.20 the results are shown. Figure 8.20 shows the different laser devices, showing thresholds of higher values than the CdS devices, minima of about $100 \mu\text{J}/\text{cm}^2$, around 700 nm. Figure 8.20d shows the lasing modes for various grating periods, with lasing over an impressive 100 nm range. The ratio between lasing mode intensity and background PL is also much lower, it is very clear that – different than the CdS – the intensity does saturate here. Again, this can be attributed to the lower intrinsic gain. In Figure 8.20a, the spectra are shown for one specific device.

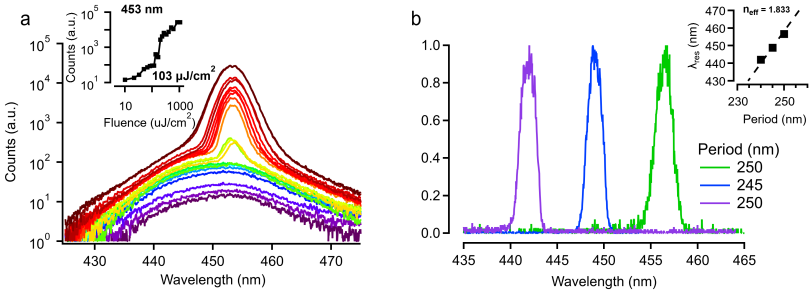


Figure 8.21: (a) ASE results on ZnSe/ZnS NCs, showing a threshold at $103 \mu\text{J}/\text{cm}^2$, at 435 nm. (b) Some lasing spectra for different grating periods using ZnSe/ZnS.

8.3.2 ZnSe ASE and Lasing

A third material that was tried were ZnSe/ZnS NCs. These still showed some confinement due to their size being comparable to the Bohr diameter, but it was quite small. We again see ASE, here with a threshold around $103 \mu\text{J}/\text{cm}^2$, at 435 nm, shown in Figure 8.21a. There were also working laser devices (Figure 8.21b), but due to high photo-induced oxidation, these were not stable enough for decent measurement. So just a couple of spectra were taken to show the different lasing lines for different periods. These materials however did give very bright emission – for as long as they survived being excited by the strong beam. Probably depositing SiOx coatings to avoid oxygen exposure would help these devices stay more stable. However, it is encouraging to see that just the first film of this material already showed very bright lasing.

8.4 Conclusions

In this Chapter, we have seen that the material properties found through TA spectroscopy translate well to thin film properties. The demonstration of ASE with bulk CdS NCs shows the complete lack of saturation, with a low threshold and very spectrally broad ASE peaks, very different from other colloidal NCs measured. The double-lobed ASE is worth further investigation through more in-depth ASE measurements. Furthermore, the VSL experiment showed that the impressive gain magnitudes also translate to thin films.

Next, when going to actual devices, we see – again – very bright lasing peaks, with low thresholds, and over a broad spectral range. The measured lasing thresholds match up well with the measurements straight on the material. As these devices were made just as a demonstration, much optimization can be done here: the framework now exists to simulate these types of devices accurately, and at this point they are well understood. The next step would be to see how far we can push these devices by performing an in-depth study on how to use e-beam lithography to accurately pattern these very small periodic structures. Adding 1st order gratings around the current 2nd order grating would be a great first start to improve the devices, together with changing the unit cell geometry, like going toward triangular patterns. Furthermore, to actually measure the FF patterns, improvements to the current, relatively simple, measurement setup need to be done. At this point, all the light is focused on a fiber, losing any information regarding the emission angle. Being able to map out the FF pattern from experiment would be a great addition to accurately understand and measure these types of devices. Finally, the process flow can still be improved, as the current SiNx/NC cladding does not give us great index contrast ($\Delta n \approx 0.4$). By going back to the SiNx/NC/SiNx stack, and etching a grating only on the top SiNx, the confinement can be improved, while decreasing the air exposure to the NCs. But since embedding NCs with SiNx tends to destroy the NC layer, at least partly, it will probably be better to take a step back from the lasers and com-

pare ASE from the SiN_x/NC stack and SiN_x/NC/SiN_x first. Growing a thin SiO_x coating through less invasive means than PECVD would also be helpful.

The fact that these bulk NCs seem to work, and the fact that we can explain why CdS operates better than CdSe, gives many possibilities as well: we need to look into materials with high binding energies to enhance the Band Gap Renormalisation effect. ZnSe and ZnS are prime candidates for this, allowing us to possibly create very bright, low threshold toward the blue or even in the UV! For the red side of the spectrum, alloying CdS:Se gives us back some of our spectral freedom we currently lost due to going to bulk NCs, since strong confinement no longer allows us to choose wavelengths at will. Naturally, when adding more selenium, the impressive gain metrics we currently see will start to disappear, so there will be a limitation on the usefulness there.

Besides all these fundamental questions, there is also the matter of the usefulness of these bulk CdS NC lasers themselves. They operate very well under femtosecond excitation, and without any photonic design optimisation also for nanosecond operation! We have found a material that satisfies all three metrics in our gain triumvirate. Can we capitalize on this? For this, the question becomes more how we can move toward Continuous Wave (CW) operation, which unavoidably leads to the question: how can we manage the thermal load in the system? This is discussed in the next Chapter, on thermal effects in colloidal NC photonic devices, Chapter 9.

Bibliography

- ¹ Burak Guzelturk, Matthew Pelton, Murat Olutas, and Hilmi Volkan Demir. Giant Modal Gain Coefficients in Colloidal II-VI Nanoplatelets. *Nano Lett.*, 19:277–282, 2018.
- ² Michael M Adachi, Fengjia Fan, Daniel P Sellan, Sjoerd Hoogland, Oleksandr Voznyy, Arjan J Houtepen, Kevin D Parrish, Pongsakorn Kanjanaboos, Jonathan A Malen, and Edward H Sargent. Microsecond-sustained lasing from colloidal quantum dot solids. *Nature communications*, 6(1):1–8, 2015.
- ³ Yuan Jin, Liang Gao, Ji Chen, Chongzhao Wu, John L Reno, and Sushil Kumar. High power surface emitting terahertz laser with hybrid second- and fourth-order bragg gratings. *Nature communications*, 9(1):1407, 2018.
- ⁴ RJ Noll and SH Macomber. Analysis of grating surface emitting lasers. *IEEE journal of quantum electronics*, 26(3):456–466, 1990.
- ⁵ Ziyue Wang, Pinyao Wang, Huanyu Lu, Bo Meng, Yanjing Wang, Cunzhu Tong, and Lijun Wang. Symmetry criterion and far-field control of photonic-crystal surface-emitting lasers. *Applied Sciences*, 12(20):10581, 2022.
- ⁶ Kyosuke Sakai, Eiji Miyai, Takui Sakaguchi, Dai Ohnishi, Takayuki Okano, and Susumu Noda. Lasing band edge identification for a surface-emitting photonic crystal laser. *IEEE Journal on Selected Areas in Communications*, 23(7):1335–1340, 2005.
- ⁷ Chathuranganie AM Senevirathne, Atula SD Sandanayaka, Buddhika SB Karunathilaka, Takashi Fujihara, Fatima Bencheikh, Chuanjiang Qin, Kenichi Goushi, Toshinori Matsushima, and Chihaya Adachi. Markedly improved performance of optically pumped organic lasers with two-dimensional distributed-feedback gratings. *ACS Photonics*, 8(5):1324–1334, 2021.

- ⁸ T Inoue, M Yoshida, MD Zoysa, K Ishizaki, and S Noda. Design of photonic-crystal surface-emitting lasers with enhanced in-plane optical feedback for high-speed operation. *Optics Express*, 28(4):5050–5057, 2020.
- ⁹ Toshihiko Baba. Slow light in photonic crystals. *Nature photonics*, 2(8):465–473, 2008.
- ¹⁰ Rik Harbers, Nikolaj Moll, Rainer F Mahrt, Daniel Erni, and Werner Bächtold. Enhancement of the mode coupling in photonic-crystal-based organic lasers. *Journal of Optics A: Pure and Applied Optics*, 7(2):S230, 2005.
- ¹¹ Mitsuru Yokoyama and Susumu Noda. Finite-difference time-domain simulation of two-dimensional photonic crystal surface-emitting laser. *Optics Express*, 13(8):2869–2880, 2005.
- ¹² W. Xie, T. Stöferle, G. Raino, T. Aubert, S. Bisschop, Y. Zhu, R.F. Mahrt, P. Geiregat, E. Brainis, Z. Hens, and D. Van Thourhout. On-Chip Integrated Quantum-Dot Silicon-Nitride Microdisk Lasers. *Advanced Materials*, page 1604866, 2017.
- ¹³ Yunpeng Zhu, Weiqiang Xie, Suzanne Bisschop, Tangi Aubert, Edouard Brainis, Pieter Geiregat, Zeger Hens, and Dries Van Thourhout. On-chip single-mode distributed feedback colloidal quantum dot laser under nanosecond pumping. *Acs Photonics*, 4(10):2446–2452, 2017.
- ¹⁴ S. Bisschop, P. Geiregat, T. Aubert, and Z. Hens. The Impact of Core/Shell Sizes on the Optical Gain Characteristics of CdSe/CdS Quantum Dots. *ACS Nano*, 12:9011–9021, 2018.
- ¹⁵ Tangi Aubert, Aleksandr A Golovatenko, Margarita Samoli, Laurent Lermusiaux, Thomas Zinn, Benjamin Abécassis, Anna V Rodina, and Zeger Hens. General expression for the size-dependent optical properties of quantum dots. *Nano Letters*, 22(4):1778–1785, 2022.

Chapter 9

Thermal Optimization of Colloidal Nanocrystal Lasers

The current colloidal NC based lasers previously reported by UGent are excited with femtosecond¹ and nanosecond² excitation. Nanosecond excitation can be considered quasi-CW operation optically speaking, as the pulses are 9 ns long and the gain lifetime in the used NCs is about 600 ps. However, going from quasi-CW to actual CW lasing poses a completely different challenge: the increase in thermal load in the system. The used nanosecond excitation source had a repetition rate of 1 kHz, which means it is turned off about 99.999% of the time. This means that for CW operation, even if optically speaking it is the same situation, the injected power would be a factor of 100.000 higher, and so would be the generated thermal power.

This can be tackled in two ways: either we can work on improving the NC layer itself, where the threshold can be decreased or higher gain can be achieved for lower necessary excitation, or we can improve the design and/or material stack in the photonic cavity itself to improve thermal

management. This Chapter will focus specifically on the latter for lasers using colloidal NCs as a gain material. The former has already been at length discussed in previous Chapters.

A couple of different approaches are taken here to reduce the thermal load of devices, mainly verified through COMSOL Multiphysics Finite Elements (FE) software. This tool allows us to do both thermal simulations and use optical mode solvers together, allowing us to check if certain changes to our material stack or geometry have, while increasing the thermal efficiency, reduced the optical confinement. This unavoidable trade-off can be engineered around as much as possible, to minimize the loss of confinement and thermal load as much as possible.

9.1 Introduction

Before discussing the simulation results, it is worth spending some time discussing the motivation behind certain choices of material parameters, powers and boundary conditions. These are highlighted here.

9.1.1 Thermal Conductivities

9.1.1.1 NC layer

The main problem with the NC based integrated lasers is the thermal conductivity of the NC layer: it is typically reported to be $0.22 \text{ Wm}^{-1}\text{K}^{-1}$.^{3,4}, this value is lower than typical values for dielectrics like SiOx and SiNx (see later), and much lower than silicon. Interestingly, it is also reported that doing a ligand exchange protocol from long organic ligands (oleylamine, $\text{C}_{18}\text{H}_{37}\text{N}$) to short inorganic ligands (SOCl_2), does not seem to impact the thermal conductivity of QDs all that much (from 0.22 to 0.24), perhaps due to there still being quite some empty space between the QDs. Nevertheless, the reduction in thickness achieved will effectively increase the modal gain in the film, which allows to use thinner films

In general, we can say that thinner films are a thermal advantage, at the cost of stronger gain. How large the actual gain value in the film is, depends on the NC material used. In this Chapter hence we will disregard the notion of gain and just look at NC film thicknesses all with the same thermal conductivity, and compare simulations with each other just for thermal effects. For an actual practical device, we can then decide on a thickness depending on the intrinsic gain in the used NC material.

A typical value used for a colloidal NC film refractive index is about 1.65. This is a combination of the semiconductor cores which have typical values of $n \approx 2.5$, with the organic ligands ($n \approx 1.45$), and the empty space between the dots ($n \approx 1$).

9.1.1.2 Dielectric Surroundings

For SiNx thin films, a wide variety of values of the thermal conductivity are reported, ranging from $0.7 \text{ Wm}^{-1}\text{K}^{-1}$ to $13 \text{ Wm}^{-1}\text{K}^{-1}$. This wide range stems from the various parameters that can be changed in the deposition, and recent work seems to suggest that for thin films the lower end of the values seem to be the correct ones⁵. For SiOx thin films, grown with thermal evaporation, values around $1 \text{ Wm}^{-1}\text{K}^{-1}$ are reported^{6,7}. As we do not have experimental information about our in-house grown films, we will use these values in the simulations. It has to be noted that these are much lower than the thermal conductivity of widely reported bulk values for SiNx ($15\text{-}30 \text{ Wm}^{-1}\text{K}^{-1}$) or SiOx ($1.4 \text{ Wm}^{-1}\text{K}^{-1}$).

Silicon is also present in our system, it is in fact the bulk of the material (considering typical silicon substrate thicknesses of 0.5 mm , while the SiOx is $1\text{-}3 \text{ }\mu\text{m}$ and the SiNx $100\text{-}200 \text{ nm}$). COMSOL has a built-in value for monocrystalline silicon of $130 \text{ Wm}^{-1}\text{K}^{-1}$ that was used in these simulations. Other materials used will have their thermal conductivities mentioned where needed.

For refractive indices, usually values for SiNx are around 2, for SiOx around 1.4 and for silicon 3.48.

9.1.2 Thermal Power in the System

The thermal load in our system is due to (1) energy lost by relaxation of carriers to the band edge ($E_{pump} - E_g$), and (2) non-radiative recombination, by trapping, Auger-recombination or others. It is worth estimating the power from both these effects to use as input in the simulation.

Contribution from non-resonant pumping We can use Beer-Lambert to calculate the absorbed power P_{abs}

$$P_{abs} = P_{pump} \cdot (1 - e^{-\alpha \cdot d_{NC}}) \quad (9.1.1)$$

For every lost photon, $E_{pump} - E_g$ is dissipated as heat. To calculate the absorbed photon flux, we simply have to divide by the energy of the

pumped photons, and to find the heating power, we can multiply with the energy lost due to heat

$$P_{heat,2D} = P_{abs} \cdot \frac{E_{pump} - E_g}{E_{pump}} = P_{pump} \cdot (1 - e^{-\alpha \cdot d_{NC}}) \cdot \frac{E_{pump} - E_g}{E_{pump}} \quad (9.1.2)$$

which, since we integrated the contributions over the thicknesses, is a power per area. If we assume the absorption is low, we can assume the absorbed power is uniform as a function of thickness, so we can find the power density by dividing by the NC layer thickness

$$P_{heat,3D} = \frac{P_{pump}}{d_{NC}} \cdot (1 - e^{-\alpha \cdot d_{NC}}) \cdot \frac{E_{pump} - E_g}{E_{pump}} \quad (9.1.3)$$

For this numerical estimation, the approximated threshold for CW lasing of $P_{pump} = 39 \text{ kW/cm}^2$ at a pump wavelength of 532 nm (2.33 eV), while the lasing occurred around 630 nm (2 eV)². To calculate the contribution of the first part, we need to check how much of the light was absorbed by the QD film. The film is $d_{QD} = 50 \text{ nm}$ thick, and we have an intrinsic absorption coefficient of 16000 cm^{-1} . Considering a packing of about 50%, we get an absorption coefficient of $\alpha = 8000 \text{ cm}^{-1}$. Filling this in we get a power density $P_{heat,3D} = 4.33 \cdot 10^7 \text{ W/cm}^3$.

Contribution due to non-radiative recombination The thermal load due to non-radiative recombination is a bit more complex to calculate. By far the biggest contributor here is because of Auger recombination in the case of 3D confined systems. Let us consider first a situation where the radiative rate is much slower than the non-radiative rate. Here, every absorbed photon will completely release its energy in heat, specifically the non-radiative recombination will release E_g of energy per photon. Translated to power, this then gives $P_{abs} - P_{heat}$. This makes sense since there is no emission here, and the total thermal energy in the system is then the total absorbed power P_{abs} .

A more realistic situation is where radiative and non-radiative recombination compete with each other, with complex laser dynamics governing the relative rates, depending on both the material properties and laser

cavity design. A higher Q -factor for long photon lifetimes, with a good gain medium for low Auger rates, will lead to more stimulated emission and less non-radiative recombination. But this is difficult to estimate. Because of this, we choose to use $2 \cdot P_{heat,3D}$ as the thermal power density in the system, and always compare temperatures in different situations relative to each other instead of treating it as an absolute temperature. The contribution for non-resonant pumping can be considered a lower limit of the thermal power in the system. As will be seen in the later Sections, the temperature increase due to these powers is, in fact, relatively low: only a few to a few tens of degrees. In reality, the lasers will be operated relatively high above threshold, perhaps $\times 2 - \times 3$ the threshold power.

9.1.3 Boundary Conditions

For combining thermal and optical simulations, it is necessary to define domains for each type of simulation considering the different boundary conditions used. For the optical mode simulations, Perfectly Matched Layer (PML) boundary conditions are used everywhere. This is an artificial absorbing layer that is designed to absorb all the light that touches it, essentially being physically equal to losing the light to the surroundings. For the thermal simulation, the device surface is considered a thermal insulator, while the bottom and the side is considered infinitely long and the outer edge is fixed at room temperature (293.15 K), since we consider that the substrate is an infinite heat sink. This is also shown in Figure 9.1.

For waveguides, typically 2D simulations are performed on a cross-section. 2D simulations with rotational symmetry are also used for disk/ring simulations.

9.1.4 Example

To conclude the introduction, consider here a simulation of a NC waveguide of 1 μm wide, and a height of 200 nm. The substrate is 1 μm SiOx, with an infinite layer of silicon below, see also Figure 9.1. Toward the

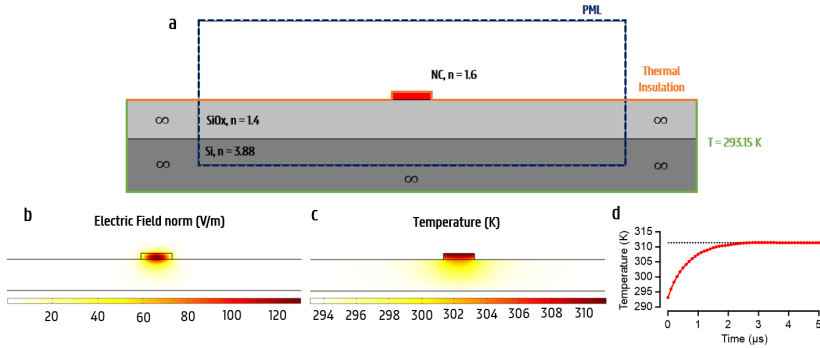


Figure 9.1: Example of thermal and optical simulations. (a) Shows the layout with some material and simulation information. (b) Shows the norm of the electric field for the fundamental mode in the waveguide, with $n_{eff} = 1.44$. (c) Shows the temperature for steady-state, with a maximum in the top of the NC layer. (d) Shows the temperature as a function of time. After about three microseconds, the system is in steady-state.

edges of the substrate (left and right), the SiOx also extends infinitely.

A fundamental optical mode is found (Figure 9.1b) with an effective index of $n_{eff} = 1.44$, showing that the confinement is pretty weak, there is quite some leakage in the SiOx layer. This can be improved upon by adding SiNx layers, with refractive indices of about 2. There is a temperature gradient of about 18 K over the structure (Figure 9.1c), with the highest drop occurring from the NC to SiOx interface. This is due to the big difference in thermal conductivity between the NC layer and the SiOx layer. Finally, Figure 9.1d shows that the system reaches a steady-state situation after about 3 microseconds.

The remaining simulations in this Chapter will follow a similar flow as shown here.

9.2 The Stack as a Series of Resistors

Before discussing full finite elements simulations of the complete stack, it is worthwhile to consider our system as a 1-dimensional series of resistors to gain some insight in the evolving temperature as a function of certain thermal conductivities. As described earlier, the typical stack is a layer of NCs on a SiOx substrate, and then on a Si substrate, keeping in mind that in general SiNx layers are added for increased optical confinement. Considering that SiOx and SiNx have relative close thermal conductivities we can neglect it for now, and add its thickness to the SiOx layer. For this calculation, we consider some T_{max} at the top of the SiOx layer and check how to optimize the stack of the substrate.

A thermal resistance is defined as

$$R = \frac{d}{k \cdot A} \quad (9.2.1)$$

where the A factor drops out for the 1-dimensional case. The thickness d is the thickness of the layer. Knowing this, we can define the resistance of the SiOx layer, R_{SiOx} , and of the Si layer, R_{Si} . The thermal power source can be defined as a current source. Combining this allows us to draw the equivalent electrical circuit, see Figure 9.2a where we assume some total power after going through the NC layer, for simplicity, yielding a simple equivalent network. Since this is a qualitative discussion, the thermal power magnitude is not really relevant, we just want to look at the temperature drops over the separate layers in the stack. We can determine three temperatures, T_0 is the temperature above the SiOx layer, T_1 between the SiOx and the Si layer, and then the final temperature which is room temperature, which we put at zero. In the resistors, the temperature drops linearly. T_0 can be found to be

$$T_0 = (R_{SiOx} + R_{Si}) \cdot P = R_{tot} \cdot P = (1 \cdot 10^{-6} + 3.84 \cdot 10^{-6}) \cdot P \quad (9.2.2)$$

and T_1 as well by using the Voltage Divider Laws (or in this case: Temperature)

$$T_1 = \frac{R_{Si}}{R_{tot}} \cdot T_{max} \quad (9.2.3)$$

Using the stack in the previous Section, we can determine the temperature drops over the two layers as a benchmark. After the SiOx layer the temperature has dropped to 66% of the maximum value. The remaining drop then happens throughout the Si layer. When changing the stack, two things will happen: (1) the slope of the temperature drop will change, due to the changed resistance (only when changing k), and (2) the maximum temperature T_0 will change. As such, it is important to keep in mind the *total* resistance, not of just the SiOx layer.

As an example, consider swapping out the entire stack for a MgF₂ substrate, which is grown monocrystalline so it is safe to say the crystalline thermal conductivity is present $k = 30 \text{ Wm}^{-1}\text{K}^{-1}$. MgF₂ has about the same refractive index as SiOx, so we could think that this is optically the same, but a thermally superior stacking. The full resistance of this stack would be, assuming the same thickness as our Si substrates (500 μm):

$$R_{MgF_2} = \frac{500 \cdot 10^{-6} \text{ m}}{30 \frac{\text{W}}{\text{mK}}} = 1.67 \cdot 10^{-5} \frac{\text{Km}^2}{\text{W}} \quad (9.2.4)$$

which is a factor 3.4 increase in resistance, leading to the same amount of increase in maximum temperature. While getting rid of the badly conducting SiOx substrate in this way might seem enticing, it can be seen from that simple calculation that it is in fact not worth it. This is shown in Figure 9.2c, where the dotted line is the case of MgF₂, showing a consistent higher temperature. Admittedly, in a more realistic situation of a 3D device, the heat will not only dissipate straight downward, and bringing a more conductive material closer to the heat source will have a larger effect. Nevertheless, the ratio of thicknesses is so large that the substrate will be by far have the highest contribution to the resistance.

Instead, it is worth looking into possibly thinning the SiOx layer to decrease the total resistance. In Figure 9.2c, the effect of thinner SiOx is shown on T_0 , showing reductions of up to 20%. A minimal oxide thickness however will be necessary for optical confinement, which is not considered here (see next Section), leading to probably a maximal reduction of 10%, going to thicknesses of 500 nm. Besides decreasing the thickness, increasing the thermal conductivity would achieve the same effect, by exchan-

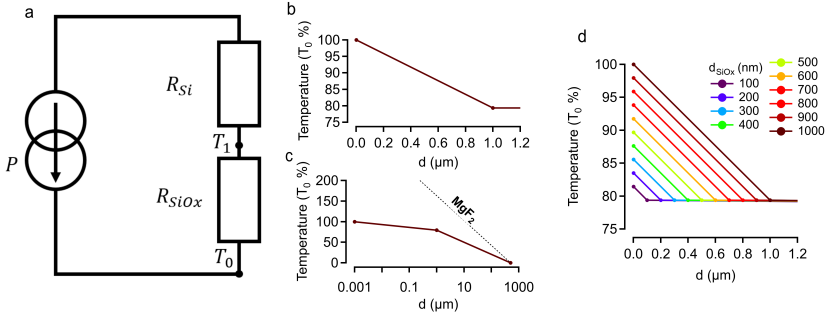


Figure 9.2: (a) Equivalent thermal network of our substrate. (b) Temperature drop over the substrate, specifically over the SiOx layer with a thickness of 1 μm . (c) Same as (b), but in a logarithmic scale, over the entire substrate. At the bottom of the Si layer the temperature drops to zero. (d) Temperatures for various SiOx widths, showing a clear drop of the maximum temperature in the stack.

ging the SiOx by some other material with the same refractive index but a higher thermal conductivity. This is discussed in the next Section. Finally, by grinding down the substrate wafer from 500 to 300 μm , a drastic decrease of the thermal resistance can be achieved as well. This is sometimes done through grinding, where 300 μm is the limit for the wafer to remain manageable. Going thinner than this causes the wafers to break easily. Although seemingly a very basic way to reduce the thermal resistance, these simple steps are some of the most beneficial methods that are discussed in this Chapter. This 1D approximation however does not paint a full picture: the smaller your heat source, the less correct it will be. For a point source, heat can travel in more directions, leading to an increased importance in having high conductances as close as possible to the device.

9.3 Thermal Substrates and Coatings

The typical stack is one of LF SiN_x/NC/MF SiN_x, with thicknesses of 100/50/100 nm on a 1 μm SiO_x substrate, as shown in Figure 3.7. There are two simple things that can be done without altering the process flow too much: (1) the substrate can be exchanged to something more thermally conductive, and (2) a certain (preferably as thermally conductive as possible) coating can be added after the complete process flow. A prime candidate for both these changes is using MgF₂, since it has a thermal conductivity of 30 Wm⁻¹K⁻¹, with a refractive index of about 1.38, and can be grown through thermal evaporation in our in-house clean-room. It is important to note however that these are values corresponding to bulk MgF₂, and as we already know from the SiN_x, thin films will not necessarily have the same conductivity. Instead of focusing on a specific material here, we will check how changing the conductivity of the substrate and adding a coating of certain thickness influences the maximum temperature.

For a first simulation, the thermal conductivity was swept from 0.1 to 170 W/m/K (as a theoretical maximal value for silicon). The resulting max temperature can be seen in Figure 9.3c, as a function of time. The lower the conductivity the higher the maximum temperature will be, and the longer it will take to reach a steady-state regime.

Secondly, a coating is added, where both the thickness and the thermal conductivity are swept. Considering this will change the mode as well, it is useful to do optical simulations here too. The optical confinement in the NC layer as a function of the coating thickness is shown in Figure 9.3d, together with the max temperature, showing a similar dependence on the coating thickness. It is important to note that even though the absolute temperature decrease in degrees is not so much, this will scale with higher input powers, while the confinement difference will only remain about one percent.

As was done in the previous Section theoretically, the thickness can also be varied of the SiO_x layer. What is important here is that, although

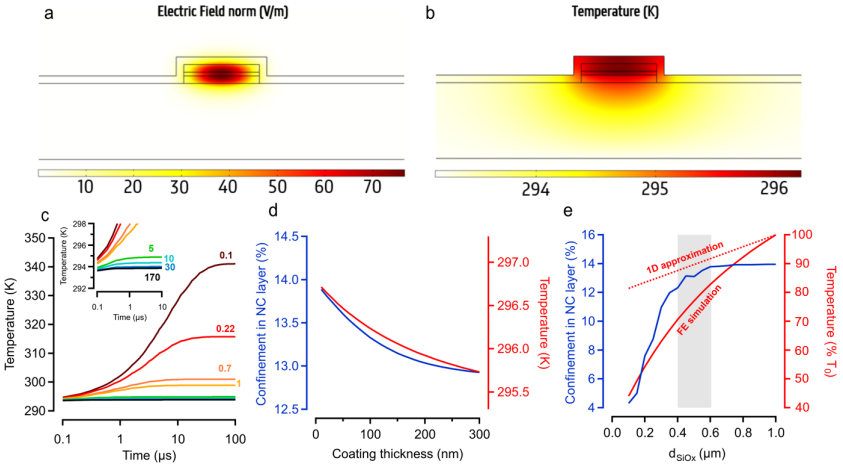


Figure 9.3: (a) Mode simulation of a SiNx/NC/SiNx waveguide with a SiOx coating of 100 nm. (b) Thermal simulation with same conditions as (a). (c) Max temperature in the structure for different thermal conductivities of the substrate. (d) Confinement in the NC layer and max temperature as a function of coating thickness.

thermally advantageous, a minimal thickness will be needed for optical confinement. The results here are shown in Figure 9.3e, again combining confinement and temperature simulations. The simulation gives a decrease in temperature much steeper for thinner SiOx layers compared to the 1D approximation. This can be explained through the approximation, since in this more realistic case the heat can move out of the NC layer in more directions than just vertically down. The confinement (blue) remains quite constant, up until about a SiOx thickness of 500 nm, where according to the simulation the temperature has already decreased with 20%.

9.4 Disk and ring lasers

Limiting the active material in a resonator helps with reducing the temperature, since less thermal power will be generated. Usually this goes hand in hand with a reduction in lasing operation due to less gain, and as such increases restrictions on the necessary confinement which can be condensed into the Q -factor, or demands higher g_i of the gain material. An exception to this is for the case of disk lasers: going from disk to ring can maintain the same optical mode and confinement, while massively reducing the thermal power, for certain thicknesses of rings. The simulations shown here have the same parameters as the previous sections, 100/50/100 nm for SiN_x/NC/SiN_x layers, with a 1 μ m SiO_x substrate.

As explained in Chapter 3, a disk laser is a cavity looped in on itself, so the resonating wavelengths are determined by the radius of the disk. The modes, referred to as Whispering-Gallery-Modes (WGMs), travel around the disk, with the maximum intensity near the edge, see also Figure 9.4a. For the lasing mode the gain material in the middle of the disk is not really relevant, besides for adding the odd spontaneous photon that can kickstart the stimulated emission of the lasing modes. So optically, going from disk to ring is the same as long as the ring width does not become too small. This is shown in Figure 9.4c, where the integrated electric field norm in the SiN_x/NC/SiN_x layers is shown for the WGM as a function of the inner radius of the ring r . This shows barely any change up until a certain point where the confinement of the mode completely disappears. As a rule of thumb it can be said that the ring needs to be at least 1 μ m smaller than the outer radius (so a waveguide width of 1 μ m). This is shown in the figure with the grey boxes, here the ring width becomes smaller than 1 μ m. It must be noted that this is a theoretical limit, in reality more sidewall scattering will start occurring for thin rings, to avoid this adding some extra thickness can be useful.

Thermally speaking the gain material in the middle makes a big difference since it is that much more volume that will generate heat. Here we assume that the pump size is much larger than the disk, and as such

is constant. We can make this assumption considering our typical disk lasers have radii between 2.5 and 7.5 μm , and the smallest spot size we have achieved is about $\sigma = 20 \mu\text{m}$. For the biggest ring, this only leads to a 15% difference in power between the center and the outer edge. This, however, means that in reality the effect of increasing the inner radius has an even larger effect than is presented here.

To calculate the total thermal power we can integrate over the total volume of the NC layer in the disk and rings with decreasing width (call r the inner radius of the ring and R the outer radius). The power will be

$$P_{tot} = P_{heat,3D} \cdot d_{NC} \cdot \pi(R^2 - r^2) \quad (9.4.1)$$

This is plotted in Figure 9.4d, at the top. For the limit where $r = R$, P_{tot} drops to zero. The thermal simulation shown in the same figure shows similar trends, although increasing the outer radius of the disk/ring R has less impact on the maximum temperature than on the thermal power.

The idea in this Section can be generalised: only have NCs where they contribute to the lasing mode. This might seem trivial, but typically NC based integrated devices are made by spincoating a NC layer, which means there are NCs everywhere, not just where they are needed. For disk/ring lasers, this can be circumvented through designing an optimal device. Alternatively, lift-off or inkjet printing can be used to only deposit NCs on the necessary location. An alternative to all this is to only excite the NCs, by filtering the pump light where it is not needed, for example by blocking the gaussian beam in the center, effectively turning the pump into a ring shaped beam as well. This comes with its own problems regarding alignment, which becomes much more critical.

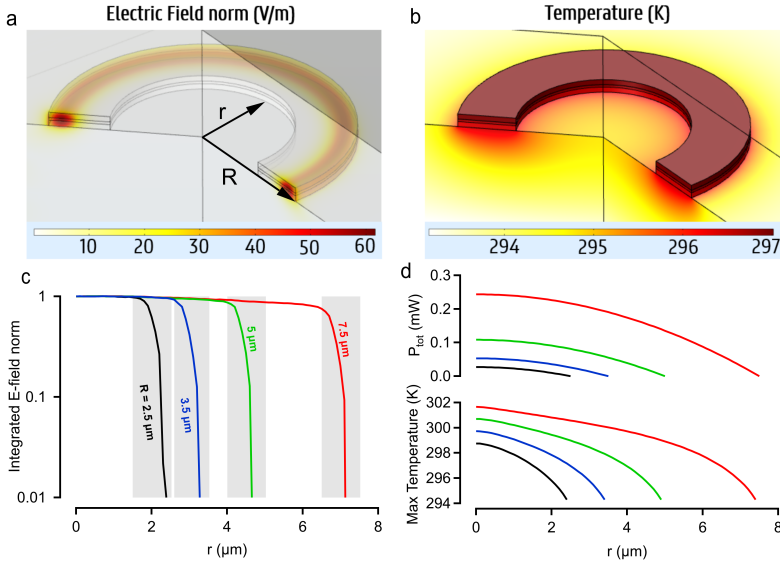


Figure 9.4: (a) Whispering-Gallery-Mode (WGM) of a ring with $R = 2.5 \mu\text{m}$ and $r = 1 \mu\text{m}$. (b) Thermal simulation with the same geometry as in (a). (c) Integrated electric field norm in the SiNx/NC/SiNx stack. (d) Theoretical P_{tot} value as calculated in Eq 9.4.1 are shown in the top graph. The max temperatures in the device found from the simulation are shown in the bottom graph.

9.5 Slot Waveguides

An alternative method of altering the processing to reduce the thermal load, and actually *increasing* the optical confinement is by using slot waveguides. Essentially, this “rotates” the stack by 90 degrees, having the successive SiNx/NC/SiNx layers perpendicular to the substrate instead of parallel. This connects the NC layer to the substrate by three interfaces instead of the two for the traditional SiNx/NC/SiNx waveguides. Adding a coating to this structure completely surrounds the NC layer.

The necessary process flow to create these kind of structures is achievable by modifying the NC liftoff process. Instead of spincoating the NCs straight after the development, first a SiNx etch is done to etch away the

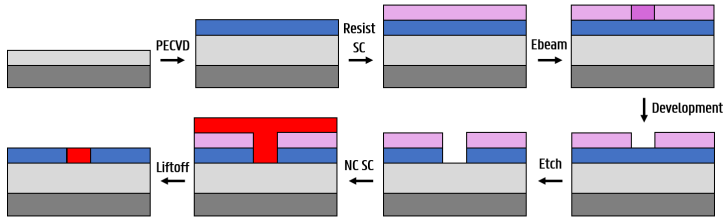


Figure 9.5: Process flow to etch a slot in a SiNx layer and fill it with NCs in the same lithography step.

gap. Only after this the NCs are spincoated, and then the liftoff is performed, ending up with etching the slot and actually filling it in a single processing step. In a secondary lithography step the waveguides can then be completed. This flow is shown in Figure 9.5. It is important to note here that compared to a regular liftoff, a thicker resist is needed. Keeping in mind the typical 200 nm needed for a good liftoff, the etching time and rate of the resist needs to be included in the total thickness (considering an etch rate of 50 nm/min about 400 nm resist is enough).

9.5.1 Simulations

For slot waveguides it is interesting to sweep both the width of the SiNx waveguides (W_{SiNx}), and the width of the slot containing the NCs (W_{NC}). The height of the waveguides was taken to be fixed at 200 nm, the NC width goes from 50 nm to 1000 nm, in steps of 50 nm, and the SiNx width goes from 100 nm to 1000 nm in steps of 50 nm. The resulting maximum temperature and confinement in the NC layer is shown in Figure 9.6, together with a simulation example. From Figure 9.6c we see that higher confinements can be reached compared to the traditional stacking, although it has to be noted that the thickness is higher. Still, comparing the total amount of NCs in the structure, it can be seen that there is a comparable amount for many of the combinations chosen here (the traditional stack has $1000 \times 50 = 5 \cdot 10^4 \text{ nm}^2$, equating for the slot waveguides to a thickness of 250 nm when the height is 200 nm). The greyed area is

the area where there are less NCs compared to the traditional stack, and for the right width combination it can be seen that up to 20% confinement in the NC layer can be reached, with the same total NC volume.

The temperature is shown in Figure 9.6d. Again, higher temperatures are found compared to the traditional stack, although this is only the case when the total NC volume is higher. For the same or smaller volumes, lower temperatures are found. Maybe not surprisingly the biggest effect on the maximum temperature is the NC layer width, since increasing this will increase the heat in the system. Wider SiNx layers do have a slight effect on the temperature as well, although this is an unacceptable change due to the bad confinement for these wide SiNx layers. This shows that slot waveguides with well chosen design parameters have better thermal management for the same amount of NC material, *and* improved confinement. The same reasoning for improving the thermal conductivity and/or adding a coating can also be applied here, for even better thermal management.

9.5.2 Processing

As this is a change to a regular process flow (NC lift-off, which can be considered established), some optimisation needed to be done: NC concentration (translating to film thickness), e-beam dose, resist thickness all needed to be optimized to make nicely filled slots. Right of the bat, the regular resist ARP617.06 that is usually used for NC lift-off was not useable since the resist could not reach the necessary thickness for etching and lift-off (300 nm at 4000 RPM). A denser version, ARP617.08, was used, which could reach the necessary thickness (500 nm at 4000 RPM).

First trials mostly showed issues with the NC concentration (here CdSe/CdS core/shell QDs are used, for which the lift-off process is optimized), showing pillars of QDs sticking out of the SiNx slot, see Figure 9.7a. More diluted samples as such were necessary. With better suited concentrations issues of a different kind arose: The NC film looks fine before lift-off, but after lift-off the remaining NCs in the slot seem to have

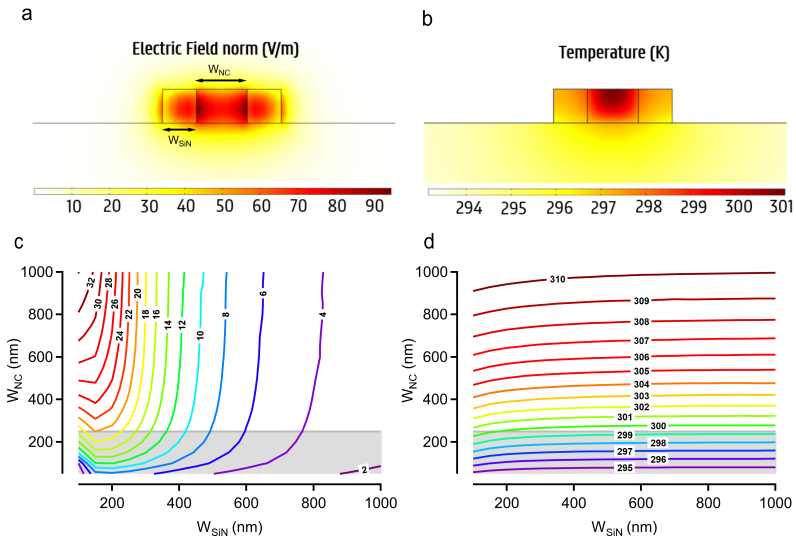


Figure 9.6: (a) Electrical field norm for a slot waveguide with a NC width of 300 nm, and SiNx widths of 200 nm. The height of the waveguide is 200 nm. (b) Temperature for same stack as in (a). (c) Confinement in NC layer shown for combinations of NC width W_{NC} and SiNx width W_{SiN} . The grey area is where there are less NCs in the device compared to the traditional stack. (d) The same as (c), but showing the maximum temperature. Here it is clear that the main dependence of the highest temperature is the amount of NCs in the device, although adding wider SiNx layers also slightly reduces it.

shrunk, as shown in Figure 9.7b.

This is more of an issue than one would initially think: the shrinking causes small bends inside of the slot (Figure 9.7c) and a “dirty” interface between the SiNx and the NCs, causing high amounts of scattering. By illuminating the NCs with UV light while putting the sample under a microscope, we can see emission from the NCs only in the slot (Figure 9.7e,f). Sadly, no amplification is observed when performing VSL measurements.

Current thinking is that due to capillary effects, not all the solvent evaporates during the initial spincoating and some remains in the slot, hence why the NCs look good before the actual lift-off. The aggressive

washing with acetone washes away the remaining solvent, causing the remaining NCs to shrink. To fix this, a lift-off can also be done with various concentrations of toluene and acetone, as performed in the work of Xie *et al.*⁸, where it was shown that by using a ratio of 1:4 acetone/toluene, the best liftoff was performed, although this was for monolayers of NCs. So this optimisation was repeated by trying different ratios of acetone/toluene. But the result was the same as before: either the lift-off just did not happen, or the same shrinking of the NC film occurred. The effect was very chaotic, no correlation could be found between acetone/toluene concentrations and size of the gaps.

Alternatives to the processing were by not doing a lift-off and just etching a slot waveguide on its own. After this, NCs could be deposited by spincoating, although this could give issues with the slot not being filled (due to too high aspect ratios). For only local deposition of the NCs, inkjet printing can be done. Using this technique, the NCs could be deposited straight on the slot. Since the accuracy of this technique makes it impossible to deposit only in 100-300 nm gaps the NCs would be deposited in the trench next to the slot waveguide as well, which in fact had minimal impact on the optical mode. First trials of using this have been done with satisfactory results regarding the deposition and filling, but no amplification has been observed as of yet. This could possibly be a sidewall issue, where the inside of the slot (where the optical mode is at its maximum) effectively “feels” these sidewalls very strongly, causing a lot of scattering. A very clean sidewall is necessary in this situation, and could be improved upon in the future.

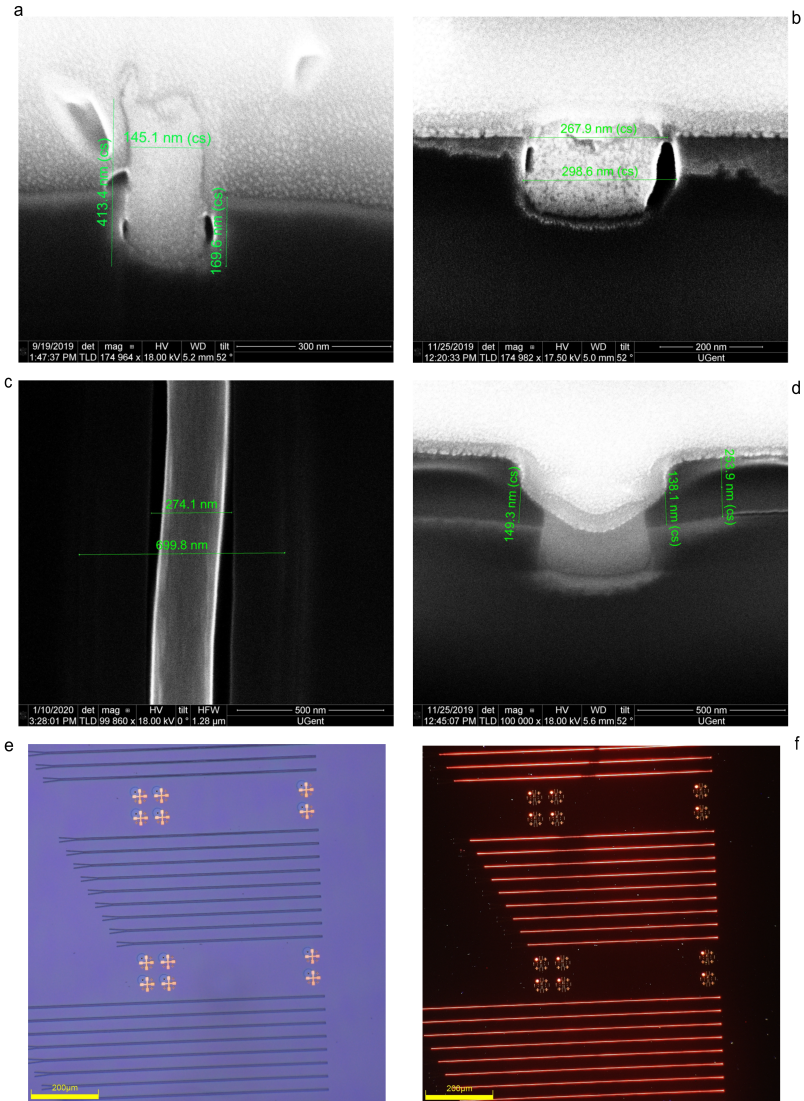


Figure 9.7: (a) Slot where lift-off was done with too highly concentrated NC samples. (b) Slot where the NC sample had the right concentration. Notice the rough surface, and the holes at the SiNx sidewalls (specifically the big gap on the right side). (c) Top view of SiNx slot (the straight lines), and showing that the NCs inside have shrunk and sometimes bend. (d) Slot waveguide before lift-off, showing good filling of the gap with NCs. (e) Optical microscope image of slot waveguides of various lengths and visible gold markers. (f) Same as (e), but illuminated with UV light to show that the NCs are only located within the slots.

9.6 Conclusions

This Chapter tries to paint a complete picture in heating mechanisms in colloidal NC based integrated photonic devices from a simulation side. From an analytical, simplified case, to straight, active waveguides, disks and rings, periodic structures and slot waveguides, we have presented the impact of making changes to the stack, and their impact on both the optical mode, and the thermal load.

The results can, for a very general case, be briefly summarized as follows: (1) Surround the NCs with as much material as possible, do not leave any edges exposed. The NCs are always by far the worst thermal conductor in the stack, so extracting the heat from them as much as possible is necessary. (2) Localise NCs only where the optical mode is at its maximum. Other NCs only add to the thermal load, while not contributing to the lasing action. As discussed, this can be done by turning disks into rings, or by making the NC layers thinner for situations where this is possible. (3) Reduce the resistance of the substrate as much as possible, either by making the SiOx thinner, or exchanging the SiOx by a better conductor, like the prime candidate MgF₂. Combining all these relatively small changes to the laser, while only having minimal impact on the optical mode, drastically reduce the maximal temperature. To reach the goal of CW lasing, keeping this insight in mind while designing is necessary. A thermally optimal design, together with NCs that combine the three metrics of the gain trifecta into one material, will give us our best chance of creating the next generation colloidal NC based integrated lasers.

Bibliography

- ¹ Weiqiang Xie, Thilo Stöferle, Gabriele Raino, Tangi Aubert, Suzanne Bisschop, Yunpeng Zhu, Rainer F Mahrt, Pieter Geiregat, Edouard Brainis, and Zeger Hens. On-chip integrated quantum-dot–silicon-nitride microdisk lasers. *Adv. Mater.*, 29(16):1604866, 2017.
- ² Yunpeng Zhu, Weiqiang Xie, Suzanne Bisschop, Tangi Aubert, Edouard Brainis, Pieter Geiregat, Zeger Hens, and Dries Van Thourhout. On-chip single-mode distributed feedback colloidal quantum dot laser under nanosecond pumping. *Acs Photonics*, 4(10):2446–2452, 2017.
- ³ Michael M Adachi, Fengjia Fan, Daniel P Sellan, Sjoerd Hoogland, Oleksandr Voznyy, Arjan J Houtepen, Kevin D Parrish, Pongsakorn Kanjanaboos, Jonathan A Malen, and Edward H Sargent. Microsecond-sustained lasing from colloidal quantum dot solids. *Nature communications*, 6(1):1–8, 2015.
- ⁴ Wee-Liat Ong, Sara M Rupich, Dmitri V Talapin, Alan JH McGaughey, and Jonathan A Malen. Surface chemistry mediates thermal transport in three-dimensional nanocrystal arrays. *Nature materials*, 12(5):410–415, 2013.
- ⁵ M Hadi, S Pailhès, R Debord, A Benamrouche, Emmanuel Drouard, Thomas Gehin, Claude Botella, J-L Leclercq, P Noe, F Fillot, et al. Transient thermal conductivity in pecvd sinx at high temperature: The thermal signature of an on-going irreversible modification. *Materialia*, 26:101574, 2022.
- ⁶ David G Cahill, My Katiyar, and JR Abelson. Thermal conductivity of a-si: H thin films. *Physical review B*, 50(9):6077, 1994.
- ⁷ Michael B Kleiner, Stefan A Kuhn, and Werner Weber. Thermal conductivity measurements of thin silicon dioxide films in integrated circuits. *IEEE Transactions on electron devices*, 43(9):1602–1609, 1996.

- ⁸ Weiqiang Xie, Raquel Gomes, Tangi Aubert, Suzanne Bisschop, Yunpeng Zhu, Zeger Hens, Edouard Brainis, and Dries Van Thourhout. Nanoscale and single-dot patterning of colloidal quantum dots. *Nano letters*, 15(11):7481–7487, 2015.

Chapter 10

Transient Phase in Integrated Devices

Based on the work done in Chapter 7, the foundations have been built to make modulators based on colloidal NCs, which will be discussed in this Chapter. Here, we look at how we can translate the derived refractive index information to phase shifts in waveguides for Mach-Zehnder Interferometers and the first measurements performed with such devices. Furthermore, we look into index changes in devices that are perhaps not favourable, i.e. in lasers. A refractive index change here has effect on the location of the lasing modes, as is shown in this Chapter.

10.1 Introduction

The results discussed in Chapter 7 show and discuss the possibilities for modulation: by looking in a wavelength region where ϵ_I is not modified, but ϵ_R is. This way, a phase change can be induced without additional losses. Interestingly, due to the $1/\lambda^2$ relation between ϵ_I and ϵ_R , a resonance in the imaginary part (linked to a strong absorption peak, like at 510 nm for the 4.5ML CdSe NPLs) can lead to a very broad effect in the real part. This in turn then translates to the refractive index and extinction coefficient, and finally, to the change in phase. This effect specifically is what we will try to exploit as discussed below.

A typical modulator operates by locally changing the refractive index through applying a voltage, for example by locally doping certain materials, which will then be more sensitive to an applied bias. Here however this is not the case: we change the refractive index by injecting a large amount of photons (by using a femtosecond pulsed laser) in our NC layer. It does not even have to be said that this is needlessly impractical for an actual device compared to applying voltages. This study is more out of interest of the NC material, to make a demonstration of the effect: can we get a MZI to work using colloidal NCs? Can we span a broad wavelength region as the TA data suggests? How fast could we possibly switch those devices? How small can we make them?

As mentioned previously, the CdSe/CdS core/shell QD system is the most mature in terms of film formation and stability over time. Although NPLs and bulk CdS NCs seem very promising regarding very large refractive index changes under excitation, it seemed a good first step to check it on the most mature platform. For that reason we limit the discussion here to CdSe/CdS, which is also the only material we have used in devices.

10.2 Optically operated Mach-Zehnder Interferometers based on CdSe/CdS QDs

The goal is to create MZIs which either attenuate or let propagate light of a certain wavelength depending whether or not the device is being illuminated or not. As the principle behind MZIs is explained in Chapter 3, we only discuss here the specific situation where colloidal NCs are excited which causes a change in refractive index. The numbers will be derived here, along with explaining certain design choices and characterisation, ending with a potential method of measuring the actual phase shifts that are occurring.

10.2.1 From Intrinsic to Device Properties

By locally injecting carriers in our device, we modify the refractive index. The TA data shows this effect and its magnitude. This, however, is for intrinsic colloidal NCs, so first we need to calculate the effect in an actual film, and the refractive index change felt by an optical mode passing through a waveguide in contact with this NC film. For ease of processing, we assume here that a passive MZI is made out of a 200 nm high SiNx film, which we afterward overcoat with 50 nm CdSe/CdS QDs through spincoating. The change in refractive index will then be $\Delta n_{WG} = \Delta n_{NC} \cdot \Gamma \cdot f$, where again typically $f \approx 50\%$.

For the MZI, we limit ourselves to wavelengths between 675 and 1000 nm, since this is far enough redshifted from the bandgap such that there is no more absorption (or induced absorption), this is shown in Figure 10.1a. As was already shown in Chapter 7, there is are still induced refractive index changes in this region (Figure 10.1b). Since our experiment is limited to about 725 nm, but knowing the theoretical $1/\lambda^2$ relation, we can extend our region by applying a fitting as shown in Figure 10.1c. This fitting uses the points in the grey box (starting from about 685 nm), and fixes the modulation to become zero at 1000 nm. That choice was made to achieve the best fit. Making it zero at 1000 nm can be considered an

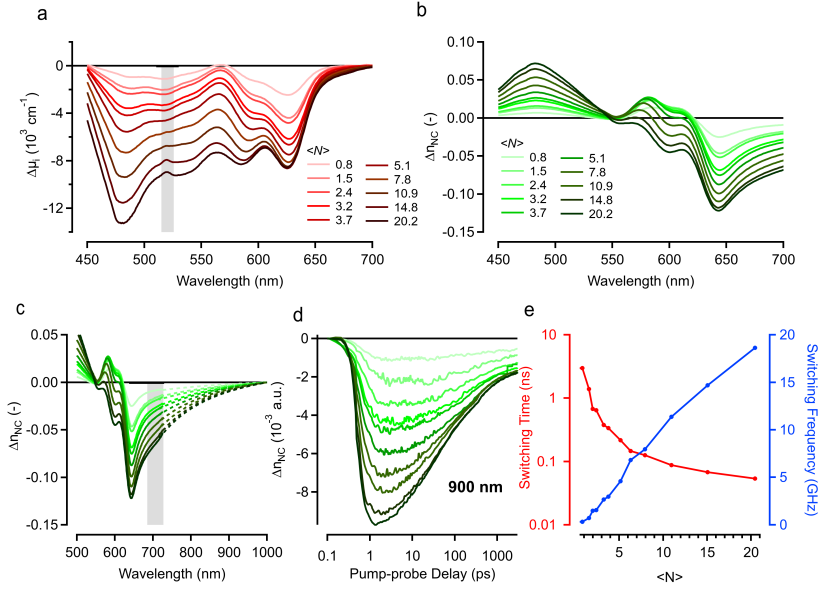


Figure 10.1: (a) $\Delta\mu_i$ for different excitation powers. The grey box shows where the QDs were excited. (b) Δn_{NC} for different excitation powers. (c) Extension of Δn_{NC} spectrum by using a $1/\lambda^2$ fitting. (d) Δn_{NC} as a function of the pump-probe delay, at 900 nm. (e) Max switching time and frequency shown for different excitation powers.

arbitrary choice, but it did give good fits. Also, shifting this zero point does not change the discussion all that much, since the effect as a function of fluence is pretty linear. By doing this fit for all different excitation powers, and all different pump-probe delays, we can find decay rates for Δn_{NC} for all wavelengths in this region, in Figure 10.1d an example is shown at 900 nm. Note that the decay rate is similar for all wavelengths above the bandgap, since they come from the same physical effect. As such, in this region we can start deducing some properties like the best possible switching time or switching frequency as a function of excitation power (Figure 10.1e). This plot shows at lower excitation (and coincidentally, this will influence the MZI size, as seen later) only slower switching is possible, while at higher excitation (and shorter MZI arm length) faster

switching is possible, at the cost of operation at higher power. The intrinsic values shown in Figure 10.1 can then be translated to a device. The time is calculated as the difference between the maximum refractive index change, and when the signal drops to half that value.

For the confinement Γ we can do an optical mode simulation. For a geometry like this the mode is about 10% confined in the NC layer (see Figure 10.2a). Bear in mind that this confinement depends on the waveguide width, which is quite crucial here since we need a single mode waveguide. With the confinement and volume fraction, we can calculate the refractive index change in a waveguide induced by a certain carrier density. From the calculation here it follows that this will be about twenty times less than the intrinsic refractive index modulation Δn_{NC} . Once the modulation in the waveguide is known, we can calculate the length needed for a π -phaseshift. As shown in Equation 3.3.32, the phase depends on the *optical* length difference in the arms, which specifically here we can write as

$$\Delta\phi = \Delta n_{WG} \cdot \frac{2\pi}{\lambda} \cdot L \quad (10.2.1)$$

where we can put $\Delta\phi = \pi$ to find the necessary length L . Rewriting this equation then gives

$$L = \frac{\lambda}{2 \cdot \Delta n_{WG}} \quad (10.2.2)$$

This calculated length is shown in Figure 10.2b, again for the different excitation powers. Moving further from the band gap naturally means longer lengths are necessary since the refractive index change will become less, where at 1000 nm the length becomes infinite. Lower power densities also lead to needing longer waveguides.

10.2.2 Mach-Zehnder Interferometer Design

We opted to make assymmetric MZIs here, where one of the arms is just a straight waveguide. This is the usual choice, since local distortions make it incredibly difficult to have two arms be exactly the same length. Besides that, it also reduces the writing time in the ebeam quite significantly. We chose to design the MZIs around 890-910 nm, since a tuneable laser is

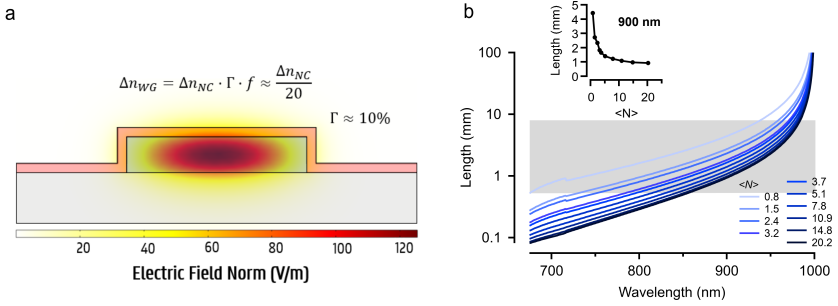


Figure 10.2: (a) Optical mode simulation of a SiNx waveguide, overcoated with NCs. The confinement in the NC layer is about 10%. (b) The calculated length necessary to induce a π -phaseshift in the device, for different wavelengths and excitation powers. The inset shows the length necessary specifically at 900 nm. The grey bar shows the lengths used in our actual devices.

available in the lab for that wavelength range, with a resolution of about 10 μm . Based on the expected refractive index changes calculated in the previous section at those wavelengths, we chose to make the difference in arm length of 500, 800, 1500, 2000, 2500, 3000, 4000, 5000, and 8000 μm , which are shown in Figure 10.2b as the grey box. This difference in arm length is added by having a spiral curled up on one of the arms. Besides this, the design also includes single waveguides (which, again, contain spirals) to check losses in the waveguides. Finally, we chose to make our waveguides stretch sufficiently far so that we could safely cleave the sample on both sides, and use butt-coupling to couple in the light. This is because we want to investigate a broad wavelength range, and grating couplers usually only work efficiently in a specific wavelength region with typically a range of about 30 nm. An optical microscope image of the design is shown in Figure 10.3a.

10.2.3 Linear Characterisation

First of, we measured the linear properties of the MZI. That means both the losses by measuring the single spiral waveguides, and the spectral

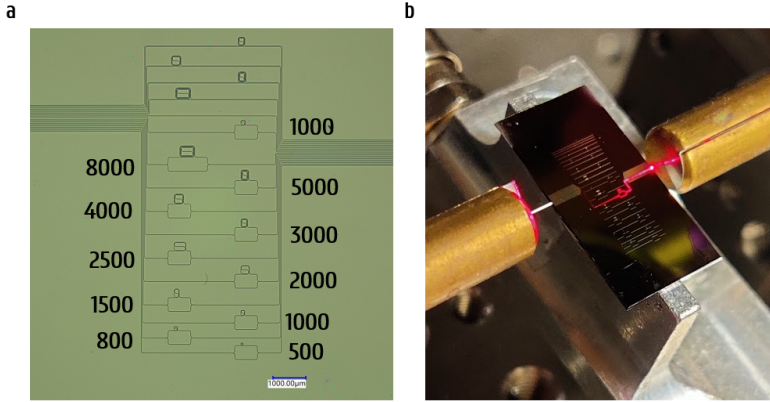


Figure 10.3: (a) Optical microscopy image of the full device. The numbers denote the lengths of the one arm of the MZI. (b) Lensed fibers coupling into a MZI with red light to check the coupling, specifically the MZI with a difference in length of 5000 μm .

behaviour of the MZIs by sweeping across the whole 890-910 nm range. This will allow us to determine the extinction ratio of the MZIs and the Free Spectral Range (FSR).

The losses for all the different lengths average out to about 1 dBm/mm, although the losses are very inconsistent over different lengths. This is probably due to the NC film, which will cause local scatter points on various locations on the chip, more so than the actual losses from the light travelling through the waveguide. It is however feasible to measure light coupling out of the waveguides, which is the goal of course of this experiment.

In Figure 10.4 the transmission spectrum is shown for both the 500 and 5000 μm length difference MZI. The extinction ratio ranges from about 15-20 dBm. For the 5000 μm length difference MZI, the resolution of the laser becomes limiting to the measurement. In Figure 10.4e, the FSR is shown for different length differences. An approximate formula for the FSR is

$$\Delta\lambda = \frac{\lambda^2}{n_{eff} \cdot L} \tag{10.2.3}$$

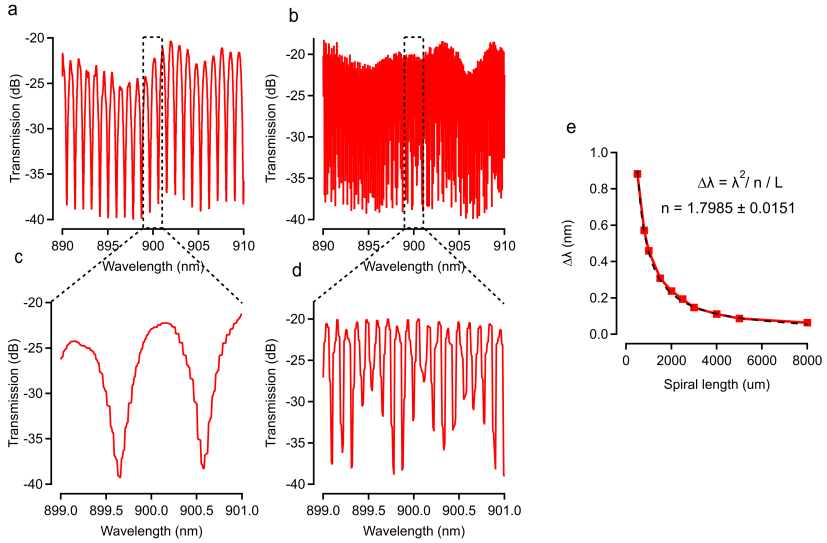


Figure 10.4: (a) Transmission spectrum of the MZI with the pathlength difference of 500 μm . (b) Transmission spectrum of the MZI with the pathlength difference of 5000 μm . (c) Zoom of (a). (d) Zoom of (b). (e) Free-Spectral-Range as a function of the spiral length. From the slope the effective index in the waveguide can be determined.

which can be fit to the graph, to find $n_{eff} \approx 1.8$. These results show that the MZIs operate as expected and can be used to check for actual modulation under influence of the pump.

10.2.4 Proposed Modulation Measurement

Finally, a measurement setup is introduced which can be used to measure these optically excited MZIs. This setup is shown in Figure 10.5. For the excitation path, a femtosecond laser at 800 nm is once again used, which is inserted in the TOPAS to get the desired wavelength. Since the fabricated devices mentioned use CdSe/CdS QDs, a wavelength of 530 nm can be used. An OD-wheel can again be used to change the power. Afterward, using a lens the pump can be focused on one arm of the MZI to induce a refractive index change.

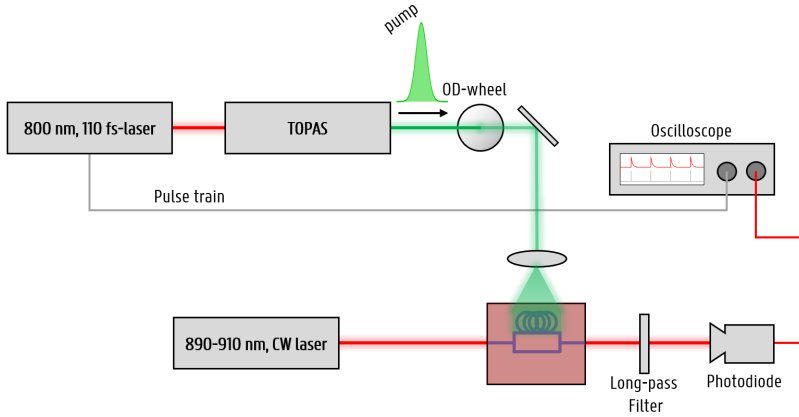


Figure 10.5: Proposed measurement of the colloidal NC MZIs.

The signal path starts from a tunable CW laser, with a range from 890 - 910 nm with an accuracy of 10 pm, the same laser that is used for the linear measurements. This laser can be swapped out for other spectral ranges for other measurements. Through butt-coupling, this laser is coupled in and out with lensed fibers. This approach is valid as we know from the linear measurements. A long-pass filter is used to get rid of the possible pump light that got coupled in the waveguide together with any NC photoluminescence, and finally this light gets measured by a photodiode. The signal from the photodiode is measured by a fast oscilloscope, matched to a pulse train from the femtosecond laser. Considering the fast switching time of around a nanosecond, a full decay trace will be difficult to measure. As a proof of concept however, seeing single or a couple of points deviate from the constant voltage can work.

Sadly, due to a lack of time these measurements have not been done yet. Bringing together a stage where the integrated sample can be butt-coupled from both sides to a lab where the femtosecond laser was available proved more difficult than anticipated. Particularly, re-measuring the linear behaviour in the new setup showed losses much higher. So high in fact that at that point it was not worthwhile to continue with the

10.2. Optically operated Mach-Zehnder Interferometers based on
CdSe/CdS QDs

excitation experiment. Hopefully this can be picked back up in a future project.

10.3 Refractive Index Change in Ring Lasers

Refractive index change due to carriers can be positive, as shown in the previous Section, where it can be used to create modulators. Besides that, when creating a device for which you do *not* want refractive index changes, these changes can be a nuisance. In this Section, we briefly put forward the effect of inducing carriers on the refractive index of a NC layer in a ring laser, and see the shifts in the lasing wavelength.

This study neglects the change of temperature that would occur by injecting these high carrier densities, which also would impact the index, and as such, the lasing wavelength. In reality, these effects can either amplify each other, or negate each other. Typically the refractive index becomes smaller close to the band-gap, since the absorption peak shrinks under influence of excitation, as is seen in Chapter 7. And usually, increase of temperature causes a decrease in refractive index as well, as this makes the material less dense. The combination of both these effects suggests a general lowering of the index, causing a blue shift of the lasing resonance (since the optical length will become smaller).

Here, we look into the change of refractive index in ring lasers with various radii, centered around a wavelength of 500 nm. The laser structure is shown in Figure 10.6a, which is the same as shown in Chapter 9. The effective index of such a structure is around 1.7. The index change is taken in a range from zero to -0.15, a range chosen from Figure 10.1c. The effective change in the waveguide itself is, similar to the previous Section, calculated as

$$\Delta n_{WG} = \Delta n_{NC} \cdot \Gamma \cdot f \quad (10.3.1)$$

where a typical confinement of $\Gamma \approx 13.5\%$ is used, and $f \approx 50\%$. For the lengths, we have chosen to fill in

$$2\pi r n_{eff} = m\lambda_m \quad (10.3.2)$$

with $\lambda = 500$ nm, and $m \in [0, 100]$. This yields ring radii r_m ranging from 46.8 nm to 4680 nm. We can calculate the new resonance wavelength by

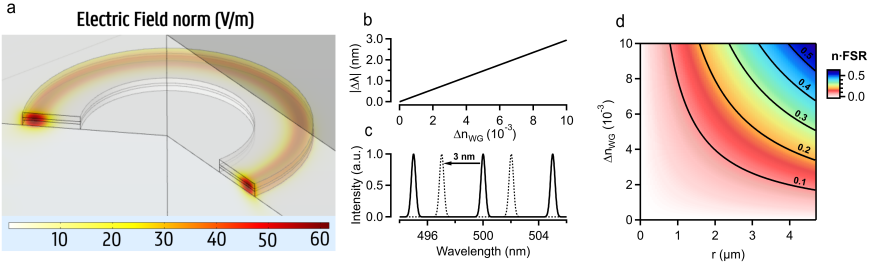


Figure 10.6: (a) Optical mode in a ring laser. (b) Absolute wavelength change due to a change in the refractive index in the NCs. (c) Spectrum of a steady state ring (black, full line), and a shifted spectrum due to a refractive index change (black, dotted). (d) Color map showing the relative wavelength shift $\Delta\lambda_{rel}$ for different ring sizes and refractive index changes.

adding Δn_{WG} , and can find the change in resonance $\Delta\lambda$ as

$$\Delta\lambda = 2\pi \frac{r_m}{m} \cdot \Delta n_{WG} \quad (10.3.3)$$

which shows that the resonance shift is actually ring radius independent and only depends on the refractive index change, as shown in Figure 10.6b. Using a maximal intrinsic refractive index change of -0.15, the resonance shifts only 3 nm, showing that these effects are not so strong. This maximum shift is shown in Figure 10.6c, for the ring with the biggest radius (4680 nm), which has an FSR of 5 nm.

Besides the absolute resonance shift, the new (FSR) is defined as

$$\text{FSR} = \frac{\lambda^2}{(n_{eff} + \Delta n_{WG}) \cdot 2\pi r_m} \quad (10.3.4)$$

from which we can now define the wavelength change relative to the FSR: $\Delta\lambda_{rel} = \Delta\lambda/\text{FSR}$. It will tell us how much of a period the resonance wavelength has shifted. This quantity does become ring radius dependent, as shown in Figure 10.6d, where a map of $\Delta\lambda_{rel}$ is shown with respect to the change of refractive index in the waveguide Δn_{WG} and the ring radius r_m . This map shows that the maximum shift will be around 60% of the FSR (which corresponds to the 3 nm shift of the ring with an FSR

of 5 nm), for quite large rings, which essentially means this is a relative small effect. This is mainly due to the relatively small part of the mode being actually confined within the NC layer.

To re-iterate, this effect will either be amplified or balanced out by thermal effects changing the refractive index of the NCs. Since this is a dynamic effect, in an actual laser all these effects will balance out until steady-state operation is reached where the optimal mode (or modes) will sustain lasing.

10.4 Conclusions

This Chapter presents some preliminary results to build the first colloidal NC based modulator. Due to the complexity to measure these types of devices and a lack of time, we sadly have not yet been able to measure the effect in a device. But the ideas, designs, and linear measurements have been performed, showing good baseline performance. The next step is now to demonstrate the effect, for which a proposed setup is outlined in Section 10.2.4.

Bibliography

- ¹Namyong Ahn, Young-Shin Park, Clément Livache, Jun Du, Kivanc Gungor, Jaehoon Kim, and Victor I Klimov. Optically excited lasing in a cavity-based, high-current-density quantum dot electroluminescent device. *Advanced Materials*, page 2206613, 2022.

Part IV

Conclusions and Perspectives

This work deals with colloidal NCs and their use in integrated photonic devices. A very vague and abstract way to encapsulate the discussed work in all the previous Chapters. Since the contents are diverse, a conclusion of each Chapter was written at the end. I would like to end by reflecting on some general topics.

I am not a big fan of reporting results without a thorough understanding of the mechanism behind it. I feel like providing a detailed explanation of how something works is essential when discussing results (sometimes to the frustration of my supervisors, I might add). I hope this fact seems clear from reading this PhD thesis: every Chapter is (almost) completely or partly about modelling and simulating the material or device of discussion. To me, it feels like this modelling is essential to decide the next step of the work, since understanding the physics behind something allows us to see where improvements can be made. It also adds, in my opinion, a reinforcement to the results, just like redoing a measurement to see if the result is the same. I feel particularly proud of the fact that all the measurements performed in my work fit into some model that I made, or adapted from someone else, and can be used to explain those measurements. It took me much time and effort, but the insight gained into ultrafast carrier dynamics especially, for example in Chapter 6 and 7, gave me great pleasure. I feel like these insights could still lead to advancements besides the main work performed on lasers, for example as outlined in Chapter 10. I hope to have atleast outlined a different use for colloidal NCs, besides their use as emitters (LEDs and lasers) or detectors (either for imaging, cameras, or for photovoltaics, something I have personally not worked on).

And now for the main conclusion of our work: we have investigated, among other things, the use of colloidal NCs for lasing in a CMOS compatible platform, the ultimate goal being the creation of an integrated, optically pumped CW laser. The usual approach to this problem is taking the CdSe/CdS system and engineering it in such a way that makes CW lasing, and as an extension, lasing with electrical injection, possible. This approach is viable, but has its limits: after 20 years of nudging closer

to the goal, the CdSe/CdS system is close to being optimized. Its qualities cannot be much more improved above what exists now. The size can be changed to increase the gain lifetime, but this leads to lower gain magnitudes. This intrinsic trade-off is an unwanted side effect because of the quantization. The DOS becomes so small that large gain magnitudes are not possible. The harsh truth is that while the CdSe/CdS system has its obvious merits, we need something radically different to overcome the losses in a cavity to reach lasing. This is evidenced by the most recent work of Ahn *et al.*¹, where despite absolutely incredibly high injected currents, lasing at room temperature still has not been shown. The first excited (1S) state is more than inverted, in fact the second excited (1P) state is completely inverted as well (one could, of course, consider building a laser cavity optimized for this 1P state). This begs the question: why even bother injecting higher currents? The modal gain cannot be pushed any higher, so solutions have to be found elsewhere. One option is by lowering the losses in the cavity, which is something also tackled in this work. Different materials are used to make sure the optical mode is confined as much as possible in the gain material. These changes are necessary for laser optimisation, but will never drastically change the gain properties.

In this work, we choose a different approach, and take a step back to compare colloidal NCs as a material. Instead of over-engineering the workhorse material that exists to date, we compare its intrinsic qualities to newly found candidate materials. Without any complex geometry, we can see that our bulk NC CdS outclasses the CdSe/CdS system in every way. By extension, we can make a case that going beyond the Bohr diameter for other colloidal NCs will achieve the same properties. In fact, since we are able to model the system, can pinpoint specifically to what is necessary for higher BGR, and as such higher gain: the exciton binding energy. Specifically, materials toward the blue and UV tend to have higher binding energy (ZnSe, ZnS), and are as such ideal contestants to continue with. Even when thinking of RoHS compatibility, where Cadmium is a no-go, a switch to ZnTe could be made which has a band

gap around 550 nm. It is quite remarkable that this newly found material can (intrinsically) compete with the state-of-the-art. But the incredible potential shown from the material properties, and the relatively easy road to translate these properties to thin films, shows great promise. Problems such as stability, and relatively low Quantum Yields, have clear pathways toward improvement. The QY can be improved through shelling and better understanding of the surface. Stability can be improved by using coatings and ligand exchanges, and also surface understanding.

Here, we emphasize the downside of strong confinement, the reduction in DOS, leading to a reduction in gain magnitude. However, the great benefit of strong confinement is the spectral control: wavelength tuning is impossible without strong confinement. Or is it? Instead of using strong confinement to tune the wavelength, we can keep the diameter fixed and turn instead to *alloying* to spectrally shift the NCs. As evidenced in Section 8.3.1, making bulk CdSe NCs also leads to lasing. By creating $\text{CdS}_x\text{Se}_{1-x}$ NCs, the gain window can be altered from cyan/green all the way to red/NIR, spanning the range from about 480 - 750 nm. Based on the bulk gain model, we do know that the gain magnitude will steadily decrease by including more and more selenium, due to the weaker binding energy. But seeing as the limit of $x=0$ already showed lasing, we will be able to produce working devices spanning this entire range. As previously mentioned, for going toward blue/UV lasing, alternatives of ZnSe and ZnS can be used.

And what of the other QDs, the ones originally considered the main competitor? Since the original pitch of colloidal NCs against these epitaxial III-V QDs, they have naturally also advanced. III-V based photonic components have also been booming, while still suffering from the expensive growth techniques necessary to make them. Thankfully, progress especially in Transfer Printing has brought these materials with relative ease to the silicon platform as well, and commercialisation of this technique is showing that there is much faith in using this to combining the best of both platforms. It is clear that competing against these multi billion dollar industries which are trying to create an industry standard will not be

easy, but who knows what the future might bring? Colloidal NCs already took the lighting and display market by storm, through their use in e.g. QLED televisions, and there are no signs that the same could not happen for integrated devices. Perhaps the field is just waiting for the next big (or should I say: bulk?) step forward.

Ivo Tanghe

Bibliography

- ¹Namyoun Ahn, Young-Shin Park, Clément Livache, Jun Du, Kivanc Gungor, Jaehoon Kim, and Victor I Klimov. Optically excited lasing in a cavity-based, high-current-density quantum dot electroluminescent device. *Advanced Materials*, page 2206613, 2022.

Part V

Appendices

Appendix A

Dielectric sphere in a uniform electric field

Consider a dielectric sphere located in the origin, with radius a and dielectric constant ϵ . This sphere is placed in an electric field, along the z -axis, with field strength E_0 . So $\vec{E} = E_0\vec{z}$, see also Figure A.1.

Since no free charges exist anywhere in the domain, we need to solve the Laplace equation for spherical coordinates to find the potential. Due to axial symmetry we know that it is of the form of a Legendre polynomial

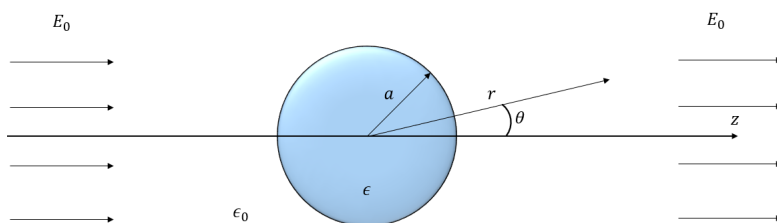


Figure A.1: To be solved problem in Appendix A.

expansion, which we can define the potential in both regions as:

$$\Phi_{in}(r, \theta) = \sum_{l=0}^{\infty} A_l r^l P_l(\cos(\theta)), r < a \quad (\text{A.0.1})$$

$$\Phi_{out}(r, \theta) = \sum_{l=0}^{\infty} (B_l r^l + C_l r^{-l-1}) P_l(\cos(\theta)), r > a \quad (\text{A.0.2})$$

where the coefficients A_l , B_l and C_l can be found from the boundary conditions. For very large r , we know that $\vec{E} = E_0 \vec{z} = E_0 \vec{r} \cos(\theta)$, from which follows that

$$\lim_{r \rightarrow \infty} \Phi_{out}(r, \theta) = -E_0 r \cos(\theta) \quad (\text{A.0.3})$$

which shows that the the only non-zero B_l factor is $B_1 = -E_0$. The other coefficients we can find from applying the boundary conditions at the surface of the sphere. The electrical potential should be continuous at the surface, and since there are no charges in the domain the electric displacement should also be continuous, which yields

$$\Phi_{in}(a, \theta) = \Phi_{out}(a, \theta) \quad (\text{A.0.4})$$

$$-\epsilon \frac{\partial \Phi_{in}(r, \theta)}{\partial r} \Big|_{r=a} = -\epsilon_0 \frac{\partial \Phi_{out}(r, \theta)}{\partial r} \Big|_{r=a} \quad (\text{A.0.5})$$

if we fill in Eq A, we get

$$\sum_{l=0}^{\infty} A_l a^l P_l(\cos(\theta)) = \sum_{l=0}^{\infty} \left(-E_0 a^l \delta_{1l} + C_l \frac{1}{a^{l+1}} \right) P_l(\cos(\theta)) \quad (\text{A.0.6})$$

this equation is valid for any θ , from which follows

$$A_1 = -E_0 + \frac{C_1}{a^3} \quad (\text{A.0.7})$$

$$\begin{cases} A_1 = -E_0 + \frac{C_1}{a^3} \\ A_l = \frac{C_l}{a^{2l+1}}, l \neq 1 \end{cases}$$

For the second boundary condition, Eq A, we find

$$\epsilon \sum_{l=0}^{\infty} l A_l a^{l-1} P_l(\cos(\theta)) = \epsilon_0 \sum_{l=0}^{\infty} \left(-E_0 \delta_{1l} - (l+1) C_l \frac{1}{a^{l+2}} \right) P_l(\cos(\theta)) \quad (\text{A.0.8})$$

for which, again for any value of θ , we find

$$\begin{cases} \frac{\epsilon}{\epsilon_0} A_1 = -E_0 + \frac{2C_1}{a^3} \\ \frac{\epsilon}{\epsilon_0} l A_l = -(l+1) \frac{C_l}{a^{2l+1}}, l \neq 1 \end{cases}$$

Both of the boundary conditions can only be valid for $A_l = C_l = 0$ for all $l \neq 1$. The case where $l = 1$ we can solve for

$$A_1 = -\frac{3\epsilon_0}{\epsilon + 2\epsilon_0} \cdot E_0 \quad (\text{A.0.9})$$

$$C_1 = a^3 \frac{\epsilon - \epsilon_0}{\epsilon + 2\epsilon_0} \cdot E_0 \quad (\text{A.0.10})$$

With which we can completely fill in the solutions, knowing also that $P_l(x) = x$:

$$\Phi_{in}(r, \theta) = -\frac{3\epsilon_0}{\epsilon + 2\epsilon_0} \cdot E_0 \cdot r \cos(\theta) \quad (\text{A.0.11})$$

$$\Phi_{out}(r, \theta) = -E_0 \cdot r \cos(\theta) + \frac{\epsilon - \epsilon_0}{\epsilon + 2\epsilon_0} E_0 \frac{a^3}{r^2} \cos(\theta) \quad (\text{A.0.12})$$

which allows us to find back certain parameters defined back in the main text. We can determine the electric field inside of the sphere \vec{E}_{in} as

$$\vec{E}_{in} = \frac{3\epsilon_0}{\epsilon + 2\epsilon_0} \cdot \vec{E}_0 \quad (\text{A.0.13})$$

from which we find back the local-field factor f_{LF} . The electric field outside equals the external electric field plus the electric field induced by a dipole at location $r = 0$:

$$\vec{p} = 4\pi\epsilon_0 a^3 \frac{\epsilon - \epsilon_0}{\epsilon + 2\epsilon_0} \vec{E} \quad (\text{A.0.14})$$

from which, knowing $\vec{d} = \alpha \cdot \vec{E}$, we find the polarizability α . Note the $4\pi\epsilon_0$ factor extra compared to the main text, which is due to different definitions of polarizability. To get the same definition of the main text, we define a polarizability with units of volume, by dividing by $4\pi\epsilon_0$.



Appendix B

Extras on $k \cdot p$ simulations

B.1 Theoretical Analysis of the electronic Structure

Our system is a heterostructure, with pure wurtzite crystal phase. We divide the $k \cdot p$ analysis in three steps. First, we study the electronic structure within zinc-blende (cubic and quasi-cubic) descriptions. This is customary in the analysis of CdSe nanocrystals, where it was found to provide a good approximation to the energy levels, with the additional advantage of enabling labelling of states according to angular momentum and parity symmetries, which simplifies the spectral assignment.¹⁻⁴ Second, we investigate how switching to a truly hexagonal (wurtzite) crystal structure perturbs the quasi-cubic results, mostly through the inclusion of crystal field splitting.^{5,6} Third, we study how strain and piezoelectricity imposed by the CdS coating modify the electronic structure.⁷

B.1.1 Overview on Selection Rules in Spherical Nanocrystals

Early theoretical works studied spherical nanocrystals using isotropic effective mass models (neglecting band coupling) for carriers in a spherical box with infinite barriers.⁸ Electron and hole envelope states were then described by nL_j labels, where L is the angular momentum of the envelope function, j the band (e for electrons of the conduction band, h for holes of the valence band) and n denotes the n -th state with L_j (radial quantum number). It is customary to use $S, P, D...$ labels for $L = 0, L = 1, L = 2...$ angular momenta. In turn, electron and hole Bloch (periodic) functions had angular momenta $J = 1/2$ (s-orbital plus spin) and $J = 3/2$ (p-orbital plus spin). In interband transitions, the photon angular momentum is employed to couple the Bloch functions of conduction and valence bands, so that the envelope selection rule is simply $\Delta n = 0$ and $\Delta L = 0$. That is, allowed transitions are $1S_e - 1S_h, 1P_e - 1P_h, 2S_e - 2S_h...$

The above description was fairly accurate for conduction electrons in wide band gap materials such as CdSe, because the conduction band is only weakly coupled to other bands. However, it was soon realised that a proper comparison with experiments required considering the substructure of the valence band. In zinc-blende, the latter is formed by heavy hole subband (Bloch function $|J, J_z\rangle = |3/2, \pm 3/2\rangle$), light hole subband ($|J, J_z\rangle = |3/2, \pm 1/2\rangle$) and split-off subband ($|J, J_z\rangle = |1/2, \pm 1/2\rangle$). The coupling between these bands is described in $k \cdot p$ theory by the Luttinger-Kohn Hamiltonian.⁹ Within this framework, the three subbands couple such that the hole envelope (L_h) and Bloch (J) angular momenta are no longer conserved, and only the total ($F = L_h + J$) angular momentum is a good quantum number. In addition, the Hamiltonian is invariant under inversion symmetry. Then, parity symmetry (ν) is also a good quantum number. Hole states with a definite parity ν (even or odd) and total angular momentum (F) are spinors formed by two components of different subbands with angular momentum L and $L + 2$, e.g. heavy hole com-

ponent with S character plus light hole component with D character.² This is known as S - D *mixing*. Within the spectroscopic notation, hole states are labelled as nL_F , with L being the smallest envelope angular momentum in the spinor and n the n -th state with L_F . It is then possible to have allowed transitions between electron-hole states with $\Delta L = 0, \pm 2$. Because conduction and valence bands have now different Hamiltonians, the selection rule $\Delta n = 0$ is also relaxed, e.g. $1S$ electron orbitals are not necessarily orthogonal to $2S_{3/2}$ orbitals. With the above considerations, a typical sequence of optical transitions in CdSe nanocrystals, from smaller to larger energy is $1S_e - 1S_{3/2}$, $1S_e - 2S_{3/2}$, $1P_e - 1P_{3/2}$, $1P_e - 1P_{1/2} \dots$ ^{1,2}.

B.1.2 Electronic Structure of CdSe/CdS Nanocrystals

We start by calculating electron and hole states in CdSe/CdS nanocrystals within cubic (zinc-blende, ZB) and quasi-cubic (zinc-blende/wurtzite, qc-wz) approximations. Electron states are described with a single-band effective mass Hamiltonian. Hole states in the cubic approximation are calculated with a six-band $k \cdot p$ Hamiltonian for spherical, heterostructured nanocrystals, following Pokatilov and co-workers.¹⁰ Coupling between heavy hole, light hole and split-off subband is hence taken into account, along with finite band offset between core and shell. Effective masses, Luttinger parameters, band offset potentials and other parameters for cubic CdSe and CdS are given in Table B.1 and B.2. Notice that Luttinger parameters obey the spherical approximation ($\gamma_2^L = \gamma_3^L = \gamma$). Quasi-cubic calculations are performed with a six-band wurtzite (wz) Hamiltonian imposing due parameter restrictions.^{11,12}

We consider a nanocrystal with fixed overall diameter $D_{cs} = 15\text{nm}$, similar to the experimental samples, and variable core diameter D_c (see sketch in Figure B.1a). Figure B.1b and Figures B.1c,d show the calculated energy levels of electrons and holes, respectively, with the dot colour indicating the L_F label (see legend). Strain and piezoelectricity are not yet considered at this stage. $1S_e$ states show a monotonic stabilization in

B.1. Theoretical Analysis of the electronic Structure

Material Parameters (Cubic and Quasi-Cubic Approximation)					
Description	Symbol	CdSe	CdS	Units	CdSe & CdS Ref.
Elastic modulus tensor	C_{11}	74.1	86.5	GPa	13
	C_{12}	45.2	54	GPa	13
	C_{13}	38.9	47.3	GPa	13
	C_{33}	84.3	94.4	GPa	13
	C_{44}	13.4	15	GPa	13
Piezoelectric constants	e_{31}	-0.16	-0.24	$C \cdot m^{-2}$	13
	e_{33}	0.347	0.44	$C \cdot m^{-2}$	13
	e_{15}	-0.138	-0.21	$C \cdot m^{-2}$	13
Dielectric constant	ϵ_{xy}	9.29	8.28	ϵ_0	13
	ϵ_z	10.16	8.73	ϵ_0	13
Lattice constants	a	4.3	4.135	Å	13
	c	7.01	6.749	Å	13
Crystal field splitting	Δ_1	0.027	0.039	eV	14
Spin-orbit matrix element	Δ_2	0.13	0.02016	eV	14
	Δ_3	0.13	0.02016	eV	14
Gamma parameters	γ_1	-0.18	-0.27	$1/m_0$	15
	γ_2	-0.65	-0.49	$1/m_0$	15
	γ_3	-0.65	-0.49	$1/m_0$	15
Luttinger parameters	γ_1^L	$\gamma_1 + \frac{E_F}{3E_g}$		$1/m_0$	10
	γ_2^L	$\gamma_2 + \frac{E_F}{6E_g}$		$1/m_0$	10
	γ_3^L	γ_2^L		$1/m_0$	10
Cubic Energy Gap	E_g	1.66	2.4	eV	15
Kane Energy	E_p	16.5	21	eV	15
Hole mass parameter	A_1	$-\gamma_1^L - 4\gamma_3^L$		$1/m_0$	10
	A_2	$-\gamma_1^L + 2\gamma_3^L$		$1/m_0$	10
	A_3	$6\gamma_3^L$		$1/m_0$	10, 11
	A_4	$-3\gamma_3^L$		$1/m_0$	10, 11
	A_5	$-\gamma_2^L - 2\gamma_3^L$		$1/m_0$	10, 11
	A_6	$-\sqrt{2}(2\gamma_2^L + \gamma_3^L)$		$1/m_0$	10, 11

Table B.1: Material parameters used in the calculation for cubic phase CdSe and CdS.

energy (roughly proportional to $1/D_c^2$), see blue dots in Figure B.1b. The same occurs for all the hole states under study (Figures B.1c,d). This indicates that the states are largely confined to the CdSe core and their behaviour is similar to core-only nanocrystals. However, $1P_e$ and higher

Material Parameters (Cubic and Quasi-Cubic Approximation)					
Description	Symbol	CdSe	CdS	Units	CdSe & CdS Ref.
VB Deformation potential	D_1	-0.76	-2.8	eV	16
	D_2	-3.7	-4.5	eV	16
	D_3	-2.94	-1.7	eV	11
	D_4	1.47	0.85	eV	11
	D_5	-1.2	1.5	eV	11
	D_6	-5.47	3.04	eV	11
Valence Band Offset	vbo	0	-0.4	eV	17
Dissymmetry parameter	χ	$\frac{1}{3}(2\gamma_2 + 3\gamma_3 - \gamma_1 - 1)$		$1/m_0$	10
Electron effective mass	$m_{e,xy}^*$	0.11	0.21	m_0	17
	$m_{e,z}^*$	0.11	0.21	m_0	17
CB Deformation potential	$a_c^{(xy)}$	-7.8	-1.76	eV	16
	$a_c^{(z)}$	-8.2	-4.5	eV	16
Conduction Band Offset	cbo	0	0.32	eV	17

Table B.2: Material parameters used in the calculation for cubic phase CdSe and CdS (continued).

electron states behave differently. They remain fairly insensitive to the core diameter up to $D_c = 4$ nm (green dots in Figure B.1b). This reflects that the state is delocalized over the shell and gets trapped into the core only when $D_c > 4$ nm (see plots of charge densities in Figure B.5).

As a first step to study the effect of switching from zb to zw phase, we compare the hole states (the Hamiltonian for electrons is the same) using cubic and quasi-cubic Hamiltonians. The main physical factors introduced by the latter model as compared to the ZB one, are crystal field splitting and a more realistic description of mass anisotropy. Figures B.1c,d shows the resulting hole energy levels against core diameter D_c . When comparing the qc-wz system (Figure B.1d) with the ZB one (Figure B.1c), we observe that the main effect of the crystal field is to lift the total angular momentum symmetry. Only its projection is preserved. For example, the four-fold degenerate $1S_{3/2}$ hole state ($F = 3/2$, $F_z = \pm 3/2, \pm 1/2$) splits into a ground state doublet with $F_z = \pm 3/2$ and an

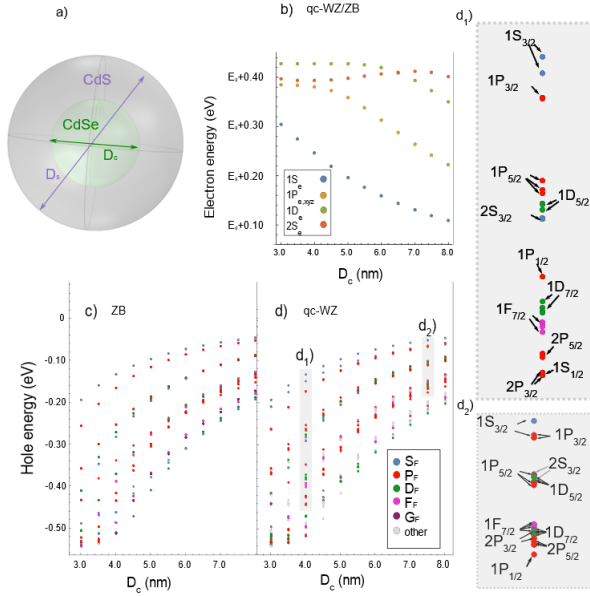


Figure B.1: Energy levels of CdSe/CdS nanocrystals against core diameter with cubic and quasi-cubic description. (a) Sketch of the heterostructure under study. (b) Electron states. (c) Hole states in zinc-blende (ZB) description. (d) Hole states in quasi-cubic approximation wurtzite (qc-wz) description. (d₁,d₂) Zoom of hole states $D_c = 4$ nm and $D_c = 7.5$ nm, respectively. Energies are referred to the top of the CdSe valence band (in bulk). E_g is the bulk gap value of CdSe. The dot colour indicates the (lowest) envelope angular momentum.

excited state with $F_z = \pm 1/2$ (see blue dots at the top of Figure B.1c and Figure B.1d). The former (latter) has predominant heavy hole (light hole) character. The energy splittings are however moderate.

A few examples of the different localization of electron and hole states in core/shell nanocrystals are illustrated in Figure B.5. The figure shows the calculated charge density of the four first electron states ($1S_e$, $1P_e$, $1D_e$, $2S_e$) and two first hole states ($1S_{3/2}$, $1P_{3/2}$), for qc-wz nanocrystals in the absence of strain and piezoelectricity. Two core dimensions are considered: a small core ($D_c = 3$ nm) and a large core ($D_c = 7$ nm). One

can see that most states are largely confined in the CdSe core. This should translate into large electron-hole overlap, and hence bright transitions, similar to core-only nanocrystals. Nonetheless, small cores constitute an exception. Here states above the cbo with non-zero angular momentum ($1P_e, 1D_e$) delocalize over the CdS shell and place their nodes inside the core. The $2S_e$ state places the radial node on the CdSe/CdS interface and has significant density both in core and shell. By way of example, one can then expect the $1P_e - 1P_{3/2}$ overlap of small-core CdSe/CdS nanocrystals to be small, and the associated transition dim. We confirm this below.

Figure B.2 shows the calculated optical transitions of CdSe/CdS nanocrystals with a thick shell, as a function of the core diameter. All energies are referred to that of the fundamental transition ($1S_e - 1S_{3/2}$). We consider the different scenarios we have posed, namely zb and qc-wz approximations. The resulting spectra can be interpreted from the energetic and charge density considerations discussed above. Thus, from Figure B.2, it is easy to see how the overlap between $1P_e - nP_j$ increases as the core diameter increases. This overlap is explained as the pouring of 1Pe charge density into the core for $D_c > 4\text{nm}$. In contrast, $1S_e - nS_j$ remains essentially unchanged. Also, notice the total angular momentum symmetry lift of hole states in the qc-wz case. This symmetry lifting produces more observable transitions. These are the main differences between the optical spectra of CdSe/CdS core-shell and core-only¹ nanocrystals, within an unstrained description.

To test the validity of the qc-wz approximation, we next switch to a full wz description using Chuang's Hamiltonian with hexagonal symmetry.^{11,12} Specific parameters used for this description are displayed in Table B.3. More general parameters for electrons and holes are already listed in Table B.1 and B.2.

When we compare between qc-wz and wz calculations, a few differences are observed. For the electron states, as we use a single-band Hamiltonian, there is no difference in the energy levels (Figure S1b) nor in charge densities (electron panels in Figure B.5). However, for the hole states, a few differences arise in the charge densities (compare hole panels in Figure

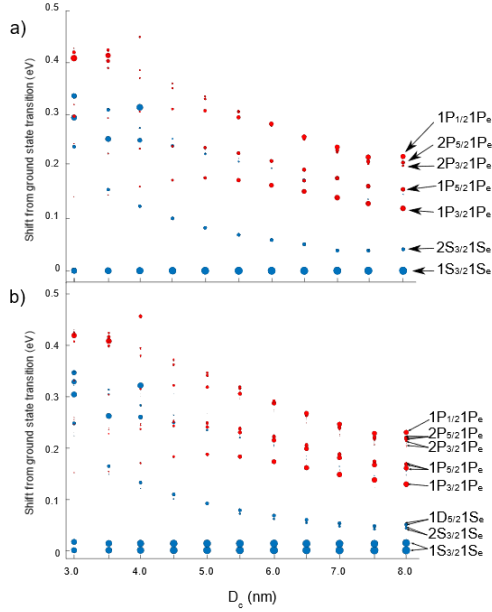


Figure B.2: Optical transitions in CdSe/CdS nanocrystals with thick shell ($D_{cs} = 15$ nm) and varying core diameter. (a) ZB structure. (b) qc-wz structure. Blue (red) dots are used for transitions involving $1S_e$ ($1P_e$) states. The dot thickness stands for the electron-hole overlap.

B.5 and Figure B.3) and energies, which can be noticed when comparing optical transitions (compare Figure B.2b and Figure B.3). For instance, $1S_{3/2}$ states, which are involved in $1S_e - 1S_{3/2}$ transitions, get more split than in qc-wz. The enhanced splitting is explained by the anisotropy introduced by hole mass parameters which lead to a larger contribution of light-hole subband. One can see in Figure B.3 that hole states in wz description are more anisotropic than in the quasi-cubic picture (Figure B.5). This is because the hexagonal lattice reduces the symmetry as compared to the cubic one. The degeneracy of heavy- and light-hole subbands is lifted, and their admixture is modified. This is shown in Table B.4, which gives the weight of each subband for $1S_{3/2}$ and $1P_{3/2}$ states.

Hole Parameters (Wurtzite)					
Description	Symbol	CdSe	CdS	Units	CdSe & CdS Ref.
Hole mass parameter	A_1	-5.06	-4.53	$1/m_0$	14
	A_2	-0.43	-0.39	$1/m_0$	14
	A_3	4.5	4.02	$1/m_0$	14
	A_4	-1.29	-1.92	$1/m_0$	14
	A_5	-1.29	-1.92	$1/m_0$	14
	A_6	-0.47	-2.59	$1/m_0$	14
VB Deformation potential	D_1	-0.76	-2.8	eV	16
	D_2	-3.7	-4.5	eV	16
	D_3	4	1.3	eV	16
	D_4	-2.2	-2.9	eV	16
	D_5	1.2	-1.5	eV	16
	D_6	1.5	1.2	eV	16

Table B.3: Material parameters used in the calculation of wurtzite (wz) CdSe and CdS.

Clearly, as the system evolves from zb to wz, the percentage of heavy and light hole character becomes increasingly different. Because the two kinds of holes have anisotropic masses, the charge density becomes increasingly anisotropic. Thus, the larger contribution of light holes in $1S_{3/2}$ states of the wz system turns their charge density more prolate due to their lighter mass along the z-direction, see Figure B.3. For $1P_{3/2}$ states, this modification on subbands proportion (heavy hole – light hole) stabilizes their levels with respect to qc-wz description. Therefore, it reduces the splitting between $1P_{3/2}$ doublets from ~ 3 to ~ 2 meV. Despite these subtle differences on energies due to their subband composition, the electron-hole overlap remains practically the same. Thus, similar optical activity to that we observed in qc-wz it is expected for the wz description.

	ZB		qc-wz		wz	
	HH (%)	LH (%)	HH (%)	LH (%)	HH (%)	LH (%)
$1S_{3/2}$	50	50	47	53	40	60
$1P_{3/2}$	53	47	60	40	64	36

 Table B.4: Heavy hole and light hole mixture in CdSe and CdS for $1S_{3/2}$ and $1P_{3/2}$ in zb (left column), qc-wz (middle column) and wz (right column).

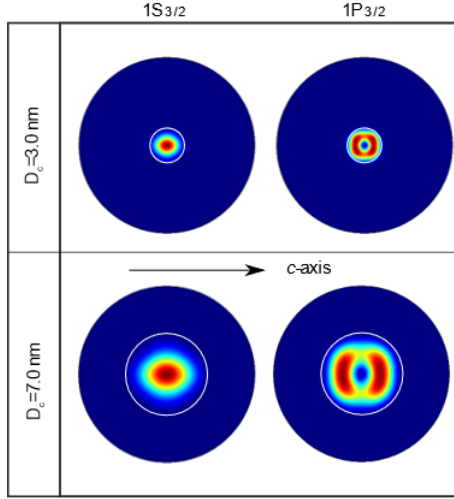


Figure B.3: Charge density of the averaged four lowest hole states in CdSe/CdS core/shell wz nanocrystals, in the absence of strain and piezoelectricity.

We also studied possible additional features in the spectra of CdSe/CdS nanocrystals arising from strain and piezoelectricity, which result from the lattice mismatch between wz CdSe core and CdS shell (3.86 % along the c -axis and 3.99 % along the a -axis). The compressive strain inside the core is known to blue shift both conduction and valence bands through a deformation potential. In turn, strain-induced piezoelectricity is known to create an in-built electric dipole inside the core, whose potential drop increases with core size.⁷ The latter term further reduces the spherical symmetry in the system, presumably relaxing selection rules.

Figure B.6a,b show the energy levels of electrons and holes in the presence of strain and piezoelectricity, as expected from the compressive strain, all states localized in the core are blue shifted as compared to the unstrained cases (compare Figure B.6 to Figure B.1). Moreover, piezoelectricity enhances the energy splitting between states with the same total angular momentum but different projection. Unlike the crystal field, this term affects not only holes but also electrons. Notice for instance in Fig-

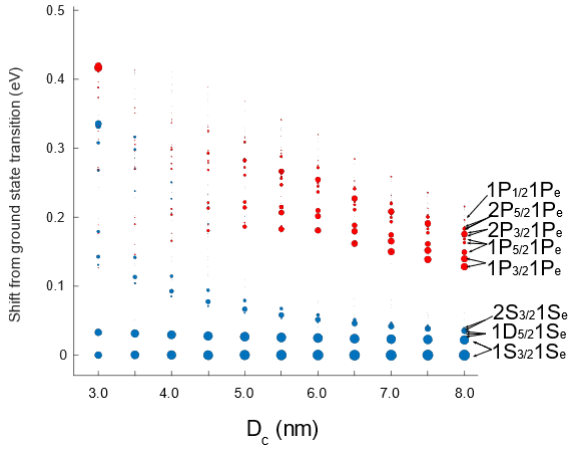


Figure B.4: Optical transitions in CdSe/CdS nanocrystals with thick shell ($D_s = 15$ nm) and varying core radius for wz structure. Strain is not included. Blue (red) dots are used for transitions involving $1S_e$ ($1P_e$) states. Dots thickness are proportional to the electron-hole overlap.

ure B.6 that $1P_e$ states split into $1P_{xy}$ ($L = 1, L_z = \pm 1$) and $1P_z$ ($L = 1, L_z = 0$). The latter is significantly stabilized by the piezoelectric potential well.

The effect of strain and piezoelectricity on the charge densities can be visualized in Figure B.7. The piezoelectric potential drop between the two poles of the core scales roughly linearly with the core size.⁷ The effect on the charge density is then weaker for small cores and stronger for large ones. Thus, for $D_c = 3$ nm, the hole ground state $1S_{3/2}$ is like the unstrained case. For electrons, however, the corresponding $1S_e$ orbital ($D_c = 3$ nm) shifts towards one pole of the core. This is because hydrostatic strain reduces the conduction band offset, favouring electron leakage into the shell and the piezoelectric potential presents a minimum in the CdS side of the core/shell interface (see inset in Figure B.6a). The leakage allows the wave function to place charge density in such a well (see state $1S_e$ for $D_c = 3$ nm in Figure B.7). The different behaviour of electrons and hole charge densities under the piezoelectric potential

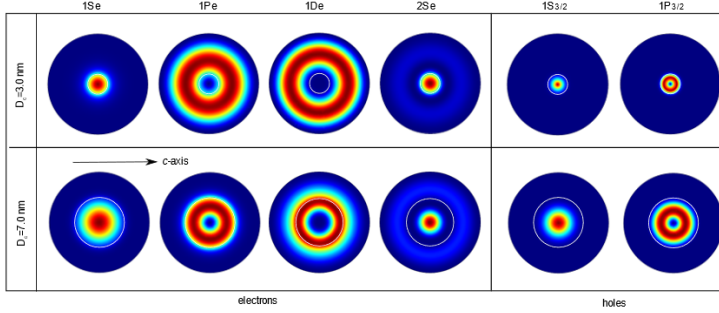


Figure B.5: Charge density of a few low-energy electron and hole states in CdSe/CdS core/shell nanocrystals within the qc-wz approximation, in the absence of strain, piezoelectricity and crystal field splitting. For small cores ($D_c = 3nm$), $1P_e$, $1D_e$ and $2S_e$ orbitals are mostly localized in the shell. The hole charge density is averaged over all four lowest states.

will reduce the electron-hole overlap and hence the optical brightness of the $1S_e - 1S_{3/2}$ transition. In large cores the same physics holds, but the stronger piezoelectric potential and weaker core confinement permit further dissociating electron and hole, which move towards opposite poles (see Figure B.7 for $D_c = 7$ nm). The electron-hole overlap will then be even smaller. This is confirmed in Figure B.8, which shows the optical spectrum as a function of the core diameter. As compared to the spectrum of the unstrained system (Figure B.4), we observe that the ground state transition (and most transitions involving the $1S_e$ orbital in fact, see blue dots) are significantly weakened as the core size increases. Transitions involving $1P_{e,z}$ orbitals (red dots) are comparatively stronger because the larger kinetic energy reduces the influence of the piezoelectric field potential. It goes without saying that $1P_{e,xy}$ do not participate in optical activity in these systems since their charge density always remains in the shell. Thus, it prevents any chance of an efficient electron-hole overlap.

Figure B.8 suggests piezoelectricity may have a effect on the optical spectrum. While this has been confirmed in experiments with elongated rod-shaped heterostructures¹⁷, the actual effect on the ground state of the current CdSe/CdS spherical heterostructures seems sizable but less

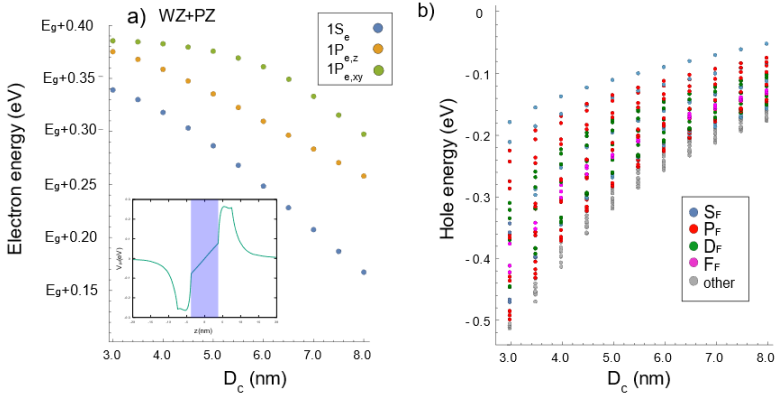


Figure B.6: Energy levels of wz CdSe/CdS nanocrystals vs core radius, in the presence of strain and piezoelectricity. (a) Electron states. (b) Hole states. The inset shows the piezoelectric potential in a nanocrystal with $D_c = 3 - 8$ nm.

drastic.⁷ A possible reason is that the models used so far, we have considered independent electron and hole states. This approximation is valid for small cores (except for a rigid energy shift of states due to perturbational effect of electron-hole Coulomb interaction²), but starts failing as the core becomes larger, which is precisely when piezoelectricity scales up. One should bear in mind that the electron-hole Coulomb attraction and piezoelectricity have opposite effects on the wave function (dissociation versus association). Hence, the inclusion of excitonic effects should partly compensate for piezoelectricity. However, in a multi-band description with low symmetry, a full inclusion of Coulomb interactions for the large number of excited hole states involved in the optical spectra that we study (over 40), is beyond our computational capabilities. To obtain some insight into the influence of Coulomb interaction in large-core CdSe/CdS nanocrystals, we computed $1S$ and $1P$ electron and hole states up to the first iteration of a self-consistent process in a nanocrystal with $D_c = 7$ nm, using a Schrödinger-Poisson scheme⁷. We consider the Coulomb potential exerted by $1S_{3/2}$ holes (averaging the charge density of

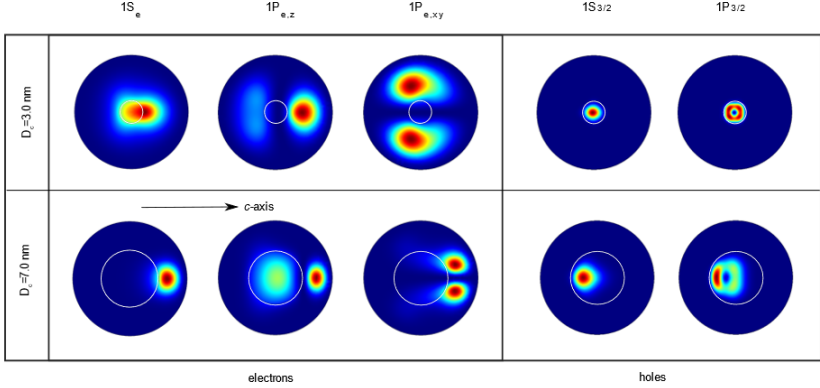


Figure B.7: Same as Figure B.5 but in the presence of strain and piezoelectricity.

different F_z projections) on $1S_e$ electrons (and vice-versa), and that of (averaged) $1P_{3/2}$ holes on $1P_e$ electrons (and vice-versa). The results are summarized in Figure B.9. The left part of the figure (wz) shows the electron and hole states in the absence of strain and Coulomb effects. As discussed above, the inclusion of strain and piezoelectricity (centre of figure, wz+PZ) blue shifts both electron and hole states, and splits states with the same total angular momentum, such as $1P_e$ (three-fold degenerate) which now splits into $1P_{xy}$ (two-fold degenerate) and $1P_z$ (see red dots in the middle of the top panel). The inclusion of Coulomb interaction (right of the figure, wz+PZ+COUL) stabilizes both electron and hole states energetically. The effect is more pronounced on P orbitals than on S orbitals, because $1P_e - 1P_{3/2}$ states are more delocalized and hence have larger overlap than $1S_e - 1S_{3/2}$ states (recall Figure B.8). Consequently, P -orbitals energetically approach S -orbitals. It is important to note that for holes this means $1S_{3/2}$ and $1P_{3/2}$ states can both be within thermal energy at room temperature, and even cross each other.

All in all, the self-consistent calculations show that in large-core nanocrystals, piezoelectricity prevails over Coulomb interactions in determining the electronic structure. Importantly however, in our experiments the splitting between transitions corresponding to $1P_{e,z}$ and $1P_{e,xy}$ states is

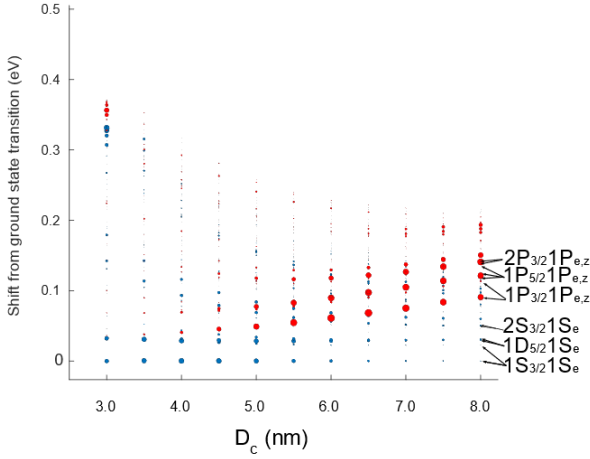


Figure B.8: Same as Figure B.4, for a wz structure including strain and piezoelectricity. Blue (red) dots are used for transitions involving $1S_e$ ($1P_{e,z}$) states.

not resolved. Likewise, the measured transient absorption spectra do not reflect particularly weak fundamental transitions ($1S_e - 1S_{3/2}$) even in the case of the large-core nanocrystals. This suggests that the effect of the piezoelectric potential is overestimated in our calculations. Core/shell interface alloying -which reduces strain and piezoelectric contrast- may be responsible for this deviation. Therefore, in the main text we opt to assign spectral bands simply using a wz Hamiltonian, disregarding strain and Coulomb effects. Yet, in the analysis of the results, we bear in mind the main qualitative features reported here: piezoelectricity may split electron orbitals with $L > 0$ ($1P_e$, $1D_e$...) and reduce electron-hole overlap, especially for low-energy states; Coulomb interactions lead to an approach of P -state excitons (mainly those with P_z projection) to S -state excitons. Figures B.6-B.9 provide upper bounds for such effects.

B.1.3 Supporting Experimental Data

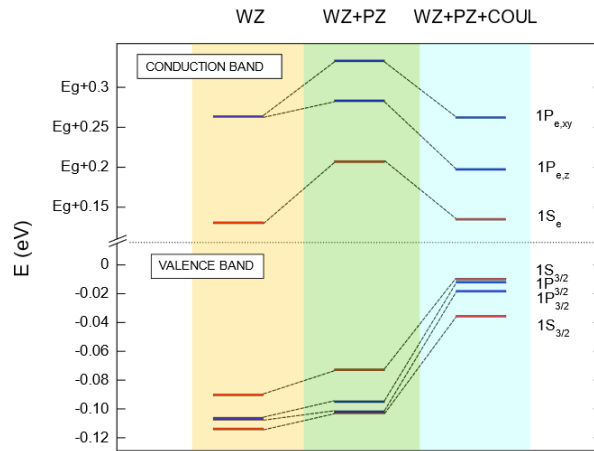


Figure B.9: Sketch of 3 different cases involving $1S_e$ and $1P_e$ with $1S_{3/2}$ and $1P_{3/2}$ energy levels: no inclusion of piezoelectricity nor strain (left), only inclusion of piezoelectricity (middle) and strain + piezoelectricity inclusion (right). Red (blue) bars stand for S (P) states. Guide lines are displayed for tracking energy levels through the different cases for $D_c = 7$ nm and $D_s = 15$ nm.

Transition	λ_{Abs} (nm)	λ_{Gain} (nm)	Pop (%)	Transition	λ_{Abs} (nm)	λ_{Gain} (nm)	Pop (%)
$1S_e - 1S_{3/2}$	640	627	48.39	$1D_e - 1D_{5/2}$	561	551	1.33
$1S_e - 1S_{3/2}$	631	618	15.48	$1D_e - 1D_{5/2}$	557	547	0.69
$1S_e - 1D_{5/2}$	613	601	1.79	$2P_e - 1P_{3/2}$	560	550	14.47
$1S_e - 1D_{5/2}$	611	599	1.33	$2P_e - 1P_{3/2}$	557	547	9.47
$1S_e - 1D_{5/2}$	606	594	0.69	$1D_e - 2S_{3/2}$	557	547	0.69
$1S_e - 2S_{3/2}$	606	594	0.69	$1D_e - 2S_{3/2}$	555	545	0.57
$1S_e - 2S_{3/2}$	605	593	0.57	$1P_e - 2P_{5/2}$	554	544	0.07
$2S_e - 1S_{3/2}$	595	584	48.39	$1P_e - 2P_{5/2}$	553	543	0.07
$2S_e - 1S_{3/2}$	587	576	15.48	$1P_e - 2P_{5/2}$	553	543	0.06
$1P_e - 1P_{3/2}$	590	579	14.47	$1F_e - 1P_{3/2}$	554	544	3.31
$1P_e - 1P_{3/2}$	587	576	9.47	$1F_e - 1P_{3/2}$	552	542	2.39
$1D_e - 1S_{3/2}$	585	574	48.39	$1F_e - 1P_{3/2}$	539	529	0.27
$1D_e - 1S_{3/2}$	577	567	15.48	$2P_e - 1P_{5/2}$	551	541	3.31
$1S_e - 1S_{1/2}$	579	568	0.02	$2P_e - 1P_{5/2}$	549	539	2.39
$1P_e - 1P_{5/2}$	579	569	3.31	$2P_e - 1P_{5/2}$	535	526	0.27
$1P_e - 1P_{5/2}$	577	566	2.39	$2S_e - 1S_{1/2}$	542	532	0.02
$1P_e - 1P_{5/2}$	563	552	0.27	$1F_e - 1P_{1/2}$	538	529	0.25
$2S_e - 1D_{5/2}$	572	561	1.79	$2P_e - 1P_{1/2}$	535	526	0.25
$2S_e - 1D_{5/2}$	570	559	1.33	$1D_e - 1S_{1/2}$	534	524	0.02
$2S_e - 1D_{5/2}$	565	555	0.69	$1F_e - 2F_{5/2}$	531	522	0.07
$2S_e - 2S_{3/2}$	565	555	0.69	$1F_e - 2F_{5/2}$	530	521	0.07
$2S_e - 2S_{3/2}$	564	554	0.57	$1F_e - 2P_{5/2}$	530	521	0.06
$1F_e - 1P_{3/2}$	564	553	14.47	$2P_e - 2P_{5/2}$	528	519	0.07
$1F_e - 1P_{3/2}$	561	551	9.47	$2P_e - 2P_{5/2}$	527	518	0.07
$1P_e - 1P_{1/2}$	562	552	0.25	$2P_e - 2P_{5/2}$	527	518	0.06
$1D_e - 1D_{5/2}$	563	553	1.79				

Table B.5: Transition wavelengths and fractional hole population, normalized to all hole calculated hole states, for sample A with a 4.0 nm core. Bold states and corresponding wavelengths correspond to either $1S_e$ electron states, or S - and P -hole states with sizeable thermal population. To match the calculated transitions to the experimental TA bleach spectra, a fixed 177 meV red shift is applied to all transitions. To match calculated transitions to the experimental gain spectra, we applied a shift of 137 meV.

B.1. Theoretical Analysis of the electronic Structure

Transition	λ_{Abs} (nm)	λ_{Gain} (nm)	Pop (%)	Transition	λ_{Abs} (nm)	λ_{Gain} (nm)	Pop (%)
$1S_e - 1S_{3/2}$	650	652	19.41	$2S_e - 2S_{3/2}$	548	550	5.22
$1S_e - 1S_{3/2}$	642	644	8.06	$2S_e - 2S_{3/2}$	547	549	4.4
$1S_e - 1S_{3/2}$	639	640	5.22	$2S_e - 1D_{5/2}$	547	548	4.06
$1S_e - 1S_{3/2}$	637	639	4.4	$2S_e - 1D_{5/2}$	546	548	3.63
$1S_e - 1D_{5/2}$	636	638	4.06	$2S_e - 1D_{5/2}$	545	547	3.13
$1S_e - 1D_{5/2}$	635	637	3.63	$1F_e - 1P_{3/2}$	538	540	10.94
$1S_e - 1D_{5/2}$	634	636	3.13	$1F_e - 1P_{3/2}$	538	540	10.5
$1P_e - 1P_{3/2}$	606	608	10.94	$1F_e - 1P_{5/2}$	535	537	6.26
$1P_e - 1P_{3/2}$	605	607	10.5	$1F_e - 1P_{5/2}$	533	534	4.38
$1P_e - 1P_{5/2}$	602	603	6.26	$1F_e - 1P_{5/2}$	529	531	2.32
$1P_e - 1P_{5/2}$	599	601	4.38	$2P_e - 1P_{3/2}$	532	534	10.94
$1P_e - 1P_{5/2}$	594	596	2.32	$2P_e - 1P_{3/2}$	532	533	10.5
$1P_e - 2P_{3/2}$	590	592	1.37	$2P_e - 1P_{5/2}$	529	530	6.26
$1P_e - 2P_{3/2}$	588	589	0.96	$2P_e - 1P_{5/2}$	527	528	4.38
$1P_e - 2P_{3/2}$	588	589	0.95	$2P_e - 1P_{5/2}$	523	525	2.32
$1P_e - 2P_{5/2}$	587	589	0.85	$1F_e - 2P_{3/2}$	526	528	1.37
$1P_e - 2P_{5/2}$	587	588	0.81	$1F_e - 2P_{3/2}$	524	526	0.96
$1D_e - 1S_{3/2}$	572	573	19.41	$1F_e - 2P_{5/2}$	524	526	0.95
$1D_e - 1S_{3/2}$	566	567	8.06	$1F_e - 2P_{5/2}$	524	525	0.85
$1D_e - 2S_{3/2}$	563	564	5.22	$1F_e - 2P_{5/2}$	523	525	0.81
$1D_e - 2S_{3/2}$	562	563	4.4	$2P_e - 2P_{3/2}$	520	522	1.37
$1D_e - 1D_{5/2}$	561	563	4.06	$2P_e - 2P_{3/2}$	518	520	0.96
$1D_e - 1D_{5/2}$	561	562	3.63	$2P_e - 2P_{5/2}$	518	520	0.95
$1D_e - 1D_{5/2}$	560	561	3.13	$2P_e - 2P_{5/2}$	518	519	0.85
$2S_e - 1S_{3/2}$	557	558	19.41	$2P_e - 2P_{5/2}$	517	519	0.81
$2S_e - 1S_{3/2}$	551	553	8.06				

Table B.6: Transition wavelengths and fractional hole population, normalized to all hole calculated hole states, for sample B with a 7.5 nm core. Bold states and corresponding wavelengths correspond to either $1S_e$ electron states, or S - and P -hole states with sizeable thermal population. To match the calculated transitions to the experimental spectrum, a fixed 20.5 meV red shift is applied to all transitions. To match calculated transitions to the experimental gain spectra, we applied a shift of 26.4 meV.

Bibliography

- ¹ David J Norris and MG Bawendi. Measurement and assignment of the size-dependent optical spectrum in cdse quantum dots. *Physical Review B*, 53(24):16338, 1996.
- ² Alexey I Ekimov, F Hache, MC Schanne-Klein, D Ricard, Chr Flytzanis, IA Kudryavtsev, TV Yazeva, AV Rodina, and Al L Efros. Absorption and intensity-dependent photoluminescence measurements on cdse quantum dots: assignment of the first electronic transitions. *JOSA B*, 10(1):100–107, 1993.
- ³ Al L Efros and M Rosen. Quantum size level structure of narrow-gap semiconductor nanocrystals: Effect of band coupling. *Physical Review B*, 58(11):7120, 1998.
- ⁴ Jian-Bai Xia. Electronic structures of zero-dimensional quantum wells. *Physical Review B*, 40(12):8500, 1989.
- ⁵ Jian-Bai Xia and Jingbo Li. Electronic structure of quantum spheres with wurtzite structure. *Physical Review B*, 60(16):11540, 1999.
- ⁶ Yu M Sirenko, JB Jeon, BC Lee, KW Kim, MA Littlejohn, MA Stroschio, and GJ Iafrate. Hole scattering and optical transitions in wide-band-gap nitrides: Wurtzite and zinc-blende structures. *Physical Review B*, 55(7):4360, 1997.
- ⁷ Carlos Segarra, Juan I Climente, Anatolii Polovitsyn, Fernando Rajadell, Iwan Moreels, and Josep Planelles. Piezoelectric control of the exciton wave function in colloidal cdse/cds nanocrystals. *The Journal of Physical Chemistry Letters*, 7(12):2182–2188, 2016.
- ⁸ Louis E Brus. A simple model for the ionization potential, electron affinity, and aqueous redox potentials of small semiconductor crystallites. *The Journal of chemical physics*, 79(11):5566–5571, 1983.

- ⁹ J Mi Luttinger. Quantum theory of cyclotron resonance in semiconductors: General theory. *Physical review*, 102(4):1030, 1956.
- ¹⁰ EP Pokatilov, VA Fonoberov, VM Fomin, and JT Devreese. Development of an eight-band theory for quantum dot heterostructures. *Physical Review B*, 64(24):245328, 2001.
- ¹¹ SL Chuang and CS Chang. kp method for strained wurtzite semiconductors. *Physical Review B*, 54(4):2491, 1996.
- ¹² Josep Planelles, F Rajadell, and Juan I Climente. Hole band mixing in cds and cdse quantum dots and quantum rods. *The Journal of Physical Chemistry C*, 114(18):8337–8342, 2010.
- ¹³ Josep Planelles, Fernando Rajadell, and Juan I Climente. Electronic origin of linearly polarized emission in cdse/cds dot-in-rod heterostructures. *The Journal of Physical Chemistry C*, 120(48):27724–27730, 2016.
- ¹⁴ J-B Jeon, Yu M Sirenko, KW Kim, MA Littlejohn, and MA Stroscio. Valence band parameters of wurtzite materials. *Solid state communications*, 99(6):423–426, 1996.
- ¹⁵ S. Ithurria, M. D. Tessier, B. Mahler, R. P. S. M. Lobo, B. Dubertret, and Al. L. Efros. Colloidal Nanoplatelets with Two-Dimensional Electronic Structure. *Nat. Mater.*, 10(10):1–6, oct 2011.
- ¹⁶ DW Langer, RN Euwema, Koh Era, and Takao Koda. Spin exchange in excitons, the quasicubic model and deformation potentials in ii-vi compounds. *Physical Review B*, 2(10):4005, 1970.
- ¹⁷ Sotirios Christodoulou, Fernando Rajadell, Alberto Casu, Gianfranco Vaccaro, Joel Q Grim, Alessandro Genovese, Liberato Manna, Juan I Climente, Francesco Meinardi, Gabriele Raino, et al. Band structure engineering via piezoelectric fields in strained anisotropic cdse/cds nanocrystals. *Nature communications*, 6(1):1–8, 2015.

